AD-A192 169 RESEARCH ON AERO-THERMODYNAMIC DISTORTION INDUCED STRUCTURAL DYNAMIC RESP..(U) PURDUE UNIV LAFAYETTE IND THERMAL SCIENCES AND PROPULSION CEN.. S FLEETER

1/3

UNCLASSIFIED 15 JAN 88 ME-TSPC-TR-88-10 AFOSR-TR-88-0045 F/G 1/1 NL

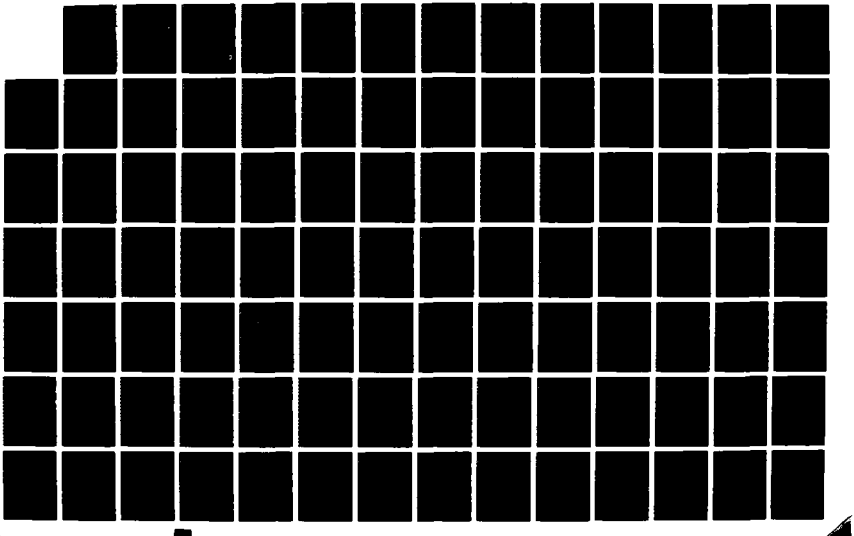

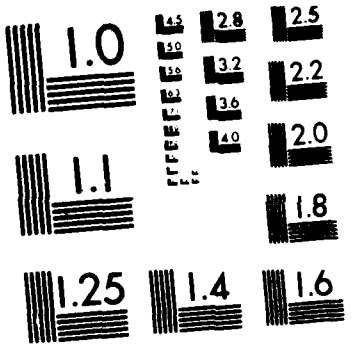

AD-A192 169 FILE COPY

REPORT DOCUMENTATION PAGE

Unclassified	1b. RESTRICTIVE MARKINGS
2a. SECURITY CLASSIFICATION AUTHORITY	3. DISTRIBUTION / AVAILABILITY OF REPORT: Approved for public release; distribution is unlimited.
2b. DECLASSIFICATION / DOWNGRADING SCHEDULE	
4. PERFORMING ORGANIZATION REPORT NUMBER(S): ME-TSPC-TR-88-10	5. MONITORING ORGANIZATION REPORT NUMBER(S): AFOSR-TR-88-0045
6a. NAME OF PERFORMING ORGANIZATION: School of Mechanical Engr. Purdue University; 6b. OFFICE SYMBOL (If applicable):	7a. NAME OF MONITORING ORGANIZATION: AFOSR/NA
6c. ADDRESS (City, State, and ZIP Code): Thermal Sciences & Propulsion Center Purdue University West Lafayette, IN 47907	7b. ADDRESS (City, State, and ZIP Code): Building 410, Bolling AFB DC 20332-6448
8a. NAME OF FUNDING / SPONSORING ORGANIZATION: AFOSR/NA; 8b. OFFICE SYMBOL (If applicable): NA	9. PROCUREMENT INSTRUMENT IDENTIFICATION NUMBER: F49620-83-K-0029
8c. ADDRESS (City, State, and ZIP Code): Building 410, Bolling AFB DC 20332-6448	10. SOURCE OF FUNDING NUMBERS: PROGRAM ELEMENT NO. 61102F; PROJECT NO. 2307; TASK NO. A4; WORK UNIT ACCESSION NO.
11. TITLE (Include Security Classification): (U) Research on Aero-Thermodynamic Distortion Induced Structural Dynamical Response of Multi-Stage Compressor Blading	
12. PERSONAL AUTHOR(S): Sanford Fleeter	
13a. TYPE OF REPORT: Final; 13b. TIME COVERED: FROM 4/83 TO 11/87	14. DATE OF REPORT (Year, Month, Day): 88-1-15; 15. PAGE COUNT: 237
16. SUPPLEMENTARY NOTATION	
17. COSATI CODES: FIELD / GROUP / SUB-GROUP	18. SUBJECT TERMS (Continue on reverse if necessary and identify by block number): Gas Turbine, Aeroelasticity Structural Dynamics, Unsteady Aerodynamics

19. ABSTRACT (Continue on reverse if necessary and identify by block number)

The overall objective of this research program was to quantitatively investigate the fundamental phenomena relevant to aero-thermodynamic distortion induced structural dynamic blade responses in multi-stage gas turbine engine components. The technical approach involved both experiment and analysis. (1) The flow physics of multi-stage blade row interactions has been experimentally investigated, with unique high reduced frequency unsteady aerodynamic data obtained to understand, quantify, and discriminate the fundamental flow phenomena as well as to direct the modeling of advanced analyses. (2) The development of an unsteady viscous flow analysis appropriate for aerodynamic forced response predictions was initiated. (3) A structural dynamics model based on an energy balance technique coupled with the unsteady aerodynamic analyses under development is being utilized to investigate aerodynamically forced response of turbomachine blade rows.

Keywords:

20. DISTRIBUTION / AVAILABILITY OF ABSTRACT: ☒ UNCLASSIFIED/UNLIMITED ☒ SAME AS RPT ☐ OTIC USERS	21. ABSTRACT SECURITY CLASSIFICATION: Unclassified
22a. NAME OF RESPONSIBLE INDIVIDUAL: Dr. Henry Helin	22b. TELEPHONE (Include Area Code): (202) 767-4935; 22c. OFFICE SYMBOL: AFOSR/NA

DD FORM 1473, 84 MAR 83 APR edition may be used until exhausted. All other editions are obsolete.

SECURITY CLASSIFICATION OF THIS PAGE: UNCLASSIFIED

Report ME-TSPC-TR-88-10

FINAL TECHNICAL REPORT

GRANT F 49620-83-K-0029

RESEARCH ON

AERO-THERMODYNAMIC DISTORTION INDUCED STRUCTURAL DYNAMIC RESPONSE OF MULTI-STAGE COMPRESSOR BLADING

Sanford Fleeter

January 1988

Thermal Sciences and Propulsion Center
School of Mechanical Engineering
Purdue University
West Lafayette, Indiana 47907

Prepared For

Directorate of Aerospace Sciences
Air Force Office of Scientific Research

TABLE OF CONTENTS

ABSTRACT

This report summarizes the results obtained on Grant F-49620-83-K-0029. The overall objective of this research program was to quantitatively investigate the fundamental phenomena relevant to aero-thermodynamic distortion induced structural dynamic blade responses in multi-stage gas turbine engine components. The technical approach involved both experiment and analysis. (1) The flow physics of multistage blade row interactions have been experimentally investigated, with unique unsteady aerodynamic data obtained to understand, quantify, and discriminate the fundamental flow phenomena as well as to direct the modeling of advanced analyses. In particular, data have been obtained to define the potential and viscous flow interactions and their effect on both the aerodynamic forcing function and the resulting unsteady aerodynamics of turbomachine rotor blades and stator vanes in a multistage environment at realistic high reduced frequency values for the first time. (2) Analytically, the development of an unsteady viscous flow analysis appropriate for aerodynamic forced response predictions was initiated. (3) A structural dynamics model based on an energy balance technique was developed and utilized to investigate aerodynamically forced response of turbomachine blade rows, accomplished by coupling this model with the unsteady aerodynamic analyses under development.

I. INTRODUCTION

The structural dynamic response of fan, compressor, and turbine blading to aero-thermodynamic distortion induced excitations is an item of rapidly increasing concern to designers and manufacturers of gas turbine engines for advanced technology applications. Destructive aerodynamically forced responses of turbomachinery blading have been generated by a wide variety of aero-thermodynamic distortion sources including: blade wakes; multistage interactions; large angle of attack or yaw; engine exhaust recirculation; cross-flow at the inlet; pressure variations on the engine due to external aerodynamics; and armament firing.

The primary mechanism of blade failure is fatigue caused by vibration at levels exceeding the material endurance limits. These vibrations occur when a periodic forcing function, with frequency equal to a natural blade resonant frequency, acts upon a blade row. Because a blade may have as many critical points of high stress as it has natural modes, the designer must determine which particular modes have the greatest potential for aerodynamic excitation. With the resonant airfoil frequencies able to be accurately predicted with finite element structural models, Campbell diagrams are the key design tool. These display the natural frequency of each blade mode versus rotor speed and, on the same figure, the aerodynamic forcing function frequency versus rotor speed. At each intersection point, an aerodynamically induced vibration problem is possible. Thus these intersection points, termed resonant speeds, define the operating conditions for potentially

significant increases in vibratory blade response. However, Campbell diagrams provide no measure of the amplitude of the resulting stress at a resonant speed.

The accurate first principles prediction of the aerodynamically forced response vibratory behavior of a rotating or stationary airfoil row requires a definition of the unsteady aerodynamic forcing function in terms of its harmonics. The time-variant aerodynamic response of the airfoil to each harmonic of this forcing function is then assumed to be comprised of two parts: the disturbance being swept past the nonresponding airfoils and the airfoil vibratory response to this disturbance. The blade row response is then predicted with an aeroelastic model which is typically based on a classical Newton's second law approach, with the unsteady aerodynamics combined with a lumped parameter airfoil model and an iterative solution procedure utilized.

The unsteady aerodynamic generally are modeled by two distinct analyses. A gust analysis is used to predict the time-variant aerodynamics of the nonresponding airfoils to each harmonic of the disturbance. A motion-induced unsteady aerodynamic analysis wherein the airfoils are assumed to be harmonically oscillating is then used to determine the additional unsteady aerodynamic effects due to the airfoil vibratory response. Typically, the superposition of these two effects can only be performed with knowledge of the modal pattern and amplitude of response of the airfoils.

Unsteady aerodynamic models are generally based on potential flow theory, with the unsteady flow generated by periodic gusts or oscillating airfoils considered to be a small perturbation to a uniform mean flow. In this linear approximation, the

steady and unsteady flow fields are uncoupled. However, these unsteady linear theories are not valid for flows about lifting airfoils or loaded airfoils where the thickness, camber, and incidence angle are not too small. For these situations, nonuniform mean flows must be considered, resulting in a coupling between the unsteady and steady flow fields.

There are many analytical and physical assumptions inherent in the various mathematical models. However, minimal attention has been given to either the aerodynamic forcing function or to the blade row interactions, i.e., only isolated airfoil rows are considered. Also, there is a fundamental question concerning the applicability of the Kutta condition for unsteady flows, particularly at the high reduced frequency values inherent in turbomachines, with viscous effects only beginning to be considered.

Experimentally, very limited appropriate fundamental unsteady aerodynamic data exist to verify existing models, with these data generally not suitable to discriminate and quantify the fundamental flow phenomena and direct the development of advanced mathematical models. Also, all of the existing data have been obtained in isolated blade rows or in single stages. Thus, the important effects associated with multistaging, including the blade row potential and viscous flow interactions, have not been investigated.

II. PROGRAM OBJECTIVES & TECHNICAL APPROACH

The overall objective of this research program was to quantitatively investigate the fundamental phenomena relevant to aero-thermodynamic distortion induced structural dynamic blade responses in multistage gas turbine engine components.

The technical approach required both experiment and analysis, with the program objectives achieved as follows.

* The flow physics of multistage blade row interactions were experimentally investigated, with unique unsteady aerodynamic data obtained to understand, quantify, and discriminate the fundamental flow phenomena as well as to direct the modeling in advanced analyses. These data defined the potential and viscous flow interactions and their effect on both the aerodynamic forcing function and the resulting unsteady aerodynamics of compressor airfoils in a multistage environment at realistic high reduced frequency values for the first time.

* The development of an unsteady aerodynamic model which considers viscous effects was initiated.

* A structural dynamics model based on an energy balance technique was developed and utilized to investigate aerodynamically forced response of turbomachine blade rows.

This research program was thus directed at providing fundamental time-variant aerodynamic data which not only address the validity of the most basic assumptions inherent in unsteady aerodynamics analyses and in the structure of

forced response design systems, but also are appropriate to direct the development of advanced models as well as to validate and indicate refinements to the current state-of-the-art unsteady aerodynamic gust analyses. Also, first principles predictive aerodynamically forced response models, including viscous effects, are being developed.

III. RESULTS

An overview of the accomplishments of this research program is presented in the following. The detailed results are contained in both the publications and the graduate student theses. These research results are categorized as: (1) Unsteady Aerodynamic Experiments; (2) Unsteady Aerodynamic Modeling; and (3) Aeroelasticity.

A. UNSTEADY AERODYNAMIC EXPERIMENTS

STATIONARY VANE ROWS

* Unsteady data analysis techniques were developed and applied to stationary vane rows.

* The variations in the instantaneous rotor wake data, the aerodynamic forcing function to the downstream stator vanes, were shown to be due to the vortex street structure contained in the wakes.

The unsteady (and steady) aerodynamics on each vane row of a multistage compressor were investigated, including the effects of both the transverse, v^+, and the chordwise, u^+, first harmonic gust components on the resulting vane row unsteady pressure differences for the first time. Analysis of these unique data determined the following.

* There is a strong coupling between the gust generated vane surface unsteady aerodynamic magnitude and phase data and the detailed steady loading distribution, not the incidence angle, on the individual stator vane surfaces.

* The relative magnitude of the transverse and chordwise gust components has a significant effect on the vane surface unsteady aerodynamics. In particular, the transverse gust component, v^+, influences both the magnitude and phase of the vane surface unsteady pressure distributions. The chordwise gust component, u^+, also affects both the surface unsteady pressure magnitude and phase data, but with a larger effect on the phase than either the steady loading or the transverse component of the gust.

* The solidity of the vane row primarily affects the phase of the unsteady pressure generated by the gust.

* Multistage potential interactions have no effect on the steady aerodynamics. However, these interactions have a significant affect on the unsteady aerodynamics of the individual vane surfaces.

* For a very low solidity vane row, i.e., an isolated airfoil, steady flow separation influences both the surface unsteady pressure magnitude and phase data, with the primary effect being on the phase.

* For the very low solidity vane row, steady flow separation affects both the harmonic content and the waveform of the unsteady pressure on the suction surface upstream of the chordwise position of the flow separation.

ROTATING BLADE ROWS

* Rotating blade row unsteady data acquisition and analysis techniques were developed. These are being utilized to obtain gust generated unsteady aerodynamic data on the rotor blade row of an extensively instrumented multistage axial flow research compressor. In particular, a series of experiments have been initiated to investigate the effects of steady aerodynamic loading on the unsteady gust aerodynamics of a first stage rotor blade, with the high reduced frequency gust generated by the wakes from the inlet guide vanes. The multistage effects associated with compressor rotor-stator blade row operation in the superresonant flow regime wherein acoustic waves propagate are also being considered. These initial first stage rotor blade row experiments have demonstrated the following.

* Steady loading affects the static pressure distribution on the front portion of the rotor blade pressure surface and over the entire suction surface.

* Loading has only a small effect on the unsteady pressure surface phase data, but a large effect on the magnitude data over the front half of the surface, corresponding to the steady data.

* The unsteady pressure magnitude and phase data on the entire suction surface are influenced by the level of steady aerodynamic loading, corresponding to the steady surface data.

* As the steady loading is increased, the decreased magnitude region near the front of the suction surface moves forward, with the minimum corresponding to the location where the steady flow acceleration changes to a

deceleration.

* Loading primarily affects the unsteady phase data on the aft half of the blade suction surface.

* As the incidence angle is increased, the linear chordwise distribution of the phase data show a wave phenomenon on the suction surface convected at the mean axial velocity of the flow through the rotor blade row.

* The effects of loading on the pressure and suction surface unsteady data are reflected in the dynamic pressure difference data.

A superresonant condition was also established in the compressor, accomplished by altering the number of vanes in each downstream stator row. This resulted in the generation of a relatively large amplitude upstream propagating acoustic wave generated by the interactions between the downstream rotor and stator rows.

* Upstream, at the entrance to the first stage rotor blade row, the acoustic wave has a larger amplitude than that generated by the first harmonic of the inlet guide vane wakes.

* Loading has minimal effect on the resulting rotor blade surface acoustic wave generated unsteady pressure magnitude data, with increased loading increasing the level but not the chordwise distribution of the phase data.

* The linear, constant slope, chordwise distributions of the rotor blade surface phase data corresponds to a wave speed equal to the speed of propagation of an upstream traveling acoustic wave.

EXPERIMENT IMPLICATIONS

* Unsteady aerodynamic data acquisition and analysis techniques need in-depth consideration in order to obtain valid data.

* The detailed steady loading, not the incidence angle, is the key parameter with regard to unsteady aerodynamics. Thus, valid unsteady aerodynamic models and experiments require an accurate description of the steady aerodynamics.

* Subtle steady aerodynamic experimental changes can result in large effects on the blade row interactions and the aerodynamic forcing function as well as the resulting blade and vane row unsteady aerodynamics.

* The interactions of both upstream and downstream airfoil rows have a significant effect on the gust generated unsteady aerodynamics.

* Potential interactions as well as viscous interactions are important.

* The variation of the waveform of the unsteady data cannot be predicted with harmonic unsteady aerodynamic models.

* Small perturbation models may not be appropriate for unsteady separated flows.

* The ability demonstrated in these experiments to experimentally control the two-dimensional gust transverse and chordwise components indicates the feasibility of aeroelastic tailoring for potentially large steady performance gains by control of unsteady aerodynamics and the various airfoil row interactions.

B. UNSTEADY AERODYNAMIC MODELING

An analysis has been developed which models the unsteady aerodynamics of an harmonically oscillating flat plate airfoil, including the effects of mean flow incidence angle, in an incompressible laminar flow at moderate values of the Reynolds number. The unsteady viscous flow is assumed to be a small perturbation to the steady viscous flow field. Hence, the Kutta condition is not appropriate for either the steady or the unsteady flow fields. The steady flow field is described by the Navier-Stokes equations. It is thus nonlinear and nonuniform. Also, the steady flow field is independent of the unsteady flow field. The small perturbation unsteady viscous flow is described by a system of linear partial differential equations that are coupled to the steady flow field, thereby modeling the strong dependence of the unsteady aerodynamics on the steady flow.

Solutions for both the steady and the unsteady viscous flow fields are obtained by developing a locally analytical method in which the discrete algebraic equations which represent the flow field equations are obtained from analytical solutions in individual grid elements. For the steady viscous flow, this is accomplished by first locally linearizing the nonlinear convective terms in the Navier-Stokes equations. General analytical solutions to the flow field equations are then determined. Locally analytical solutions are developed by applying these solutions to individual grid elements, with the integration and separation constants determined from the boundary conditions on each grid element. The complete flow field solutions are then obtained through the application of the global boundary conditions. It should be noted that the nonlinear character of the complete steady flow field is preserved

as the flow is only locally linearized, i.e., independently linearized solutions are obtained in individual grid elements.

C. AEROELASTICITY

Arbitrary profile isolated airfoil gust and motion induced models have been combined with an energy balance technique for the prediction of aerodynamically forced response. In particular, an energy balance was performed between the unsteady aerodynamic work and the energy dissipated through the airfoil structural and aerodynamic damping. Also, a model has been implemented to predict the random, torsion mode vibrations of a blade row generated by turbulence.

IV. PUBLICATIONS

A. UNSTEADY AERODYNAMIC EXPERIMENTS

Capece, V. and Fleeter, S., "First Stage Stator Vane Unsteady Aerodynamic Response in a Multi-Stage Compressor," *AIAA Paper 84-1209*, June 1984.

Fleeter, S. and Capece, V.R., "Stator Row Unsteady Aerodynamics Due to Wake Excitations," *International Symposium on Unsteady Aerodynamics of Turbomachines and Propellers*, Cambridge, England, September 1984.

Hill, Vincent C., "Unsteady Pressure Measurements in a Three Stage Axial Flow Compressor," *Purdue University M.S.E. Thesis*, August 1984.

Fleeter, S. and Capece, V.R., "Unsteady Aerodynamics of a Stator Vane Row" *Seventh International Symposium on Air Breathing Engines*, Beijing, People's Republic of China, September 1985.

Capece, V.R., Manwaring, S.R., and Fleeter, S., "Unsteady Blade Row Interactions in a Multi-Stage Compressor," *(AIAA Paper 85-1134), AIAA Journal of Propulsion and Power*, Vol. 2, No. 2, March-April, 1986.

Capece, V.R. and Fleeter, S., "Wake Induced Unsteady Interactions In a Multi-Stage Compressor," *(AIAA Paper 86-1455), AIAA Journal of Propulsion and Power*, accepted for publication.

Capece, V.R. and Fleeter, S., "The Unsteady Aerodynamics of a First Stage Vane Row," *Experiments in Fluids*, Vol. 4, No. 2, 1986.

Capece, V.R. and Fleeter, S., "Time-Variant Data Acquisition and Analysis for Gas Turbine Airfoil Rows," *Institution of Mechanical Engineers, (International Conference on Computers in Engine Technology)*, Cambridge, March 1987.

Capece, Vincent R., "Forced Response Unsteady Aerodynamics in a Multistage Compressor," *Purdue University Ph.D. Thesis*, May 1987.

Capece, V.R. and Fleeter, S., "Unsteady Aerodynamic Interactions in a Multi-Stage Compressor," (ASME Paper 87-GT-171), *ASME Journal of Turbomachinery*, Vol. 109, No. 3, July 1987.

Capece, V.R. and Fleeter, S., "Experimental Investigation of Multi-Stage Interaction Gust Aerodynamics," *4th International Symposium on Unsteady Aerodynamics and Aeroelasticity of Turbomachines and Propellers*," Aachen, West Germany, September, 1987.

Capece, V.R. and Fleeter, S., "Measurement and Analysis of Unsteady Flow Structures in Rotor Blade Wakes," *Experiments in Fluids*, accepted for publication.

Capece, V.R. and Fleeter, S., "Experimental Investigation of Multistage Interaction Gust Aerodynamics," *ASME Paper 88-GT- , ASME Gas Turbine Conference, June 1988 (accepted for publication, ASME Journal of Turbomachinery).*

B. UNSTEADY AERODYNAMIC MODELING

Schroeder, L.M. and Fleeter, S., "Local Linearization Numerical Method for Steady Internal Viscous Flows," *SIAM Paper 86-30*, SIAM 1986 National Meeting, July 1986.

Chiang, H.D. and Fleeter, S., "Locally Analytic Oscillating Airfoil Aerodynamics," *IACM First World Congress on Computational Mechanics*, September 1986.

Schroeder, Linda M., "Prediction of the Incompressible Viscous Flow Past An Oscillating Flat Plate Airfoil by a Locally Analytic Method," *Purdue University M.S.M.E. Thesis*, December 1986.

Chiang, H.D., and Fleeter, S., "Prediction of Loaded Airfoil Unsteady Aerodynamic Gust Response by a Locally Analytical Method,"*(Sixth International Conference on Mathematical Modeling*, August, 1987 Invited paper.) *International Journal of Mathematical Modeling*, accepted for publication.

Schroeder, L. and Fleeter, S., "Locally Analytic Numerical Method and Application to Viscous Internal and External Flows," *International Journal of Computers and Mathematics with Applications*, accepted for publication.

Chiang, H.D., and Fleeter, S., "Prediction of Oscillating Thick Cambered Airfoil Aerodynamics by a Locally Analytic Method," *International Journal for Numerical Methods in Fluids*, accepted for publication.

Schroeder, L.M. and Fleeter, S., Viscous Aerodynamic Analysis of an Oscillating Flat Plate Airfoil with a Locally Analytical Solution," *AIAA Paper 88-0130*, January 1988.

C. AEROELASTICITY

Hoyniak, D. and Fleeter, S., "Prediction of Aerodynamically Induced Vibrations in Turbomachinery Blading," *ASME Journal of Fluids Engineering*, Vol. 105, No. 4, December 1983.

Hoyniak, D. and Fleeter, S., "The Coupled Response of Turbomachinery Blading to Aerodynamic Excitations," *AIAA Journal of Aircraft*, Vol. 21, No. 4, April 1984.

Chiang, H.D. and Fleeter, S., "Flow Induced Vibratory Response of a Loaded Airfoil," *Chinese-American Academic & Professional Convention*, July 1987 (Invited Paper).

Chiang, H.D., and Fleeter, S., "Aerodynamically Forced Response of an Airfoil Including Profile and Incidence Effects," *20th Midwestern Mechanics Conference*, September, 1987.

V. STATUS OF GRADUATED STUDENTS SUPPORTED BY AFOSR

Vincent Hill, M.S.E. - August 1984
Engineer, Garrett Turbine Engine Company
Phoenix, Arizona

Daniel Hoyniak, Ph.D. - May 1986
Aerospace Engineer, NASA-Lewis Research Center
Cleveland, Ohio

Linda Schroeder, M.S.M.E. - December 1986
Senior Engineer
TurboMach (Solar Gas Turbines)
San Diego, California

Vincent Capece, Ph.D. - May 1987
Senior Engineer, Pratt & Whitney
West Palm Beach, Florida

Steven Manwaring, M.S.M.E. - December 1984
Currently Ph.D. candidate
AFRAPT Trainee - General Electric

APPENDIX I

TIME-VARIANT DATA ACQUISITION AND ANALYSIS FOR GAS TURBINE AIRFOIL ROWS

INSTITUTION OF MECHANICAL ENGINEERS

C30/87

Time-variant data acquisition and analysis for gas turbine aerofoil rows

V R CAPECE and **S FLEETER**, PhD
Thermal Sciences and Propulsion Centre, School of Mechanical Engineering, Purdue University, Indiana, USA

SYNOPSIS **Computer based time-variant digital data acquisition and analysis techniques are developed and utilized to investigate the unsteady aerodynamics of airfoil rows, accomplished with a dynamically instrumented first stage vane row of a research compressor. Ensemble averaging is demonstrated, with the removal of higher harmonics by ensemble averaging considered. The fluctuating aerodynamic forcing function to the first stage vane row and the effect of steady aerodynamic loading on the resulting vane surface harmonic pressure distributions are then quantified. Also, the level of steady aerodynamic loading, not the incidence angle, is shown to be the key parameter to obtain good correlation with flat plate airfoil cascade models.**

NOMENCLATURE

C	airfoil chord
C_l	steady lift coefficient, $L'/\frac{1}{2}\rho U_t^2 C$
$C_{\Delta p}$	dynamic pressure difference coefficient, $\Delta p/\rho V_x v^+$
$\bar{C}_p$	vane surface static pressure coefficient, $(\bar{p} - \bar{p}_{ref})/\frac{1}{2}\rho U_t^2$
$f(t)$	time-variant signal
$f^p(t)$	periodic signal
$f^r(t)$	random fluctuating signal
$\bar{f}$	steady state signal
k	reduced frequency, $\omega C/2V_x$
i	incidence angle
L'	steady lift per unit span, $\int_0^C (\bar{p}_p - \bar{p}_s)dx$
N	number of rotor revolutions
$\bar{p}$	vane surface static pressure
$\bar{p}_{ref}$	vane row exit static pressure
Δp	dynamic pressure difference across vane chordline
$s(t)$	time-variant signal composed of periodic and fluctuating components
$\langle s_t \rangle$	ensemble averaged signal
t	time
u^+	inlet velocity parallel to vane
U_t	rotor blade tip speed
v^+	inlet velocity normal to vane
V	absolute velocity
V_x	absolute axial velocity
ρ	stator vane row inlet air density
ω	blade passing frequency

INTRODUCTION

At present, the unsteady flow inherent in gas turbine engines is generally detrimental to both aerodynamic efficiency and durability, references 1 through 4. This is due to the lack of basic knowledge and understanding of the fundamental unsteady flow phenomena.

To eliminate these detrimental effects in advanced high performance components, it is necessary to provide the designer with experimentally verified unsteady aerodynamic models of the fundamental time-variant flow phenomena. However, there is a dearth of appropriate data, with only basic single blade row math models having been developed. Thus, fundamental unsteady data are required to provide a quantitative understanding of the basic unsteady flow phenomena and to validate and direct the development of advanced models.

The most common unsteady aerodynamic forces are the wakes shed by upstream blade or vane rows. For example, in the single compressor stage depicted schematically in Figure 1, the wakes from the upstream rotor are the primary source of the unsteady aerodynamics on the downstream stator vanes, i.e., the exit flow field from the upstream rotor defines the unsteady aerodynamic forcing function to the downstream stator vanes. This aerodynamic forcing function is defined by the velocity components parallel and normal to the vane chord, u^+ and v^+.

The fundamental time-variant data of primary interest define the aerodynamic forcing function and the resulting airfoil surface pressure distributions. The acquisition and analysis of such data has only recently become possible with the development and availability of miniature high-response transducers, digital instrumentation, and computers for both control of instrumentation and digital data analysis.

In this paper, computer based time-variant digital data acquisition and analysis techniques, including ensemble averaging and Fast Fourier Transforms (FFT), are developed for periodic data. The fundamental harmonic airfoil row unsteady aerodynamics are then investigated by applying these techniques to the time-variant signals from high response instrumentation in the first stage vane row of a research compressor. First the digital data acquisition and analysis techniques are demonstrated. Then the fluctuating aerodynamic forcing function to the first stage vane row and the effect of steady aerodynamic loading on the resulting vane surface harmonic pressure distributions are quantified. These vane surface data are also correlated with predictions obtained from a small perturbation flat plate airfoil cascade model.

RESEARCH COMPRESSOR

The Purdue University axial flow research compressor simulates the fundamental time-variant aerodynamic phenomena inherent in gas turbine unsteady blade row interactions. These include the incidence angle, the velocity and pressure variations, the aerodynamic forcing function waveforms, the reduced frequency, and the blade row interactions. This compressor is driven by a 15 HP DC electric motor over a speed range of 300 to 3,000 RPM. The 43 rotor blades and 41 stator vanes of the three identical compressor stages have free vortex design airfoils with a British C4 section profile.

INSTRUMENTATION

Both steady-state and time-variant data are required. The steady-state data define the overall compressor operating point and the detailed vane surface aerodynamic loading. The unsteady data quantify the fluctuating aerodynamic forcing function to the first stage vane row, i.e., the vane row unsteady inlet flow field, and the resulting chordwise distribution of the time-variant pressure on the surfaces of a single vane in the row.

Conventional steady-state instrumentation is used to determine the flow properties throughout the compressor. The steady aerodynamic loading on the vane surfaces is determined by instrumenting a pair of stator vanes with chordwise distributions of mid-span surface static pressure taps. These vanes are positioned in the vane row such that one complete flow passage is instrumented, depicted schematically in Figure 1.

The unsteady aerodynamic forcing function to the vane row, the time-variant vane row inlet flow field, is measured with a cross hot-wire probe positioned axially midway between the rotor and stator rows at mid-stator circumferential spacing, Figure 1. The vane row mean absolute inlet flow angle is determined by rotating the cross-wire probe until a zero voltage difference is obtained between the two hot-wire signals. This mean angle is subsequently used as a reference to calculate the vane incidence angle and the instantaneous absolute and relative flow angles.

The vane surface time-variant pressure measurements are accomplished with ultra-miniature high response transducers. To minimize potential flow disturbances due to the transducer mounting or the inability of the transducer diaphragm to exactly maintain the surface curvature of the vane, a reverse mounting technique is utilized. The pressure surface of one vane and the suction surface of a second are instrumented, with the transducers embedded in the non-measurement surface and connected to the measurement surface by a static tap. As time-variant data on a single vane are of primary interest, this somewhat complicates the data analysis, as will be discussed. These two instrumented airfoils are positioned in the compressor vane row such that one flow passage is instrumented.

DIGITAL DATA ACQUISITION

The digital data acquisition and analysis system schematically depicted in Figure 2, is centered on a Hewlett-Packard HP-1000 computer. It is used to acquire and analyze on-line both steady and time-variant data. The steady data quantify the compressor performance and the aerodynamic loading distributions on the vane surfaces. The time-variant data define the fluctuating aerodynamic forcing function to the vane row and the resulting vane surface unsteady pressure distributions.

The steady-state pressure data are acquired with a 48 channel Scanivalve system. Under computer control, the Scanivalve is calibrated each time data is acquired, with compensation automatically made for variations in the zero and span output. As part of the steady-state data acquisition and analysis process, a root-mean-square error analysis is performed. The steady data are defined as the mean of 30 samples, with the 95% confidence interval determined.

The time-variant data from the hot-wire probe and the dynamic pressure transducers are obtained under computer control by first conditioning their signals and then digitizing them with a high speed A-D system. This eight channel A-D system is able to digitize signals simultaneously at rates to 5 MHz per channel, storing 2048 points per channel. Because of the relatively large number of dynamic pressure transducers, groups of six pressure signals at a time are switched to the signal conditioning and the A-D system by a signal multiplexer. In addition, after conditioning, the time-variant hot-wire probe and pressure transducer signals are monitored by a dynamic signal processor which can digitize, average, and Fourier decompose unsteady analog signals.

The time-variant data of interest are periodic, being generated at rotor blade passing frequency, with a digital ensemble averaging technique used for data analysis. As will be discussed, the key to this technique is the ability to sample data at a preset time. This is accomplished by means of an optical

encoder mounted on the rotor shaft. The microsecond range square wave voltage signal from the encoder is the time or data initiation reference, and triggers the high speed A-D multiplexer system.

PERIODIC DATA ANALYSIS

In general, the time-variant signals from the hot-wire probe and the dynamic pressure transducers are composed of three components: (1) a steady-state component; (2) the periodic component of interest: and (3) a random fluctuating component.

$$f(t) = f^s + f^p(t) + f^r(t) \qquad (1)$$

where f^s, f^p and f^r , denote the steady-state, harmonic, and randomly fluctuating components, respectively.

The steady-state signal component is typically measured independently. Thus f^s is assumed to be known, and the time-variant transducer signal, s(t), may be considered to be composed of the sum of the periodic and random components.

$$s(t) = f^p(t) + f^r(t) \qquad (2)$$

The periodic signal component is determined by a digital ensemble averaging technique based on the signal enhancement concept initially considered by Gostelow, reference 5. The time-variant signal is sampled and digitized over a time frame that is greater than the periodic signal component characteristic time. With the same data initiation reference, i.e., the signal from the rotor shaft mounted optical encoder, a series of corresponding digitized signals is generated by repeating this signal sampling and digitization process. The time-variant signal ensemble average is then determined by averaging this series of digital data samples, Equation 3.

$$\langle s_j \rangle = \frac{1}{N} \sum_{n=1}^{N} s_{jn} \quad j = 1,2,3,\ldots,m \qquad (3)$$

$$= \frac{1}{N} \sum_{n=1}^{N} f^p_{jn} + \frac{1}{N} \sum_{n=1}^{N} f^r_{jn}$$

For a sufficiently large number of digital signals in the series, $N >> 1$, the ensemble average of the random signal component will be zero.

$$\frac{1}{N} \sum_{n=1}^{N} f^r_{jn} = 0 \qquad (4)$$

Thus, the periodic component of the time-variant signal, relative to the data initiation reference, is determined by this ensemble averaging technique.

$$\langle s_j \rangle = \frac{1}{N} \sum_{n=1}^{N} f^p_{jn}, \quad N \gg 1 \quad j = 1,2,3,\ldots,n \qquad (5)$$

The periodic components of the vane row inlet flow field and the resulting unsteady vane surface pressures are determined by applying this digital ensemble averaging technique to the time-variant signals from the cross hot-wire probe and the vane surface dynamic pressure transducers. Digital Fast Fourier Transform techniques are then applied to determine the first harmonic magnitude and phase of each of these periodic signal components.

These hot-wire probe and dynamic pressure transducer data are each referenced to the optical encoder signal which initiates the digital data acquisition. However, the hot-wire probe is positioned upstream of the leading edge plane of the vane row, Figure 1. Thus, it is necessary to time-relate these data to one another, i.e., time-relate the harmonic vane row inlet flow field to the resulting unsteady vane surface pressures.

As depicted in Figure 1, the rotor blade wake velocity deficit creates a fluctuating velocity vector in the absolute frame of reference of the vane row which is measured with the crossed hot-wire probe. These hot-wire data are analyzed to determine the harmonic fluctuating inlet flow angle and velocity to the vane row and, in particular, the fluctuating velocity components parallel and normal to the vane, u^* and v^*, which are the aerodynamic forcing functions to the vane row.

The harmonic vane row inlet flow field is then time-related to the resulting unsteady vane surface pressures with the following assumptions: (1) the wakes are identical at the hot-wire and the vane leading edge planes; and (2) the wakes are fixed in the rotor relative reference frame. The circumferential rotor blade and stator vane spacing, as well as the axial spacing between the vane and hot-wire probe leading edge planes are known. Using the above two assumptions, the wake is located relative to the hot-wire and vane row leading edge planes, and the time for the wake to travel between these two planes determined. This time is then transposed to a phase angle difference between the harmonic fluctuating velocity components parallel and normal to the vane and the vane leading edge plane.

To determine the harmonic pressure difference across the chordline of a representative vane, and thus the unsteady lift and moment acting on a vane, it is necessary to time-relate the pressure and suction surfaces. This is a result of having instrumented the pressure surface of one vane and the suction surface of another. The first harmonic data on each vane surface are individually adjusted in phase such that the fluctuating velocity component normal to the vane is at zero degrees at the leading edge of each surface. From the geometry, the time at which this would occur is calculated, transposed into a phase difference, and then used to adjust the pressure data on each surface. The pressure difference across the chordline of an equivalent single vane is then determined by the subtraction of these complex time-related vane pressure and suction surface data.

The final form of the unsteady pressure data defines the chordwise variation of the first harmonic pressure difference across the chordline of a stator vane, and is presented as a complex dynamic pressure coefficient, C_p, in the format of the magnitude and the phase lag referenced to a transverse gust at the airfoil leading edge.

RESULTS

At each steady-state operating point, an ensemble averaged time-variant data set consisting of the cross hot-wire probe and the dynamic pressure transducer signals digitized at a rate of 200 kHz is obtained. This sample rate results in approximately 91 points defining the periodic vane inlet flow field, i.e., the time-variant flow field between adjacent rotor blades, at the design speed of the compressor.

Ensemble Averaging

The effect of ensemble averaging the time-variant signals is demonstrated in Figure 3, which presents a typical digitized pressure transducer signal for 1 rotor revolution and averaged over 25, 50, 75, 100 and 200 rotor revolutions. The ensemble averaging significantly reduces the random fluctuations which are superimposed on the periodic signal, with the time-variant signals essentially unchanged when averaged over 75 or more rotor revolutions. For the data to be presented, 200 averages are obtained for both the hot-wire probe and the vane pressure transducer signals.

Signal Harmonic Content

Figure 4 shows the FFT decomposition of a typical ensemble averaged time-variant pressure transducer signal. There is a dominant fundamental frequency at rotor blade passing, with much smaller higher harmonics and minimal non-harmonic content. Also shown is the digitized signal together with the first three harmonics and their sum. This summation is seen to yield a good approximation to the original digitized signal, further demonstrating that the time-variant signal is primarily composed of the first three harmonics of rotor blade passing frequency.

FFT & Ensemble Averaging

There are two data analysis approaches which could be applied to the time-variant digital data. In one, the data are Fourier decomposed and then ensemble averaged. The second approach significantly reduces the data storage requirements, with the digital data first ensemble averaged and then Fourier decomposed. Also, the previously presented results showing that the ensemble averaged time-variant data are composed primarily of only the lower harmonics raises the question of which approach is appropriate. Namely, does ensemble averaging remove the higher order harmonics which would be retained by averaging the Fourier decomposed data. This is addressed by considering the differences between (a) ensemble averaging and then Fourier decomposing the time-variant data and (b) Fourier decomposing and then averaging the time-variant data.

Figure 5 presents the results of these two time-variant data analysis approaches for a representative vane surface dynamic pressure transducer signal. There is no difference between averaging the signal 200 times before the Fourier analysis and Fourier decomposing the signal before taking the 200 averages. Ensemble averaging the signals and then Fourier decomposition is used in the following first stage vane row unsteady aerodynamic experiments because of the significantly reduced data storage requirements.

Vane Row Unsteady Aerodynamics

The detailed time-variant aerodynamic forcing function to the first stage vane row, in particular the parallel and normal inlet velocity components, and the effect of steady aerodynamic loading on the resulting vane surface harmonic pressure distributions are now investigated and quantified. This is accomplished by applying these digital data acquisition and analysis techniques to the time-variant signals from the high response instrumentation in the first stage vane row of the research compressor. Two steady-state operating conditions on the 60% speed line which have different levels of vane aerodynamic loading are considered.

The chordwise distributions of the static pressure on the pressure and suction surfaces of the vane for these two compressor operating conditions are presented in Figure 6. The level of aerodynamic loading has a strong effect on these distributions, with the -6.5° incidence angle data corresponding to a low level of aerodynamic loading, and the -0.4° incidence angle case to a moderate loading level.

For these two compressor operating conditions, the aerodynamic forcing function to the stator row, the parallel and normal inlet velocity components, are presented in Figure 7. The amplitudes of the chordwise and transverse gust components are different. However, in terms of the first harmonics, these two forcing functions are equivalent. In particular, the ratios of the magnitudes of the first harmonic of these gust components (u^+/v^+) are 0.696 and 0.709 for these two vane loadings. It is interesting to note that these inlet velocity components are not small as compared to the free-stream velocity, having ratios on the order of 0.3 and 0.45 for the parallel and normal components, respectively, at -0.4° of incidence. This may have implications regarding the validity of the small perturbation assumption in various mathematical models for unsteady aerodynamics.

The resulting first harmonic complex dynamic pressure chordwise distributions are shown in Figure 8. As a reference, the corresponding prediction from the periodic small perturbation model of reference 6 is also presented. This model considers the inviscid, irrotational flow of a perfect gas and analyzes the uniform subsonic compressible flow past a two-dimensional flat plate airfoil cascade, with small unsteady normal velocity perturbations superimposed and convected downstream.

There are relatively large differences in the complex dynamic pressure coefficient data presented in Figure 8. As it was previously determined that the first harmonic aerodynamic forcing functions for these two compressor operating conditions were nearly identical, these dynamic pressure coefficient differences are attributed to the effect of steady aerodynamic loading. Also, although the level of

loading affects both the phase and the magnitude of these coefficient data, it has a larger effect on the coefficient magnitude data.

The correlation of these dynamic pressure coefficient data with the flat plate cascade predictions are also of interest. The phase of the dynamic pressure difference coefficient data show a somewhat different trend than the prediction. This is attributed to the vane camber and the detailed steady chordwise loading distribution on the vane surfaces. However, very good correlation is obtained for the -6.5° incidence angle magnitude data, with poor correlation for the corresponding -0.4° incidence angle data. This is associated with the steady vane aerodynamic loading level. Namely, the prediction is for an unloaded flat plate airfoil cascade. Hence the good correlation of the low steady aerodynamic loading -6.5° incidence angle data and the poor correlation of the moderate loading -0.4° incidence angle data. In general, different airfoil designs will produce different steady surface pressure distributions and resulting steady lift for the same incidence angle. Thus, the level of steady aerodynamic loading, not the incidence angle, is the key parameter to obtain good correlation with flat plate airfoil cascade mathematical models.

SUMMARY AND CONCLUSIONS

Computer based time-variant digital data acquisition and analysis techniques, including ensemble averaging and Fast Fourier Transforms, were developed for periodic data. These techniques were then applied to the time-variant signals from high response instrumentation in the first stage vane row of a research compressor.

Ensemble averaging of time-variant signals was demonstrated and shown to significantly reduce the random fluctuations superimposed on the periodic signal. By considering two alternative data analysis approaches, it was then shown that ensemble averaging does not remove the higher order harmonics which would be retained by averaging the Fourier decomposed data.

The detailed time-variant aerodynamic forcing function to the first stage vane row, in particular the parallel and normal inlet velocity components, and the effect of steady aerodynamic loading on the resulting vane surface harmonic pressure distributions were then investigated and quantified.

The strong effect of the level of aerodynamic loading on the chordwise distributions of the static pressure on the pressure and suction surfaces of the vane was shown, with the -6.5° incidence angle data corresponding to a low level of aerodynamic loading, and the -0.4° incidence angle case to a moderate loading.

For these two compressor operating conditions, there were only small differences in the aerodynamic forcing function to the stator row, the parallel and normal inlet velocity components, with the first harmonics being nearly identical. Also, it was found that these inlet velocity components were not small as compared to the free-stream velocity.

The resulting vane surface harmonic pressure data exhibited large differences in both the phase and magnitude of the complex dynamic pressure coefficient, with a larger effect on the coefficient magnitude data. As the aerodynamic forcing functions for these two compressor operating conditions were nearly identical, these dynamic pressure coefficient differences are attributed to the effect of steady aerodynamic loading.

The correlation of these dynamic pressure coefficient data with predictions obtained from a flat plate cascade mathematical model was also considered. The steady vane surface pressure distribution and lift for a given incidence angle will be a function of airfoil design. Thus, the level of steady aerodynamic loading, not the incidence angle, was shown to be the key parameter to obtain good correlation with such models.

ACKNOWLEDGEMENTS

Support of this experimental research program by the Air Force Office of Scientific Research, Dr. James Wilson program manager, is gratefully acknowledged.

REFERENCES

1. Mikolajczak, A.A., "The Practical Importance of Unsteady Flow," *AGARD-CP-177 Unsteady Phenomena in Turbomachinery*, 1976.

2. Pfeil, H., Herbst, R., and Schroder, T., "Investigation of the Laminar-Turbulent Transition of Boundary Layers Disturbed by Wakes," *ASME Paper 82-GT-124*, 1982.

3. Sharma, O.P., Butler, T.L., Joslyn, H.D., and Dring, R.P., "Three-Dimensional Unsteady Flow in an Axial Flow Turbine," *AIAA Journal of Propulsion and Power*, Vol. 1, No. 1, January-February 1985.

4. Greitzer, E.M., "The stability of Pumping Systems," *ASME Journal of Fluids Engineering*, Vol. 103, June 1981.

5. Gostelow, J.P., "A New Approach to the Experimental Study of Turbomachinery Flow Phenomena," *ASME Journal of Engineering for Power*, Volume 99, January 1977.

6. Fleeter, S., "The Fluctuating Lift and Moment Coefficients for Cascaded Airfoils in a Nonuniform Compressible Flow," *AIAA Journal of Aircraft*, Volume 10, February 1973.

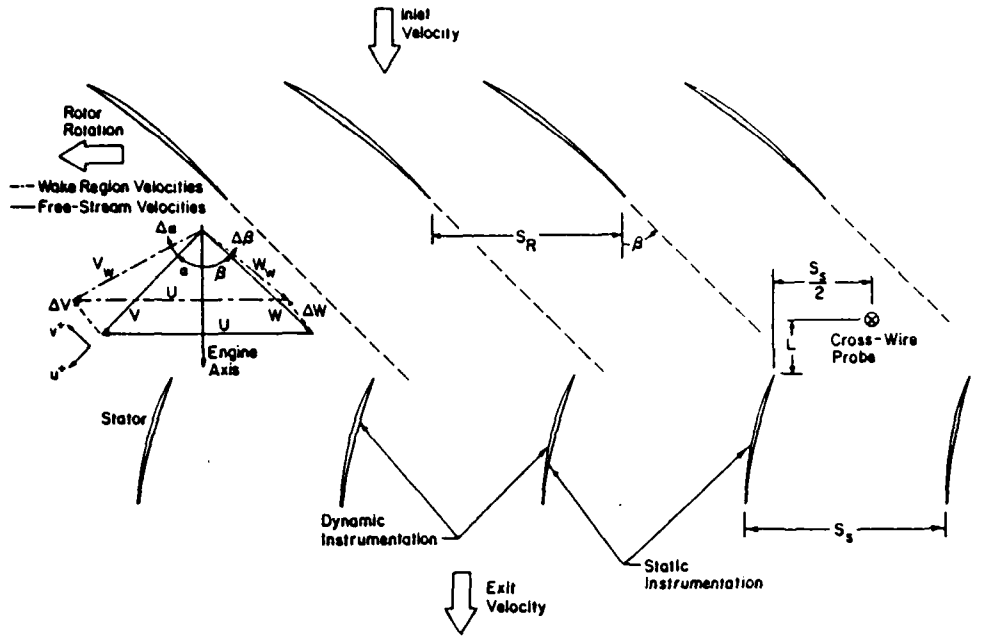

Fig 1 Schematic of flow field

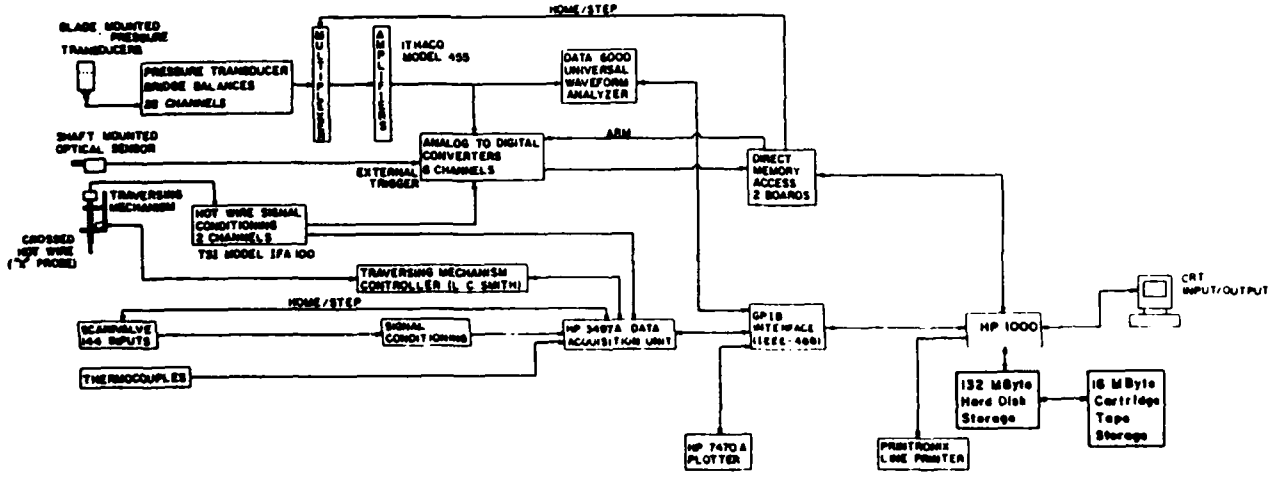

Fig 2 Digital data acquisition and analysis system

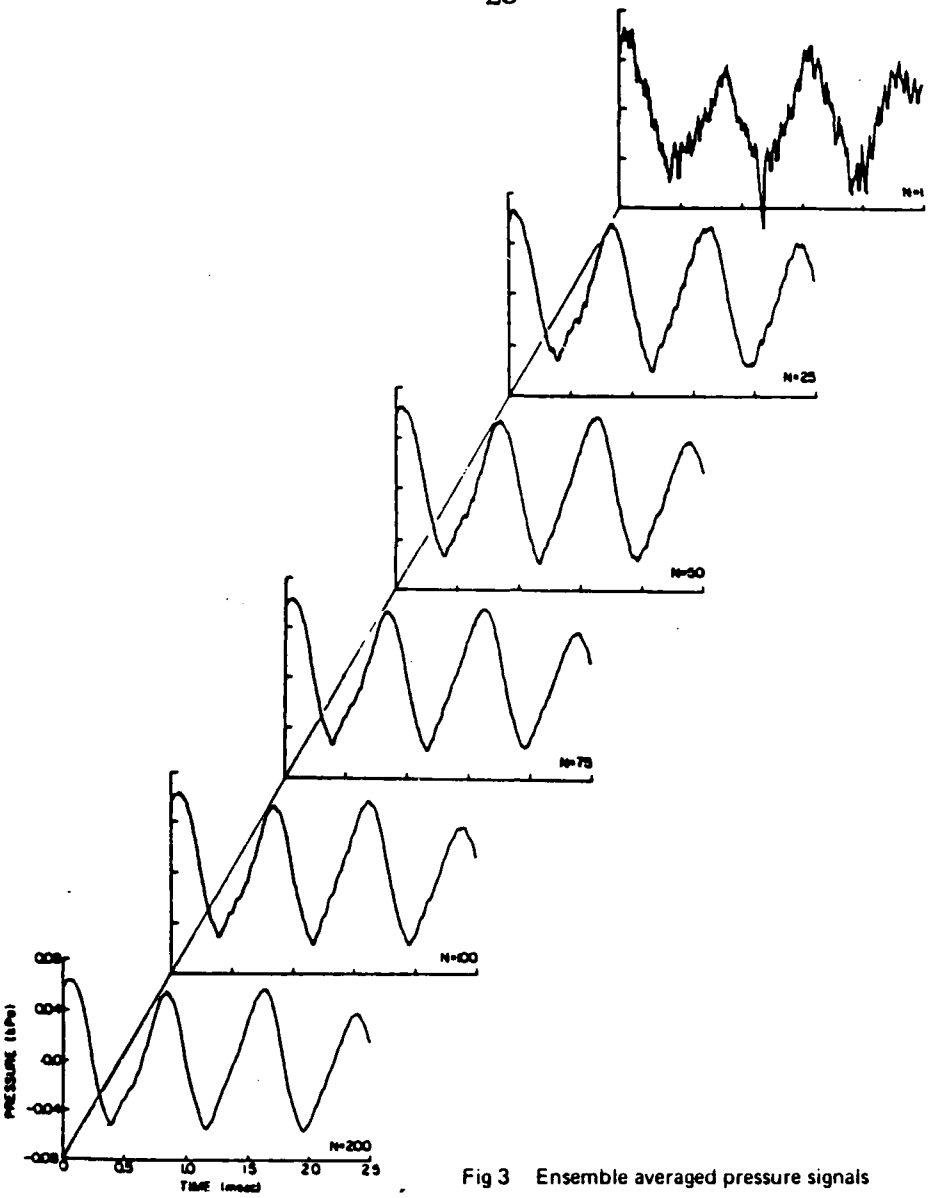

Fig 3 Ensemble averaged pressure signals

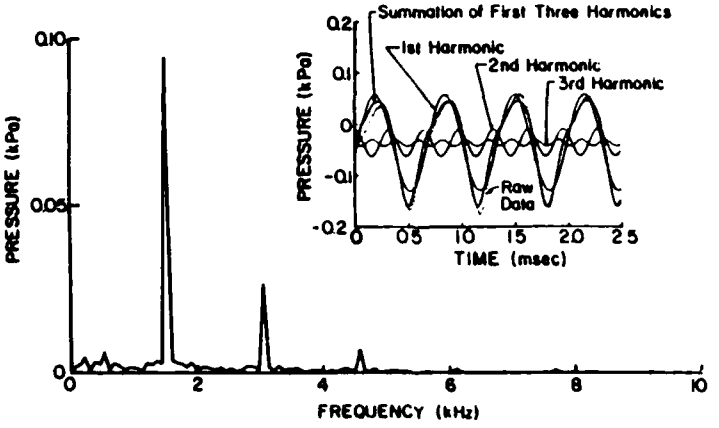

Fig 4 Fourier decomposition of averaged pressure signal

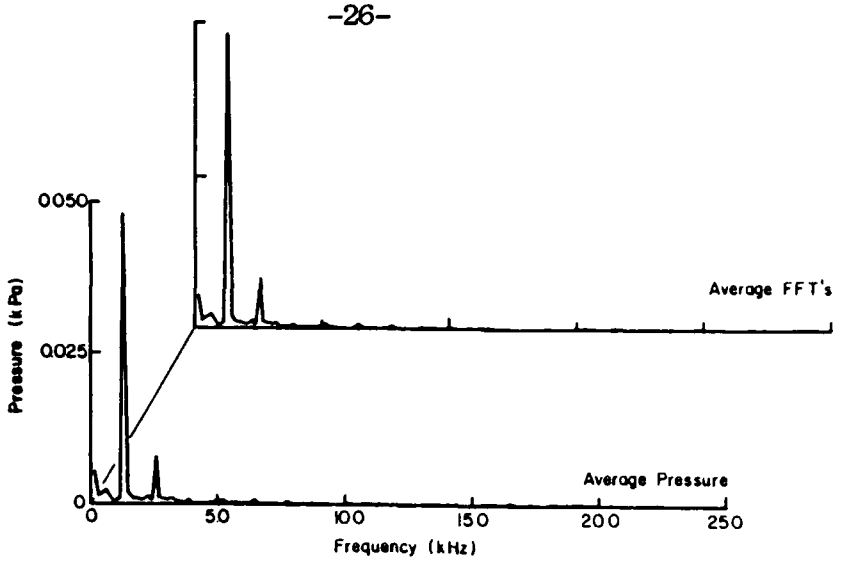

Fig 5 Effect of ensemble averaging and fourier decomposition on dynamic pressure signal harmonic content

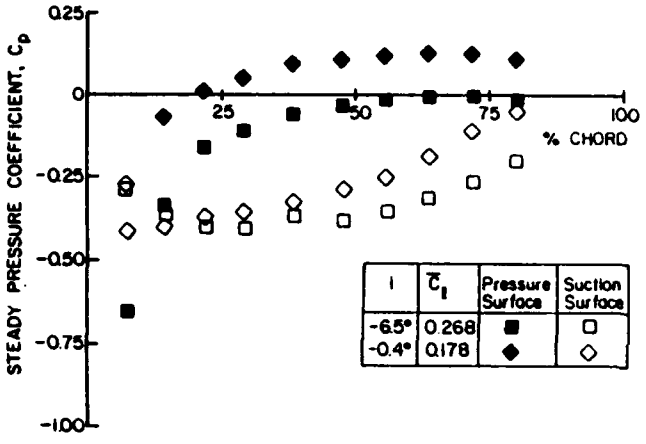

Fig 6 Variation of vane surface static pressure coefficient with loading

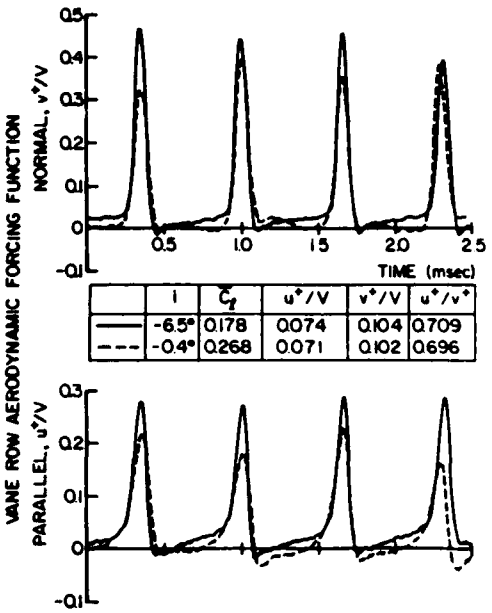

Fig 7 Effect of loading on the vane row aerodynamic forcing functions

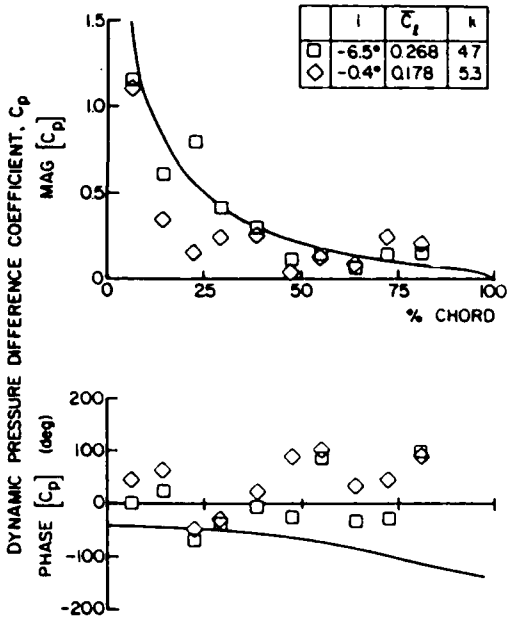

Fig 8 Variation of first harmonic complex unsteady pressure coefficient with loading

APPENDIX II

THE UNSTEADY AERODYNAMICS OF A FIRST STAGE VANE ROW

EXPERIMENTS IN FLUIDS

Experiments in Fluids 4:72–78 (1986)

Experiments in Fluids

© Springer-Verlag 1986

The unsteady aerodynamics of a first stage stator vane row

V. R. Capece and S. Fleeter

Thermal Sciences and Propulsion Center, School of Mechanical Engineering, Purdue University, West Lafayette, IN 47907, USA

Abstract. The fundamental unsteady aerodynamics on a vane row of an axial flow research compressor stage are experimentally investigated, demonstrating the effects of airfoil camber and steady loading. In particular, the rotor wake generated unsteady surface pressure distributions on the first stage vane row are quantified over a range of operating conditions. These cambered airfoil unsteady data are correlated with predictions from a flat plate cascade inviscid flow model. At the design point, the unsteady pressure difference coefficient data exhibit good correlation with the nonseparated predictions, with the aerodynamic phase lag data exhibiting fair trendwise correlation. The quantitative phase lag differences are associated with the camber of the airfoil. An aft suction surface flow separation region is indicated by the steady state surface static pressure data as the aerodynamic loading is increased. This separation affects the increased incidence angle unsteady pressure data.

List of symbols

b	airfoil semi-chord
c	airfoil chord
C_p	dynamic pressure coefficient, $\frac{\Delta p}{\rho U^2 \cdot \frac{1}{2}}$
$C_{\bar{p}}$	static pressure coefficient, $\frac{\Delta \bar{p}}{1/2\,\rho U_T^2}$
i	incidence angle
k	reduced frequency, $\frac{\omega b}{U_{axial}}$
N	number of rotor revolutions
Δp	dynamic pressure difference
$\Delta \bar{p}$	static pressure difference, $\bar{p}_{up} - \bar{p}_{low}$
S	stator vane circumferential spacing
U_T	rotor blade tip speed
u	longitudinal perturbation velocity
U	absolute velocity
U_{axial}	absolute axial velocity
v	transverse perturbation velocity
x_{sep}	location of separation point
β	inlet angle
ρ	inlet air density
ω	blade passing angular frequency

1 Introduction

Destructive aerodynamic forced responses of turbomachinery blading have been generated by a wide variety of aerodynamic sources including, for example, blade wakes, multi-stage interactions, large angle of attack or yaw, and inlet flow distortions. As a result, the structural dynamic response of fan, compressor, and turbine blading resulting from aerodynamic excitations is an item of rapidly increasing concern to designers of gas turbine engines for advanced technology applications.

Aerodynamically induced failure level vibratory responses of blading occur when a periodic aerodynamic forcing function, with frequency equal to a natural blade resonant frequency, acts upon an airfoil row. The operating conditions at which these aerodynamically forced blade responses may occur are predicted with frequency-speed resonance or Campbell diagrams (Oates 1978). These display the natural frequency of each blade mode versus rotor speed, with the excitation source variation with rotor speed superimposed, as schematically depicted in Fig. 1. The intersection points define the rotor speeds at which significant responses may be found.

However, Campbell diagrams give no indication of the amplitude of the response. The response amplitude can only be determined by first relating the periodic excitation source to the resulting unsteady aerodynamic forces and moments acting on the individual blades. The blade response can then be predicted by analyzing the interaction of these unsteady forces and moments with the structural characteristics of the blading, accomplished through either a classical Newton's second law approach (Tung 1969) or a balance of energy technique (Hoyniak & Fleeter 1983, 1984).

The development of cascade analyses to predict the unsteady aerodynamics acting on the blading is currently an item of fundamental research interest, for example, the following references: Fleeter 1973; Goldstein & Atassi 1976; Verdon & Caspar 1981; Englert 1982; Nagashima & Tanida 1984. Thus, the unsteady aerodynamic forces and moments acting on the individual blades cannot, in general, be predicted. As a result, the amplitude of the blading response cannot be accurately analyzed.

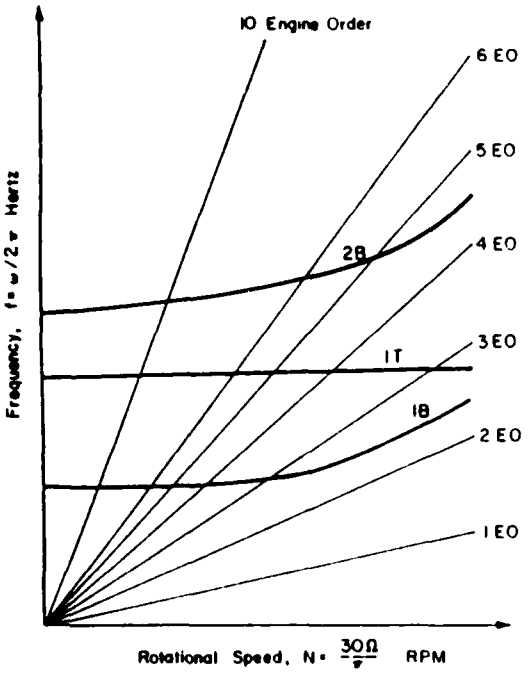

Fig. 1. Campbell diagram

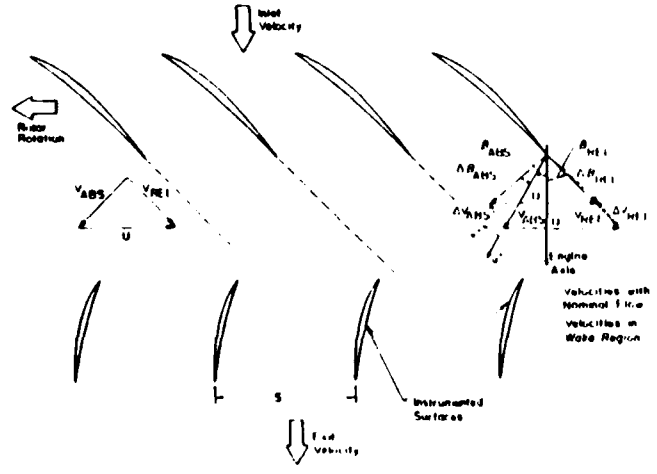

Fig. 2. Schematic of flow field

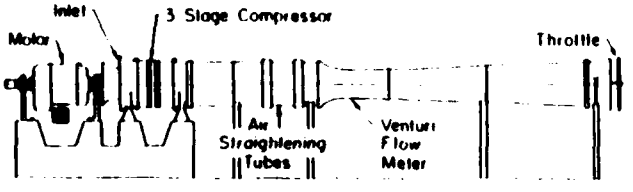

Fig. 3. Schematic of three-stage research compressor

Table 1. Airfoil mean section characteristics and compressor design point conditions

	Rotor	Stator
Type of airfoil	C4	C4
Number of blades	43	41
Chord, C (mm)	30	30
Solidity, C/S	1.14	1.09
Camber	27.95	27.70
Stagger angle	36	−36.1
Aspect ratio	2.0	2.0
Thickness/chord (%)	10	10
Flow rate (kg/second)	2.66	
Rotor-stator axial spacing (mm)	22.2	
Design axial velocity (meters/sec)	32.0	
Rotational speed (RPM)	3000	
Number of stages	3	
Stage pressure ratio	1.003	
Inlet tip diameter (mm)	420	
Hub/tip radius ratio	0.714	
Stage efficiency (%)	85	

To direct the development of unsteady aerodynamic models and to evaluate these advanced analyses as well as existing ones, data obtained from experiments which model the fundamental unsteady phenomena inherent in turbomachine blade rows are required. The objective of the experiments described herein is to investigate the rotor wake generated forced response unsteady aerodynamics on a vane row in a multi-stage compressor. In particular, the rotor wake generated chordwise distribution of the unsteady surface pressures on the first stage vane row of a three stage axial flow research compressor are determined over a range of steady operating conditions. These data are correlated with appropriate predictions.

2 Research compressor

The wakes from the rotor blades are the primary source of the unsteady surface pressures on the first stage stator vanes, i.e., the rotor wakes define the forcing function to the downstream stator vanes, as depicted in Fig. 2. Hence, it is necessary to experimentally model the basic unsteady aerodynamic phenomena inherent in this time-variant interaction, including the incidence angle effects, the velocity and pressure variations, and the reduced frequency.

These fundamental phenomena are all simulated in the Purdue University three stage axial flow research compressor, depicted schematically in Fig. 3. The compressor is driven by a 15 HP DC electric motor with a speed range of 300 to 3000 RPM. The inlet section is located aft of the drive motor. At the exit of this section are 38 variable geometry guide vanes which direct the flow into the test section. Three identical compressor stages are mounted in

the test section, which has an annulus with constant hub (0.300 m) and tip (0.420 m) diameters. The exit flow from the test section is directed through a series of flow straighteners into a venturi meter which enables the mass flow rate to be determined. To throttle the compressor, an adjustable plate is located at the exit of the diffuser of the venturi.

Each of the three identical compressor stages consists of 43 rotor blades and 41 stator vanes. Hence, the interblade phase angle for these experiments is 17.56°. These free vortex design airfoils have a British C-4 section profile, a chord of 30 mm, and a maximum thickness-to-chord ratio of 0.10. The overall airfoil and compressor characteristics are presented in Table 1.

3 Instrumentation

Conventional steady-state instrumentation is used to determine the flow properties in the compressor. The inlet temperature is measured by four equally spaced thermocouples at the inlet of the compressor. Casing static taps, equally spaced circumferentially, allow the measurement of the static pressure between each blade row. Traversing gear instrument stations provided between each blade row are used to measure the mean flow incidence angle on the first stage stator vanes. Chordwise distributions of vane surface static pressure taps are used to determine the steady aerodynamic loading. A thermocouple and Kiel probe located downstream are used to measure the compressor exit temperature and total pressure, respectively. The mass flow is measured with the calibrated venturi meter located downstream of the compressor test section. A shaft mounted 60 tooth gear and a magnetic pickup provide the rotor speed.

The unsteady data of fundamental interest are the chordwise distribution of the complex time-variant pressure difference across the chordline of the first stage stator vane. These data are obtained using Kulite thin-line design dynamic pressure transducers. Two instrumented vanes are used. The suction surface of one vane and the pressure surface of another are instrumented with these transducers at 14.1, 29.1, 47.1, and 63.7% of the stator vane chord. To minimize any flow disturbances generated by the transducers, they are embedded in the vanes and connected to the surface by a static pressure tap with the lead wires placed in milled slots and carried out through hollow trunnions. These vanes are located in the stator vane row such that a complete flow passage is instrumented.

4 Data acquisition and analysis

The steady state data of interest include: (1) the static pressures on the stator vane surfaces, accomplished with chordwise distributions of surface static pressure taps; (2) the pressures and temperatures throughout the compressor, thereby permitting the compressor operating map to be determined. The compressor map is used to define the operating points, in terms of overall pressure ratio and corrected mass flow rate, at which the unsteady surface pressure measurements are obtained.

Steady state data acquisition follows the standard evaluation procedure. At the selected corrected speed, the compressor is stabilized for approximately 10 minutes, after which the steady state data acquisition is initiated and controlled by a PDP 11-23 computer. The data are then analyzed, and the corrected mass flow, pressure ratio, and corrected speed determined.

The time-variant data acquisition and analysis technique used is based on a data averaging or signal enhancement concept (Gostelow 1977). The key to such a technique is the ability to sample data at a preset time. In this investigation, the data of interest are generated at the blade passing frequency. Hence, an optical encoder delivering a square wave voltage signal with a duration in the microsecond range, was mounted on the rotor shaft and used as the time or data initiation reference to trigger the A/D multiplexer system. This system is capable of digitizing signals simultaneously at rates to 5 megahertz per channel, storing 2048 data points per channel.

The effect of averaging the time-variant digitized pressure signals from the blade mounted dynamic pressure transducers was considered. Figure 4 displays the time-variant pressure signal from the 14.1% chord pressure surface dynamic pressure transducer for 1 rotor revolution and averaged over 25, 50, 75, and 100 rotor revolutions. Averaging is seen to greatly reduce the random fluctuations superimposed on the harmonic pressure signal. Also these time-variant pressure signals are essentially unchanged when averaged over 75 or more rotor revolutions.

At each steady state operating point, an averaged time-variant data set, consisting of the Kulite dynamic pressure transducer signals digitized at a rate of 20 kHz and averaged over 100 rotor revolutions, was obtained. These rotor revolutions were not consecutive due to the finite time required for the A-D multiplexer system to sample the data and the computer to then read the digitized data.

Each of these digitized signals is Fourier decomposed into harmonics by means of an FFT algorithm. Figure 5 shows an example of this decomposition for the 14.1% chord pressure surface transducer signal. As seen, the transducer signal contains a dominant fundamental frequency equal to the blade passing frequency and a much smaller second harmonic component. In addition, the averaged signal exhibits minimal non-harmonic content. From this Fourier decomposition, both the magnitude of each component and its phase lag as referenced to the optical encoder pulse are determined.

Cascade gust unsteady aerodynamic analyses predict the unsteady pressure difference across the vane as a func-

tion of airfoil chord in the form of an unsteady pressure difference coefficient and an aerodynamic phase lag. The unsteady pressure difference coefficient is normalized with respect to the steady state properties of the flow and the magnitude of the transverse gust. The aerodynamic phase lag is referenced to a transverse gust at the leading edge of the reference airfoil. Hence, to enhance the experiment-theory correlation process, the data were adjusted in phase and magnitude to agree with the predictions at the leading edge transducer location. Thus, the final form of the time-variant data consists of an unsteady pressure difference coefficient, C_p, and an aerodynamic phase lag.

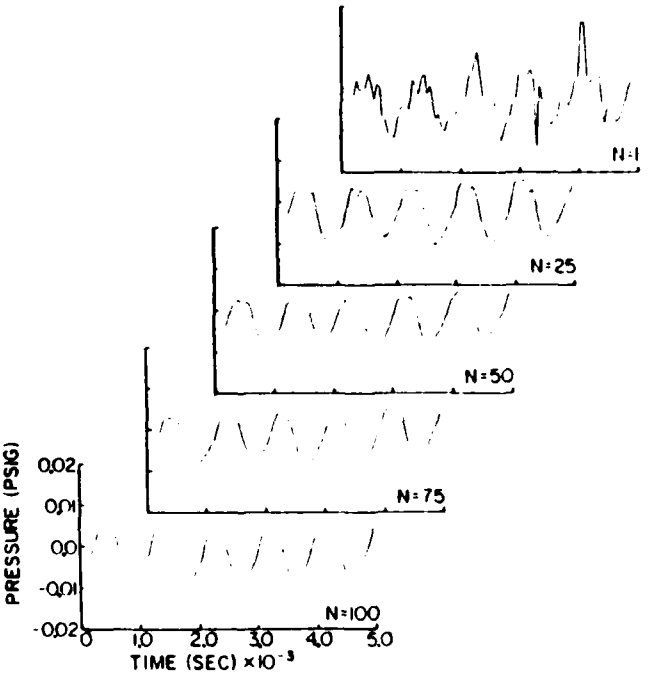

Fig. 4. Digitized pressure signals averaged over N rotor revolutions

5 Results

The steady state first stage vane surface static pressure distributions quantify the effect of aerodynamic loading. Figure 6 presents the aerodynamic loading distributions at 49.1% span in the form of a static pressure coefficient for five levels of loading, corresponding to incidence angles ranging from −7.0° to +6.9°.

As the incidence angle is increased from −7.0° to −2.0°, the aerodynamic loading increases, with no surface flow separation indicated by the static pressure data. Increasing the incidence angle to 0.0°, results in further increased aerodynamic loading. The flattening out of the aft suction surface static pressure data is indicative of a constant pressure separation in the trailing edge region of this surface. Thus, −2.0° of incidence corresponds to the steady design point operation of this span position. The region of constant static pressure becomes somewhat more apparent as the loading is further increased, to 2.9° and 6.9° of incidence, extending further forward with increased incidence angle values. This is associated with the aft suction surface flow separation, with the separation point moving forward as the incidence angle is increased.

The stator vane surface first harmonic unsteady pressure coefficient and aerodynamic phase lag data are correlated with predictions obtained from a cascade aerodynamic gust model which considers the inviscid, irrotational, flow of a perfect gas. This model considers the

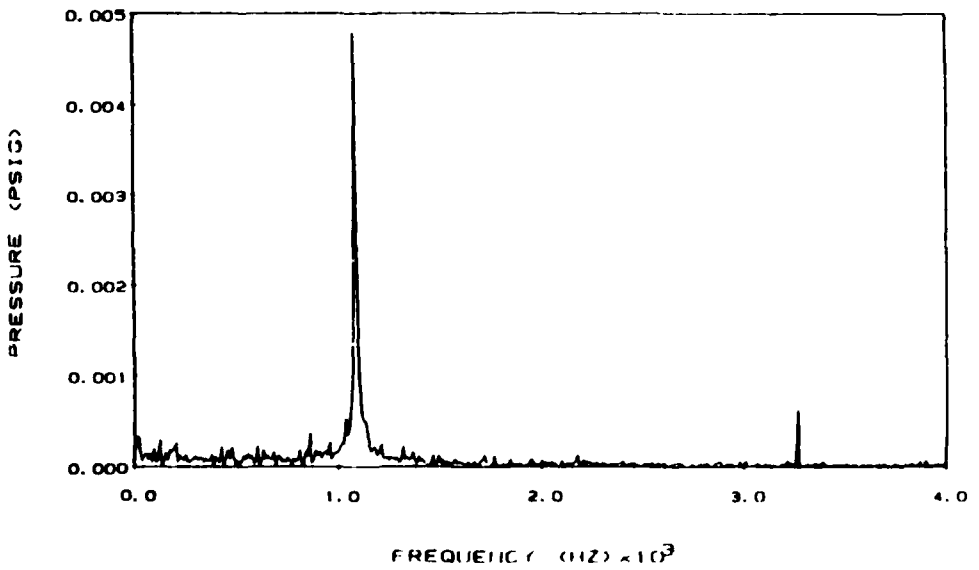

Fig. 5. Fourier analysis of averaged pressure signal at 14.1% chord on the pressure surface

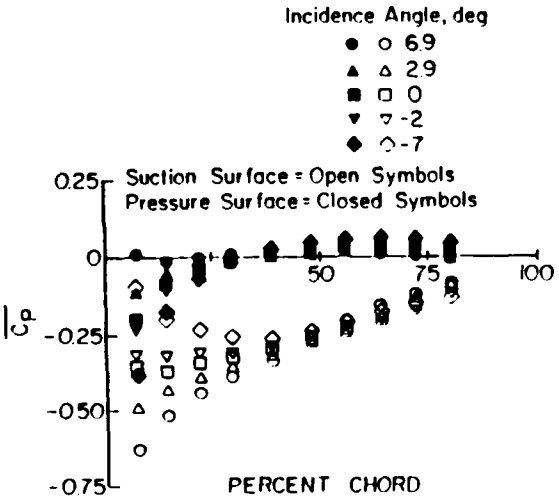

Fig. 6. Airfoil static pressure coefficient as a function of airfoil chord

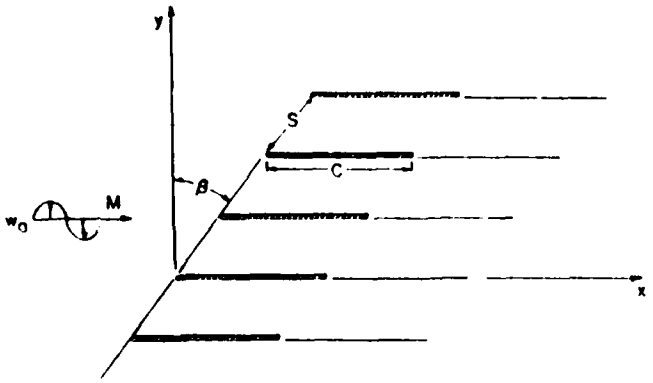

Fig. 7. Cascade aerodynamic gust model

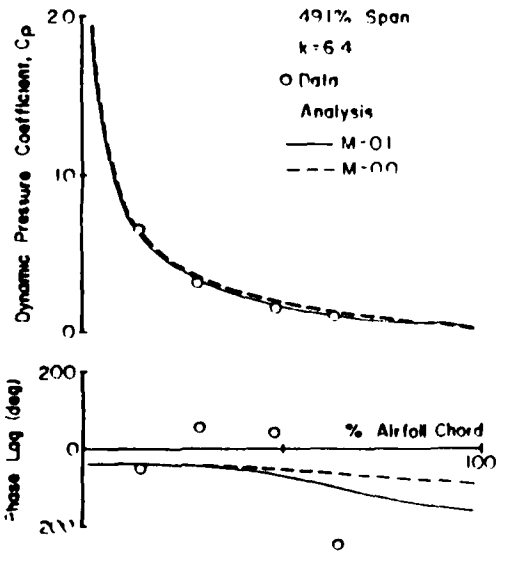

Fig. 8. Chordwise variation of the dynamic pressure coefficient and aerodynamic phase lag at −2.0° of incidence

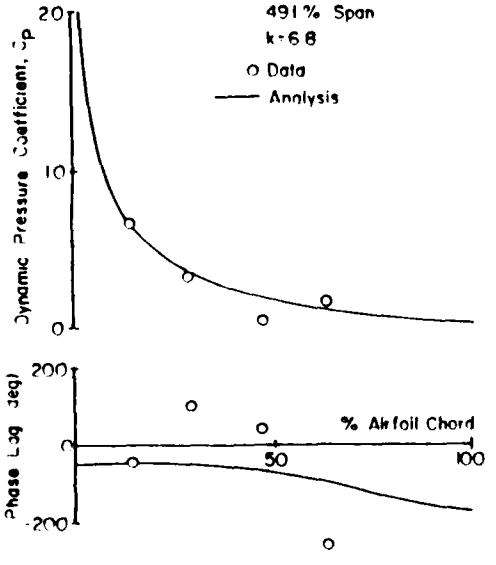

Fig. 9. Chordwise variation of the dynamic pressure coefficient and aerodynamic phase lag at 0° of incidence

uniform subsonic compressible, nonseparated steady flow past a two-dimensional flat plate airfoil cascade, with small unsteady normal velocity perturbations superimposed and convected downstream, Fig. 7. The parameters modeled include the cascade solidity and stagger angle, the interblade phase angle, the inlet Mach number, and the reduced frequency.

Figure 8 presents the unsteady pressure data at the steady-state design point, −2.0° of incidence, together with the incompressible (Mach = 0.0) and the appropriate compressible (Mach = 0.1) predictions. The differences between the two predictions is of interest. The axial velocity is approximately 32 m/s, and thus the steady-state experiments are incompressible. However, the compressible reduced frequency parameter, $kM/\sqrt{1-M^2}$, is on the order of 0.7 which is in the range wherein compressibility effects are important. Thus, the unsteady data are compressible flow data. As a result, all of the unsteady data presented are correlated with the compressible (Mach = 0.1) predictions.

As also seen in Fig. 8, good correlation exists between the unsteady pressure difference coefficient data and the prediction, with both decreasing with increasing chordwise position. However, the aerodynamic phase lag data exhibit a somewhat different chordwise distribution than the prediction. In particular, the phase lag data first increase and then decrease relative to the flat plate cascade prediction as the chord is traversed. This result is attributed to the camber of the stator vane.

The zero incidence angle results are presented in Fig. 9. As seen, the correlation of the unsteady pressure difference coefficient data with the nonseparated predictions is reasonably good, with the data decreased at 47.4% chord and slightly increased at 63.7% chord as compared to the

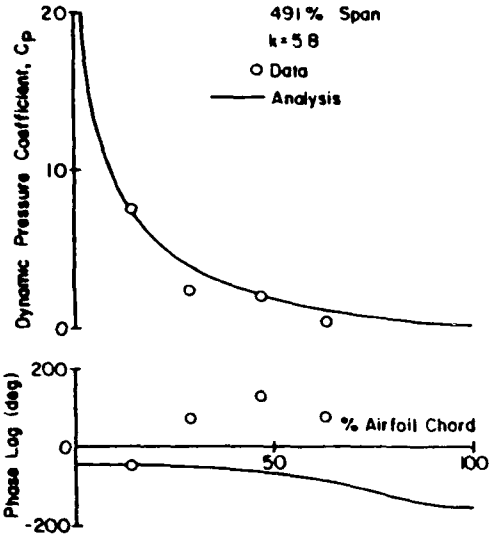

Fig. 10. Chordwise variation of the dynamic pressure coefficient and aerodynamic phase lag at – 7° of incidence

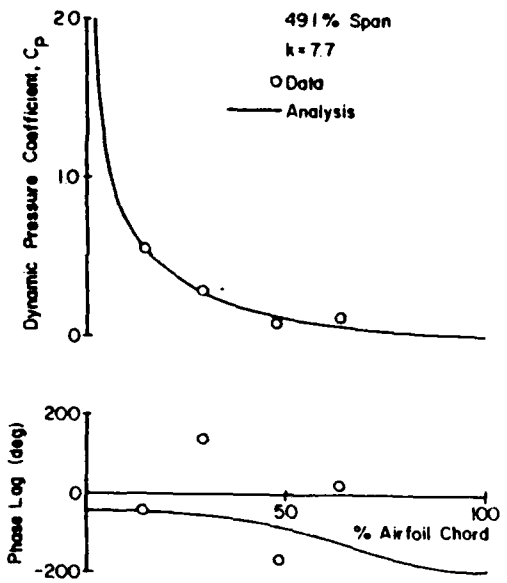

Fig. 11. Chordwise variation of the dynamic pressure coefficient and aerodynamic phase lag at 2.9° of incidence

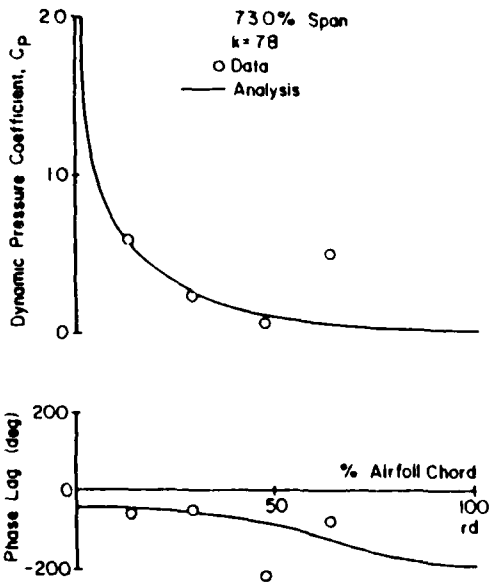

Fig. 12. Chordwise variation of the dynamic pressure coefficient and aerodynamic phase lag at 3° of incidence

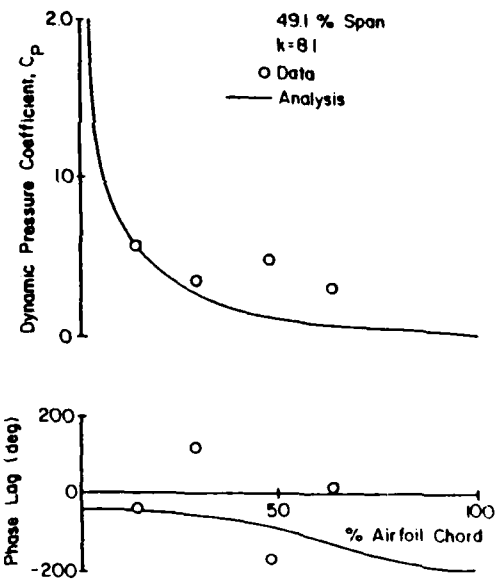

Fig. 13. Chordwise variation of the dynamic pressure coefficient and aerodynamic phase lag at 6.9° of incidence

predictions. The phase lag data exhibit the previously noted design point effect of airfoil camber.

Figure 10 presents the large negative incidence angle, – 7°, off-design results. The correlation of these unsteady pressure difference coefficient data with the prediction is not as good as the design point results, with the 29.1% and the 63.7% chord data noticeably decreased in value in relation to the prediction. Also, the phase lag data first increase and then decrease relative to the prediction as the chord is traversed. However, the decrease is not nearly as large as found at the design condition. This decreased correlation is associated with the large differences between the design and this off design steady aerodynamic loading distributions, per Fig. 6.

Figures 11 through 13 present the correlation of the positive incidence angle unsteady pressure data. All of these positive incidence angle data exhibit similar correlation trends. Analogous to the design point results, over the front part of the airfoil chord the unsteady pressure difference data exhibit good correlation with predictions whereas the aerodynamic phase lag data first increase and then decrease relative to the predictions. In the mid and

aft chord regions, the unsteady pressure difference and phase lag data exhibit poor correlation with the predictions. In particular, the unsteady pressure difference coefficient data and the predictions decrease as the chord position is increased over the front of the airfoil. However, whereas the prediction continues to decrease over the mid and aft part of the airfoil chord, the data show increased values, with the higher incidence angle data exhibiting the largest increase. Also, the aerodynamic phase lag data increase and then decrease relative to the predictions over the front part of the airfoil, as noted. In the mid and aft chord region, the phase lag data increase while the prediction decreases. This poor correlation of these high incidence angle data is attributed to the flow separation over the aft portion of the suction surface indicated by the steady-state surface static pressure data, an effect not modeled by the analysis.

6 Summary and conclusions

The effects of airfoil camber and steady loading on the fundamental unsteady aerodynamics of the first stage vane row of an axial flow compressor have been demonstrated. In particular, the unsteady vane surface pressure distributions, with the primary source of excitation being the wakes from the first stage rotor blades, were measured by *means of embedded Kulite dynamic pressure transducers*. These time-variant data were analyzed using data averaging and FFT techniques to determine the unsteady pressure difference and the aerodynamic phase lag. These were then correlated with predictions obtained from a compressible transverse gust flat plate cascade analysis which considers nonseparated steady flow.

At the design point incidence angle, the unsteady pressure difference coefficient data exhibited good correlation with the predictions, with the aerodynamic phase lag data exhibiting fair trendwise correlation. The quantitative phase lag differences between the data and the predictions are a result of the camber of the airfoil. As the steady airfoil loading is increased, the steady-state surface static pressure distributions indicated an aft suction surface flow separation. This separation affected the unsteady pressure data, with these data exhibiting poor correlation with the predictions over the aft portion of the vane.

Acknowledgements

Support of this experimental research program by the Air Force Office of Scientific Research is gratefully acknowledged.

References

Oates, G. C. (ed.) 1978: The aero-thermodynamics of aircraft gas turbine engines. AFAPL-TR-78-52, July

Fung, Y. C. 1969: An introduction to the theory of aeroelasticity. London: Dover Publ.

Hoyniak, D., Fleeter, S. 1983: Prediction of aerodynamically induced vibrations in turbomachinery blading. ASME J. Fluids Eng. 105, 375–381

Hoyniak, D., Fleeter, S. 1984: The coupled response of turbomachinery blading to aerodynamic excitations. AIAA J. Aircraft, 21, 278–286

Fleeter, S. 1973: Fluctuating lift and moment coefficients for cascaded airfoils in a nonuniform compressible flow. AIAA J. Aircraft 10, 93–98

Goldstein, M. E.; Atassi, H. 1976: A complete second order theory for the unsteady flow about an airfoil due to a periodic gust. J. Fluid Mechanics 74, 695–720

Verdon, J. M., Caspar, J. R. 1981: Development of an unsteady aerodynamic analysis for finite deflection subsonic cascades. NASA CR-3455, September

Englert, G. W. 1982: Interaction of upstream flow distortions with high Mach number cascades. ASME Paper 82-GT-137

Nagashima, T., Tanida, Y. 1984: Aerodynamic response of airfoils in sinusoidal oblique gust. AIAA J. Aircraft 21, 302–308

Costelow, J. P. 1977: A new approach to the experimental study of turbomachinery flow phenomena. ASME J. Eng. Power 99, 97–105

Received April 19, 1985

APPENDIX III

UNSTEADY BLADE ROW INTERACTIONS IN A MULTISTAGE COMPRESSOR

AIAA JOURNAL OF PROPULSION AND POWER

Unsteady Blade Row Interactions in a Multistage Compressor

V. R. Capece,* S. R. Manwaring,* and S. Fleeter†
Purdue University, West Lafayette, Indiana

A three-stage research compressor has been utilized to investigate the multistage blade row interaction gust aerodynamics for the first time. The aerodynamic forcing functions as well as the chordwise distributions of the steady surface pressures and the first harmonic unsteady pressure differences on the first and second stage stator vane rows were experimentally determined over a range of operating and geometric conditions. This series of experiments determined that the complex unsteady aerodynamic loading on downstream blade rows is directly related to the forcing function to the blade row, with this forcing function significantly affected by multistage blade row interactions. These results have an implication towards the modeling of unsteady aerodynamic blade row interaction phenomena. Namely, the variations of the second stage unsteady data with forcing function waveform cannot be predicted by harmonic gust models.

Nomenclature

b	= airfoil semi-chord
C_p	= dynamic pressure coefficient, $\dfrac{\Delta p}{p V^2_{max}(v/V_{axial})}$
$\bar{C}_p$	= static pressure coefficient, $(\Delta\bar{p}/\frac{1}{2}\rho U_t^2)$
i	= incidence angle
k	= reduced frequency, $(\omega b/V_{axial})$
N	= number of rotor revolutions
S	= stator vane circumferential spacing
U_t	= rotor blade tip speed
u	= longitudinal perturbation velocity
V	= absolute velocity
V_{axial}	= absolute axial velocity
v	= transverse perturbation velocity
β	= inlet angle
Δp	= dynamic pressure difference
$\Delta\bar{p}$	= static pressure difference, $\bar{p} - P_{exit}$
ρ	= inlet air density
ω	= blade passing angular frequency

Introduction

THE demand for gas turbines with increased durability has made the structural dynamic response of turbomachinery blade rows to periodic aerodynamic loading a problem of increasing concern. In particular, as part of the engine design process, the alternating blade stresses due to resonant vibratory response must be predicted. The failure to accurately account for this vibratory behavior can lead to premature engine failure and reduced engine life.

Vibratory responses of blade rows occur when a periodic aerodynamic forcing function with frequency equal to a natural blade resonant frequency acts upon a blade row. The rotor speeds at which these aerodynamically induced vibrations may occur are predicted with Campbell diagrams. However, Campbell diagrams yield no information about the amplitude of the resulting stresses.

The structural behavior of turbomachinery blade rows in terms of airfoil frequencies and mode shapes can be accurately predicted from geometric and material considerations. However, the overall vibratory response of the blade row is influenced not only by the structural dynamics, but also by the unsteady aerodynamics of the blade row. Unfortunately, a general predictive capability for the unsteady aerodynamics due to periodic disturbances does not yet exist. Thus, due to the inadequacies of current unsteady aerodynamic models, accurate predictions cannot be made for the amplitude of the resulting vibration and stress.

Small perturbation models for the periodic disturbance unsteady aerodynamics have been developed which consider a gust convected with the freestream past zero thickness cascade flat plate airfoils operating at zero mean incidence in both subsonic and supersonic flowfields, for example, Refs. 1-3. Atassi[4] has developed an analysis for incompressible unsteady flow past an isolated thick cambered airfoil including incidence effects. Caruthers[5] and Caspar and Verdon[6] have developed subsonic compressible cascade analyses which consider thick, cambered airfoils operating at incidence.

To verify such mathematical models, experiments in single stage research compressors have been performed.[7-9] The upstream rotor wake and the resultant first harmonic unsteady pressures on the surfaces of the downstream stator vanes are measured and correlated with predictions obtained from harmonic cascade gust models.

However, these analyses and experiments consider only one blade row at a time, with the effect of the upstream blade rows represented by the harmonic aerodynamic gust, i.e., multistage blade row aerodynamic interactions are not directly considered.

In this paper, the fundamental multistage interaction gust unsteady aerodynamics of nonresponding airfoils are experimentally investigated for the first time. In particular, the aerodynamic forcing functions as well as the chordwise distributions of the steady pressures and first harmonic unsteady pressure differences on the first and second stage stator vane rows of a three-stage research compressor are experimentally determined over a range of operating and geometric conditions.

Presented as Paper 85-1134 at the AIAA/SAE/ASME/ASEE 21st Joint Propulsion Conference, Monterey, CA, July 8-11, 1985; received Jan. 29, 1986.

*Air Force Research in Aero Propulsion Technology trainee, Thermal Sciences and Propulsion Center School of Mechanical Engineering. Student member AIAA.

†Professor, School of Mechanical Engineering; and Director, Thermal Sciences and Propulsion Center. Associate Fellow AIAA.

Research Compressor

The wakes from upstream blade and vane rows are the primary source of the unsteady aerodynamics on the downstream blade rows, i.e., the upstream airfoil wakes define the forcing function to the downstream airfoil rows. Hence, it is necessary to experimentally model the basic unsteady aerodynamic phenomena inherent in this time-variant interaction, including the incidence angle, velocity and pressure variations, aerodynamic forcing function waveforms, reduced frequency, and blade row interactions.

These fundamental phenomena are all simulated in the Purdue University three-stage axial flow research compressor (Fig. 1). The compressor is driven by a 15 hp DC electric motor over a speed range of 300 to 3000 rpm. The inlet section is located aft of the drive motor. In the exit of this section are 38 variable geometry guide vanes which direct the flow into the test section. Three identical compressor stages are mounted in the test section, which has an annulus with constant hub (0.300 m) and tip (0.420 m) diameters. The exit flow from the test section is directed through a series of flow straighteners into a venturi meter which enables the mass flow rate to be determined. To throttle the compressor, an adjustable plate is located at the exit of the diffuser of the venturi.

Each of the three identical compressor stages consists of 43 rotor blades and 41 stator vanes. These free vortex design airfoils have a British C4 section profile, a chord of 30 mm, and a maximum thickness-to-chord ratio of 0.10. The overall airfoil and compressor characteristics are presented in Table 1. For the case of rotor generated forced response unsteady aerodynamics, the interblade phase angle is specified by the ratio of the number of rotor blades to stator vanes. Hence the interblade phase angle for these experiments is 17.56 deg.

Instrumentation

The steady state data of interest include the overall compressor performance and the aerodynamic loading distributions on the first and second stage stator vane rows.

Conventional steady state instrumentation is used to determine the flow properties in the compressor. The inlet temperature is measured by four equally spaced thermocouples at the inlet of the compressor. Casing static taps, equally spaced circumferentially, allow the measurement of the static pressure between each blade row. The traversing gear instrument stations provided each blade row are used to measure the mean flow incidence angle. A thermocouple and Kiel probe located downstream are used to measure the compressor exit temperature and total pressure, respectively. The mass flow is measured with the calibrated venturi meter located downstream of the compressor test section. A shaft mounted 60 tooth gear and a magnetic pickup provide the rotor speed.

The steady state aerodynamic loading of the vane rows is determined by instrumenting a pair of stator vanes with chordwise distributions of surface static pressure taps. It is only necessary to instrument one pair of vanes as the first and second stage vane rows are identical and interchangeable.

The unsteady aerodynamic data of fundamental interest are: 1) the fluctuating aerodynamic forcing function to the first and second stage stators, i.e., the wakes from the upstream blade rows; and 2) the resulting chordwise distribution of the complex time-variant pressure difference across the chordline of the first and second stage stator vane rows.

The aerodynamic forcing function to the vane rows is measured with a cross-wire probe calibrated and linearized to 45 m/s and ±35 deg angular variation. The mean absolute exit flow angle from the rotor is determined by rotating the cross-wire probe until a zero voltage difference is obtained between the two linearized hot-wire signals. This mean angle is then used as a reference for calculating the instantaneous absolute and relative flow angles. The output from each channel is corrected for tangential cooling effects, with individual fluctuating velocity components parallel and normal to the mean flow angle, i.e., the components of the aerodynamic gust, calculated from the corrected quantities. For this velocity and flow angle range, the accurcy of the velocity magnitude and angle are ±4% and ±2 deg, respectively.

The airfoil surface dynamic pressure measurements are accomplished with Kulite thin-line design dynamic pressure transducers. As per the steady instrumentation on the stator vanes, only two vanes are instrumented. The suction surface of one vane and the pressure surface of the second are instrumented with these transducers at 14.1, 29.1, 47.4, and 63.7% of the vane chord. To minimize any flow disturbances generated by the transducers, they are embedded in the vanes and connected to the surface by a static pressure tap with the lead wires placed in milled slots and carried out through hollow trunnions. Calibrations of the transducers showed the accuracy of the unsteady pressure measurements to be ±3.5%.

As schematically depicted in Fig. 2, each set of instrumented vanes are located such that a flow passage is instrumented. Also, the cross-wire probe is located axially upstream of the leading edge of the stator row at midstator circumferential spacing in a noninstrumented vane passage.

Data Acquisition and Analysis

The steady state compressor performance data acquisition follows the standard evaluation procedure. At the selected corrected speed, the compressor is stabilized for approximately 10 min, after which the steady state data acquisition is initiated and controlled by a PDP 11-23 computer. The data are then analyzed, and the corrected mass flow, pressure ratio, corrected speed, and vane surface static pressure distributions determined.

The time-variant data acquisition and analysis technique used is based on a data averaging or signal enhancement concept.[10] The key to such a technique is the ability to sample data at a preset time. In this investigation, the data of interest are generated at the blade passing frequency. Hence, an optical encoder, delivering a square wave voltage

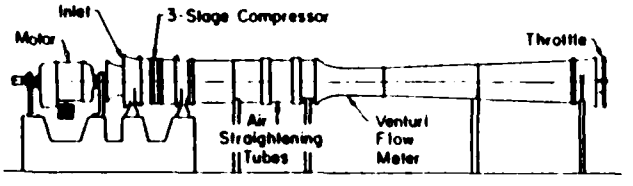

Fig. 1 Three-stage axial flow research compressors.

Table 1 Airfoil mean section characteristics and compressor design point conditions

	Rotor	Stator
Type of Airfoil	C4	C4
Number of Blades	43	41
Chord, C(mm)	30	30
Solidity, C/S	1.14	1.09
Camber	27.95	27.70
Aspect Ratio	2.0	2.0
Thickness/Chord (%)	10	10
Flow Rate (kg/s)	2.66	
Rotor-Stator Axial Spacing (mm)	22.2	
Design Axial Velocity (m/s)	32.0	
Rotational Speed (rpm)	3000	
Number of Stages	3	
Stage Pressure Ratio	1.003	
Inlet Tip Diameter (mm)	420	
Hub/Tip x Radius Ratio	0.714	
Stage Efficiency (%)	85	

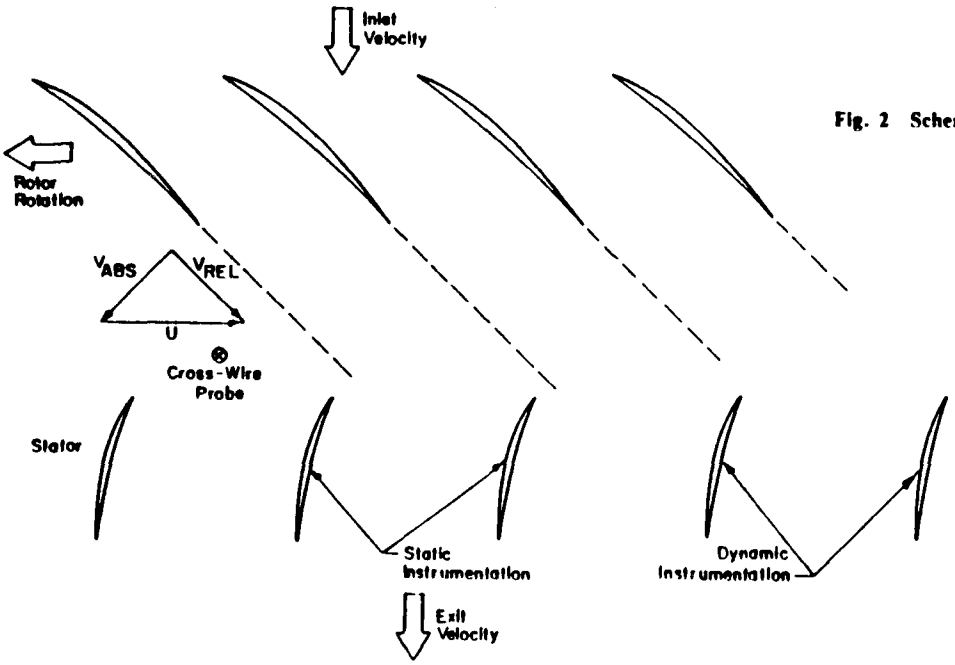

Fig. 2 Schematic of flowfield and instrumentation.

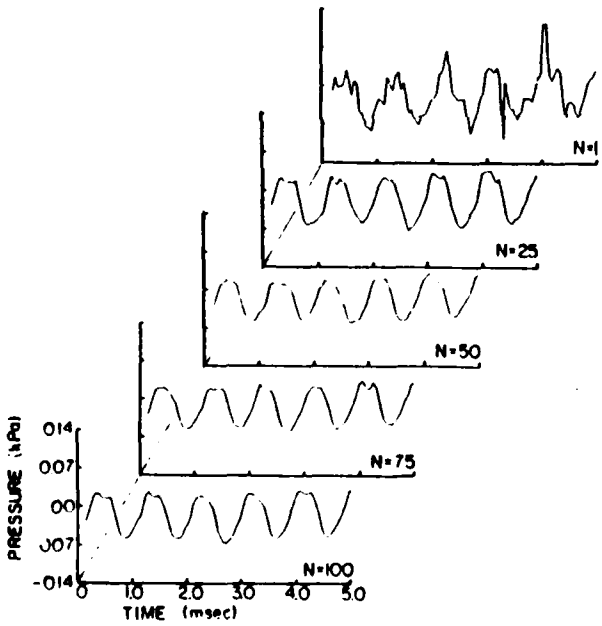

Fig. 3 Averaging of unsteady pressure signals.

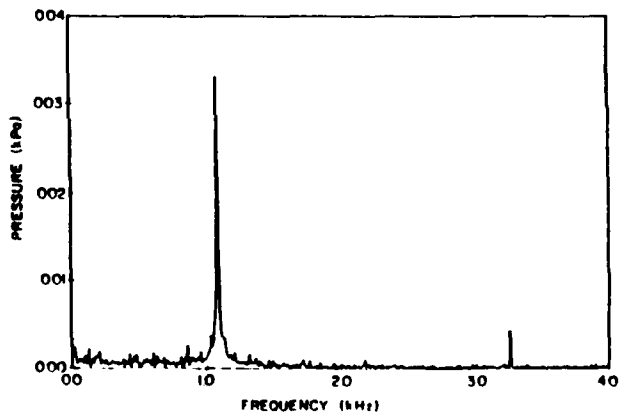

Fig. 4 Fourier decomposition on averaged unsteady pressure signal.

signal with a duration in the microsecond range, was mounted on the rotor shaft and used as the time or data initiation reference to trigger the A-D multiplexer system. This system is capable of digitizing signals simultaneously at rates to 5 MHz per channel, storing 2048 data points per channel.

The effect of averaging the time-variant digitized pressure signals from the blade mounted dynamic pressure transducers was considered. Figure 3 displays the time-variant pressure signal from the 14.1% chord pressure surface dynamic pressure transducer for 1 rotor revolution and averaged over 25, 50, 75, and 100 rotor revolutions. As seen, averaging greatly reduces the random fluctuations superimposed on the harmonic pressure signal. Also, these time-variant pressure signals are essentially unchanged when averaged over 75 or more rotor revolutions.

At each steady state operating point, an averaged time-Kulite dynamic pressure transducer signals digitized at a rate of 200 KHz and averaged over 100 rotor revolutions, are not consecutive due to the finite time required for the A-D multiplexer system to sample the data and the computer to then read the digitized data.

Each of these digitized signals is Fourier decomposed into harmonics by means of an FFT algorithm. Figure 4 shows an example of this decomposition for the 14.1% chord pressure surface transducer signal. As seen, the transducer signal contains a dominant fundamental frequency at the blade passing frequency and much smaller higher harmonics. In addition, the averaged signal exhibits minimal nonharmonic content. From this Fourier decomposition, both the magnitude of each component and its phase lag as referenced to the optical encoder pulse are determined.

Figure 5 presents the digitized signal from the trailing edge transducer on the pressure surface together with the sum of the first three harmonics of this signal. As seen, the addition of the first three harmonics yields a good approximation to the signal, thereby demonstrating that this signal is composed primarily of the first three harmonics of the rotor blade passage frequency.

From the Fourier analyses performed on the data, the magnitude and phase angle of the first harmonic as refer-

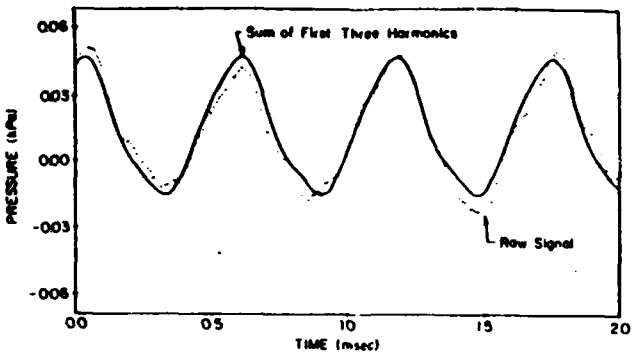

Fig. 5 Digitized signal together with the sum of the first three harmonics.

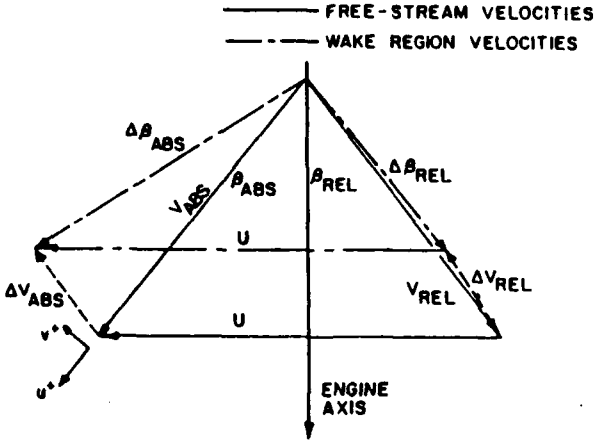

Fig. 6 Variation of absolute velocity due to rotor blade wakes.

the wake generated velocity profiles with the first harmonic surface dynamic pressures on the instrumented vanes, the rotor exit velocity triangles are examined. Fig. 6 shows the change in rotor relative exit velocity which occurs as a result of the presence of the blade. A deficit in the velocity in this relative frame creates a change in the absolute velocity vector as indicated. This velocity change is measured with the crossed hot-wires. From this instantaneous absolute angle and velocity, the rotor exit relative angle and velocity as well as the magnitude and phase of the perturbation quantities are determined.

As noted previously, the hot-wire probe is positioned upstream of the leading edge of the stator row. To relate the time based events as measured by this hot-wire probe to the unsteady pressures on the vane surfaces, the following assumptions are made: 1) the wakes are identical at the hot-wire and the stator leading edge planes; and 2) the wakes are fixed in the relative frame. A schematic of the rotor wakes, the instrumented vanes, and the hot-wire probe was presented in Fig. 2. The rotor blade spacing, vane spacing, length of the hot-wire probe, and axial spacing between the vane leading edge plane and the probe holder centerline are known quantities. At a steady operating point, the hot-wire data is analyzed to determine the absolute flow angle and the rotor exit relative flow angle. Using the above two assumptions, the wake is located relative to the hot-wires and the leading edges of the instrumented vane suction and pressure surfaces. From this, the times at which the wake is present at various locations is determined. The increment times between occurrences at the hot-wire and the vane leading edge plane are then related to phase differences between the perturbation velocities and the vane surface.

To simplify the experiment-theory correlation process, the first harmonic data is adjusted in phase such that the

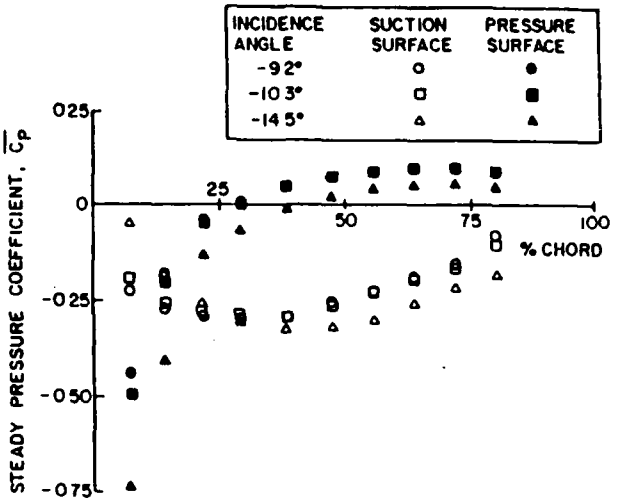

Fig. 7 First stage vane static pressure coefficient distribution.

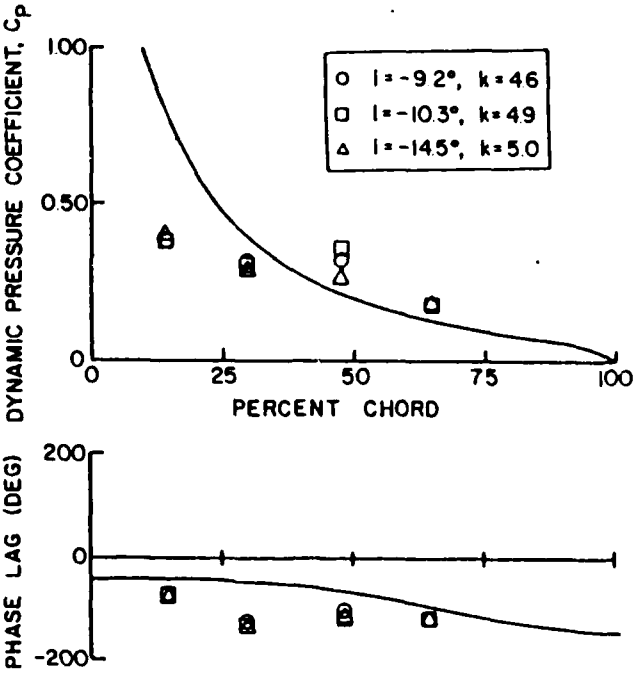

Fig. 8 First harmonic unsteady data correlation for first stage vane.

transverse perturbation is at zero degrees at the vane suction surface leading edge. From the geometry indicated in Fig. 2, the time at which this would occur is calculated and transposed into a phase difference. This difference is then used to adjust the pressure data from the suction surface. A similar operation is performed on the pressure surface data so that the surfaces of the vanes are time related; i.e., time relating the data results in data equivalent to that for a single instrumented vane. Following this procedure, the first harmonic pressure differences across an equivalent single vane at each transducer location are calculated. The final form of the unsteady pressure data describes the chordwise variation of the first harmonic pressure difference across a stator vane and is presented as an aerodynamic phase lag referenced to a transverse gust at the airfoil leading edge and the dynamic pressure coefficient,

$$C_p = \frac{\Delta p}{\rho V_{axial}^2 (v/V_{axial})}$$

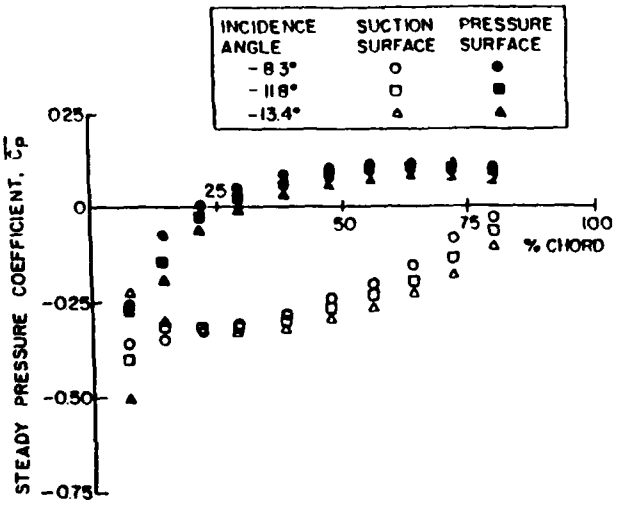

Fig. 9 Second stage vane static pressure coefficient distribution.

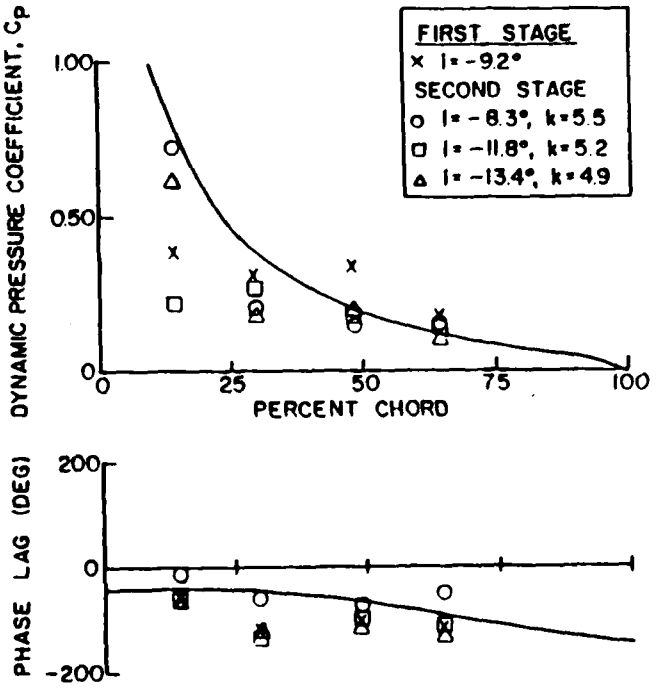

Fig. 10 First harmonic unsteady data correlation for second stage vane.

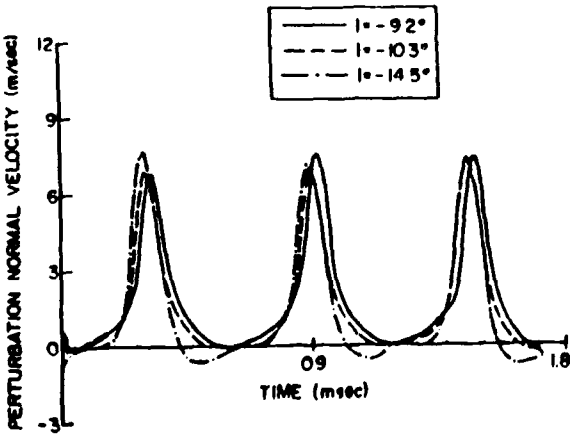

Results

The objective of this series of experiments is the quantitative investigation of the blade row interaction first harmonic gust unsteady aerodynamics. This is accomplished by measuring the aerodynamic forcing functions and the chordwise distributions of the steady pressures and the first harmonic unsteady pressure differences on the first and second stage stator vane rows of a three-stage research compressor over a range of operating and geometric conditions.

The chordwise distributions of the first harmonic of the complex unsteady pressure differences across the vane rows are correlated with predictions obtained from a periodic gust model which considers the inviscid, irrotational flow of a perfect gas. This model[2] analyzes the uniform subsonic compressible flow past a two-dimensional flat plate airfoil cascade, with small unsteady normal velocity perturbations superimposed and convected downstream. The parameters include the cascade solidity and stagger angle, the interblade phase angle, inlet Mach number, and reduced frequency.

The first stage vane steady and first harmonic unsteady data at incidence angles of -9.2, -10.3, and -14.5 deg, are presented in Figs. 7 and 8, respectively. No evidence of flow separation is evident in the vane surface static pressure distributions, with the steady aerodynamic loading a function of the incidence angle, as expected. However, the first harmonic unsteady data, Fig. 8, are nearly independent of the incidence angle and the steady loading over this range of operating conditions. The difference between the zero incidence flat plate predictions and these unsteady data are attributed to the camber of the airfoil and incidence angle ef-

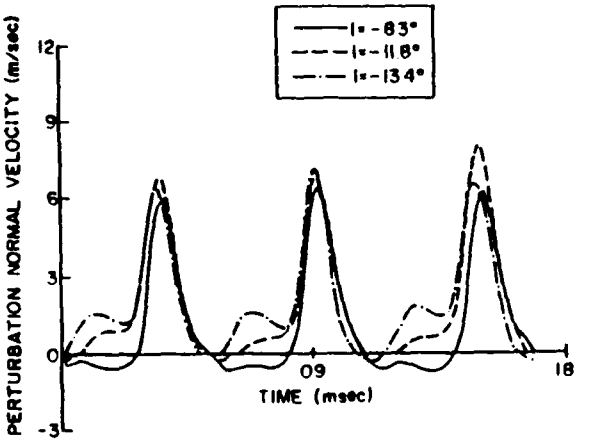

Fig. 12 Second stage vane aerodynamic forcing function waveform.

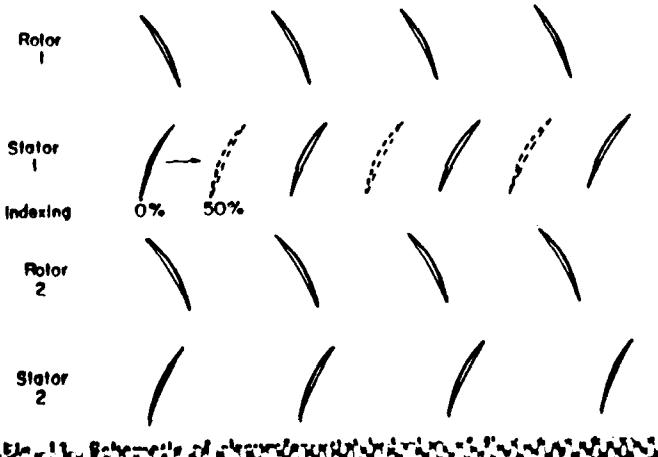

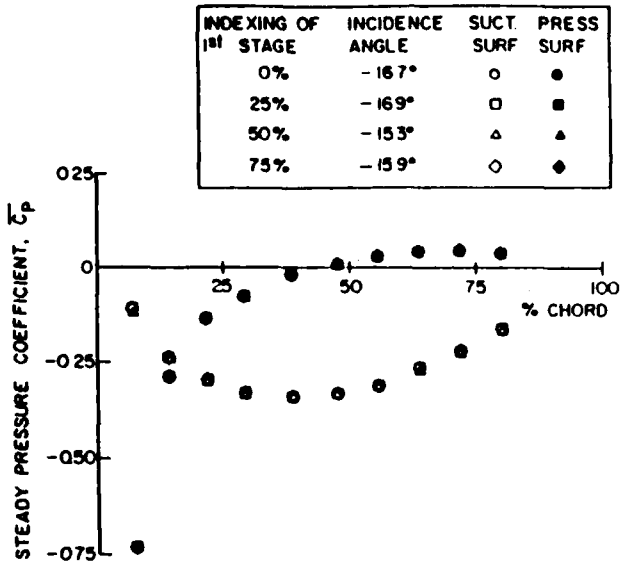

Fig. 14 Effect of first stage stator indexing on second stage vane static pressure coefficient.

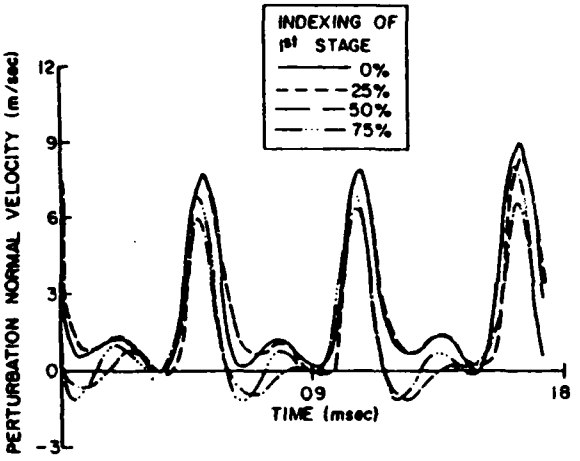

Fig. 15 Effect of first stage stator indexing on second stage vane forcing function waveform.

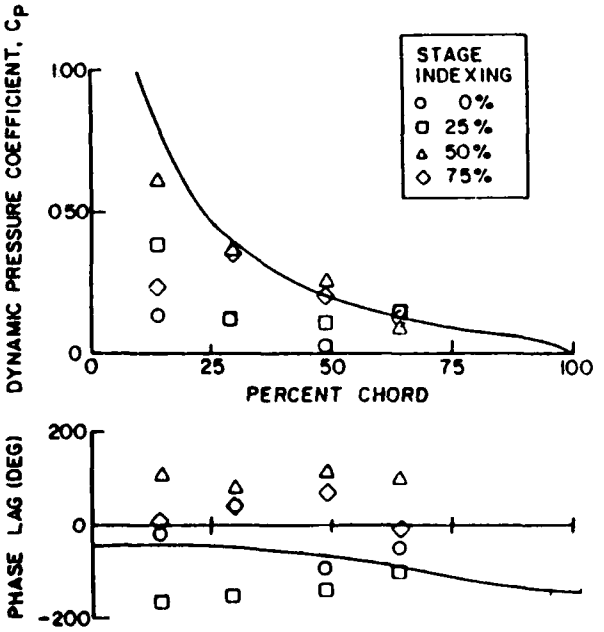

Fig. 16 Effect of first stage vane indexing on second stage vane unsteady data at -16 deg of incidence.

fects, analogous to the single stage experimental results of Refs. 8, 9, and 10.

The second stage steady loading distribution and the correlation of the first and second stage unsteady data for this same range of incidence angles and reduced frequency values are presented in Figs. 9 and 10, respectively. The chordwise static pressure distributions on the vane surfaces are similar for both stages, with the steady aerodynamic loading a function of the incidence angle and no evidence of flow separation. The second stage unsteady data exhibit the same overall trends as that of the first stage. However, unlike the first stage results, these second stage unsteady data, particularly the dynamic pressure coefficient, are a function of the incidence angle and, thus, the steady state loading.

To understand this difference in the effect of incidence angle on the first and second stage unsteady data, it is necessary to consider the aerodynamic forcing functions for the unsteady pressure data, i.e., the upstream wakes impinging on the downstream stator vanes. Figure 11 presents the wake normal perturbation velocity waveforms which are the forcing function to the first stage vane row data of Fig. 8. As seen, these waveforms are nearly identical to one another. The corresponding second stage vane row inlet normal perturbation velocity waveforms are presented in Fig. 12. These waveforms differ significantly from one another and also from the first stage wake waveforms. This variation in waveform of the second stage forcing function with steady operating point is a multistage blade row interaction effect, with the second stage rotor wake being modulated by the wakes from upstream first stage rotor and stator airfoils.

The research compressor used in this study offers the ability to investigate this multistage unsteady blade row interaction effect. This is because the first stage stator vanes can be indexed circumferentially relative to the second stage vane row. Thus, this multistage unsteady blade row interaction is investigated at a fixed steady state operating point by indexing the first stage stator row relative to the second stage vane row, as schematically depicted in Fig. 13. Specifically, with the first stage stators indexed 0, 25, 50, and 75%, relative to the second stage vane, complete steady and unsteady second stage vane row data sets are obtained.

The circumferential indexing of the first stage stator vanes has no effect on the second stage vane steady state loading distributions (Fig. 14). However, it does have a significant effect on the waveform of the aerodynamic forcing function to the second stage vanes. In particular, the relative stator positioning results in the modulation of the waveform of the second stage rotor wakes, as seen in Fig. 15. This waveform modulation of the primary forcing function to the second stage vane row affects the complex unsteady pressure distributions on this vane row (Fig. 16).

These variations of the unsteady data with forcing function waveform cannot be predicted by harmonic gust models. This is because the forcing function waveforms and the resulting unsteady pressure distributions have been Fourier decomposed, with the first harmonics of the unsteady data presented. Thus, all of these first harmonic unsteady data are correlated with the same prediction curve, as indicated in Fig. 16, i.e., the predictions from these harmonic gust models are identical for all of the forcing function waveforms.

Summary and Conclusions

A three-stage research compressor has been utilized to investigate the fundamental multistage blade row interaction gust unsteady aerodynamics for the first time. The aerodynamic forcing functions as well as the chordwise distributions of the steady surface pressures and the first harmonic unsteady pressure differences on the first and second stage stator vane rows were experimentally determined over a range of operating conditions, including the indexing of the first stage stator row relative to the second stage vane row.

This series of experiments demonstrated the major effect of multistage blade row interactions on the unsteady aerodynamics of downstream blade rows. In particular, the first stage blade rows modulated the waveform of the aerodynamic forcing function to the second stage vane row. This has no effect on the steady loading of the second stage vanes, but does have a significant effect on the resulting complex unsteady chordwise pressure difference distributions. Thus, the complex unsteady aerodynamic loading on downstream blade rows is directly related to the forcing function to that blade row, with this forcing function significantly affected by multistage blade row interaction phenomena. These results have an implication towards the modeling of unsteady aerodynamic blade row interaction phenomena. Namely, the variations of the second stage unsteady data with forcing function waveform cannot be predicted by harmonic gust models, i.e, the predictions from these gust models would be identical for all of the forcing function waveforms.

Acknowledgment

Support of this experimental research program by the Air Force Office of Scientific Research, Dr. James Wilson, program manager, is gratefully acknowledged.

References

[1]Whitehead, D. S., "Force and Moment Coefficients for Vibrating Airfoils in Cascade," Aeronautical Research Council R&M3254, Feb. 1960.

[2]Fleeter, S., "The Fluctuating Lift and Moment Coefficients for Cascaded Airfoils in a Nonuniform Compressible Flow," *Journal of Aircraft*, Vol. 10, Feb. 1973.

[3]Englert, G. W., "Interaction of Upstream Flow Distortions with High Mach Number Cascades," ASME Paper 82-GT-137, 1982.

[4]Atassi, H. M., "The Sears Problem for a Lifting Airfoil Revisited—New Results," *Journal of Fluid Mechanics*, Vol. 141, 1984.

[5]Caruthers, J. E., "Wake Induced Vibration of Axial Components," NASA/AIR FORCE/NAVY Symposium on Aeroelasticity of Turbine Engine, Cleveland, OH, Oct. 1980.

[6]Verdon, J. M. and Caspar, J. R., "Development of an Unsteady Aerodynamic Analysis for Finite Deflection Subsonic Cascades," NASA-CR-3455, Sept. 1981.

[7]Fleeter, S., Jay, R. L., and Bennett, W. A., "Rotor Wake Generated Unsteady Aerodynamic Response of a Compressor Stator," *ASME Journal of Engineering for Power*, Vol. 100, Oct. 1978.

[8]Fleeter, S., Jay, R. L., and Bennett, W. A., "The Time-Variant Aerodynamic Response of a Stator Row Including the Effects of Airfoil Camber," *ASME Journal of Engineering for Power*, Vol. 102, April 1980.

[9]Fleeter, S. and Capece, V., "Stator Row Unsteady Aerodynamics Due to Wake Excitations," Symposium on Unsteady Aerodynamics of Turbomachines and Propellers, Cambridge, England, 1984, pp. 427-446.

[10]Ciostelow, J. P., "A New Approach to the Experimental Study of Turbomachinery Flow Phenomena," *ASME Journal of Engineering for Power*, Vol. 99, Jan. 1977.

APPENDIX IV

WAKE INDUCED UNSTEADY INTERACTIONS IN A MULTISTAGE COMPRESSOR

AIAA JOURNAL OF PROPULSION AND POWER

(TO APPEAR)

WAKE INDUCED UNSTEADY AERODYNAMIC INTERACTIONS IN A MULTI-STAGE COMPRESSOR

Vincent R. Capece*
Sanford Fleeter**
Thermal Sciences and Propulsion Center
School of Mechanical Engineering
Purdue University
West Lafayette, Indiana 47907 U.S.A.

ABSTRACT

The effects of steady loading and the detailed aerodynamic forcing function on airfoil row unsteady aerodynamics are investigated and quantified at high reduced frequency values. For the first time, both parallel and normal gust components of the forcing function are considered. This is accomplished by a series of experiments which quantify the unsteady aerodynamics of the first stage vane row of a research compressor. The effects of steady vane aerodynamic loading with both non-constant and constant aerodynamic forcing functions are quantified. These data show that the steady loading affects only the magnitude of the complex dynamic pressure coefficient whereas the ratios of the maximum amplitudes of the parallel and normal components of the aerodynamic forcing function affects both the magnitude and the phase lag. The relative effects of the two components of the time-variant inlet velocity field on the resulting vane row unsteady aerodynamics are also investigated, showing that the parallel component of the aerodynamic forcing function affects only the dynamic pressure coefficient phase lag. The correlation of the dynamic pressure coefficient data with flat plate predictions is also considered. The level and chordwise distribution of the steady aerodynamic loading, not the incidence angle, are revealed to be the key parameters to obtain good correlation with such mathematical models.

NOMENCLATURE

b	airfoil semi-chord
C_p	dynamic pressure coefficient, $\Delta p/\rho V_x^2(\frac{v^+}{V_x})$
$\bar{C}_p$	static pressure coefficient, $(\bar{p}-\bar{p}_{exit})/\frac{1}{2}\rho U_t^2$
k	reduced frequency, $\omega b/V_x$
i	incidence angle
N	number of rotor revolutions
$\bar{p}$	stator vane surface static pressure
$\bar{p}_{exit}$	stator vane exit static pressure
Δp	dynamic pressure difference across chordline
u^+	inlet velocity parallel to vane
U_t	rotor blade tip speed
v^+	inlet velocity normal to vane
V	absolute velocity
V_x	absolute axial velocity
ρ	inlet air density
ω	blade passing frequency

INTRODUCTION

An item of concern for high-performance gas turbine engines is the structural dynamic response of fan, compressor, and turbine blading to aerodynamic excitations. The spatially periodic variations in pressure, velocity, and flow direction of the exit flow field of an upstream airfoil row appear as temporally varying in a coordinate system fixed to a downstream row of airfoils. This periodic inlet flow field is an aerodynamic forcing function to the downstream airfoil row which may lead to vibrations of these airfoils. In particular, when the frequency of the aerodynamic forcing function is equal to one of the natural frequencies of the downstream airfoils, vibrations result which can have large amplitudes and associated high vibratory stress levels.

At present, these resonant stress levels can not be accurately predicted. Thus, they are unknown until the first testing of the blade or vane row. If this testing reveals stresses in excess of a predetermined allowable level, airfoil life considerations then require a redesign to reduce these stresses.

To predict the aerodynamically forced response vibratory behavior of an airfoil row requires a definition of the unsteady forcing function in terms of its harmonics. The periodic aerodynamic response of the airfoil row to each forcing function harmonic is then assumed to be comprised of two distinct but related unsteady aerodynamic parts. One is due to the chordwise and normal components of the harmonic forcing function being swept past the non-responding fixed airfoil row, termed the normal (or transverse) and chordwise gust responses, respectively. The second, the self-induced unsteady aerodynamics, is associated with the resulting harmonic oscillatory response of the airfoils.

There are many analytical and physical assumptions inherent in the various gust and self-induced unsteady aerodynamic models, references 1 through 6 for example. However, only very limited experimental data exists to assess the range of validity and to direct the refinements necessary to develop valid predictive design systems.

---

* AFRAPT Trainee
**Professor, School of Mechanical Engineering
Director, Thermal Sciences and Propulsion Center
MEMBER AIAA

At very low values of the reduced frequency, fundamental data for both self-induced unsteady and normal gust aerodynamics have been obtained in linear cascades. Carta and St. Hilaire [7,8] performed a series of oscillating airfoil experiments and demonstrated the effect of aerodynamic loading on self-induced unsteady aerodynamics, with the interblade phase angle found to be the principle parameter affecting stability. Ostdiek [9] developed an oscillating inlet wind tunnel and investigated the normal component gust aerodynamics.

At the high values of reduced frequency characteristic of turbomachinery, low speed single and multi-stage research compressors have been used to investigate normal component gust aerodynamics. These experiments considered the effect of airfoil camber and rotor-stator axial spacing, references 10 to 11, and also showed that the aerodynamic forcing function waveform has an important influence on the fundamental normal gust unsteady aerodynamics [12].

In this paper, the effects of steady airfoil loading and the detailed aerodynamic forcing function on airfoil row unsteady aerodynamics are investigated and quantified at high reduced frequency values. For the first time, both parallel and normal gust components of the forcing function are considered. This is accomplished by the acquisition and analysis of unique data which describe the unsteady aerodynamics of the first stage vane row of a research compressor over a range of steady operating conditions.

As schematically depicted in Figure 1, the wakes from the rotor blades are the primary source of the unsteady aerodynamics of the first stage stator vanes, i.e., the exit flow field from the rotor defines the forcing function to the downstream stator vanes. This aerodynamic forcing function is defined by the velocity components parallel and normal to the vane chord, u+ and v+ respectively. The variation in the forcing function is accomplished by altering the setting angle of the inlet guide vanes which establish the first stage rotor flow field, including the rotor exit flow field which is the aerodynamic forcing function to the downstream first stage vane row.

RESEARCH COMPRESSOR

It is necessary to experimentally model the basic unsteady aerodynamic phenomena inherent in the time-variant blade row flow interaction including the incidence angle, the velocity and pressure variations, the aerodynamic forcing function waveforms, the reduced frequency, and the blade row interactions. These are all simulated in the Purdue University axial flow research compressor, Figure 2. This compressor is driven by a 15 HP DC electric motor over a speed range of 300 to 3,000 RPM. Each of the three identical compressor stages contains 43 rotor blades and 41 stator vanes, with the first stage rotor flow field established by a row of variable setting angle inlet guide vanes. The airfoils are of free vortex design and have British C4 section profiles.

INSTRUMENTATION

Both steady-state and time-variant data are of interest. The steady data describe the overall compressor operating point and the detailed vane surface steady loading. The unsteady data define the time-variant aerodynamic vane row inlet flow field, i.e., the vane row aerodynamic forcing function, and the resulting vane surface unsteady pressure distributions.

Steady-State

Conventional steady-state instrumentation is used to determine the flow properties throughout the compressor. The inlet temperature is measured by four equal circumferentially spaced inlet thermocouples. The static pressures between each blade row are measured with casing static taps. Traversing stations between each blade row are used to measure the mean flow incidence angles. A downstream thermocouple and Kiel probe determine the compressor exit temperature and total pressure, respectively. The mass flow is measured with the calibrated venturi meter located downstream of the compressor test section. A shaft mounted 60 tooth gear and a magnetic pick-up provide the rotor speed.

The steady-state aerodynamic loading on the vane surfaces is determined by instrumenting a pair of stator vanes with chordwise distributions of midspan surface static pressure taps. Flow visualization showed the flow to be two-dimensional along this streamline. These vanes are positioned such that one complete flow passage is instrumented, Figure 1.

Time-Variant

The airfoil surface time-variant pressure measurements are accomplished with Kulite thin-line design high response transducers. A reverse mounting technique is utilized, with the transducers embedded in the vanes from the backside and connected to the measurement surface by a static tap. This minimizes any disturbance generated by the inability of the transducer or mounting to exactly maintain the vane surface curvature. As also depicted in Figure 1, these vanes are positioned such that a complete flow passage is instrumented.

The embedded transducers are statically and dynamically calibrated. The static calibrations exhibit good linearity and no discernible hysteresis. The dynamic calibrations demonstrate that the frequency response, in terms of gain attenuation and phase shift, is not affected by the transducer mounting. The accuracy of the unsteady pressure measurements, determined from the calibrations, is ±3.5%

The time-variant inlet flow field to the vane row is measured with a cross hot-wire probe positioned midway between rotor and stator at mid-stator circumferential spacing, Figure 1. These probes are calibrated and linearized to 45 m/sec and ±35° angular variation, with the accuracy of the velocity magnitude and angle of ± 4% and ±2°, respectively. The mean absolute flow angle is determined by rotating the probe until a zero vol-

tage difference between the two linearized hot-wire signals is obtained. This mean angle is subsequently used as a reference for calculating the instantaneous absolute and relative flow angles.

DATA ACQUISITION AND ANALYSIS

A digital data acquisition and analysis system centered around a Hewlett-Packard HP-1000 computer is utilized to acquire and analyze on-line both the steady and unsteady data.

Steady-State

A 48 channel Scanivalve system is used to acquire the steady pressure data. Under computer control, the Scanivalve is calibrated each time steady-state data are acquired, with compensation automatically made for variations in the zero and span output. As part of this steady-state data analysis sequence, a root-mean-square error analysis is performed, with the steady data defined as the mean of 30 samples, with the 95% confidence intervals determined.

Time-Variant

The time-variant data from the hot-wire probe and the dynamic pressure transducers are obtained under computer control by first conditioning their signals and then digitizing them with a high speed A-D system. This eight channel A-D system is able to digitize signals simultaneously at rates to 5 MHz per channel, storing 2048 points per channel.

The time-variant data of interest are periodic, being generated at rotor blade passing frequency, with a digital ensemble averaging technique used for data analysis. The key to this technique is the ability to sample data at a preset time. This is accomplished by an optical encoder mounted on the rotor shaft. The microsecond range square wave voltage signal from the encoder serves as the time or data initiation reference and triggers a high speed A-D multiplexer system.

The time-variant hot-wire probe and dynamic pressure transducer signals are analyzed to determine their periodic components by means of a digital ensemble averaging data analysis technique based on the signal enhancement concept of Gostelow [13]. This ensemble averaging is demonstrated in Figure 3, which shows a typical digitized pressure transducer signal for 1 rotor revolution and averaged over 25, 50, 75, 100, and 200 rotor revolutions. Averaging significantly reduces the random fluctuations superimposed on the periodic signal, with the time-variant signals essentially unchanged when averaged over 75 or more rotor revolutions. For the data to be presented herein, 200 averages are used for both the hot-wire and vane pressure transducer signals.

The periodic hot-wire probe and dynamic pressure transducer signals are each then Fourier decomposed into harmonics by means of a Fast Fourier Transform (FFT) algorithm. This Fourier analysis determines the magnitude and phase of the first harmonic of the vane inlet flow field, i.e., the aerodynamic forcing function, and the resulting vane surface unsteady pressure distributions. These are each referenced to the initiation of the data acquisition. However, the hot-wire probe is positioned upstream of the leading edge plane of the vane row. Thus, it is necessary to time-relate the harmonic vane row inlet flow field to the resulting unsteady vane surface pressures.

As was depicted in Figure 1, the rotor blade wake velocity deficit creates a fluctuating velocity vector in the absolute frame of reference of the vane row which is measured with the crossed hot-wire probe. These hot-wire data are analyzed to determine the harmonic fluctuating vane inlet flow angle and velocity, in particular, the fluctuating velocity components parallel and normal to the vane, u+ and v+, which define the vane row aerodynamic forcing function.

The hot-wire probe is positioned upstream of the leading edge of the stator vane row. To relate time based events measured by this hot-wire probe to the resulting unsteady pressures on the vane surfaces, the following assumptions are made: (1) the wakes are identical at the hot-wire and the vane leading edge planes; and (2) the wakes are fixed in the rotor relative reference frame. The rotor blade spacing, the vane spacing, and the axial spacing between the vane leading edge plane and the probe centerline are known.

At a steady operating point, the hot-wire data are analyzed to determine the absolute flow angle and the rotor exit relative flow angle. Using the above two assumptions, the wake is located relative to the hot-wire probe and the leading edges of the instrumented vane. From this, the times at which the wakes are present at various locations are determined. The incremented times between occurrences at the hot-wire and the vane leading edge plane are then related to phase differences between velocities and the vane surface.

To simplify the experiment-theory correlation, the first harmonic data are adjusted in phase such that the transverse inlet velocity component is at zero degrees at the vane suction surface leading edge. From the geometry, the time at which this would occur is calculated and transposed into a phase difference which is then used to adjust the pressure data from the suction surface. An analogous procedure is utilized for the pressure surface data so that the two instrumented stator vanes are time related. The pressure difference across the chordline of an equivalent single vane is then determined by the subtraction of these complex time-related vane pressure and suction surface data.

The final form of the unsteady pressure data describes the chordwise variation of the first harmonic pressure difference across the chordline of a stator vane and is presented as a complex dynamic pressure coefficient, Cp, in the format of the magnitude and the phase lag referenced to a transverse gust at the airfoil leading edge. As a reference, also presented with these complex dynamic pressure coefficient data are predictions obtained from a periodic small perturbation model which considers the inviscid, irrotational flow of a perfect gas, reference 2. This model analyzes the uniform subsonic compressible flow past a two-dimensional flat plate airfoil cascade, with

small unsteady normal velocity perturbations superimposed and convected downstream.

RESULTS

A series of experiments on the 60% speedline of the compressor are performed to determine and quantify the effects of steady loading and the detailed aerodynamic forcing function, including the effects of both the parallel and normal gust components, on the resulting airfoil row unsteady aerodynamics. The variation in the forcing function is accomplished by altering the setting angle of the row of inlet guide vanes, as schematically depicted in Figure 4, which changes the rotor flow field. In particular, a change in the inlet guide vane setting angle alters the rotor exit flow field, i.e. it changes the aerodynamic forcing function to the downstream first stage vane row, including the parallel and normal gust components, u+ and v+.

At each steady-state operating point, an averaged time-variant data set consisting of the hot-wire and dynamic pressure transducer signals digitized at a rate of 200 kHz is obtained. This sample rate allows approximately 91 points between each rotor blade at the design rotational speed.

VANE LOADING EFFECTS

Non-Constant Forcing Functions

The effect of the steady airfoil aerodynamic loading distribution on the vane row unsteady aerodynamics including the influence of the detailed aerodynamic forcing function, both the parallel and normal aerodynamic forcing function components, is considered first. For two particular inlet guide vane settings, the stator row inlet flow field is shown in Figure 5, with the corresponding parallel and normal inlet velocity components shown in Figure 6. For these two configurations, the ratios of the maximum amplitude of the parallel component to that of the normal component are approximately 0.5 and 0.7. Also, it is interesting to note that these inlet velocity components are not small as compared to the free-stream velocity, having ratios on the order of 0.4-0.6 and 0.2-0.4 for the normal and parallel components, respectively.

The steady-state vane surface static pressure distributions are presented in Figure 7. The suction surface distributions are nearly identical except near the leading and trailing edge regions, with larger differences apparent on the vane pressure surface. Also, these configurations correspond to a high level of vane aerodynamic loading, with the vane incidence angles nearly the same, 5.7° and 5.8°.

Figure 8 presents the data describing the chordwise distributions of the first harmonic complex dynamic pressure coefficient. For these two cases, both the magnitudes and the phase lags of these dynamic pressure coefficient data vary over the vane chord, with the magnitude data exhibiting somewhat larger differences. Also, as will be further discussed, the high level of aerodynamic loading on the vanes results in the differences between these data and the prediction.

There are two potential mechanisms which cause the above noted variations in the complex dynamic pressure coefficient: (1) the steady aerodynamic loading on the vane; and (2) the differences in the vane row aerodynamic forcing function. These are individually investigated in the following.

Constant Forcing Functions

The effect of the steady airfoil aerodynamic loading distribution on the vane row unsteady aerodynamics for the same aerodynamic forcing function is now considered. A third inlet guide vane setting was established such that the parallel and normal inlet velocity components are nearly identical with one previously investigated. Figure 9 shows that for these two configurations, there are only minimal variations in the time-variant aerodynamic forcing function to the vane row, with the first harmonics of these components being nearly identical.

The vane row is highly loaded aerodynamically for these two configurations, with small differences in the vane surface static pressure distributions associated with these two configurations, Figure 10. The suction surface distributions are nearly identical, with differences apparent in the leading and trailing edge regions. The pressure surface distributions exhibit differences near the leading edge and aft of the quarter chord. Also, these configurations have only small differences in the vane incidence angle, 5.1° for one configuration and 5.7° for the other.

The chordwise distributions of the first harmonic complex dynamic pressure coefficient data are shown in Figure 11. For these two configurations and steady loading distributions, the dynamic pressure coefficient magnitude data differ near the leading edge and aft of quarter chord, with only a minimal effect on the phase lag data near the leading edge. These differences in the data correspond to the differences previously noted in the vane surface static pressure distributions, i.e., near the leading edge and aft of quarter chord. As the first harmonic aerodynamic forcing functions generating these distributions are nearly identical, these differences in the dynamic pressure coefficient data are attributed to steady vane aerodynamic loading effects.

A comparison of the variation of these dynamic pressure coefficient magnitude data with steady loading and a constant forcing function, Figure 11, and the corresponding data differences previously found with steady loading and a non-constant forcing function, Figure 8, reveals that the magnitude data differences for these two cases are not analogous to one another. Thus, it can be concluded that whereas steady loading affects only the magnitude of the complex dynamic pressure coefficient, the detailed aerodynamic forcing function, in particular, the ratios of the maximum amplitudes of the parallel and normal components of the aerodynamic forcing function, affects both the magnitude and the phase lag of the dynamic pressure coefficient.

EFFECT OF FORCING FUNCTION PARALLEL COMPONENT

To determine the relative effects of the two components of the time-variant inlet velocity

field on the resulting vane row unsteady aerodynamics, two new inlet guide vane settings were established such that the parallel components of the aerodynamic forcing function were different while the normal components were nearly the same, Figure 12. For these two configurations, the vane aerodynamic loading level is low, with only small incidence angle differences, -4.3° and -4.8°. The corresponding steady-state vane surface static pressure distributions are presented in Figure 13. The pressure surface distributions are nearly identical, with only very small differences noted on the vane suction surface.

Figure 14 shows the chordwise distributions of the first harmonic complex dynamic pressure coefficient data. The magnitude data are almost identical, with differences existing in the phase lag data. Previous results determined that for a constant aerodynamic forcing function, steady vane loading differences primarily resulted in differences in the magnitude data of the dynamic pressure coefficient. Hence, these differences in only the dynamic pressure coefficient phase lag data, are attributable to the differences in the time variant inlet flow field, in this particular case, the parallel component of the aerodynamic forcing function. Thus, the parallel component of the aerodynamic forcing function only has an effect on the dynamic pressure coefficient phase lag and has no effect on its magnitude.

PREDICTION-DATA CORRELATION

The correlation of the complex dynamic pressure coefficient data with the flat plate predictions, presented in Figures 8, 11, and 14, are also of interest. With regard to the correlation of the phase lag, relatively good correlation is evident for all cases. However, this is not true for the correlation of the magnitude of the dynamic pressure coefficient.

By far, the best correlation of the dynamic pressure coefficient data and the corresponding prediction is obtained for the -4.8° and -4.3° incidence angle cases, Figure 14, with good correlation apparent over the aft 75% of the vane chord. These correlation results are associated with the steady vane aerodynamic loading. Namely, the prediction is for an unloaded flat plate airfoil cascade. The -4.8° and -4.3° incidence angle data have a much lower level of aerodynamic loading than the other cases, as determined by a comparison of Figures 7, 10, and 13. Also, for the low loading cases, the good correlation over the aft 75% vane chord and poor correlation over the front 25% corresponds to the steady aerodynamic loading distributions on the vane surface, Figure 13.

To verify this effect of steady loading on the correlations, the vane row was re-staggered and a compressor operating point established such that there was a significantly lower level of vane steady loading, characterized by an incidence angle of -8.6°. The resulting excellent correlation of the dynamic pressure coefficient data with the prediction for this minimal loading condition is shown in Figure 15. Thus, the level of the steady aerodynamic loading, not the incidence angle, is a key parameter for correlation with flat plate cascade mathematical models.

SUMMARY AND CONCLUSIONS

A series of experiments was performed to investigate and quantify the effects of steady airfoil loading and the detailed aerodynamic forcing function on airfoil row unsteady aerodynamics at high reduced frequency values. For the first time, both parallel and normal gust components of the forcing function are considered. This was accomplished by the acquisition and analysis of unique data which describe the unsteady aerodynamics of the first stage vane row of a research compressor over a range of steady operating conditions.

The exit flow field from the rotor defines the forcing function to the downstream stator vanes, with this aerodynamic forcing function defined by the velocity components parallel and normal to the vane chord. The variations in this forcing function were accomplished by changing the inlet guide vane setting angle to alter the rotor exit flow field.

Data defining the effect of steady vane aerodynamic loading with non-constant aerodynamic forcing function components on the vane row unsteady aerodynamics were analyzed. These data demonstrated that the ratios of the maximum amplitude of the parallel component of the aerodynamic forcing function to that of the normal component affect both the magnitude and the phase lag of the resulting complex dynamic pressure coefficient.

The effect of steady airfoil aerodynamic loading on the vane row unsteady aerodynamics with a constant aerodynamic forcing function was then considered. The resulting data determined that steady aerodynamic loading affects the magnitude of the complex dynamic pressure coefficient, but not the aerodynamic phase lag.

The relative effects of the two components of the time-variant inlet velocity field on the resulting vane row unsteady aerodynamics were also investigated. The parallel component of the aerodynamic forcing function was found to affect only the phase lag of the dynamic pressure coefficient and not the magnitude.

The correlation of the complex dynamic pressure coefficient data with the flat plate predictions was also considered. Good correlation of the phase lag is evident for all cases. However, the level and chordwise distribution of the steady aerodynamic loading, not the incidence angle, were shown to be the key parameters to obtain good correlation with flat plate airfoil cascade mathematical models.

ACKNOWLEDGEMENTS

Support of this experimental research program by the Air Force Office of Scientific Research, Dr. James Wilson program manager, is gratefully acknowledged.

REFERENCES

1. Whitehead, D.S., "Force and Moment Coefficients for Vibrating Aerofoils in Cascade," Aeronautical Research Council R&M 3254, February 1960.

2. Fleeter, S., "Fluctuating Lift and Moment Coefficients for Cascaded Airfoils in a Nonuniform Compressible Flow," AIAA Journal of Aircraft, Volume 10, February 1973.

3. Atassi, H. and Akai, T.J., "Aerodynamic and Aeroelastic Characteristics of Oscillating Loaded Cascades at Low Mach Number," ASME Paper 79-GT-111, March 1979.

4. Naumann, H. and Yeh, H., "Lift and Pressure Fluctuations of a Cambered Airfoil Under Periodic Gusts and Applications in Turbomachinery," ASME Journal of Engineering for Power, January 1973.

5. Horlock, J.H., "Fluctuating Lift Forces on Aerofoils Moving Through Transverse and Chordwise Gusts," ASME Journal of Basic Engineering, December 1968.

6. Verdon, J.M. and Caspar, J.R., "Development of an Unsteady Aerodynamic Analysis for Finite Deflection Subsonic Cascades," NASA-CR-3455, September 1981.

7. Carta, F.O. and St. Hilaire, A.D., "Experimentally Determined Stability Parameters of a Subsonic Cascade Oscillating Near Stall," ASME Paper 77-GT-47, 1977.

8. Carta, F.O. and St. Hilaire, A.D., "Effect of Interblade Phase Angle and Incidence Angle on Cascade Pitching Stability," ASME Paper 79-GT-153, 1979.

9. Ostdiek, F.R., "A Cascade in Unsteady Flow," Ph.D. Thesis, The Ohio State University, 1975.

10. Fleeter, S., Jay, R.L., and Bennett, W.A., "Rotor Wake Generated Unsteady Aerodynamic Response of a Compressor Stator," ASME Journal of Engineering for Power, Volume 100, October 1978.

11. Fleeter, S., Bennett, W.A., and Jay, R.L., "The Time-Variant Aerodynamic Response of a Stator Row Including the Effects of Airfoil Camber," ASME Journal of Engineering for Power, Volume 102, April 1980.

12. Capece, V.R., Manwaring, S.R. and Fleeter, S., "Unsteady Blade Row Interactions in a Multi-Stage Compressor," AIAA Journal of Propulsion, Volume 2, No. 2, March-April 1986.

13. Gostelow, J.P., "A New Approach to the Experimental Study of Turbomachinery Flow Phenomena," ASME Journal of Engineering for Power, Volume 99, January 1977.

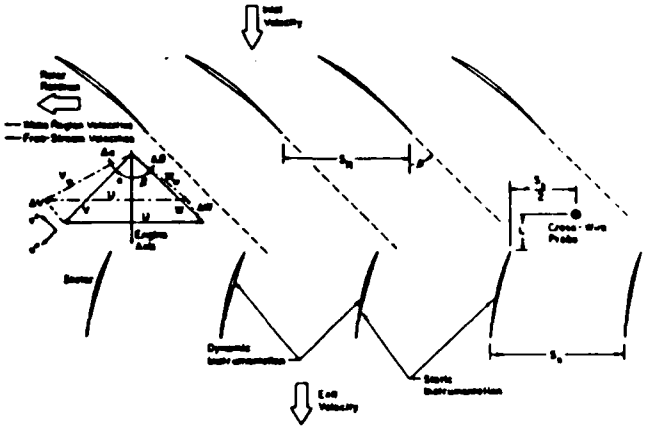

Figure 1. Schematic of flow field and instrumentation

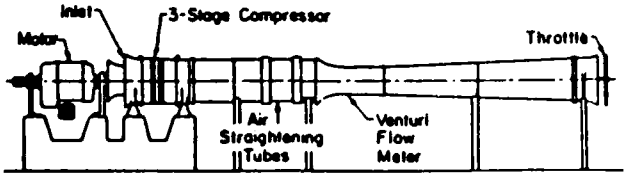

Figure 2. Three-stage axial flow research compressor

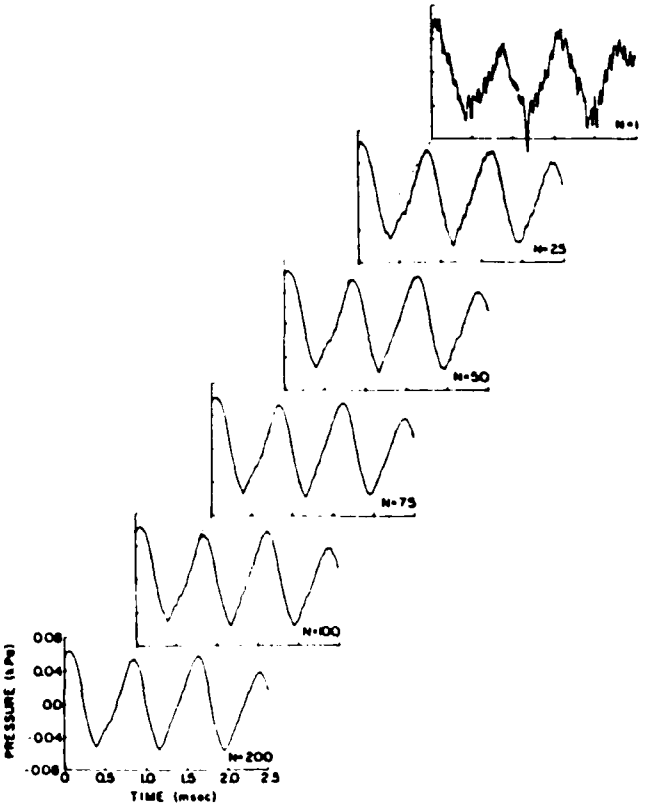

Figure 3. Ensemble averaging of unsteady pressure signals

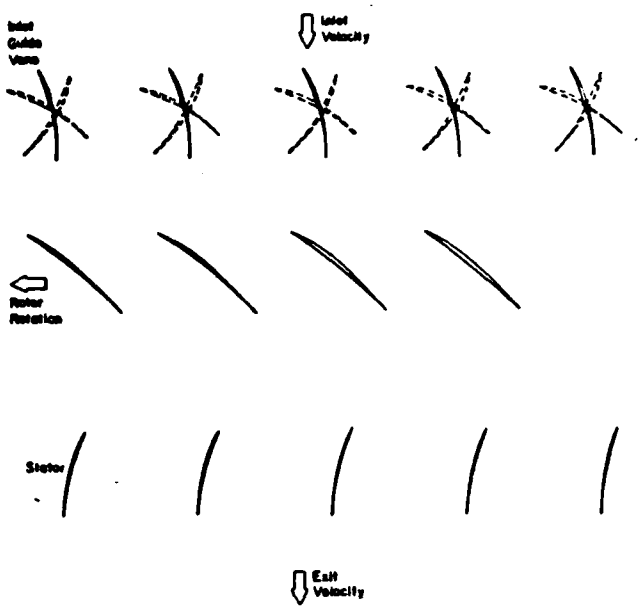

Figure 4. Schematic of inlet guide vane setting angle indexing

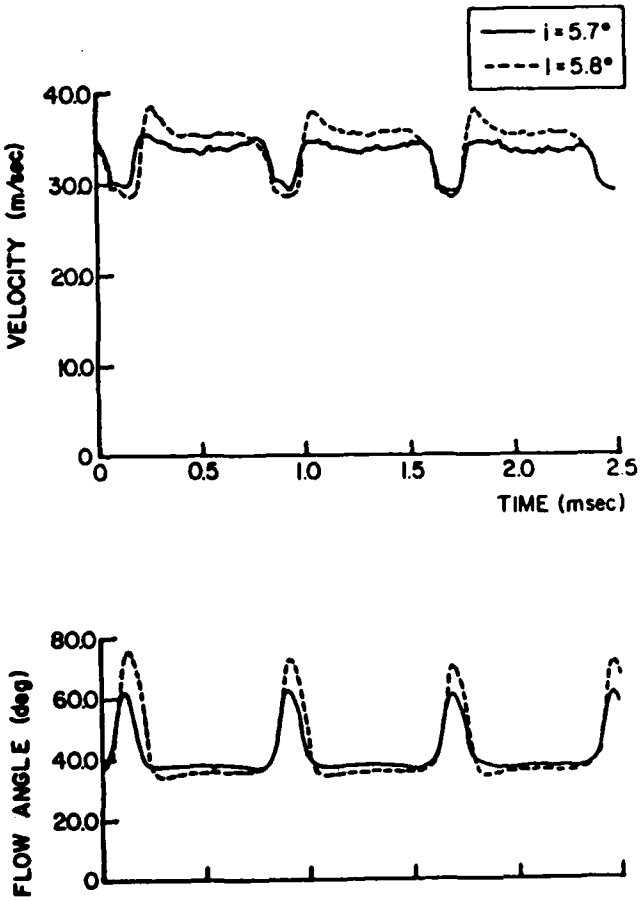

Figure 5. Stator vane inlet flow field at 5.7° and 5.8° of incidence

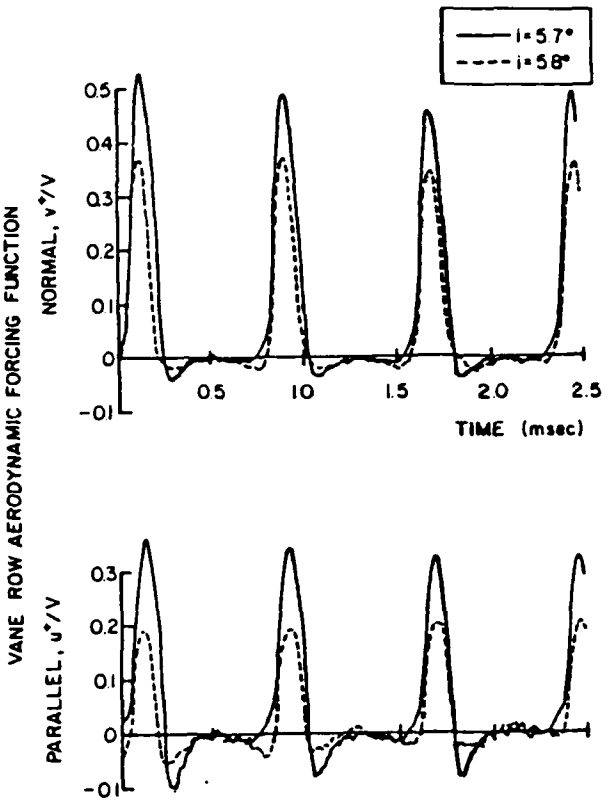

Figure 6. Normal and parallel stator vane aerodynamic forcing functions at 5.7° and 5.8° of incidence

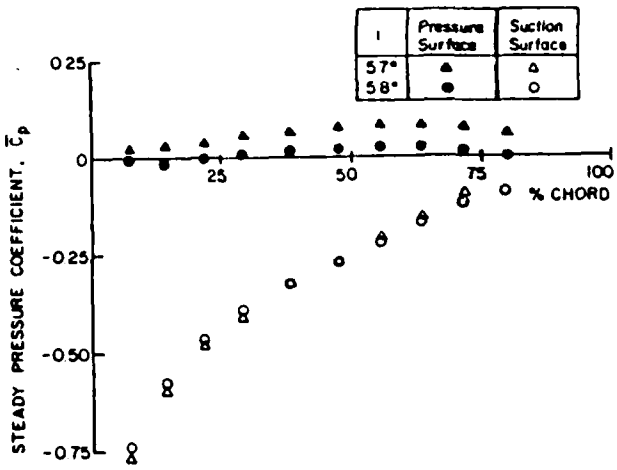

Figure 7. Loading effects on the static pressure coefficient for non-constant forcing function

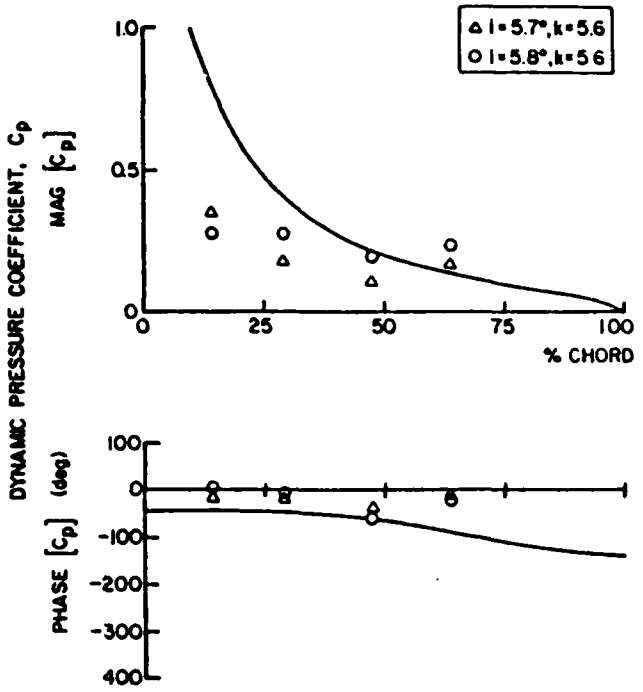

Figure 8. Effect of loading on the first harmonic unsteady data for non-constant forcing function

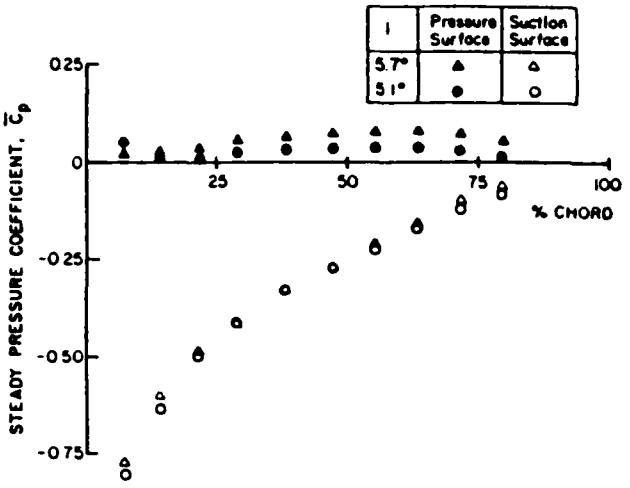

Figure 10. Effect of loading on the static pressure coefficient for constant forcing function

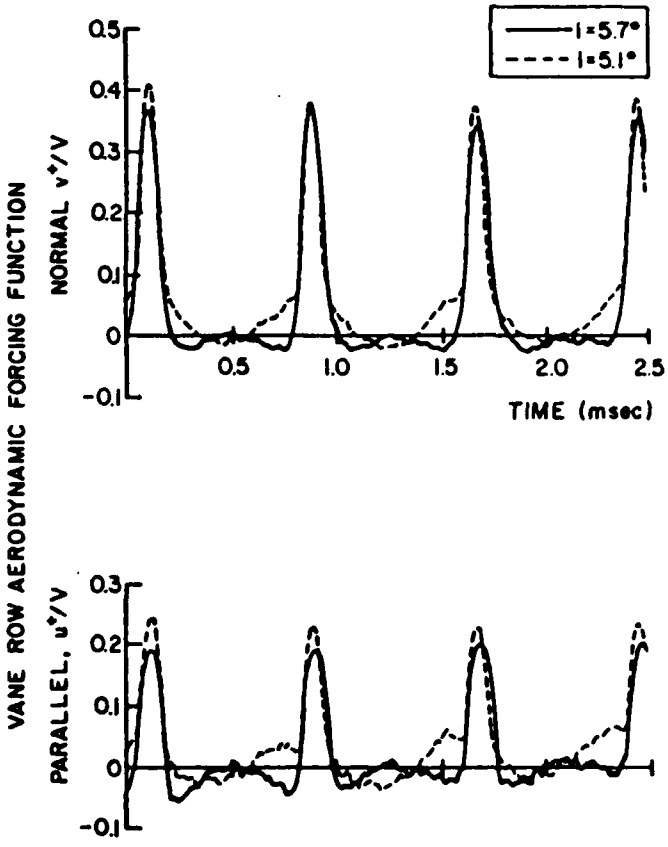

Figure 9. Normal and parallel stator vane aerodynamic forcing functions at 5.1° and 5.7° of incidence.

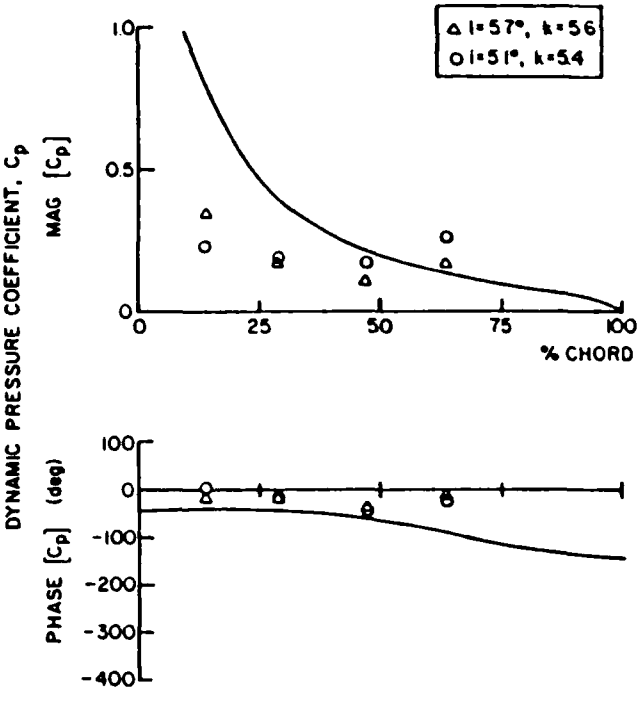

Figure 11. Effect of loading on the first harmonic unsteady data for constant forcing function

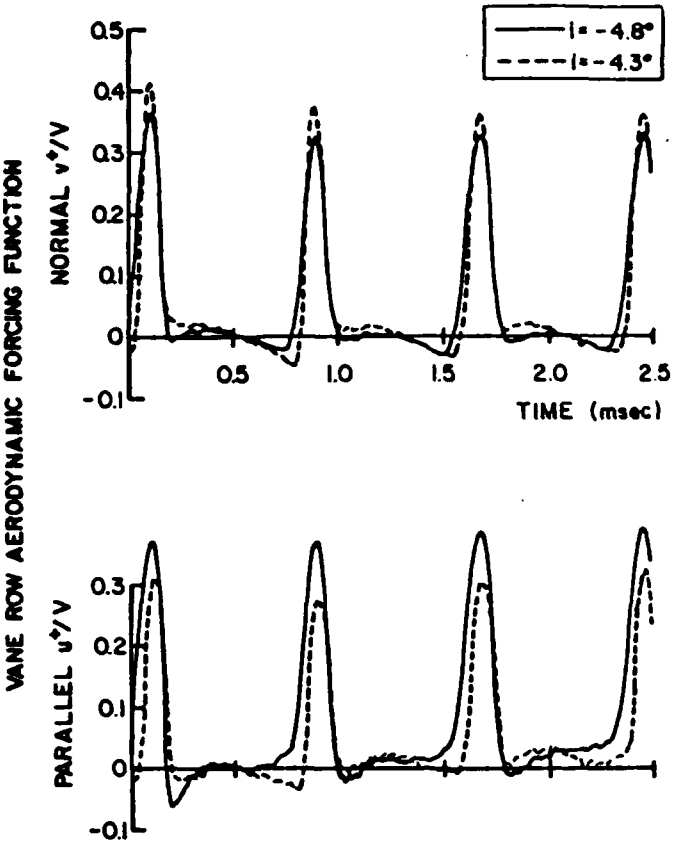

Figure 12. Normal and parallel stator vane aerodynamic forcing functions at -4.3° and -4.8° of incidence

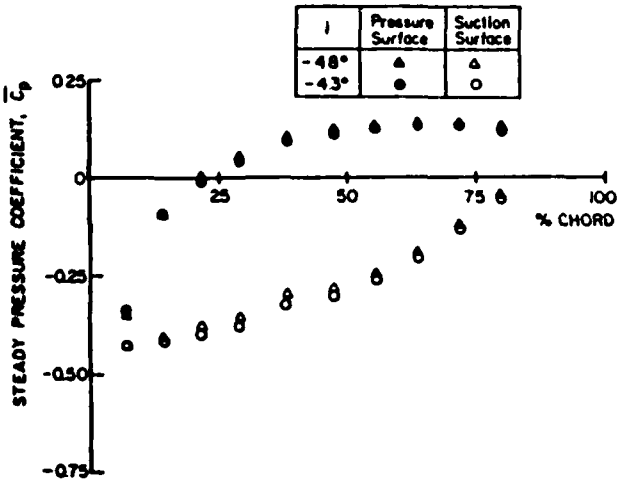

Figure 13. Stator vane static pressure coefficient distributions for -4.3° and -4.8° of incidence

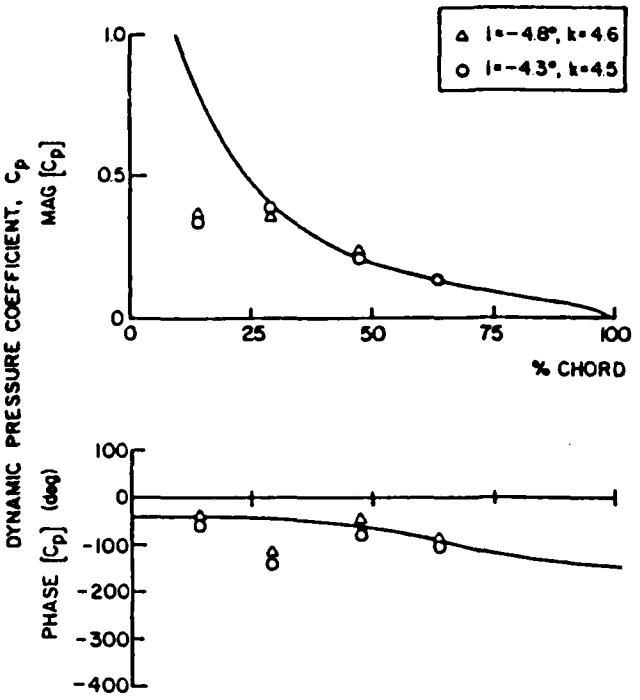

Figure 14. Effect of forcing function parallel component on first harmonic unsteady data

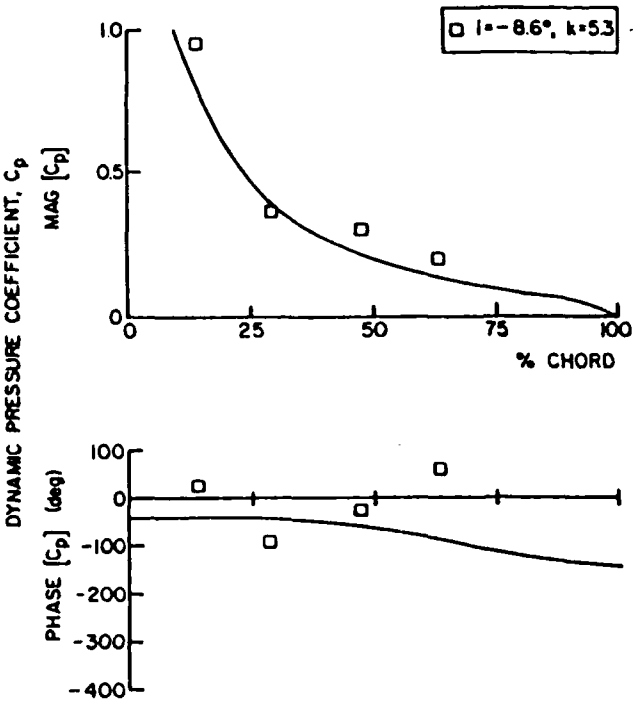

Figure 15. Correlation of low steady loading first harmonic data with flat plate cascade predictions

APPENDIX V

UNSTEADY AERODYNAMIC INTERACTIONS IN A MULTISTAGE COMPRESSOR

ASME JOURNAL OF TURBOMACHINERY

Unsteady Aerodynamic Interactions in a Multistage Compressor

V. R. Capece

S. Fleeter

Thermal Sciences and Propulsion Center,
School of Mechanical Engineering,
Purdue University,
West Lafayette, IN 47907

The fundamental flow physics of multistage blade row interactions is experimentally investigated, with unique data obtained which quantify the unsteady harmonic aerodynamic interaction phenomena. In particular, a series of experiments is performed in a three-stage axial flow research compressor over a range of operating and geometric conditions at high reduced frequency values. The multistage unsteady interaction effects of the following on each of the three vane rows are investigated: (1) the steady vane aerodynamic loading, (2) the waveform of the aerodynamic forcing function to each vane row, including both the chordwise and traverse gust components.

Introduction

Fan, compressor, and turbine airfoils are susceptible to destructive aerodynamically induced vibrational responses when a periodic aerodynamic excitation source with a frequency equal to an airfoil natural frequency acts on an airfoil row. With the resonant airfoil frequencies accurately predicted with finite element structural models, Campbell diagrams are utilized to determine the rotor speed at which the airfoil row may be susceptible to significant aerodynamically induced vibrational response. However, accurate predictions for the amplitude of the resulting vibration and stress cannot be made due to the inadequacies existing in current state-of-the-art unsteady aerodynamics models for both the aerodynamic forcing function and the resulting airfoil row unsteady aerodynamics.

The most common aerodynamic excitation sources are the wakes shed by upstream blade or vane rows. For example, in the single compressor stage schematically depicted in Fig. 1, the wakes from the upstream rotor are the primary source of the unsteady aerodynamics on the downstream stator vanes, i.e., the exit flow field from the upstream rotor defines the unsteady aerodynamic forcing function to the downstream stator vanes. This aerodynamic forcing function is defined by the velocity components parallel and normal to the vane chord, u' and v', respectively.

First principles predictive techniques for aerodynamically induced airfoil response require a definition of the unsteady forcing function in terms of its harmonics. The periodic response of the airfoil row to each harmonic is assumed to be comprised of two components. One is due to the chordwise and normal components of the harmonic forcing function being swept past the nonresponding airfoil row, termed the transverse (normal) and chordwise (parallel) gust responses, respectively. The second, the self-induced unsteady aerodynamics, arises when the airfoil row responds to the aerodynamic forcing function.

Gust and self-induced unsteady aerodynamic models have been and continue to be developed [1-7]. These models are inviscid, considering small unsteady perturbations superimposed on a steady throughflow. There are many analytical and physical assumptions inherent in these mathematical models. Unfortunately, at the high reduced frequency values characteristic of turbomachinery, only a very limited quantity of appropriate fundamental unsteady aerodynamic data exists to verify these models. Data have been obtained in single stages of low-speed research compressors. In experiments which considered only transverse gust aerodynamics, the effects of airfoil camber and rotor-stator axial spacing were investigated, with the data demonstrating that the waveform of the aerodynamic forcing function has an important influence on the unsteady aerodynamic gust response of the airfoil row [8, 9]. In [10], the significant effects of steady airfoil loading and the detailed aerodynamic forcing function transverse gust component on the unsteady aerodynamic response of an airfoil row were investigated.

However, the significant effects associated with multistage flow field interactions have not been experimentally (or mathematically) considered. For example, in the single stage depicted in Fig. 1, the wakes from the upstream rotor blades define the unsteady aerodynamic forcing function to the downstream stator vanes, with this forcing function defined by the velocity components parallel and normal to the vane chord. However, in a multistage turbomachine, the aerodynamic forcing function to a downstream vane row is determined by all of the upstream airfoil wakes and the unsteady aerodynamic interactions between the various upstream blade and vane rows.

In this paper, the fundamental flow physics of multistage blade row interactions are experimentally investigated for the first time, with unique data obtained to describe the fun-

Contributed by the Gas Turbine Division of The American Society of Mechanical Engineers and presented at the 32nd International Gas Turbine Conference and Exhibit, Anaheim, California, May 31-June 4, 1987. Manuscript received at ASME Headquarters February 17, 1987. Paper No. 87-GT-171.

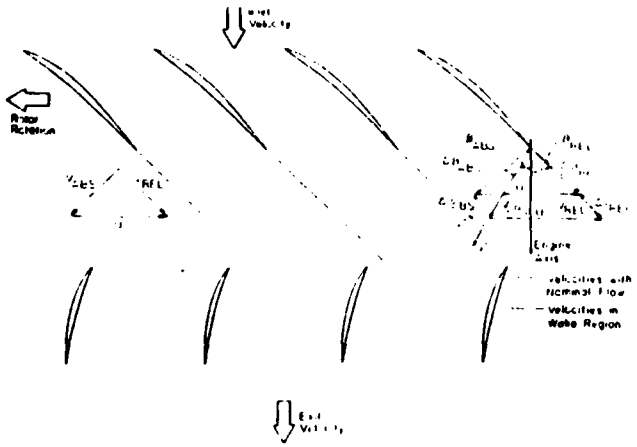

Fig. 1 Schematic of single-stage compressor flow field

damental unsteady aerodynamic interaction phenomena. In particular, a series of experiments is performed which utilize the versatility of the Purdue University Three-Stage Axial Flow Research Compressor to investigate the multistage unsteady interaction effects of the following on each of the three individual vane rows: (1) the steady vane aerodynamic loading, and (2) the waveform of the aerodynamic forcing function to each vane row, including both the chordwise and transverse gust components.

Research Compressor

The Purdue University Axial Flow Research Compressor experimentally models the fundamental turbomachine unsteady aerodynamic multistage interaction phenomena including the incidence angle, the velocity and pressure variations, the aerodynamic forcing function waveforms, the reduced frequency, and the unsteady blade row interactions. The compressor is driven by a 15 hp d-c electric motor over a speed range of 300 to 3000 rpm. Each of the three identical stages contains 43 rotor blades and 41 stator vanes having a British C4 airfoil profile, with the first stage rotor inlet flow field established by a row of variable setting angle inlet guide vanes.

Instrumentation

Both steady and unsteady data are required to quantify the aerodynamics of each of the three vane rows. The steady data specify the overall compressor operating point and the detailed vane surface steady loading. The unsteady data define the time-variant aerodynamic inlet flow field to each vane row, i.e., the individual vane row aerodynamic forcing function, as well as the resulting vane surface unsteady pressure distributions.

Conventional steady instrumentation is used to determine the flow properties throughout the compressor. The steady aerodynamic loading on the surfaces of the vanes is measured with chordwise distributions of midspan surface static pressure taps.

The unsteady aerodynamic inlet flow field to each vane row is measured with a cross hot-wire probe positioned midway between each rotor and stator at midstator circumferential spacing. The probe is calibrated and linearized to 60 m/s and ±35 deg angular variation, with the accuracy of the velocity magnitude and angle of ±4 percent and ±2 deg, respectively. The mean absolute flow angle is determined by rotating the probe until a zero voltage difference between the two linearized hot-wire signals is obtained. This mean angle is subsequently used as a reference for the calculation of the instantaneous absolute and relative flow angles.

The measurement of the midspan vane surface unsteady pressures is accomplished with ultraminiature high response transducers. To minimize the potential of flow disturbances generated by the transducers, the transducers are embedded in the vanes from the backside and connected to the measurement surface by a static tap. These dynamically instrumented vanes are positioned such that a complete flow passage is instrumented in each vane row.

The embedded dynamic transducers are statically and dynamically calibrated. The static calibrations show good linearity and no discernible hysteresis. The dynamic calibrations demonstrate that the frequency response, in terms of gain attenuation and phase shift, is not affected by the transducer mounting. The accuracy of the unsteady pressure measurements, determined from the calibrations, is ±3.5 percent.

Unsteady Data Acquisition and Analysis

The unsteady data of interest are periodic, being generated at rotor blade passing frequency. Thus, a digital ensemble-averaging technique based on the signal enhancement concept of Gostelow [11] is used for the data analysis. The key to this technique is the ability to sample data at a preset time. This is accomplished by an optical encoder mounted on the rotor shaft. The microsecond range square wave voltage signal from the encoder is the data initiation time reference and triggers a high speed A-D multiplexer system. This averaging significantly reduces the random fluctuations superimposed on the periodic signals, with the unsteady signals essentially unchanged when averaged over 75 or more rotor revolutions. For the data presented herein, 200 averages are used.

The resulting ensemble-averaged digital periodic hot-wire and dynamic pressure transducer signals are each Fourier decomposed into harmonics by means of a Fast Fourier Transform (FFT) algorithm. This Fourier analysis determines the magnitude and the phase of the first harmonic of both the inlet flow field to each vane row, i.e., the aerodynamic forcing function, and the resulting vane surface unsteady pressures. These are each referenced to the initiation of the data acquisition. However, the hot-wire probe is positioned upstream of the leading edge plane of the vane row. Thus, it is necessary to time relate the harmonic vane row inlet flow field to the resulting unsteady vane surface pressures.

Nomenclature

c = airfoil chord
$\bar{C}_l$ = steady lift coefficient = $L'/\frac{1}{2}\rho U_t^2 c$
C_p = dynamic pressure coefficient = $\Delta p/\rho V_x v'$
$\bar{C}_p$ = static pressure coefficient = $(\bar{p} - \bar{p}_{exit})/\frac{1}{2}\rho U_t^2$
k = reduced frequency = $\omega c/2V_x$
i = incidence angle
L' = steady lift per unit span = $\int_0^c (\bar{p}_p - \bar{p}_s)dx$
$\bar{p}$ = stator vane surface static pressure
$\bar{p}_{exit}$ = stator vane row exit static pressure
Δp = dynamic pressure difference across vane chordline
u' = inlet velocity parallel to vane
U_t = rotor blade tip speed
v' = inlet velocity normal to vane
V = absolute velocity
V_x = absolute axial velocity
ω = blade passing frequency

The hot-wire data are analyzed to determine the harmonic unsteady inlet flow angle and velocity to each vane row, in particular, the unsteady velocity components parallel and normal to each vane row, u' and v' of Fig. 1, which define the unsteady forcing function. The hot-wire probe is positioned upstream of the leading edge of each stator vane row. To relate time-based events measured by the hot-wire probe to the resulting unsteady pressures on the vane surfaces, the following assumptions are made: (1) the wakes are identical at the hot-wire and the vane leading edge planes; (2) the wakes are fixed in the rotor relative reference frame. The rotor blade spacing, the vane spacing, and the axial spacing between the vane leading edge plane and the probe centerline are known.

At a steady operating point for each vane row, the hot-wire data are analyzed to determine the absolute flow angle and the upstream rotor exit relative flow angle. Using the above two assumptions, the wake is located relative to the hot-wire probe and the leading edges of the instrumented vanes. From this, the times at which the wakes are present at various locations are determined. The incremented times between occurrences at the hot-wire and the vane leading edge plane are then converted to phase differences between velocities and the vane surface.

To simplify the experiment-theory correlation, the first harmonic data for each vane row are adjusted in phase such that the transverse inlet velocity component is at 0 deg at the vane suction surface leading edge. From the geometry, the time at which this would occur is calculated and transposed into a phase difference which is then used to adjust the pressure data from the suction surface. An analogous procedure is utilized for the pressure surface data so that the two instrumented stator vanes in each vane row are time related. The pressure difference across the chordline of an equivalent single vane in each row is then determined by the subtraction of these complex time-related vane pressure and suction surface data.

The final form of the unsteady pressure data defines the chordwise variation of the first harmonic pressure difference across the chordline of a stator vane and is presented as a complex dynamic pressure coefficient C_p in the format of the magnitude and the phase lag referenced to a transverse gust at the vane leading edge. As a reference, also presented are predictions obtained from a periodic small perturbation model which considers the inviscid, irrotational flow of a perfect gas [2]. This model analyzes the uniform subsonic compressible flow past a two-dimensional flat plate airfoil cascade, with small unsteady normal velocity perturbations superimposed and convected downstream.

Results

To investigate the rotor wake generated gust aerodynamics on each vane row of a three stage axial flow research compressor, including the multistage interactions, a series of experiments were performed. In these, the effects of the following on the unsteady aerodynamics of each vane row were quantified: (1) the steady aerodynamic loading; (2) the detailed waveform of the aerodynamic forcing function, including the chordwise and transverse gust components.

The variations in the steady loading of each vane row were accomplished by adjusting the setting angles of the stators, thereby altering the incidence angle to the vanes. This enables both the aerodynamic forcing function waveform to be maintained while varying the steady aerodynamic loading, and also the matching of the steady vane aerodynamic loading for different aerodynamic forcing functions. The detailed steady aerodynamic loading of the vane rows is specified by the chordwise distribution of the vane surface steady static pressure coefficient $\bar{C}_p$, with the overall loading level given by the incidence angle and the steady lift coefficient $\bar{C}_l$.

The detailed waveform of the aerodynamic forcing function is specified by the chordwise and transverse gust components, u' and v'. These were experimentally varied as follows. Changing the setting angle of the inlet guide vanes alters the inlet flow to the first stage rotor. This results in a change in the detailed rotor blade exit flow field, in particular the chordwise and transverse gust components. Thus, the variations in the aerodynamic forcing function to the first-stage vane row were accomplished by altering the setting angle of the inlet guide vanes, as schematically depicted in Fig. 2. The forcing function waveform variations for the second and third-stage vane rows were accomplished by independently circumferentially indexing the upstream vane rows relative to one another, as also depicted in Fig. 2. In these cases, the steady aerodynamic loading of the vane row was maintained constant.

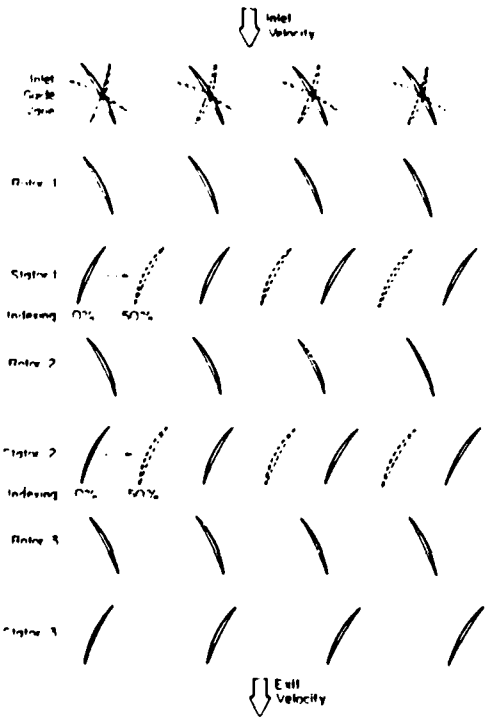

Fig. 2 Schematic of compressor geometry variations to alter the downstream vane row aerodynamic forcing functions

First-Stage Vane Row Experiments

Vane Loading Effects. Figures 3 and 4 present the steady vane surface static pressure distributions and the aerodynamic forcing function in the form of the two gust components, respectively, for two relatively low levels of aerodynamic loading. The surface static pressure distributions are smooth and show no indication of flow separation, with the loading differences in the leading edge region due to the differences in the incidence angles. The amplitudes of the chordwise and transverse gust components are different. However, in terms of the first harmonics, these two forcing functions are equivalent. In particular, the ratios of the magnitudes of the first harmonic of these gust components (u'/v') are 0.447 and 0.430 for these two vane loadings. Also, it should be noted that relative to the absolute velocity, these gusts are not small, particularly at -4.7 deg of incidence where the transverse and chordwise gusts are approximately 50 and 20 percent of the absolute velocity. This may have implications regarding the validity of the small perturbation assumption in the various mathematical models.

The resulting chordwise distributions of the dynamic pressure difference coefficient on the first-stage vanes are shown in Fig. 5. Also presented are the predictions from the

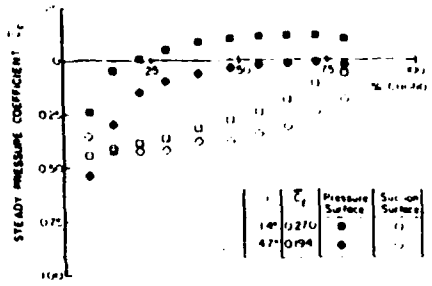

Fig. 3 Chordwise distribution of the first stage vane surface static pressure coefficient at low loading levels

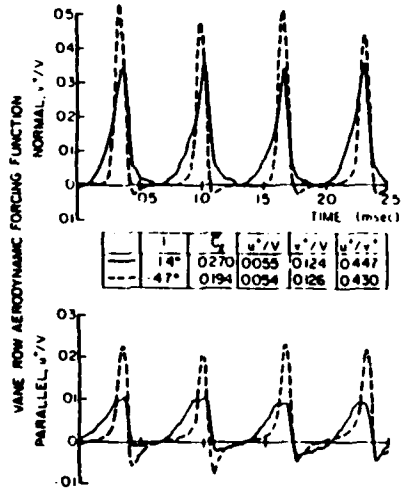

Fig. 4 Aerodynamic forcing function to the first-stage vane row at low loading levels

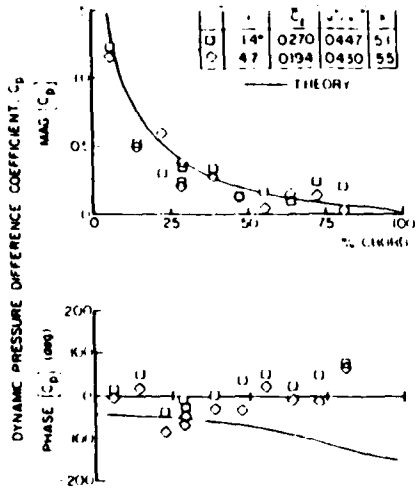

Fig. 5 Chordwise distribution of the dynamic pressure difference coefficient on the first stage vanes at low loading

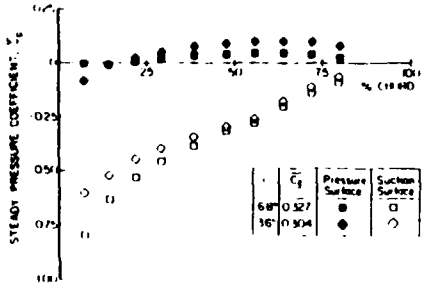

Fig. 6 Chordwise distribution of the first-stage vane surface static pressure coefficient at high loading levels

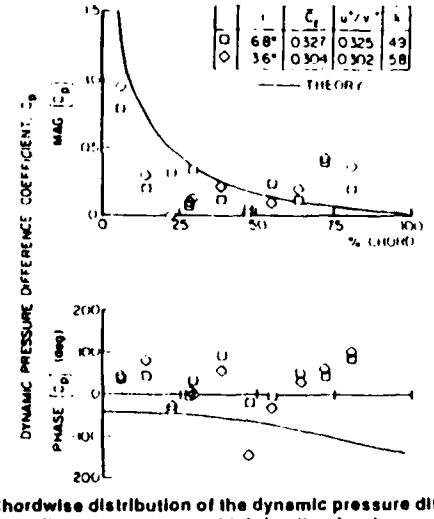

Fig. 7 Chordwise distribution of the dynamic pressure difference coefficient on the first stage vanes at high loading levels

flat plate airfoil cascade transverse gust model of [2]. The magnitude data exhibit good correlation with the prediction, with both decreasing with increasing chordwise position. As the loading is increased, the magnitude data show an increase above both the prediction and the lower loading data aft of 60 percent chord. The phase of the dynamic pressure difference coefficient data exhibits a somewhat different chordwise distribution than the prediction. This is attributed to the vane camber and the detailed steady chordwise loading distribution on the vane surfaces.

The effects of higher levels of steady aerodynamic loading (Fig. 6) on the first-stage vane row unsteady aerodynamics, with the u' and v' gust components maintained relatively constant, were also investigated. At these higher loadings, the suction surface distributions are nearly identical over the aft part of the vane, with the differences in the front part of the vane due to the differences in the incidence angles. On the pressure surface, larger variations between the two loading conditions are apparent over the entire vane chord. Again, there is no evidence of flow separation.

The dynamic pressure difference coefficient data for this higher loading case are presented in Fig. 7. A comparison of these high loading data with the corresponding lower loading data of Fig. 5 reveals large differences. As the aerodynamic forcing functions are the same, aerodynamic loading has a significant effect on the unsteady aerodynamics of the vane row. Increasing the aerodynamic loading results in poorer correlation of the dynamic pressure difference coefficient magnitude data with the flat plate cascade prediction, as expected. Also, as the loading is increased, the magnitude data in the trailing edge region of the airfoil are increased in value. As will be shown, the data on the third-stage vane row, the last airfoil row in the compressor, for similar steady loading do not exhibit this increase in the magnitude data in the trailing edge region. Hence, this is most probably a multistage blade row interaction effect.

Thus, the best correlation of the dynamic pressure difference coefficient data and the flat plate cascade predictions is obtained at the low level of steady aerodynamic loading, indicating that the steady loading, not the incidence angle, is a

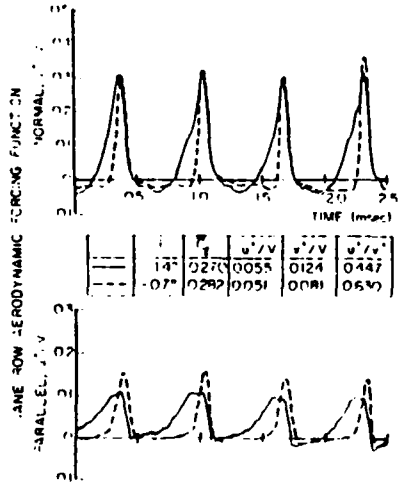

Fig. 8 Variations in the transverse gust aerodynamic forcing function to the first-stage vane row

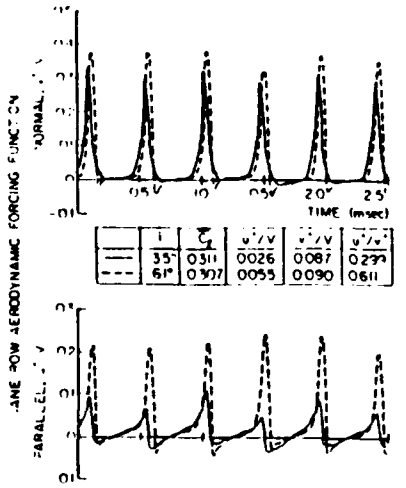

Fig. 11 Variations in the chordwise gust aerodynamic forcing function to the first-stage vane row

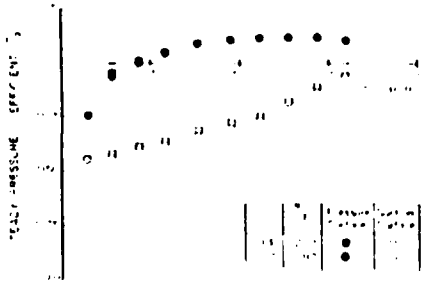

Fig. 9 Effect of the transverse gust aerodynamic forcing function on the first-stage vane surface static pressure coefficient

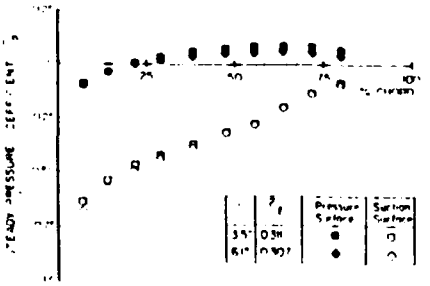

Fig. 12 Effect of the chordwise gust aerodynamic forcing function on the first-stage vane surface static pressure coefficient

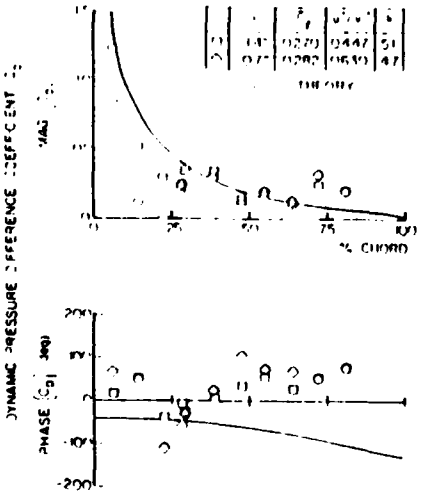

Fig. 10 Variation of the first stage vane dynamic pressure difference coefficient with transverse gust aerodynamic forcing function

key parameter. Also, the steady loading level and distribution have a significant effect on the unsteady aerodynamics of the vane row.

Aerodynamic Forcing Function Effects. The effects of variations in the aerodynamic forcing function transverse gust component v' on the first-stage vane row unsteady aerodynamics are investigated. This is accomplished by means of two configurations such that the chordwise gust component u', and the steady aerodynamic loadings are maintained relatively constant. Figure 8 shows these aerodynamic forcing functions, with the ratios of the gust components (u'/v') being 0.447 and 0.630. The chordwise distributions of the steady vane surface static pressure at this moderate loading for these forcing functions are presented in Fig. 9.

The resulting first stage vane chordwise distributions of the dynamic pressure difference coefficient data and the corresponding flat plate cascade prediction are presented in Fig. 10. The magnitude data are decreased in value relative to the prediction over the leading 30 percent of the vane, with the (u'/v') data of 0.630 having a decreased amplitude relative to the (u'/v') data of 0.447. However, in the midchord region, the magnitude data correlate well with each other and with the prediction. Aft of 70 percent of the chord, the magnitude data are increased in value at this moderate level of steady loading, analogous to the previous high steady loading results. The phase data are increased with respect to the prediction over the front part of the vane, becoming nearly constant over the aft half of the vane.

The effects of variations in the aerodynamic forcing function chordwise gust component u' on the first stage vane row unsteady aerodynamics are also investigated. This is accomplished by means of two configurations such that the transverse gust component v', and the steady aerodynamic loading are maintained relatively constant. The aerodynamic forcing functions are shown in Fig. 11, with the ratios of the gust components (u'/v') being 0.299 and 0.611. The chordwise distributions of the steady vane surface static pressures at this high loading are presented in Fig. 12.

The resulting chordwise distributions of the dynamic pressure difference coefficient data and the corresponding flat

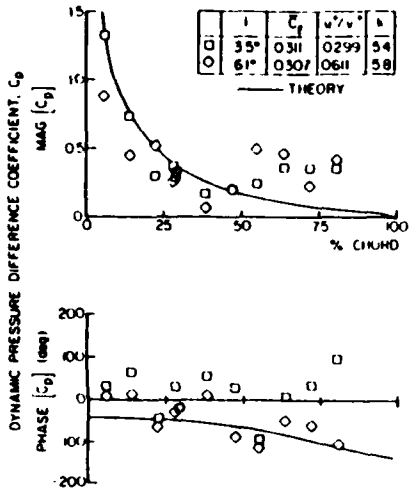

Fig. 13 Variation of the first-stage vane dynamic pressure difference coefficent with chordwise gust aerodynamic forcing function

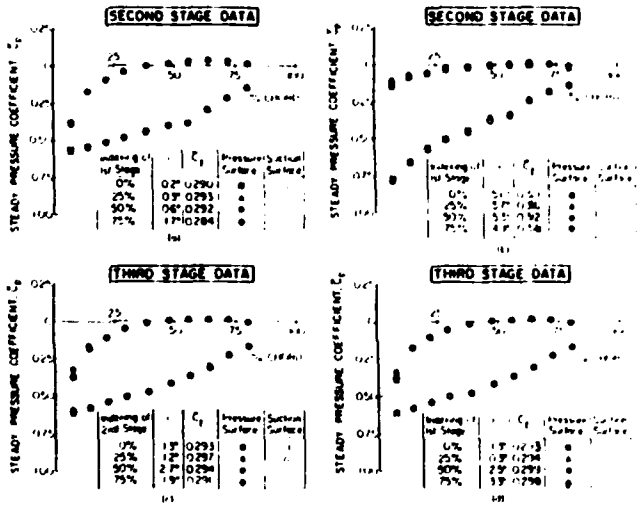

Fig. 14 Effect of circumferentially indexing the upstream stators on the downstream vane surface static pressure coefficients

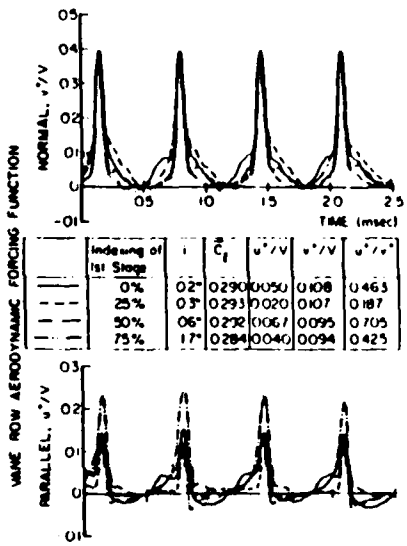

Fig. 15 Second-stage vane aerodynamic forcing function variation due to the indexing of the first-stage stators at moderate loading

plate cascade prediction are presented in Fig. 13. The magnitude data both exhibit analogous trends, decreasing over the front part of the vane chord and increasing over the aft part of the vane, analogous to the high and moderate loading cases previously considered. There is good correlaton with the prediction over the front half of the vane for a (u'/v') of 0.299, with the corresponding data for a (u'/v') of 0.611 somewhat decreased in value but exhibiting the same trends. The phase data for a (u'/v') value of 0.299 show trends similar to those obtained with a different aerodynamic forcing function but an analogous high level of aerodynamic loading (Fig. 7).

Thus, the transverse gust component of the aerodynamic forcing function has a larger effect on the phase of the dynamic pressure difference coefficient than either the steady loading or the chordwise gust component. However, both the chordwise and the transverse gust components, and the steady aerodynamic loading, influence the magnitude of the dynamic pressure difference coefficient.

Aft-Stage Vane Row Experiments

To investigate the aft-stage unsteady blade row interactions at a fixed operating point, the upstream stators are indexed circumferentially relative to the downstream instrumented vane rows, as previously noted and depicted in Fig. 2. Figure 14 presents the surface static pressure distributions on the downstream vane rows with the upstream stators indexed circumferentially 0, 25, 50, and 75 percent. The surface static pressure distributions are seen to be nearly independent of the circumferential indexing of the upstream stators, with only small variations apparent near the leading edge. Also, there is no evidence of flow separation.

Unsteady Aerodynamics—Adjacent Vane Row Indexing. The effect of indexing circumferentially (1) the first-stage stators on the second-stage vane row unsteady aerodynamics and (2) the second-stage stators on the third-stage vane row unsteady aerodynamics are considered.

Indexing the first-stage stators has a significant effect on the aerodynamic forcing function to the second-stage vane row. Figure 15 shows that the forcing functions differ significantly from one another and from the previously measured first-stage vane row forcing functions. This variation in the second-stage vane row forcing function at a single operating point is a multistage blade row interaction effect, with the second-stage rotor wake being modulated by the wakes from the upstream inlet guide vanes and the first stage rotor blades and stator vanes. Also, this indexing is seen to have a larger effect on the amplitude of the chordwise gust than on the transverse gust, indicated by the wide range of values of the ratio (u'/v').

The resulting chordwise distributions of the unsteady pressure difference coefficient on the second-stage vane row are presented in Fig. 16. At this moderate level of steady aerodynamic loading, the effects of circumferential indexing on the magnitude data are primarily found over the front 25 percent of the vane, with these magnitude data coalescing over the aft 75 percent of the chord. In contrast, the indexing affects the phase data over the complete vane chord. Also, the magnitude and phase data exhibit trends analogous to the previously presented first-stage vane row results, with the magnitude data decreased over the front part of the vane and increased over the aft part relative to the prediction. As the steady aerodynamic loading is independent of the indexing of the first stage stators, these effects are attributed to the differences in the chordwise and transverse gust components with indexing.

The effects of steady loading level and circumferential indexing of the first-stage stators are investigated by establishing a new compressor operating point. Figure 17 shows the effect of this indexing on the aerodynamic forcing function to the

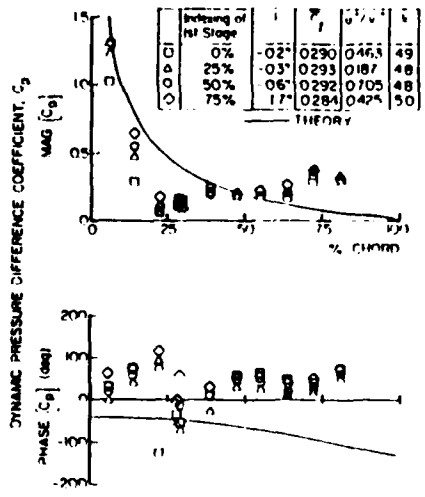

Fig. 16 Effect of first-stage stator indexing on second-stage vane unsteady pressure difference coefficient at moderate loading

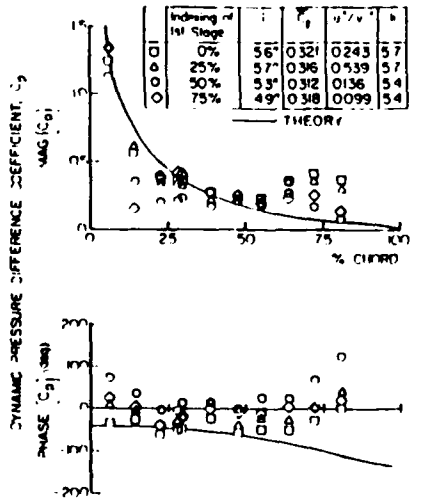

Fig. 18 Effect of first-stage stator indexing on second-stage vane unsteady pressure difference coefficients at high loading

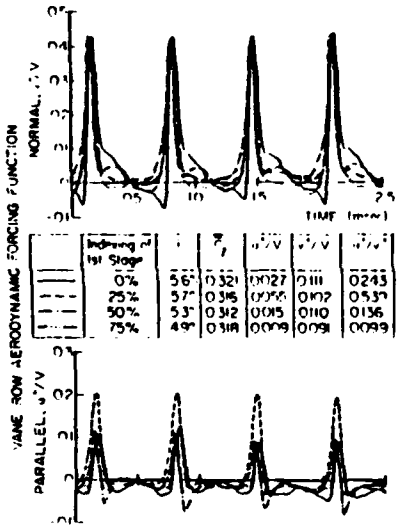

Fig. 17 Second-stage vane aerodynamic forcing function variation due to the indexing of the first-stage stators at high loading

second-stage vane row at this high loading condition. The indexing primarily influences the chordwise gust component, analogous to the lower loading case. Comparing the forcing functions at the two loading levels (Figs. 15 and 17) indicates that the compressor operating point has an effect on the forcing function.

The resulting chordwise distributions of the unsteady pressure difference coefficient in the second-stage vane row associated with these variations in the aerodynamic forcing function at this high loading level are presented in Fig. 18. The effect of this indexing is evident in the magnitude data over the front and aft part of the vane, not just the front as at the lower loading level, with the phase data still affected over the complete vane chord. Also, the magnitude data are decreased over the front and increased over the aft part of the vane as compared to the prediction. However, in the aft chord region, the magnitude data for the 0 and 25 percent indexing differ from that with 50 and 75 percent indexing. Namely, for 0 and 25 percent indexing, the magnitude data continue to increase as the trailing edge is approached relative to the prediction whereas the 50 and 75 percent indexing data decrease and correlate with the prediction in this aft chord region. This [illegible]

associated with the much smaller magnitudes of the chordwise gust component, as the normal gusts are nearly the same for all indexing positions. Again, the steady aerodynamic loading is independent of the indexing of the first-stage stators. Thus, these effects are attributed to the differences in the chordwise and transverse gust components with indexing.

The effect of indexing the second-stage stators on the aerodynamic forcing function to the third-stage vane row and the resulting chordwise distributions of the unsteady pressure difference coefficient on the third-stage vane row are presented in Figs. 19 and 20, respectively. The magnitudes of the gust components indicated by the values of the (u'/v') ratio are similar to those found for the second stage at the same level of steady loading (Figs. 17 and 19). However, the aerodynamic forcing functions are different than those for the second-stage vane row at the same level of steady loading. This results from the third-stage vane row forcing function being affected by all of the individual component blade rows in the compressor, i.e., the wakes from the inlet guide vanes, the first and second-stage rotor blades and stator vanes, and the third-stage rotor blades.

The resulting third-stage vane row dynamic pressure difference coefficient data show that the forcing function variation with indexing affects the magnitude primarily over the front part of the vane, with the phase affected over the complete vane chord, analogous to previous results. However, these third-stage magnitude data differ from the analogous second stage data at the same level of steady loading. In particular, the first and second-stage data increase relative to the prediction in the vane trailing edge region, whereas these third-stage data do not and, in fact, exhibit good correlation with the prediction in this region. Since there are no airfoils downstream of the third-stage vane row to influence the unsteady aerodynamics on the aft part of the vane, the increase in the magnitude data relative to the prediction for the first and second-stage vane rows is a multistage interaction effect.

Unsteady Aerodynamics—Upstream Row Indexing. To complete this study, the effect of circumferentially indexing the first-stage stators on the unsteady aerodynamics of the third-stage vane row are considered. The chordwise and transverse gust components defining the aerodynamic forcing function to the third-stage vane row are presented in Fig. 21. The indexing of the first-stage stators affects the third-stage forcing function, with the primary effect being on the chordwise gust component

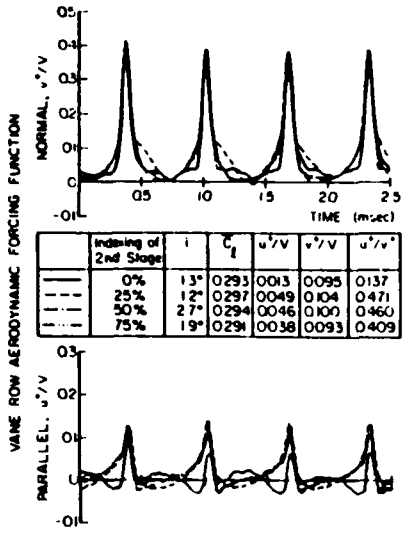

Fig. 19 Third-stage vane aerodynamic forcing function variation due to indexing of the second-stage stators

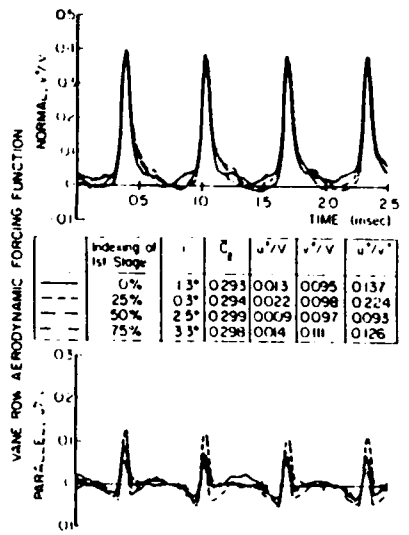

Fig. 21 Third-stage vane aerodynamic forcing function variation due to indexing of the first-stage stators

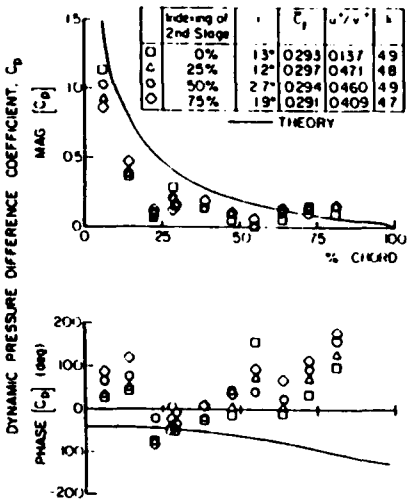

Fig. 20 Effect of second-stage stator indexing on third-stage vane unsteady pressure difference coefficient

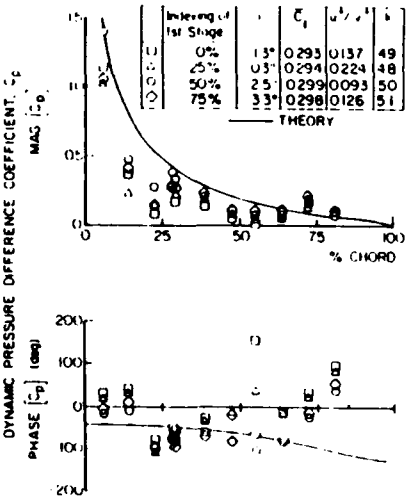

Fig. 22 Effect of first-stage stator indexing on the third-stage vane unsteady pressure difference coefficient

The resulting third-stage vane row chordwise distributions of the unsteady pressure difference coefficient are presented in Fig. 22. Again, the effect of the forcing function variation with indexing is evident in the phase data over the complete vane chord, but primarily affects the magnitude data over the front part of the vane. Also, the trailing edge region magnitude data are in good agreement with the prediction.

Summary and Conclusions

The rotor wake generated gust aerodynamics on each vane row of a three-stage axial flow research compressor, including the multistage interactions, were investigated by means of a series of experiments. In these, the effects of the following on the unsteady aerodynamics of each vane row were quantified: (1) the steady aerodynamic loading: (2) the detailed waveform of the aerodynamic forcing function, including the chordwise and transverse gust components.

The best correlation of the dynamic pressure difference coefficient data and the flat plate predictions is obtained at a low level of steady aerodynamic loading, indicating that the steady loading, not the incidence angle, is a key parameter. Also, the steady loading level and chordwise distribution have a significant effect on the unsteady aerodynamics of the vane row.

The transverse gust component of the aerodynamic forcing function has a larger effect on the phase of the dynamic pressure difference coefficient than either the steady loading or the chordwise gust component. However, the steady loading, and the chordwise and transverse gust components all influence the magnitude of the dynamic pressure difference coefficient.

The circumferential indexing of the upstream stators has no effect on the steady aerodynamic loading of downstream vane rows. However, indexing of the upstream vane rows does have a significant effect on the downstream aerodynamic forcing function and resulting chordwise pressure difference coefficient distributions, including the indexing of the first-stage stators affecting the third-stage vane row. The primary effect of the indexing is on the chordwise gust of the aerodynamic forcing function.

Circumferential indexing affects the magnitude of the dynamic pressure difference coefficient data over the front portion of the vane, with the phase data affected over the

complete vane chord. The variations in the data as a function of indexing are attributed to the differences in the gust components of the aerodynamic forcing function, primarily the chordwise gust component, since the steady loading is constant.

For moderate levels of steady loading, the dynamic pressure difference coefficient magnitude data increase significantly relative to the prediction in the trailing edge region on the first and second-stage vane rows. However, for the same steady loading, the third-stage vane row data do not show this trend and, in fact, correlate quite well with the prediction. Since there are no blade rows downstream of the third stage vane row, this increase in the magnitude data relative to the prediction for the first and second stage is a multistage blade row interaction effect.

The variations of the unsteady data with forcing function waveform cannot be predicted by harmonic gust models. This is because the forcing function waveforms and the resulting unsteady pressure distributions have been Fourier decomposed,with the first harmonics of the unsteady data presented. Thus, all of these first harmonic data are correlated with the same prediction curve, i.e., the predictions from these harmonic gust models are identical for all of the forcing function waveforms.

Acknowledgments

Support of this research program by the Air Force Office of Scientific Research, Dr. James Wilson program manager, is gratefully acknowledged.

References

1 Whitehead, D. S., "Force and Moment Coefficients for Vibrating Aerofoils in Cascade," Aeronautical Research Council R&M 3254, Feb. 1960.

2 Fleeter, S., "Fluctuating Lift and Moment Coefficients for Cascaded Airfoils in Nonuniform Compressible Flow," *AIAA Journal of Aircraft*, Vol. 10, Feb. 1973.

3 Naumann, H., and Yeh, H., "Lift and Pressure Fluctuations of a Cambered Airfoil Under Periodic Gusts and Applications in Turbomachinery," ASME JOURNAL OF ENGINEERING FOR POWER, Vol. 95, Jan. 1973.

4 Horlock, J. H., "Fluctuating Lift Forces on Aerofoils Moving Through Transverse and Chordwise Gusts," ASME *Journal of Basic Engineering*, Vol. 90, Dec. 1968.

5 Verdon, J. M., and Caspar, J. R., "Development of an Unsteady Aerodynamic Analysis for Finite Deflection Subsonic Cascades," NASA CR 3455, Sept. 1981.

6 Atassi, H. M., "The Sears Problem for a Lifting Airfoil Revisited—New Results," *Journal of Fluid Mechanics*, Vol. 141, 1984.

7 Inglert, G. W., "Interaction of Upstream Flow Distortions With High Mach Number Cascades," ASME Paper No. 82 GT 137, 1982.

8 Fleeter, S., Jay, R. L., and Bennett, W. A., "Rotor Wake Generated Unsteady Aerodynamic Response of a Compressor Stator," ASME JOURNAL OF ENGINEERING FOR POWER, Vol. 100, Oct. 1978.

9 Fleeter, S., Bennett, W. A., and Jay, R. L., "The Time Variant Aerodynamic Response of a Stator Row Including the Effects of Airfoil Camber," ASME JOURNAL OF ENGINEERING FOR POWER, Vol. 102, Apr. 1980.

10 Capece, V. R., Manwaring, S. R., and Fleeter, S., "Unsteady Blade Row Interactions in a Multistage Compressor," *AIAA Journal of Propulsion*, Vol. 2, No. 2, Mar.-Apr. 1986.

11 Gostelow, J. P., "A New Approach to the Experimental Study of Turbomachinery Flow Phenomena," ASME JOURNAL OF ENGINEERING FOR POWER, Vol. 99, Jan. 1977.

APPENDIX VI

EXPERIMENTAL INVESTIGATION OF MULTISTAGE INTERACTION GUST AERODYNAMICS

ASME JOURNAL OF TURBOMACHINERY

EXPERIMENTAL INVESTIGATION OF MULTISTAGE INTERACTION GUST AERODYNAMICS

Vincent R. Capece* and Sanford Fleeter
Thermal Sciences and Propulsion Center
School of Mechanical Engineering
Purdue University
West Lafayette, Indiana 47907

ABSTRACT

The fundamental flow physics of multistage blade row interactions are experimentally investigated at realistic reduced frequency values. Unique data are obtained which describe the fundamental unsteady aerodynamic interaction phenomena on the stator vanes of a three stage axial flow research compressor. In these experiments, the effect on vane row unsteady aerodynamics of the following are investigated and quantified: (1) steady vane aerodynamic loading; (2) aerodynamic forcing function waveform, including both the chordwise and transverse gust components; (3) solidity; (4) potential interactions; and (5) isolated airfoil steady flow separation.

NOMENCLATURE

C	vane chord
$\bar{C}_\ell$	steady lift coefficient $\int_0^C (\bar{p}_p - \bar{p}_s)dx/\frac{1}{2}\rho U_t^2 C$
C_p	first harmonic dynamic pressure coefficient $\Delta\hat{p}/\rho V_x \hat{v}^+$
$\bar{C}_p$	static pressure coefficient, $(\bar{p} - \bar{p}_{exit})/\frac{1}{2}\rho U_t^2$
i	incidence angle
k	reduced frequency, $\omega C/2V_x$
$\bar{p}$	stator surface static pressure
$\bar{p}_{exit}$	stator exit static pressure
$\Delta\hat{p}$	first harmonic dynamic pressure difference
u^+	instantaneous chordwise gust component
$\hat{u}^+$	first harmonic chordwise gust
U_t	blade tip speed
v^+	instantaneous transverse gust component
$\hat{v}^+$	first harmonic transverse gust
V_x	absolute axial velocity
$\bar{\sigma}$	solidity
ω	blade passing frequency

*Currently at Pratt & Whitney Engineering Division South

INTRODUCTION

Airfoil rows of advanced gas turbine engines are susceptible to destructive aerodynamically induced vibrational responses, with upstream blade and vane wakes the most common excitation source. For example, in the single stage compressor flow field schematically depicted in Figure 1, the rotor wake velocity deficits appear as a temporally varying excitation source to a coordinate system fixed to the downstream stator vanes, i.e., the rotor blade wakes are the forcing function to the downstream stator vanes. Also as shown, the reduction of the rotor relative velocity causes a decrease in the absolute velocity and increases the incidence to the stator vanes. This produces a fluctuating aerodynamic lift and moment on the vanes which can result in high vibratory stress and high cycle fatigue failure.

First principle forced response predictive techniques require a definition of the unsteady forcing function in terms of harmonics. The total response of the airfoil to each harmonic is then assumed to be comprised of two parts. One is due to the disturbance being swept past nonresponding airfoils. The second arises when the airfoils respond to the forcing function. A gust analysis predicts the unsteady aerodynamics of the nonresponding airfoils, with an harmonically oscillating airfoil analysis used to predict the additional motion-induced unsteady aerodynamics.

Both gust and harmonically oscillating unsteady aerodynamic models are being developed, references 1 through 5, for example. Within these models are many numerical, analytical, and physical assumptions. Unfortunately, there are only a limited quantity of high reduced frequency data appropriate for model verification and direction.

Carta and St. Hilaire [6] and Carta [7], measured the surface chordwise unsteady pressure distribution on an harmonically oscillating cascade in a linear wind tunnel. This work was extended by Hardin, Carta, and Verdon [8] to an isolated rotor with oscillating blades. In addition, inlet distortion generated gust response unsteady aerodynamics were also studied. Although the interblade phase angles in these experiments were within the range found in turbomachines, the reduced frequencies, less than 0.4, were low for forced response unsteady aerodynamics found in the mid and aft stages of multistage turbomachines where the reduced frequency is typically greater than 2.0 In references 9, 10, and 11, the effects of airfoil profile and rotor-stator axial spacing on the transverse gust unsteady aerodynamic response were

investigated in a single stage, low speed research compressor at realistic values of the reduced frequency, with these data also showing the influence of the forcing function waveform.

These previous experimental investigations were performed in linear cascades, isolated rotor rows, and single stage compressors. They did not consider the multistage and potential interaction effects which exist in the mid and aft stages of turbomachines. For multistage compressors, the unsteady aerodynamics on the first two vane rows of a three stage low speed research compressor were studied for the first time in reference 12. The transverse gust forcing function and the chordwise distributions of the first harmonic pressure difference coefficients on the first two vane rows were determined for a variety of geometric and compressor operating conditions. These results indicated that the unsteady aerodynamic loading of an airfoil row was related to the aerodynamic forcing function which itself is significantly influenced by the multistage blade row interactions. This work was extended in reference 13 to include all three vane rows, with the effects of both the transverse and chordwise gust components quantified.

In this paper, the fundamental flow physics of multistage blade row interactions are experimentally investigated at realistic reduced frequency values, with unique data obtained to describe the fundamental unsteady aerodynamic phenomena on the stator vanes of a three-stage research compressor. In particular, a series of experiments are performed to investigate and quantify the effect of the following on vane row unsteady aerodynamics: (1) steady loading; (2) forcing function waveform, including both the chordwise and transverse gust components; (3) solidity; (4) potential interactions; and (5) steady flow separation.

RESEARCH COMPRESSOR AND INSTRUMENTATION

The Purdue University Three Stage Axial Flow Research Compressor is driven by a 15 HP DC electric motor over a speed range of 300 to 3,000 RPM. The three identical compressor stages consist of 43 rotor blades and 41 stator vanes, with the first stage rotor inlet flow field controlled by variable setting angle inlet guide vanes. The free-vortex design airfoils have a British C4 section profile, a chord of 30 mm, an aspect ratio of 2, and a maximum thickness-to-chord ratio of 0.10. The overall airfoil and compressor characteristics are presented in Table I.

The aerodynamic forcing function to the stator rows are the upstream airfoil wakes. The first stage vane row forcing function is varied by changing the setting angle of the inlet guide vanes, thereby altering the inlet flow to the first stage rotor, Figure 2. This results in a change in the rotor blade exit flow field, in particular, the chordwise and transverse gust components. The second and third stage vane row forcing function variations are accomplished by independently circumferentially indexing the upstream vane rows relative to one another, as also depicted.

The stator vane forcing function is quantified by measuring the stator inlet time-variant velocity and flow angle with a cross-wire probe located midway between rotor and stator at midstator circumferential spacing, Figure 1. The rotor mean absolute exit flow angle is determined by rotating the probe until a zero voltage difference is obtained between the two hot-wire channels. This mean angle is then used as a reference for calculating the instantaneous absolute and relative flow angles and defines the vane steady incidence angle. From the instantaneous velocity triangles, the individual fluctuating velocity components parallel and normal to the mean flow, the aerodynamic gust components, are calculated. The accuracy of the velocity magnitude and angle are ± 4% and ± 2 degrees, respectively.

The steady and unsteady aerodynamic loading on the vane surfaces are measured with chordwise distributions of midspan surface pressure taps and transducers. Flow visualization along this streamline shows the flow to be two-dimensional for the operating conditions of this investigation. A reverse transducer mounting technique is utilized to minimize disturbances, with the transducer connected to the measurement surface by a pressure tap. Static and dynamic calibrations of the embedded transducers demonstrate no hysteresis, with the mounting method not affecting the frequency response. The accuracy of the unsteady pressure measurements is ± 3.5%.

DATA ACQUISITION AND ANALYSIS

The steady-state data define the steady aerodynamic loading on the vane surfaces and the compressor operating point. A root-mean-square error analysis is performed, with the steady data defined as the mean of 30 samples and their 95% confidence intervals determined. The detailed steady loading on the vanes is defined by the chordwise distribution of the vane surface steady static pressure coefficient, $\bar{C}_p$, with the overall loading level specified by the incidence angle, i, and the steady lift coefficient, $\bar{C}_\ell$.

The time-variant data quantify the aerodynamic forcing function and the resulting unsteady pressure difference on the stator vanes, and are analyzed by means of a data averaging or signal enhancement concept, as proposed by Gostelow [14]. The key to this technique is the sampling of data at a preset time, which is accomplished with a shaft mounted optical encoder. At a steady-state operating point, an averaged time-variant data set consisting of the two hot-wire and the vane mounted transducer signals, digitized at a rate of 200 kHz and averaged over 200 rotor revolutions, is obtained. Each is Fourier decomposed into harmonics by means of a Fast Fourier Transform algorithm, with the magnitude and phase angle of the first harmonic referenced to the data initiation pulse determined. Analyzing the data in this form was found to be equivalent to averaging the Fourier transforms for each rotor revolution. Also, ensemble averaging and then Fourier decomposing the signal is used because it significantly reduces the data storage requirements.

The rotor and stator spacing, the axial spacing between the vane leading edge plane and the probe, and the absolute and relative flow angles are known. To time relate the hot-wire and vane surface unsteady pressure signals, the rotor exit velocity triangles are examined and the following assumptions made: (1) the wakes are identical at the hot-wire and stator leading edge planes, and (2) the wakes are fixed in the relative frame. The wakes are located relative to the hot-wires and the leading edges of the instrumented

vanes and the times at which the wakes are present at various locations determined. The incremented times between occurrences at the hot-wire and the vane leading edge planes are then related to phase differences between unsteady velocities and the vane surfaces. These assumptions are necessary in order to correlate the data with a gust analysis which fixes the gust at the airfoil leading edge. The hot-wire was located approximately midway between the rotor and stator and was less than 25% of the stator chord upstream of its leading edge.

In final form, the detailed waveform of the aerodynamic forcing function is specified by the first harmonics of the chordwise and transverse gust components, $\hat{u}^+$ and $\hat{v}^+$, respectively. The unsteady pressure data describe the chordwise variation of the first harmonic pressure difference across a stator vane, presented as a dynamic pressure difference coefficient magnitude and phase. As a reference, these data are correlated with predictions from reference 2. This gust analysis assumes the flow to be inviscid, irrotational, two-dimensional, and compressible. Small unsteady transverse velocity perturbations, v^+, are assumed to be convected with the uniform flow past a cascade of flat plate airfoils. The parameters modeled include the cascade solidity, stagger angle, inlet Mach number, reduced frequency, and the interblade phase angle. The analysis does not consider flow separation or chordwise gust perturbations, u^+.

RESULTS

Three stator vane solidities are investigated: the design value of 1.09; a reduced value of 0.545; and 0.10 which results in a spacing between vanes large enough so that the influence of neighboring vanes is negligible; i.e., each vane is an isolated airfoil. The results are presented for each solidity for variations in one of the key parameters. All design solidity data, except for the potential interaction effects, are presented for the first stator vane row. The data sets for the other solidities are presented for the third stator vane row. Since there are no airfoil rows downstream of the third stage vane row, there are no potential interaction effects on the trailing edge region of these vanes. Data from reference 13 have been added for the design solidity in order to have a complete presentation of the results and to indicate the significant effects which solidity has on the unsteady aerodynamic response of the stator vanes. Also, the error in the static pressure coefficient data is represented by the symbol size.

VANE STEADY LOADING

Steady aerodynamic loading effects are considered for the design and reduced solidities of 1.09 and 0.545. The first harmonics of the forcing function are maintained nearly constant, Figure 3. Note that relative to the absolute velocity, the instantaneous gust components are not small. For example, the instantaneous transverse and chordwise gust components are approximately 40% and 25% of the absolute velocity at -5.9 degrees of incidence. However, in terms of the first harmonics these gust components are approximately 11% and 6% of the absolute velocity.

For each solidity, the vane surface steady pressure distributions are smooth and show no indication of flow separation, Figure 4. At the design solidity, the surface static pressures for the lift coefficient of 0.268 are greater than those for the lift coefficient of 0.176, a result of the inlet guide vane indexing altering the compressor operating point. Also, the reduced solidity has much higher pressure differences and steady lift coefficients due to the decreased number of vanes.

The resulting chordwise distributions of the dynamic pressure difference coefficient and the predictions are shown in Figure 5. At the design solidity, good correlation exists between the magnitude data and the prediction for the lift coefficient of 0.176, with an increase in lift to 0.268 resulting in poorer correlation. The higher loading data are decreased in amplitude relative to both the prediction and the lower loading data over the front 25% of the vane. Aft of 25% chord, the data correlate well with each other and the prediction until 63% chord, with both data sets then increasing to a larger value than the prediction.

The phase data exhibit a somewhat different chordwise distribution than the prediction. In particular, the phase data are increased relative to the prediction over the first 14% of the vane chord. The data then decrease to the level of the prediction and then increase to values greater than the prediction with increasing chordwise position. The phase data for both loading levels exhibit the same trends, with the higher loading data increased relative to both the prediction and the lower loading data over most of the chord. The differences between the phase data and the prediction are attributed to the vane camber and the detailed steady loading distributions on the vane surfaces.

The magnitude data for the reduced solidity are also decreased relative to the prediction over the front 50% of the vane, with the higher loading data having, in general, a decreased amplitude relative to the lower loading data. The decrease in amplitude relative to the prediction is due to the high levels of steady aerodynamic loading. Aft of 50% chord, the magnitude data increase to the level of the prediction and show better correlation. The phase data increase to a level larger than the prediction over the front 14% of the vane, then decrease towards the prediction, and from approximately 25% to 50% chord, the phase data are almost constant. Aft of 50% chord this trend changes, with the higher loading data decreased relative to both the lower loading data and the prediction, and then increasing as the chordwise position increases. Thus, from these results it is evident that steady loading primarily affects the magnitude of the dynamic pressure difference coefficient.

The best correlation of the dynamic pressure difference coefficient data and the prediction is obtained at the low level of steady loading at the design solidity, as expected, since this most closely approximates the unloaded flat plate cascade model. Also, the steady loading level and distribution have a significant effect on the unsteady aerodynamics of the vane row. In general, different airfoil designs will produce different steady surface pressure distributions and steady lift for the same incidence angle. Therefore, the level of steady aerodynamic loading, not the incidence angle, is the key parameter in obtaining good correlation with mathematical models.

AERODYNAMIC FORCING FUNCTION

The influence of each gust component on the complex dynamic pressure coefficient, with the steady aerodynamic loading held constant, is considered.

Transverse Gust

The surface static pressure distributions for each solidity are smooth, with no evidence of separation and only small variations apparent near the leading edge which result in the slight variations in the steady lift coefficients, Figure 6. As the solidity is decreased, there is an increase in the level of steady surface pressures and a corresponding increase in the steady lift coefficient. The chordwise gust, $\hat{u}^+$, is held approximately constant while the transverse gust, $\hat{v}^+$, is varied, Figure 7, with the difference between the configurations specified by the first harmonic gust ratio, $\hat{u}^+/\hat{v}^+$.

The effect of the transverse gust on the chordwise distributions of the dynamic pressure difference coefficient data is presented in Figure 8. At the design solidity, both configurations show the magnitude data to be decreased relative to the prediction over the leading 30% of the vane, with the $(\hat{u}^+/\hat{v}^+)$ data of 0.630 having a decreased amplitude relative to the 0.447 data. However, in the midchord region, the data for these two configurations correlate well with each other and with the prediction. As in the previous cases, aft of 70% chord the data increase relative to the prediction. This is a result of both the potential interaction from the downstream second stage rotor row and the parallel gust component, $\hat{u}^+$, as the design solidity data are acquired on the first stage. This phenomena will be discussed in greater detail in the section on Potential Flow Interactions.

The reduced solidity and the isolated airfoil data show a different trend with the ratio of $(\hat{u}^+/\hat{v}^+)$ than that of the design solidity, with the data for the larger values of $(\hat{u}^+/\hat{v}^+)$ increased in value relative to the lower values. This is opposite to the trend noted at the design solidity. However, examination of the magnitudes of the first harmonics of the chordwise gust component, $\hat{u}^+$, indicates that the magnitudes of the chordwise gust are lower in value than the design case. This indicates that the chordwise pressure distributions are not governed simply by the ratio of the two gust components but also by their magnitudes.

For each of the reduced solidity values, 0.545 and 0.10, the magnitude data are generally decreased relative to the prediction over the leading 50% of the vane, with the lower $(\hat{u}^+/\hat{v}^+)$ data having a decreased amplitude relative to the higher $(\hat{u}^+/\hat{v}^+)$ data. In the trailing edge portion of the vane, the magnitude data correlate well with each other but are increased in level relative to the prediction. This is a result of the chordwise gust which is not considered by the model.

The design solidity phase data are increased relative to the prediction over the front 14% of the vane, decrease to the level of the prediction at 22% chord, and then increase to values greater than the prediction with increasing chordwise position, becoming nearly constant aft of 40% chord. At the reduced solidity, the phase data are increased relative to the prediction over the entire vane chord, being nearly constant in the 22% to 38% chord region. For the isolated airfoil, the phase data show good trendwise correlation with the prediction over the leading 29% of the vane, with the $(\hat{u}^+/\hat{v}^+)$ data of 0.245 decreasing relative to both the prediction and the $(\hat{u}^+/\hat{v}^+)$ 0.218 data. Aft of 29% chord, where the vane does most of its turning, the phase data decrease until 54% chord and then increase with increasing chordwise position.

These results show that the transverse gust primarily influences the magnitude of the dynamic pressure difference coefficient. Also, the unsteady data variations with forcing function waveform cannot be predicted by harmonic gust models. This is because the forcing function waveforms and the resulting unsteady pressure distributions have been Fourier decomposed, with the first harmonic of the unsteady data presented. Thus, all of these first harmonic data are correlated with the same prediction curve; i.e., the predictions from these harmonic gust models are identical for all of the forcing function waveforms.

Chordwise Gust

The effect of the forcing function chordwise gust component, $\hat{u}^+$, on the vane row unsteady aerodynamics for each solidity is considered. This is accomplished by establishing compressor configurations such that the transverse gust and the steady aerodynamic loading are nearly identical Figures 9 and 10, respectively.

The resulting chordwise distributions of the dynamic pressure coefficient data and the predictions are presented in Figure 11. In general, the magnitude data exhibit analogous trends for each solidity, decreasing over the front of the vane and increasing over the aft part. The magnitude data increase over the prediction at the design solidity, whereas they increase up to the prediction for the other two solidity values. This is again the result of the design solidity data being acquired on the first stage, with the data for the other solidities being acquired on the third stage. Also, the higher $(\hat{u}^+/\hat{v}^+)$ data are decreased relative to both the prediction and the lower $(\hat{u}^+/\hat{v}^+)$ data for each solidity. This is particularly apparent at the design and reduced solidity.

The design solidity phase data at a $(\hat{u}^+/\hat{v}^+)$ of 0.611 show good trendwise correlation with the prediction over the aft 50% of the vane while the lower $(\hat{u}^+/\hat{v}^+)$ data are increased relative to the prediction, as seen in previous cases. Over the front 50% of the vane, the data correlate trendwise with each other but are increased compared to the prediction. The reduced solidity phase data are increased relative to the prediction and remain relatively constant over the entire vane chord, with the $(\hat{u}^+/\hat{v}^+)$ phase data of 0.634 consistently increased over the $(\hat{u}^+/\hat{v}^+)$ 0.436 data.

A somewhat different trend is evident in the phase data for the isolated airfoil than previous isolated airfoil cases and the other solidity values. In this case, the data are seen to correlate trendwise with the prediction over the front of the vane, then decrease slightly lower than the prediction and remain almost constant for the remainder of the vane. In addition, the phase data for these two configurations correlate quite well with one another over

almost the entire vane. Comparing these results to the phase data of Figure 8 for a $(\hat{u}^+/\hat{v}^+)$ of 0.218 indicates that loading has a dramatic effect on the phase as well as the magnitude data: both the phase and the magnitude data show the maximum deviations from the analysis in the 25% to 50% chord locations. Aft of this point the magnitude and phase increase to the prediction.

The differences apparent in the dynamic pressure difference coefficient phase data for the three different solidity values are a result of the details of the steady static pressure distributions and the spacing between the airfoils. As the airfoil spacing increases for low levels of aerodynamic loading, the correlation of the phase data with the predictions gets increasingly better. This indicates that the influence of adjacent airfoils is much greater than predicted by the zero incidence flat plate analysis.

Thus, both the transverse and chordwise gust components affect the magnitude data, with the chordwise gust having a larger influence on the phase, particularly at the design solidity. In addition, the magnitude of the chordwise gust is not small as compared to either the absolute velocity or the transverse gust.

POTENTIAL FLOW INTERACTIONS

Data in the vane trailing edge region are consistently increased relative to the prediction. Part of this increase is attributable to the chordwise gust which is not modeled by the prediction. However, first stage magnitude data exhibit larger deviations in the trailing edge region than third stage data with similar steady lift coefficients. To investigate this phenomenon, unsteady data are acquired on the second and the third stages at the design solidity for operating conditions where the steady loading and the forcing function are nearly identical, Figure 12. Thus the only difference between these two configurations is the presence of the third stage downstream of the second stage stator row.

The resulting dynamic pressure difference coefficient data and corresponding prediction are presented in Figure 13. The magnitude data are decreased relative to the prediction over the leading 30% of the vane due to the steady loading level, with the deviations in the amplitude attributed to the differences in the steady surface pressure distributions in the leading edge region. Aft of 30% chord, the data increase to the level of the prediction, with the second stage data higher in amplitude than the third stage data, particularly in the trailing edge region. Since the steady pressure distributions and the forcing function are nearly identical, this deviation of the second stage data is attributed to a potential interaction effect caused by the downstream third stage. The increase of the third stage data above the prediction in this region is a result of the chordwise gust since there are no downstream airfoil rows, with the further increase in the second stage data due to the potential interaction.

The phase data also show different trends in the trailing edge region due to potential interactions. Over the front part of the vane, the data are increased with respect to the prediction, but then decrease in relation to the prediction at 22% chord. The data then increase until 50% chord, with the data up to this point exhibiting good trendwise correlation. Aft of 50% chord the second stage data are nearly constant with increasing chordwise position, whereas the third stage data show another decrease in phase and then increase with increasing chordwise position.

Thus, potential interaction effects influence both the magnitude and phase, with the larger effect being upon the magnitude of the dynamic pressure difference coefficient. Hence, the downstream airfoil row is another aerodynamic excitation source to the upstream blade or vane row and would act on the trailing edge region.

ISOLATED AIRFOIL SEPARATION

The effect of separated flow on the stator vane unsteady aerodynamics for a solidity of 0.10; i.e., an isolated airfoil, is now investigated. The separated flow is generated by restaggering the stator vanes such that a mean flow incidence angle of 8.2 degrees is established. At this incidence angle, the flow separates from the vane suction surface as indicated by the region of constant static pressure which originates at 38% chord, Figure 14. The separated flow data are compared with data for a configuration where the steady lift coefficient and both the chordwise and transverse gust components are nearly identical, but the flow is not separated.

The resulting dynamic pressure difference coefficient data and the attached flow flat plate prediction are shown in Figure 15. The attached and separated flow data show somewhat different trends in the leading and trailing edge regions. The separated flow magnitude data are nearly constant over the front 14% of the vane, whereas the attached flow data and prediction indicate a decrease in amplitude with increasing chordwise position. Aft of 14% chord the data show analogous trends, with both separated and attached flow data decreasing with increasing chordwise position and attaining a minimum amplitude value at 20% chord, similar to previous isolated airfoil results. The magnitude data for both cases then gradually increase to values that are greater than the prediction at 54% chord, with the attached flow data being lower in magnitude up to this point. Both data sets then decrease with further chordwise position, with the separated data decreased in amplitude relative to both the prediction and the attached flow data. This is a result of the increased steady loading in this region of the airfoil due to the separation zone.

The attached and separated flow phase data have different trends near the separation point and in the trailing edge region. Over the front 22% of the vane, the data and the prediction show analogous trends, being nearly constant. The separated data are increased relative to the prediction, with the attached flow data exhibiting excellent correlation with the prediction. Aft of 22% chord the separated data increase whereas the attached flow data decrease relative to the prediction. In the separated flow region, both the separated and attached flow data exhibit similar trends. However, at 70% chord the separated data indicate a jump to values larger than the prediction and increase with further chordwise position. On the other hand, the attached flow phase data show a gradual increase. Thus, separation affects both the magnitude and phase of the dynamic pressure difference coefficient.

SUMMARY AND CONCLUSIONS

A series of experiments were performed to investigate the wake generated gust aerodynamics on each vane row of a three stage axial flow research compressor at high reduced frequency values, including multistage interactions. In these experiments, the effect on vane row unsteady aerodynamics of the following were investigated and quantified: (1) steady vane aerodynamic loading; (2) aerodynamic forcing function waveform, including both the chordwise and transverse gust components; (3) solidity; (4) potential interactions; and (5) isolated airfoil steady flow separation. The analysis of these unique vane row unsteady aerodynamic data determined the following.

* The steady aerodynamic loading level, not the incidence angle, is the key parameter to obtain good correlation with flat plate cascade gust models.

* The steady loading level and chordwise loading distribution have a significant effect on vane row unsteady aerodynamics, having a larger influence on the magnitude than on the phase.

* The aerodynamic forcing function chordwise gust affects both the dynamic pressure coefficient magnitude and phase, whereas the transverse gust primarily affects the magnitude. These effects cannot be predicted with harmonic gust models because these data have been Fourier decomposed, with the predictions thus identical for all forcing function waveforms.

* The chordwise gust is not small compared to either the absolute velocity or the transverse gust. Thus, to provide accurate predictions, unsteady aerodynamic models must consider this gust component.

* For closely spaced stages (the compressor rotor-stator axial spacing herein is 0.432 chord), downstream airfoil rows are potential aerodynamic excitation sources which affect the unsteady loading in the trailing edge region of the upstream airfoils. Since the trailing edge is thin, it would be highly susceptible to fatigue failure.

* Flow separation of the low solidity vane row affects the unsteady surface pressures upstream of the separation point, with the phase affected in the trailing edge region.

ACKNOWLEDGEMENT

Support of this research program by the Air Force Office of Scientific Research, Dr. James Wilson program manager, is most gratefully acknowledged.

REFERENCES

1. Verdon, J.M. and Caspar, J.R., "Development of an Unsteady Aerodynamic Analysis for Finite Deflection Subsonic Cascades," *NASA CR 3455*, September 1981.

2. Fleeter, S., "Fluctuating Lift and Moment Coefficients for Cascaded Airfoils in Nonuniform Compressible Flow," *AIAA Journal of Aircraft*, Volume 10, February 1973.

3. Atassi, H.M., "The Sears Problem for a Lifting Airfoil Revisited - New Results," *Journal of Fluid Mechanics*, Volume 141, 1984.

4. Englert, G.W., "Interaction of Upstream Flow Distortions with High Mach Number Cascades," *ASME Paper 82-GT-197*, 1982.

5. Chiang, H.D. and Fleeter, S., "Prediction of Loaded Airfoil Unsteady Aerodynamic Gust Response by a Locally Analytical Method," *International Journal of Mathematical Modeling*, accepted for publication.

6. Carta, F.O. and St. Hilaire, A.O., "Effect of Interblade Phase Angle and Incidence Angle on Cascade Pitching Stability," ASME Paper *79-GT-153*, 1979.

7. Carta, F.O., "An Experimental Investigation of Gapwise Periodicity and Unsteady Aerodynamic Response in an Oscillating Cascade, Part I: Experimental and Theoretical Results," *NASA CR 3513*, June 1982.

8. Hardin, L.W., Carta, F.O., and Verdon, J.M., "Unsteady Aerodynamic Measurements on a Rotating Compressor Blade Row at Low Mach Number," *ASME Journal of Turbomachinery*, Vol. 109, No. 4, October 1987, pp. 499-507.

9. Fleeter, S., Jay, R.L., and Bennett, W.A., "Rotor Wake Generated Unsteady Aerodynamic Response of a Compressor Stator," *ASME Journal of Engineering for Power*, Volume 100, October 1978.

10. Fleeter, S., Bennett, W.A., and Jay, R.L., "The Time Variant Aerodynamic Response of a Stator Row Including the Effects of Airfoil Camber," *ASME Journal of Engineering for Power*, Volume 102, April 1980.

11. Fleeter, S., Jay, R.L., and Bennett, W.A., "Wake Induced Time Variant Aerodynamics Including Rotor-Stator Axial Spacing Effects," *ASME Journal of Fluids Engineering*, Volume 103, No. 1, March 1981.

12. Capece, V.R., Manwaring, S.R., and Fleeter, S., "Unsteady Blade Row Interactions in a Multi-Stage Compressor," *AIAA Journal of Propulsion*, Volume 2, No. 2, March-April 1986.

13. Capece, V.R. and Fleeter, S., "Unsteady Aerodynamic Interactions in a Multi-Stage Compressor," *ASME Journal of Turbomachinery*, Volume 109, No. 3, July 1987.

14. Gostelow, J.P., "A New Approach to the Experimental Study of Turbomachinery Flow Phenomena," *ASME Journal of Engineering for Power*, Vol. 99, Jan. 1977.

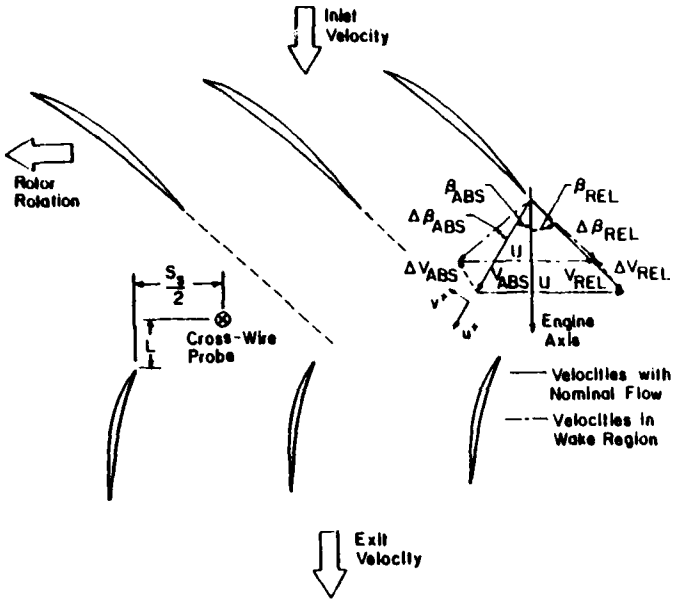

Figure 1. Single stage compressor flow field

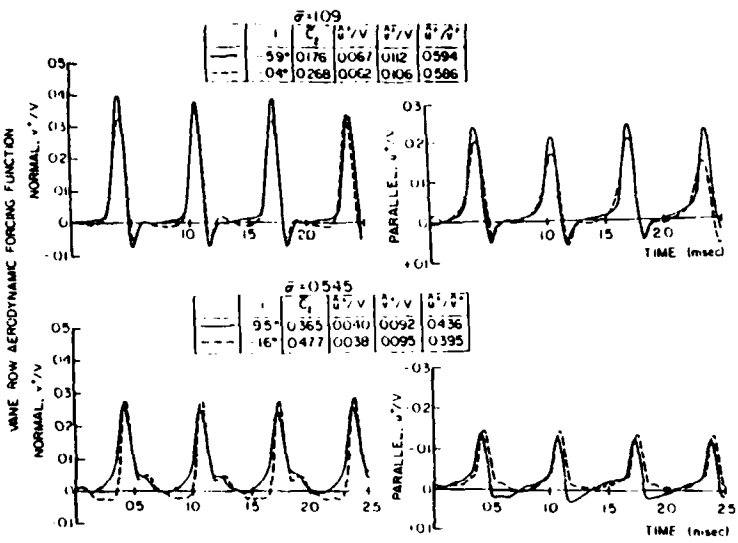

Figure 3. Aerodynamic forcing functions for steady loading study

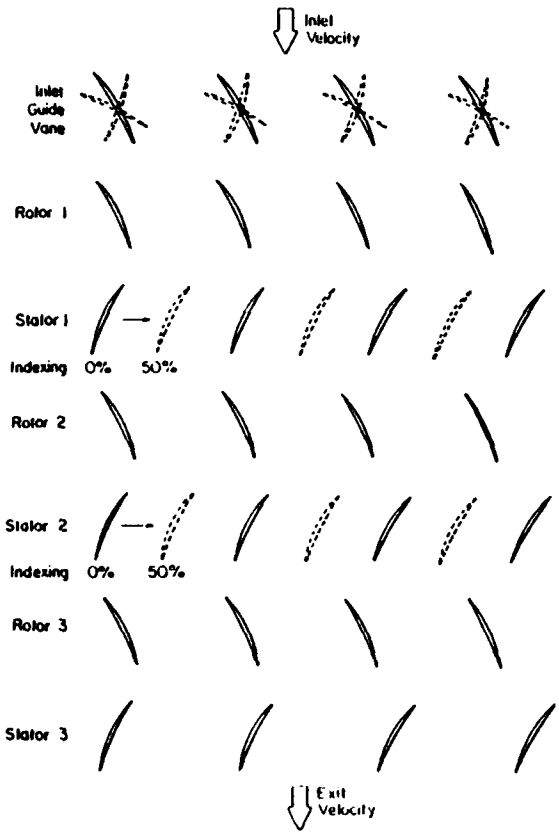

Figure 2. Compressor geometry variations to alter forcing function

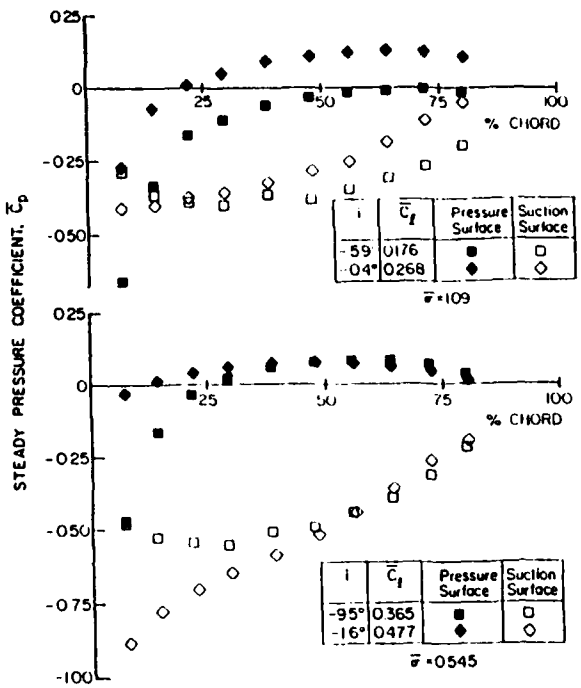

Figure 4. Vane static pressure distributions for steady loading study

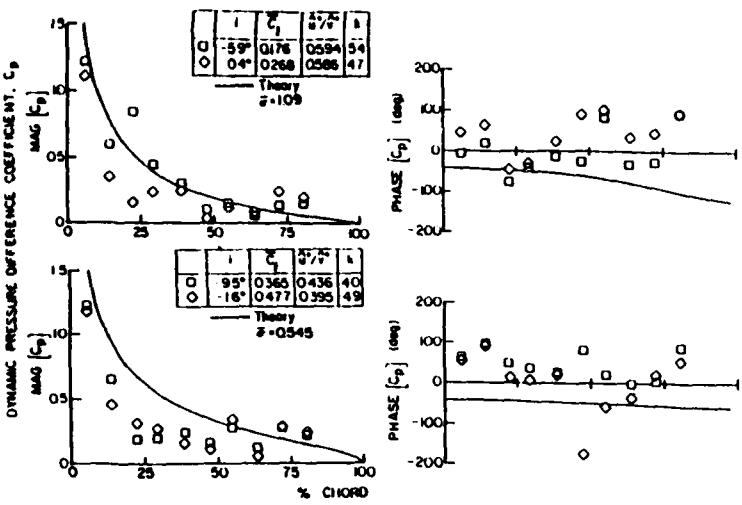

Figure 5. Effect of steady loading on the complex unsteady pressure coefficient

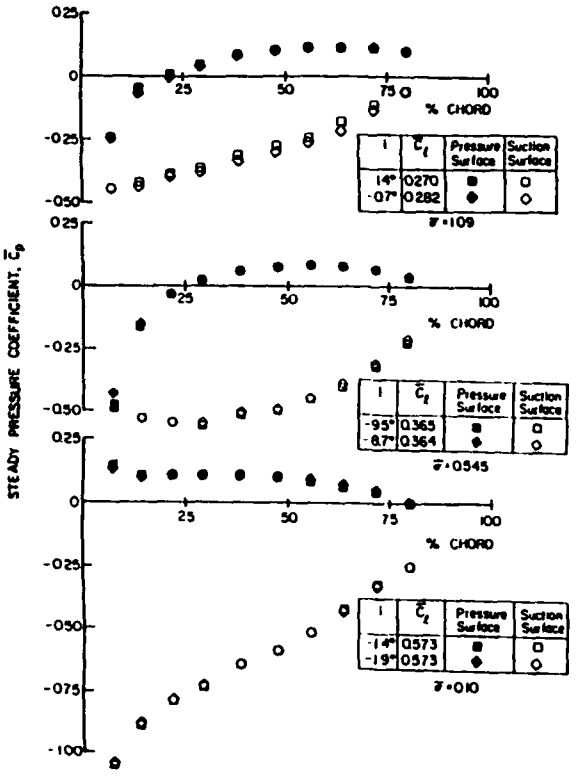

Figure 6. Surface static pressure distributions for transverse gust study

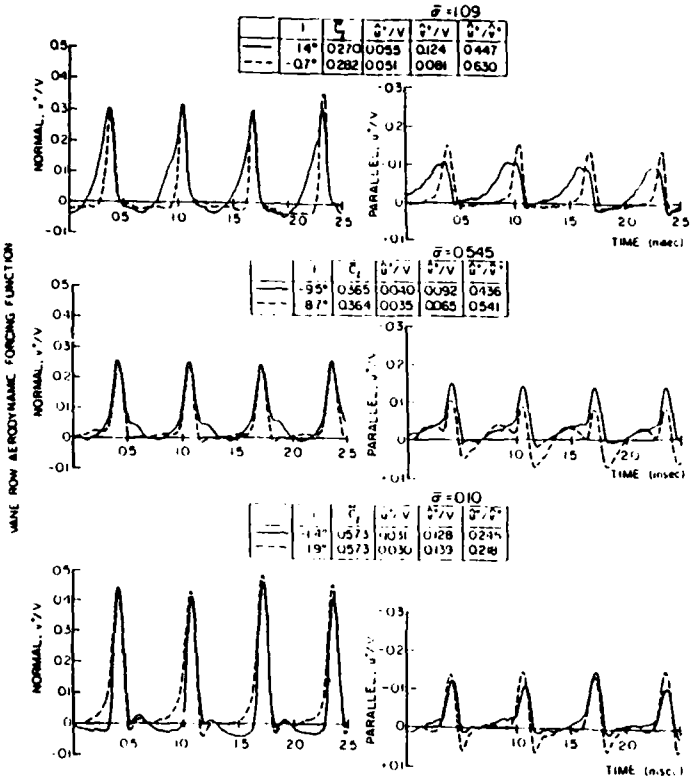

Figure 7. Aerodynamic forcing functions for transverse gust study

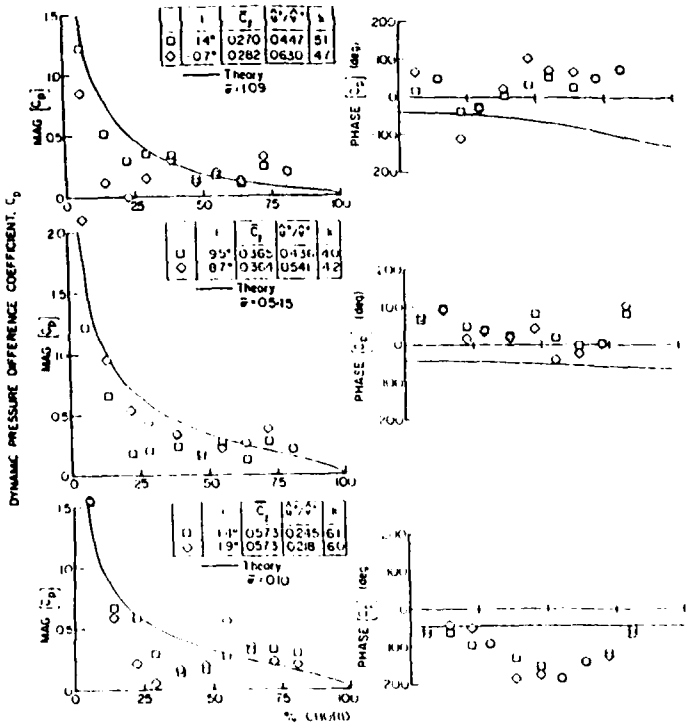

Figure 8. Effect of transverse gust on the complex unsteady pressure coefficient

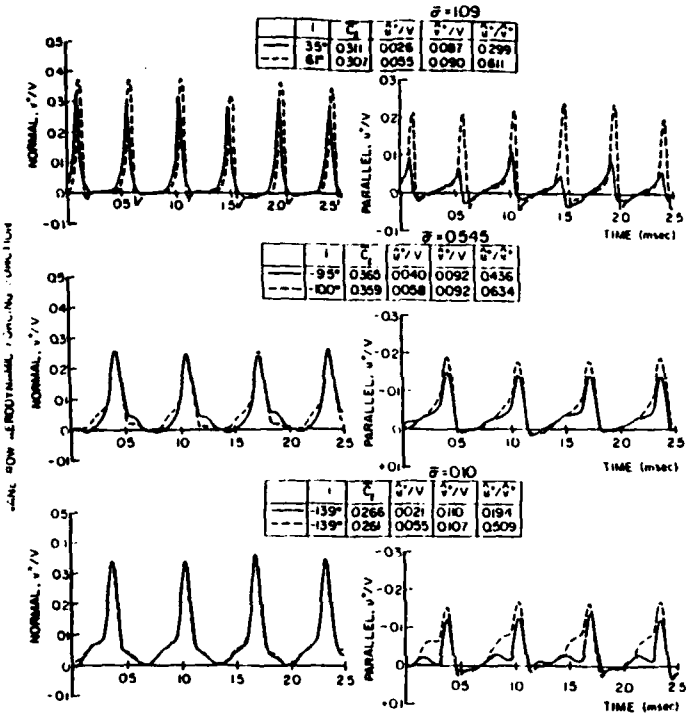

Figure 9. Aerodynamic forcing function for chordwise gust study

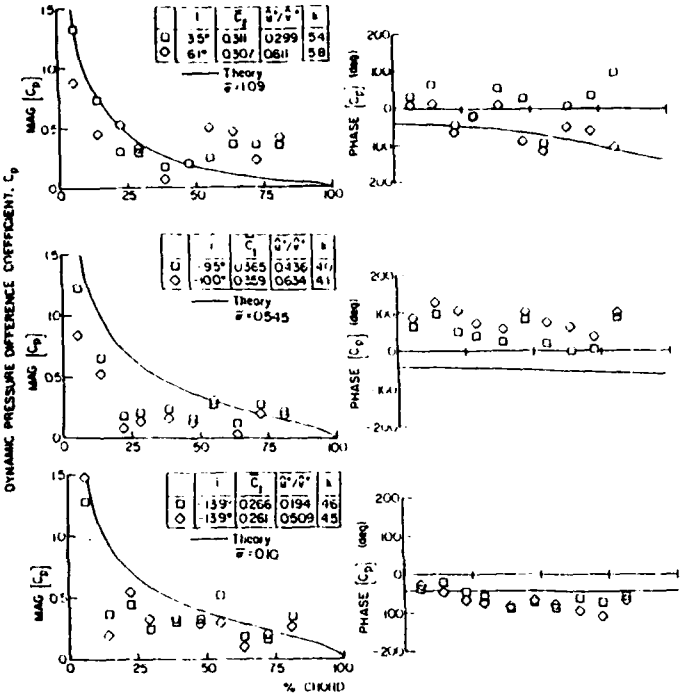

Figure 11. Effect of chordwise gust on the complex unsteady pressure coefficient

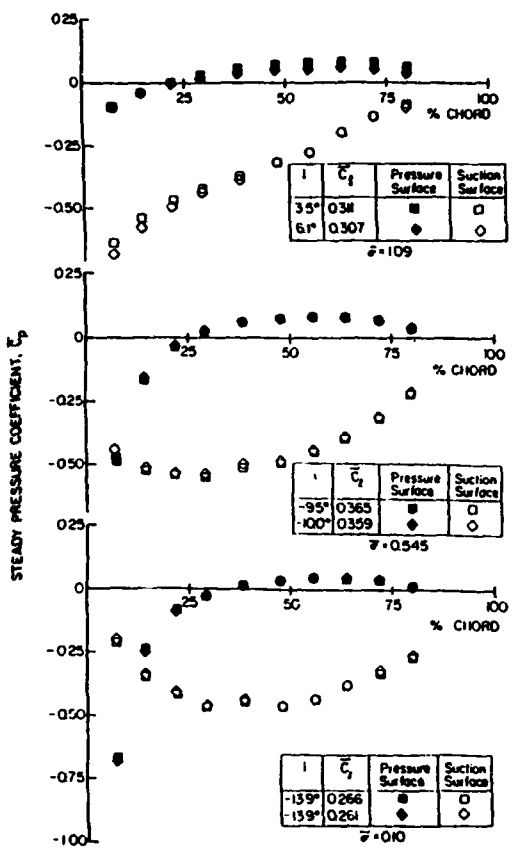

Figure 10. Steady vane loading distributions for chordwise gust study

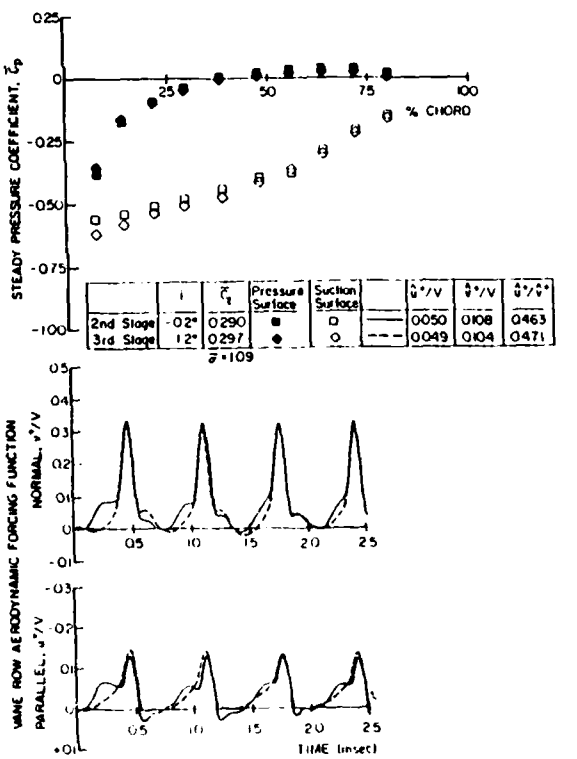

Figure 12. Steady loading and forcing functions for potential flow interaction study

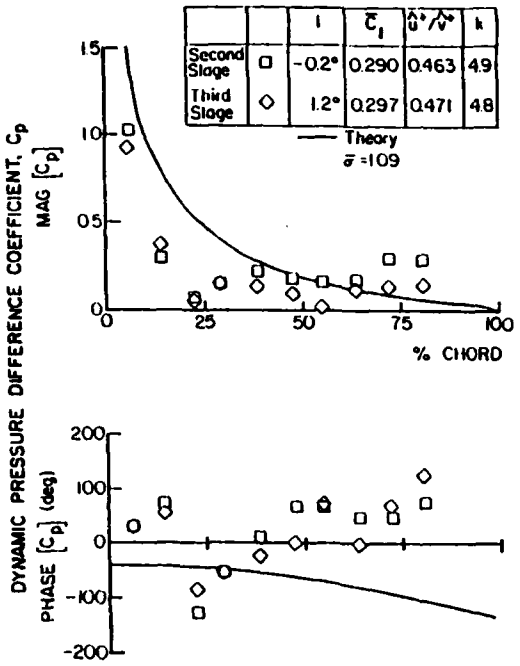

Figure 13. **Potential flow interaction effect on the complex unsteady pressure coefficient**

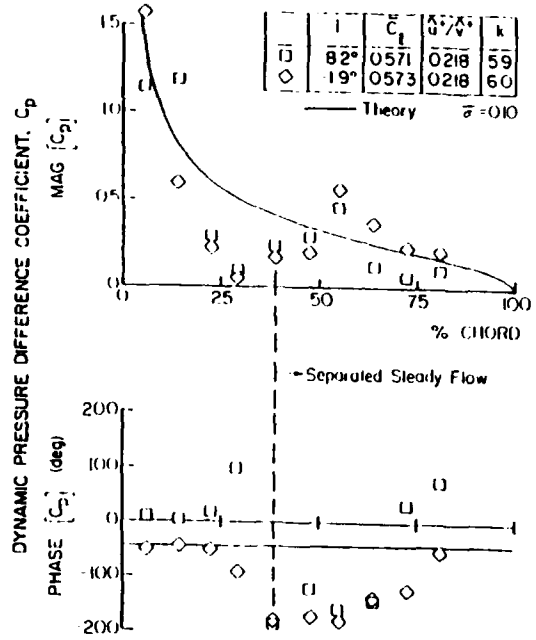

Figure 15. **Steady suction surface separation effect on the complex unsteady pressure coefficient**

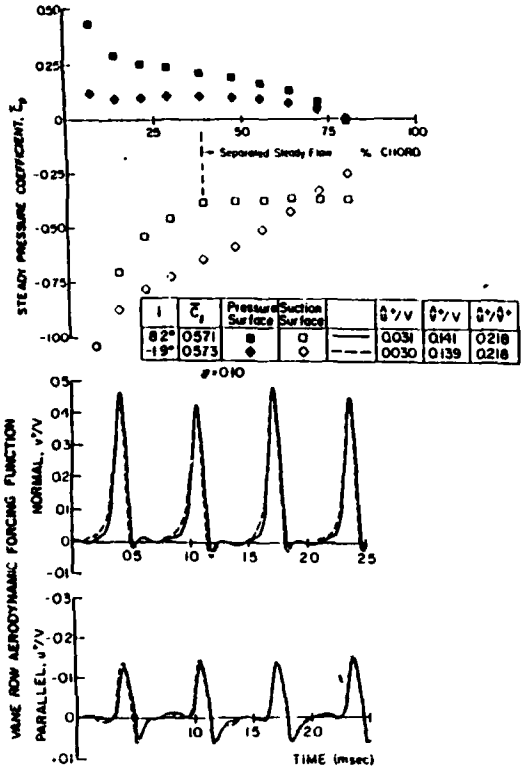

Figure 14. **Steady loading and forcing functions for isolated airfoil separated flow investigation**

	ROTOR	STATOR
Airfoil Type	C4	C4
Number of Airfoils	43	41
Chord, C (mm)	30	30
Solidity, C/S	1.14	1.09
Camber, θ	27.95	27.70
Stagger Angle, λ	36	36.1
Aspect Ratio	2.0	2.0
Thickness/Chord (%)	10	10
Axial Gap (cm)	1.27	
Flow Rate (kg/s)	2.66	
Design Axial Velocity (m/s)	32.0	
Rotational Speed (RPM)	3000	
Number of Stages	3	
Stage Pressure Ratio	1.003	
Inlet Tip Diameter (mm)	420	
Hub/Tip Radius Ratio	0.714	
Stage Efficiency (%)	85	

Table I. Overall compressor and airfoil characteristics

APPENDIX VII

UNSTEADY AERODYNAMIC GUST RESPONSE INCLUDING STEADY FLOW SEPARATION

UNSTEADY AERODYNAMIC GUST RESPONSE INCLUDING STEADY FLOW SEPARATION

Sanford Fleeter, Vincent R. Capece, and Hsiao-Wei D. Chiang

Thermal Sciences and Propulsion Center
School of Mechanical Engineering
Purdue University
West Lafayette, Indiana 47907

ABSTRACT

A series of experiments are performed to investigate and quantify the unsteady aerodynamic response of an airfoil to a high reduced frequency gust, including the effects of the gust forcing function waveform, airfoil loading, and steady flow separation. This is accomplished by utilizing an axial flow research compressor to experimentally model the high reduced frequency gust forcing function and replacing the last stage stator row with isolated instrumented airfoils. Appropriate data are correlated with predictions from flat plate and cambered airfoil convected gust models. The airfoil surface steady loading is shown to have a large effect on the unsteady aerodynamic response. Also, the steady flow separation has a significant influence on the gust response, particularly upstream of the separation point and in the airfoil trailing edge region.

NOMENCLATURE

C	airfoil chord
$\bar{C}_\ell$	steady lift coefficient $\int_0^C (\bar{p}_p - \bar{p}_s)dx/\frac{1}{2}\rho U_t^2 C$
$\hat{C}_p$	first harmonic unsteady pressure coefficient $\Delta\hat{p}/\rho V_x\hat{v}^+$
$\bar{C}_p$	static pressure coefficient, $(\bar{p} - \bar{p}_{exit})/\frac{1}{2}\rho U_t^2$
f^p	periodic signal component
f^r	random signal component
f^s	steady signal component
$\mathcal{K}$	gust propagation direction vector
k_1	reduced frequency, $\omega C/2V_x$
k_2	transvese gust wave number
$\bar{p}$	airfoil surface static pressure
$\bar{p}_{exit}$	exit static pressure
$\Delta\hat{p}$	first harmonic unsteady pressure difference
s	unsteady transducer signal
$\hat{u}^+$	first harmonic chordwise gust
U_t	rotor blade tip speed
$\hat{v}^+$	first harmonic transverse gust
V_x	absolute axial velocity
α_o	angle of attack
ρ	inlet air density

INTRODUCTION

The unsteady flow past a stationary airfoil is of primary concern in many important applications. For example, the unsteady interaction of an airfoil with gusts and similar vortical disturbances plays a significant role in the aerodynamics, dynamic loading, aeroelasticity, and acoustics of modern aircraft, missiles, helicopter rotors, advanced turboprops and turbomachines. As a result, the interest in unsteady flow theory initiated by Theodorsen [1935], Kussner [1940], and Sears [1941] has continued to the present.

Theoretical gust models have typically been restricted to thin airfoil theory, with the unsteady gust disturbance assumed to be small as compared to the mean steady potential flow field. However, in most applications, airfoils with arbitrary shape, large camber, and finite angles of attack are required. In an attempt to meet this need, Horlock [1968] extended the classical approach of Sears to consider a flat plate airfoil at small angle of attack. Naumann and Yeh [1972] then extended Horlock's analysis to consider a thin airfoil with constant small camber. These analyses showed that the unsteady aerodynamic forces acting on an airfoil were affected by both the small incidence angle and the small airfoil camber. However, these models neglect second order terms, following Sears, and also assume a small angle of attack. Thus these results are only approximate and cannot be extended to finite incidence angles or large airfoil camber.

It is apparent that the thin airfoil approach is not adequate for many applications of interest. In this regard, Goldstein and Atassi [1976] and Atassi [1984] developed a theory for the inviscid incompressible flow past an airfoil subject

to an interacting periodic gust. The theory assumes that the fluctuating flow velocity is small compared to the mean velocity, with the unsteady flow linearized about the full potential steady flow past a flat plate or Joukowski airfoil and accounts for the effects of both airfoil profile and angle of attack.

Experimental investigations have typically been restricted to low reduced frequency aerodynamic gusts. In part, this is due to the difficulties associated with generating a periodic unsteady gust, with low reduced frequency gust tunnels having been developed by Holmes [1973], Satyanarayana, Gostelow, and Henderson [1974] and Ostdiek [1976], for example. Also contributing is the difficulty in obtaining and analyzing the fundamental high frequency unsteady data that define both the aerodynamic forcing function and the resulting airfoil surface pressure distributions. The acquisition and analysis of such high frequency data has only recently become possible with the development and availability of miniature high-response pressure transducers, digital instrumentation, and computers for both control of instrumentation and digital data acquisition and analysis.

The above noted experiments and analyses are all concerned with attached steady flow. Separated flow oscillating airfoil phenomena, including stall flutter and dynamic stall, have also been addressed. Thus, oscillating airfoil models and experiments have considered the effects of steady loading and flow separation, for example, Woods [1957], Yashima and Tanaka [1977], Sisto and Perumal [1974], Ericsson and Reding [1981], Carstens [1984], Chi [1985], and Lorber and Carta [1987]. In this regard it should be noted that only minimal attention has been directed towards the effect of steady loading and flow separation on the unsteady

aerodynamic response of an airfoil to a periodic gust.

In this paper, the effects of the gust waveform, as characterized by the chordwise (parallel) and transverse (normal) gust components, u^+ and v^+ depicted in Figure 1, airfoil loading, and steady flow separation, on the unsteady aerodynamic response of an airfoil are experimentally investigated at high reduced frequency values for the first time. This is accomplished by: (1) utilizing an axial flow research compressor to experimentally model the high reduced frequency aerodynamic gust forcing function; (2) replacing the last stage stator row with instrumented isolated airfoils; (3) developing and utilizing computer based time-variant digital data acquisition and analysis techniques, including ensemble averaging and Fast Fourier Transforms (FFT), for the analysis of the periodic data. In particular, high reduced frequency aerodynamic gusts are generated by the upstream rotor blade wakes, with the unsteady aerodynamic gust response determined by replacing the downstream stator row with static and dynamically instrumented isolated airfoils. Thus, there is complete experimental modeling of the basic unsteady aerodynamic phenomena inherent in this high reduced frequency unsteady interaction including angle of attack effects, the velocity and pressure variations, and the waveform of the aerodynamic forcing function.

RESEARCH COMPRESSOR

The Purdue axial flow research compressor with the last stage stator row replaced by an isolated airfoil, is utilized for these experiments. It is driven by a 15 HP DC electric motor over a speed range of 300 to 3,000 RPM. The wakes from

the upstream rotor blades are the source of the unsteady surface pressures on the downstream isolated airfoil, i.e., the rotor wakes define the aerodynamic forcing function to the airfoil, as depicted schematically in Figure 1. The 43 rotor blades and the isolated airfoil are free vortex design airfoils with a British C4 section profile, a chord of 30 mm, and a maximum thickness-to-chord ratio of 0.10.

The variations in the airfoil steady loading are accomplished by compressor throttling and adjusting the setting angles of the instrumented airfoils, thereby altering the airfoil angle of attack. The detailed steady aerodynamic loading of the instrumented airfoils is specified by the chordwise distribution of the airfoil surface steady static pressure coefficient, with the overall loading level given by the angle of attack and the steady lift coefficient.

The waveform of the aerodynamic forcing function is defined by the first harmonic chordwise and transverse gust components, $\hat{u}^+$ and $\hat{v}^+$, respectively. The forcing function waveform variations to the instrumented last stage airfoils are accomplished by independently circumferentially indexing the upstream compressor vane rows relative to one another while maintaining a constant instrumented airfoil steady loading distribution.

INSTRUMENTATION

Both steady and unsteady data are required. The steady data define the detailed airfoil surface aerodynamic loading. The unsteady data quantify the time-variant aerodynamic forcing function to the isolated airfoil, i.e., the airfoil unsteady inlet flow field and the resulting chordwise distribution of the time-

variant pressures on the surfaces of the downstream airfoil. Flow visualization studies showed the flow to be two-dimensional on the midspan streamline. Thus, midspan chordwise distributions of airfoil surface static and dynamic instrumentation are utilized.

The unsteady aerodynamic forcing function to the airfoil, the time-variant inlet flow field, is measured with a cross hot-wire probe. The airfoil mean absolute inlet flow angle is determined by rotating the cross-wire probe until a zero voltage difference is obtained between the two hot-wire signals. This mean angle is subsequently used as a reference to calculate the airfoil angle of attack and the instantaneous absolute and relative flow angles.

The airfoil surface time-variant pressure measurements are accomplished with flush mounted ultra-miniature high response transducers. To minimize potential flow disturbances due to the transducer mounting or the inability of the transducer diaphragm to exactly maintain the surface curvature of the airfoil, a reverse mounting technique is utilized. The pressure surface of one airfoil and the suction surface of a second are instrumented, with the transducers embedded in the non-measurement surface and connected to the measurement surface by a static tap.

To assure the accuracy of the experiments as well as to minimize the number of stator row reconfigurations needed to obtain the isolated airfoil steady and unsteady data of interest, the complete last stage compressor stator row was replaced with a stator row comprised of only two airfoils, these being either the statically instrumented airfoils or the dynamically instrumented airfoils. This corresponds to a vane row with a solidity (chord/spacing) of less than 0.10, which

results in a spacing between the instrumented vanes large enough so that the influence of the neighboring vanes is negligible, i.e., each vane is essentially an isolated airfoil. Table 1 illustrates this, presenting the incompressible flow, transverse gust lift coefficient for a cascade with a solidity of 0.1 and an isolated airfoil as predicted by Sears at the typical experimental reduced frequency value of 5.0.

DIGITAL PERIODIC DATA ACQUISITION

The steady-state pressure data are acquired with a 48 channel Scanivalve system. Under computer control, the Scanivalve is calibrated each time data is acquired, with compensation automatically made for variations in the zero and span output. As part of the steady-state data acquisition and analysis process, a root-mean-square error analysis is performed. The steady data are defined as the mean of 30 samples, with the 95% confidence intervals determined.

The time-variant data from the hot-wire probe and the dynamic pressure transducers are obtained under computer control by first conditioning their signals and then digitizing them with a high speed A-D system. This eight channel system is able to digitize signals simultaneously at rates to 5 MHz per channel, storing 2048 points per channel. In addition, after conditioning, the time-variant hot-wire and pressure transducer signals are monitored by a dynamic signal processor which can digitize, average, and Fourier decompose unsteady analog signals.

The time-variant data of interest are periodic, being generated at rotor blade passing frequency, with a digital ensemble averaging technique used for data

analysis. As will be discussed, the key to this technique is the ability to sample data at a pre-set time. This is accomplished by means of an optical encoder mounted on the rotor shaft. The microsecond range square wave voltage signal from the encoder is the time or data initiation reference which triggers the high speed A-D system.

In general, the time-variant signals from the hot-wire probe and the dynamic pressure transducers are comprised of three components: (1) a steady-state component, f^s; (2) the periodic component of interest, f^p; (3) a random fluctuating component, f^r.

$$f(t) = f^s + f^p(t) + f^r(t) \tag{1}$$

The steady-state signal component is measured independently. Thus, the time-variant transducer signal, s(t), is considered to be comprised of the sum of the periodic and random components.

$$s(t) = f^p(t) + f^r(t) \tag{2}$$

The periodic signal component is determined by a digital ensemble averaging technique based on the signal enhancement concept initially considered by Gostelow [1973]. The time-variant signal is sampled and digitized over a time frame that is greater than the periodic signal component characteristic time. With the same data initiation reference, i.e., the signal from the rotor shaft mounted optical encoder, a series of corresponding digitized signals is generated by repeating this signal sampling and digitization process. The time-variant signal ensemble average is then determined by averaging this series of digital data samples.

$$\langle s_j \rangle = (1/N) \sum_{n=1}^{N} s_{jn} \qquad j=1,2,...,m$$

or

$$\langle s_j \rangle = (1/N) \sum_{n=1}^{N} f_{jn}^{p} + (1/N) \sum_{n=1}^{N} f_{jn}^{r} \qquad j=1,2,...,m \qquad (3)$$

For a sufficiently large number of digital signals in the series, N >>1, the ensemble average of the random signal component is zero.

$$(1/N) \sum_{n=1}^{N} f_{jn}^{r} = 0 \qquad N>>1,\ j=1,2,...,m \qquad (4)$$

Thus, the periodic component of the time-variant signal, relative to the data initiation reference, is determined by this ensemble averaging technique.

$$\langle s_j \rangle = (1/N) \sum_{n=1}^{N} f_{jn}^{p} \qquad j=1,2,...,m \qquad (5)$$

The effect of averaging the time-variant digitized hot-wire and pressure signals has been considered. Figure 2 displays a time-variant pressure signal for 1 rotor revolution and averaged over 25, 50, 75, 100, and 200 rotor revolutions. The ensemble averaging significantly reduces the random fluctuations which are superimposed on the periodic signal, with the time-variant pressure and hot-wire signals essentially unchanged when averaged over 75 or more rotor revolutions. For the experiments described herein, 200 rotor revolutions are used to average the hot-wire and the airfoil mounted transducer signals.

DATA ANALYSIS

At each steady-state operating point, an averaged time-variant data set is obtained which consists of the hot-wire and the airfoil mounted transducer signals digitized at a rate of 200 kHz and ensemble averaged over 200 rotor revolutions. This sample rate allows approximately 91 points between each rotor blade at the

design compressor rotational speed. These rotor revolutions are not consecutive due to the finite time required for the A/D multiplexer system to sample the data and the computer to then read the digitized data.

Each of these digitized signals is Fourier decomposed into harmonics by means of a Fast Fourier Transform algorithm. Figure 3 shows the Fourier decomposition of a typical ensemble averaged time-variant pressure transducer signal. There is a dominant fundamental frequency at rotor blade passing, with much smaller amplitude higher harmonics and minimal nonharmonic content. Also shown is the digitized signal together with the first three harmonics and their sum. This summation is seen to yield a very good approximation to the original digitized signal, further demonstrating that the time-variant signal is primarily composed of the first three harmonics of the rotor blade passing frequency.

The first harmonic magnitude and phase angle referenced to the data initiation pulse are determined from the Fourier analysis of the data. To then relate the rotor wake generated velocity profiles with the first harmonic surface dynamic pressures on the instrumented downstream airfoil, the rotor exit velocity triangles are examined. The change in the rotor relative exit velocity which occurs as a result of the wake from a rotor blade is seen in Figure 1. This velocity deficit creates a change in the absolute velocity vector which is measured with the cross-wire probe. From this instantaneous absolute flow angle and velocity, the rotor exit relative flow angle and velocity, as well as the amplitude and phase of the perturbation quantities, are determined. The normal, v^+, and parallel, u^+, perturbation velocities are determined from the following relationships.

$$u^+ = V_{mean} - V\cos(\alpha - \alpha_{mean}) \; ; \qquad v^+ = V\sin(\alpha - \alpha_{mean}) \tag{6}$$

where V_{mean} is the mean flow velocity, V is the wake velocity, α is the wake absolute flow angle, and α_{mean} is the mean absolute flow angle.

The hot-wire probe is positioned upstream of the leading edge of the instrumented airfoil. To relate time based events as measured by this hot-wire probe to the unsteady pressures on the airfoil surfaces, the following assumptions are made: (1) the wakes are identical at the hot-wire and the instrumented airfoil leading edge plane, and (2) the wakes are fixed in the relative frame. At a steady operating point, the hot-wire data are analyzed to determine the absolute flow angle and the rotor exit relative flow angle. Using the above two assumptions, the wake is located relative to the hot-wire and the leading edges of the instrumented airfoil suction and pressure surfaces. From this, the times at which the wakes are present at various locations are determined. The incremental times between occurrences at the hot-wire and the instrumented airfoil leading edge plane are then related to phase differences between perturbation velocities and the airfoil surface.

The final form of the unsteady pressure data defines the chordwise variation of the first harmonic pressure difference across the chordline of a stator vane, and is presented as a nondimensional complex unsteady pressure difference across the airfoil chord in the format of the magnitude and the phase lag referenced to a transverse gust at the airfoil leading edge.

PREDICTED GUST RESPONSE

An unsteady aerodynamic gust response model which considers steady aerodynamic loading is needed to provide a baseline for accurate interpretation of the unsteady data. This is accomplished utilizing the complete first order model, i.e., the thin airfoil approximation is not used, and locally analytical solution developed by Chiang and Fleeter. This model considers the flow of a two-dimensional unsteady aerodynamic gust convected with the mean flow past a thick, cambered, airfoil at finite angle of attack, α_o, as schematically depicted in Figure 4. The periodic gust amplitude and harmonic frequency are denoted by A and ω, respectively. The two-dimensional gust propagates in the direction $\mathcal{K} = k_1\hat{i} + k_2\hat{j}$, where k_1 is the reduced frequency and k_2 is the transverse gust wave number, i.e., the transverse component of the gust propagation direction vector.

The unsteady flow field is considered to be rotational, and is linearized about the full steady potential flow past the airfoil. Thus, the effects of airfoil thickness and camber as well as mean flow angle of attack are completely accounted for through the mean potential flow field. The steady potential flow field and the unsteady potential flow are individually described by Laplace equations, with the unsteady potential decomposed into circulatory and noncirculatory parts. The steady velocity potential is independent of the unsteady flow field. However, the strong dependence of the unsteady aerodynamics on the steady effects of airfoil geometry and angle of attack are manifested in the coupling of the unsteady and steady flow fields through the unsteady boundary conditions.

A locally analytical solution is then developed. In this method, the discrete algebraic equations which represent the flow field equations are obtained from analytical solutions in individual grid elements. A body fitted computational grid is utilized, Figure 5, which also shows the profile of the airfoil. General analytical solutions to the transformed Laplace equations are developed by applying these solutions to individual grid elements, i.e., the integration and separation constants are determined from the boundary conditions in each grid element. The complete flow field is then obtained by assembling these locally analytical solutions.

RESULTS

A series of experiments were performed to investigate and quantify the rotor wake generated high reduced frequency gust aerodynamic response of an airfoil, including the effects of airfoil steady loading, the gust forcing function waveform, and steady flow separation. To aid in the interpretation of these unique unsteady aerodynamic gust data, appropriate predictions from the classical Sears flat plate model and the thick, cambered airfoil model of Chiang and Fleeter are also presented.

NONSEPARATED FLOW

A low steady aerodynamic loading condition is established by setting the airfoil at an angle of attack of 0.06 degrees. The data defining the airfoil surface static pressure distributions are presented in Figure 6. There is a smooth chordwise pressure variation on each airfoil surface, with no indication of flow separation.

Also, there is generally good correlation between the data and the inviscid Chiang-Fleeter cambered airfoil steady flow prediction, with the exception of the airfoil leading edge region.

The aerodynamic gust waveform is characterized by the ratio of the first harmonic chordwise to normal gust component $(\hat{u}^+/\hat{v}^+)$. The effect of the gust waveform on the unsteady aerodynamic response of the airfoil is considered by establishing compressor configurations such that the airfoil angle of attack and steady surface static pressure distributions are maintained per Figure 6, but with the gust component ratio taking on values of 0.19, 0.35, and 0.53, Figure 7.

The effect of the aerodynamic gust waveform on the resulting unsteady pressure difference data is shown in Figure 8. The profile of the airfoil and, thus, the surface steady loading distribution, has a significant effect on the unsteady aerodynamic gust response. In particular, the chordwise variation of both the magnitude and the phase of the unsteady pressure difference generally exhibit much better correlation with the cambered airfoil predictions than with those from the flat plate model. The magnitude data exhibit good trendwise agreement with the cambered airfoil prediction, with this model typically overpredicting the magnitude of the pressure difference on the front 30% of the airfoil chord. This is due to the strong coupling of the unsteady prediction on an accurate representation of the steady flow field. As previously noted, the steady flow prediction did not exhibit good correlation with the steady airfoil surface static pressure data over the front part of the airfoil. Hence the poor unsteady data-prediction correlation in this region. Also, the ratio of the first harmonic gust

components, $(\hat{u}^+/\hat{v}^+)$, has an effect on both the magnitude and phase of the unsteady pressure difference, although the general chordwise variation of these data is not affected.

To investigate the effect of steady airfoil loading on the aerodynamic gust response, the airfoil angle of attack was increased to 7.6 degrees. The static pressure distributions on the airfoil suction and pressure surfaces together with the steady Chiang-Fleeter predictions are shown in Figure 9. Relatively good correlation is obtained, although not quite as good as at the lower angle of attack. Again, the correlation between the data and the predictions is not very good in the leading edge region of the airfoil.

The resulting unsteady aerodynamic gust response of the airfoil together with the flat plate and cambered airfoil predictions for a gust first harmonic component ratio of 0.22 are shown in Figure 10. It should be noted that the reduced frequency, k_1, for these intermediate angle of attack data is increased as compared to the previously presented low angle of attack data. This is associated with the use of a low speed research compressor to generate the aerodynamic gust forcing function. Again, the correlation of these complex unsteady pressure data with the cambered airfoil predictions is much better than with the flat plate model. In particular, the chordwise variations of both the magnitude and phase of the unsteady pressure difference data exhibit good trendwise agreement with the cambered predictions. However, the phase correlation is not quite as good at this loading level, with the magnitude data now overpredicted over the airfoil. This is again associated with the poor correlation

AD-A192 169 RESEARCH ON AERO-THERMODYNAMIC DISTORTION INDUCED STRUCTURAL DYNAMIC RESP..(U) PURDUE UNIV LAFAYETTE IND THERMAL SCIENCES AND PROPULSION CEN.. S FLEETER 2/3

UNCLASSIFIED 15 JAN 88 ME-TSPC-TR-88-10 AFOSR-TR-88-0043 F/G 1/1 NL

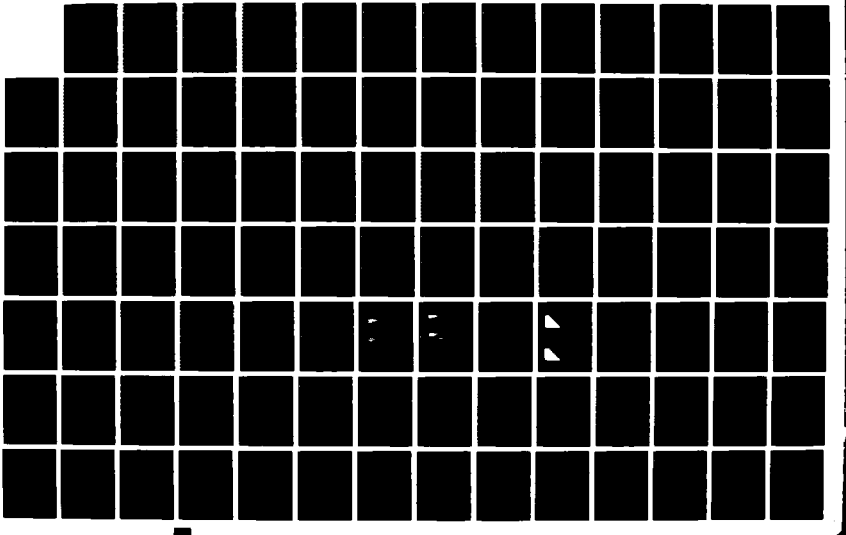

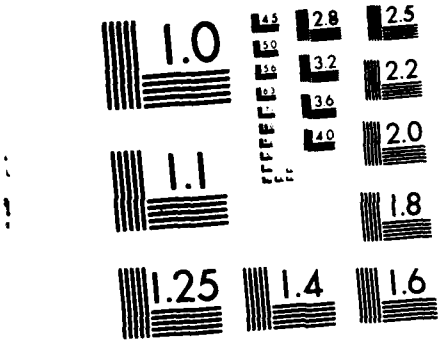

surface pressure data and the model over the front part of the airfoil and the dependence of the unsteady predictions on the steady flow field.

SEPARATED FLOW

Steady flow separation at approximately 35% of the airfoil suction surface was established by increasing the angle of attack to 14 degrees, Figure 11. The effects of this flow separation on the unsteady aerodynamic gust response are investigated by comparing the resulting separated flow gust data with corresponding data obtained at the previous intermediate airfoil angle of attack of 7.6 degrees where the steady lift coefficient is nearly the same but the steady flow is not separated. Also, both the parallel and normal gust components are maintained to be nearly identical for these two configurations, Figure 12, with the ratio of the first harmonic gust components being 0.218.

The resulting first harmonic unsteady pressure difference data are presented in Figure 13. Also shown is the nonseparated flat plate prediction of Sears. The cambered airfoil prediction is not presented because of the strong dependence of the cambered airfoil predictions on the steady flow field and the inappropriateness of the inviscid steady model for separated flow. The magnitude data for the separated flow case show somewhat different trends than that for the nonseparated flow in the leading and trailing edge regions of the airfoil. For the separated flow configuration, the magnitude data are nearly constant over the front 15% of the airfoil, whereas the nonseparated data and the prediction indicate a decreasing amplitude. Aft of 15% chord, the magnitude data show analogous trends, with

both the separated and nonseparated data decreasing with increasing chordwise position and attaining a minimum pressure amplitude value at 30% chord, similar to the previous results. The magnitude data for both cases then gradually increase to values that are greater than the prediction near midchord, with the nonseparated data being lower in amplitude up to this point due to the larger steady surface pressure differences between the suction and pressure surfaces. Both data sets then decrease with increasing chordwise position, with the separated data decreased in amplitude relative to the prediction and the nonseparated data. This is a result of the increased steady loading due to the separation in this region.

The phase data for the separated flow configuration have different trends than the nonseparated data and the flat plate prediction near the separation point and in the airfoil trailing edge region. Over the front 20% of the airfoil, the data and the prediction show analogous trends of being nearly constant, with the separated data increased relative to the prediction and the nonseparated data. Aft of 20% chord, the separated phase data increase whereas the nonseparated data decrease relative to the prediction. In the separated flow region, both the separated and nonseparated data show similar trends. However, at 70% chord the separated phase data jump to values larger than the prediction and increase with further chordwise position. On the other hand, the phase data for the nonseparated case show a gradual increase. Thus, separation affects both the magnitude and phase of the dynamic pressure difference data, with the primary effect being on the phase.

To further investigate these separation effects, individual suction surface time-variant pressure signals and their Fourier decompositions are considered. Figure 14

presents a typical unsteady pressure signal upstream of the separation point and the unsteady pressure signal at the same chordwise location for a configuration where the flow is not separated. It is clear that the downstream separation point affects both the amplitude and waveform of the unsteady pressure. This becomes more apparent in the spectrums of these nonseparated and separated unsteady pressures, Figure 15. The separated flow unsteady pressure has a much broader spectrum than the nonseparated one. This pressure field distortion is most probably due to the oscillation of the separation point generated by the periodic aerodynamic gusts. This would occur at the same frequency as the forcing function, but would be out of phase with it.

A completely different trend is found within the separated flow region. Figures 16 and 17 present the unsteady pressure signals for the separated and nonseparated flow cases for the same chordwise position and their resulting Fourier decomposition. There is little difference between the separated and nonseparated unsteady pressures. However, the nonseparated unsteady pressure has slightly more distortion which results in the higher order harmonics of the Fourier spectrum. This distortion is due to the steady flow turning and the aerodynamic loading of the airfoil. Within the separation zone, where there is a constant steady static surface pressure, the pressure fluctuations generated by the separation point oscillation are negligible, in contrast to the effect upstream of the separation point. Such a phenomenon was also noted by Mabey [1972]. The effect of the separation point oscillation is probably damped out by the mass of recirculating fluid within the separated flow region. Thus, the unsteady pressure within the separation zone

is primarily responding to the aerodynamic forcing function.

The influence of the aerodynamic gust forcing function on the airfoil unsteady aerodynamics when the steady flow is separated is considered by establishing an additional airfoil configuration where the steady loading is nearly the same, having an angle of attack on the order of 14.0 degrees, but the ratios of the gust components are different. The airfoil steady surface static pressure distributions for these two configurations are shown in Figure 18. The airfoil pressure and suction surfaces have nearly identical distributions, with a fully separated flow starting at approximately 35% of the chord. Figure 19 shows the aerodynamic forcing function to the airfoil. The first harmonic ratios of the gust components, $(\hat{u}^+ / \hat{v}^+)$, are 0.218 and 0.186, with both the normal, $\hat{v}^+$, and the parallel, $\hat{u}^+$, gust components having different values.

The first harmonic unsteady pressure difference data for these two configurations, with the nonseparated flat plate prediction as a reference, are presented in Figure 20. The magnitude data indicate analogous trends over the entire airfoil chord, with the 0.186 $(\hat{u}^+ / \hat{v}^+)$ data being decreased in value relative to both the prediction and the 0.218 $(\hat{u}^+ / \hat{v}^+)$ data. In the trailing edge region the data correlate well with each other and are decreased relative to the prediction due to the high steady loading in this region. The phase data show different trends than the previous high loading cases and with each other near the separation point and the trailing edge. Over the front 25% of the chord, the phase data show the same trends, with the 0.186 $(\hat{u}^+ / \hat{v}^+)$ data being in closer agreement with the prediction. At 30% chord, the 0.218 $(\hat{u}^+ / \hat{v}^+)$ data increase in phase whereas the

0.186 ($\hat{u}^+ / \hat{v}^+$) data continue to show good trendwise correlation with the prediction. From 40% chord to 60% chord, the phase data correlate with each other but are decreased in value with respect to the prediction. Aft of 60% chord the 0.218 ($\hat{u}^+ / \hat{v}^+$) phase data are increased relative to the prediction and increase with increasing chord. However, the phase data for 0.186 ($\hat{u}^+ / \hat{v}^+$) first increase in phase and then indicate a slight decrease with increasing chordwise position.

SUMMARY AND CONCLUSIONS

A series of experiments have been performed to investigate and quantify the unsteady aerodynamic response of an airfoil to a high reduced frequency gust, including the effects of the gust forcing function waveform, airfoil steady loading, and steady flow separation. This was accomplished by utilizing an axial flow research compressor to experimentally model the high reduced frequency gust forcing function, with the last stage stator vane row replaced with isolated instrumented airfoils. Appropriate data are correlated with predictions from flat plate and cambered airfoil convected gust models.

At low and intermediate airfoil angles of attack with the steady flow not separated, the profile of the airfoil and, thus, the surface steady loading distribution, was shown to have a significant effect on the unsteady aerodynamic gust response of the airfoil. Also, the ratio of the first harmonic gust components affects both the magnitude and phase of the unsteady pressure difference, although the general chordwise variation of these data was not affected. In adition, the chordwise variation of both the magnitude and the phase of the unsteady pressure

difference data generally exhibit much better correlation with the cambered airfoil predictions than with those from the flat plate model. However, the cambered airfoil model typically overpredicts the pressure difference magnitude on the front part of the airfoil. This is due to the strong coupling of the unsteady prediction on an accurate representation of the steady flow field, with the steady flow prediction not exhibiting good correlation with the steady airfoil surface static pressure data over the front part of the airfoil.

The steady flow separation was shown to have a significant influence on the unsteady aerodynamics on the airfoil surface upstream of the separation point and also in the trailing edge region. Also, the separation affects both the magnitude and the phase of the unsteady pressure difference data, with the primary effect being on the phase data. Consideration of the individual suction surface unsteady pressure signals and their Fourier decompositions revealed that: (1) the separation affects the magnitude and the waveform of the unsteady pressure upstream of the separation point as well as its harmonic content, possibly a result of an oscillation of the separation point due to the harmonic gust; (2) the pressure signals in the separated flow region and the corresponding signals with the flow not separated, i.e., signals at the same chordwise position, exhibit only small differences; (3) in the separated flow region, there is a constant steady static surface pressure, with the pressure fluctuations generated by the oscillation of the separation point negligible.

ACKNOWLEDGEMENT

Support of this experimental research program by the Air Force Office of Scientific Research, Dr. James Wilson program manager, is gratefully acknowledged.

REFERENCES

Atassi, H.M., "The Sears Problem for a Lifting Airfoil Revisited-New Results," *Journal of Fluid Mechanics*, 141, 1984.

Carstens, V., "Theoretical Investigations on a Two-Dimensional Cascade in Incompressible Flow," *Symposium on Unsteady Aerodynamics of Turbomachines and Propellers*, Cambridge, 1984.

Chi, R.M., "Separated Flow Unsteady Aerodynamic Theory," *AIAA Journal of Aircraft*, Vol. 22, No. 11 November 1985.

Chiang, H.D. and Fleeter, S., "Prediction of Loaded Airfoil Unsteady Aerodynamic Gust Response by a Locally Analytical Method," *International Journal of Mathematical Modeling*, accepted for publication.

Ericsson, L.E., and Reding, J.P., "Unsteady Airfoil Stall, Review and Extension," *AIAA Journal*, Vol. 8 August 1981.

Goldstein, M.E. and Atassi, H., "A Complete Second-Order Theory for the Unsteady Flow about an Airfoil due to a Periodic Gust," *Journal of Fluid Mechanics*, 74, 1976.

Gostelow, J.P., "A New Approach to the Experimental Study of Turbomachinery Flow Phenomena," *ASME Journal of Engineering for Power*, January 1977.

Holmes, D.W., "Lift Measurements on an Airfoil in Unsteady Flow," *ASME Paper 73-GT-41*, 1973.

Horlock, J.H., "Fluctuating Lift Forces on Airfoils Moving Through Transverse and Chordwise Gusts," *ASME Journal of Basic Engineering*, Vol. 90, No. 4, December 1968.

Kussner, H.G., "Das Zweidimensionale Problem der Beliebig Bewgegten Tragflache unter Berucksichtigung von Patialbewegungen der Flussigkeit, *Luftfahrtorsch*, 17, 355, 1940.

Lorber, P.F. and Carta, F.D., "Airfoil Dynamic Stall at Constant Pitch Rate an High Reynolds Number," *AIAA Paper 87-1329*, 1987.

Mabey, D.G., "Analysis and Correlation of Data on Pressure Fluctuations in Separated Flow," *AIAA Journal of Aircraft*, Vol. 9, No. 9, December 1972, pp. 642-645.

Naumann, H. and Yeh, H., "Lift and Pressure Fluctuations of a Cambered Airfoil Under Periodic Gusts and Applications to Turbomachinery," *ASME Paper* 72-GT-30, 1972.

Ostdiek, F.R., "A Cascade in Unsteady Flow," *AFAPL-TR-76-115*, 1976.

Satyanarayana, B., Gostelow, J.P., and Henderson, R.E., "A Comparison Between Experimental and Theoretical Fluctuating Lift on Cascades at Low Frequency Parameters", *ASME Paper 74-GT-78, 1974.*

Sears, W.R., "Some Aspects of Non-Stationary Airfoil Theory and its Practical Application," *Journal of the Aeronautical Sciences*, 8, 104, 1941.

Sisto, F. and Perumal, P.V.K., "Lift and Moment Predictions for an Oscillating Airfoil with a Moving Separation Point," *ASME Journal of Engineering for Power*, Vol. 96, No. 4 October 1974.

Theodorsen, T., "General Theory of Aerodynamic Instability and the Mechanism of Flutter," *NACA TR 496*, 1935.

Woods, L.C., "Aerodynamic Forces on an Oscillating Airfoil Fitted with a Spoiler," *Proceedings of the Royal Society of London*, Series A, No. 239, 1957.

Yashima, S. and Tanaka, H., "Torsional Flutter in Stalled Cascade," *ASME Paper 77-GT-72*, 1977.

	Re $[\hat{C}_\ell]$	Im $[\hat{C}_\ell]$
C/S = 0.10	-0.0809	-0.1575
ISOLATED AIRFOIL (C/S = 0)	-0.0812	-0.1596

Table 1. Predicted unsteady gust response for an isolated airfoil and a low solidity cascade (k = 5.0)

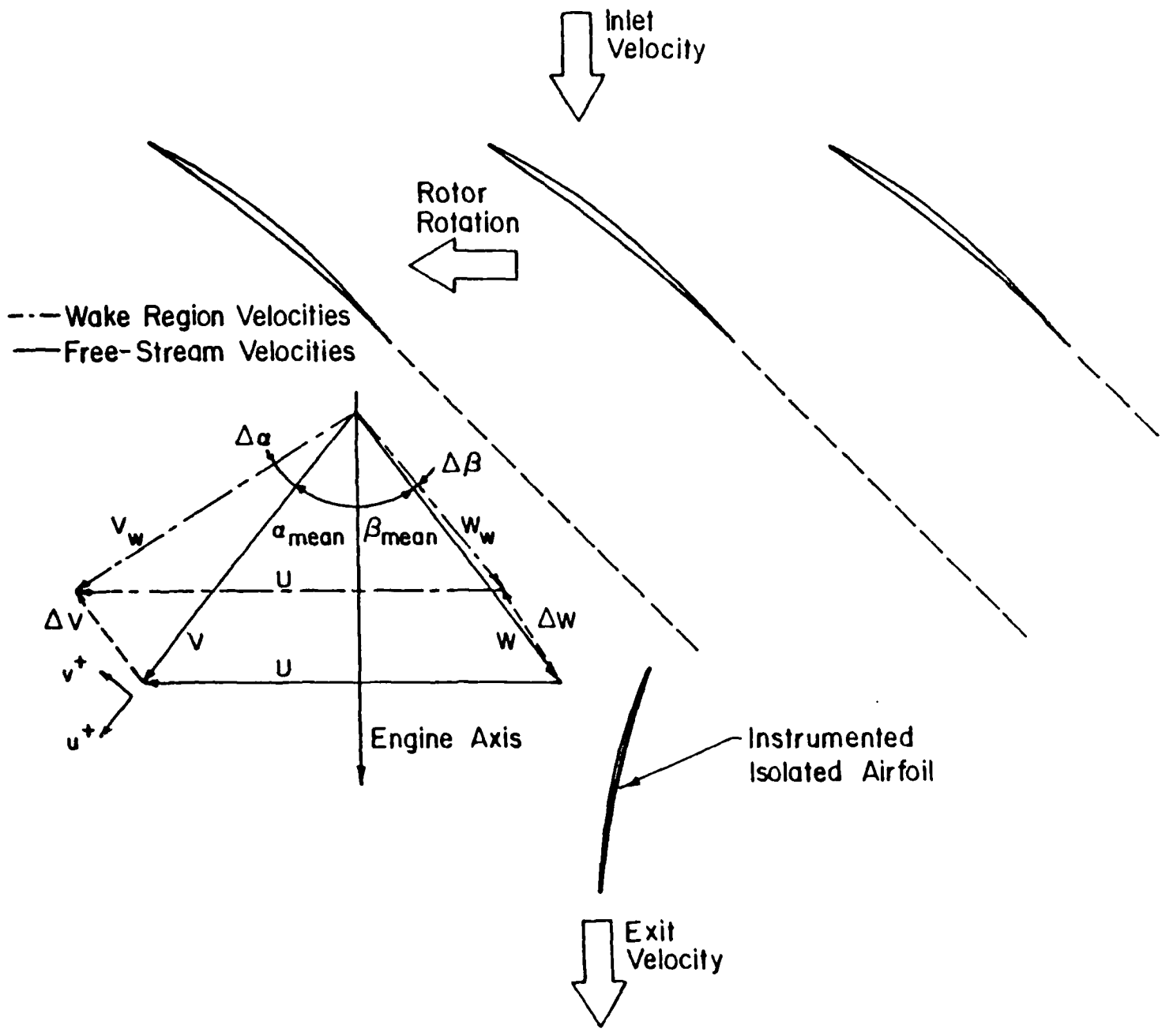

Figure 1. Schematic of flow field

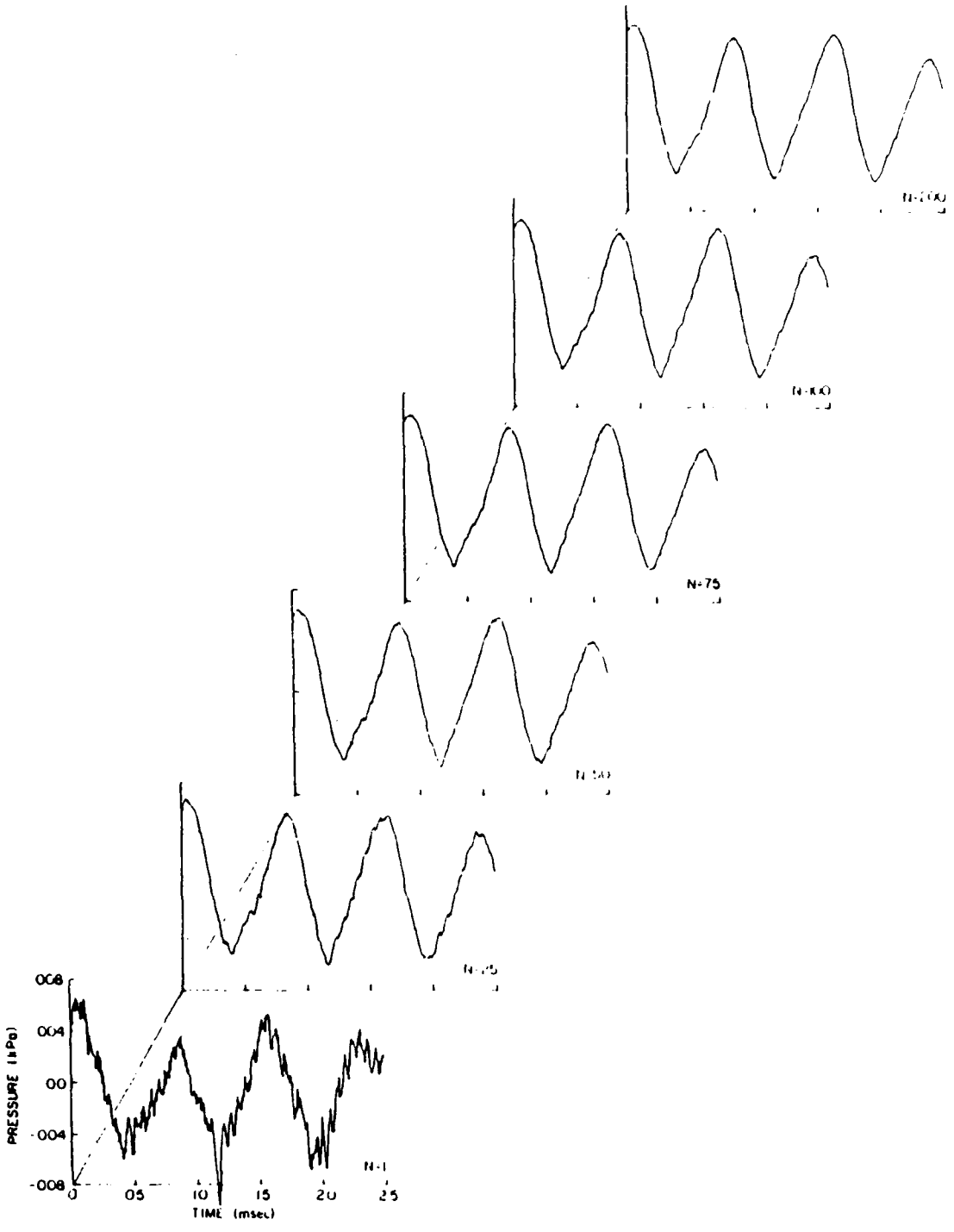

Figure 2. Ensemble averaging of unsteady pressure signals

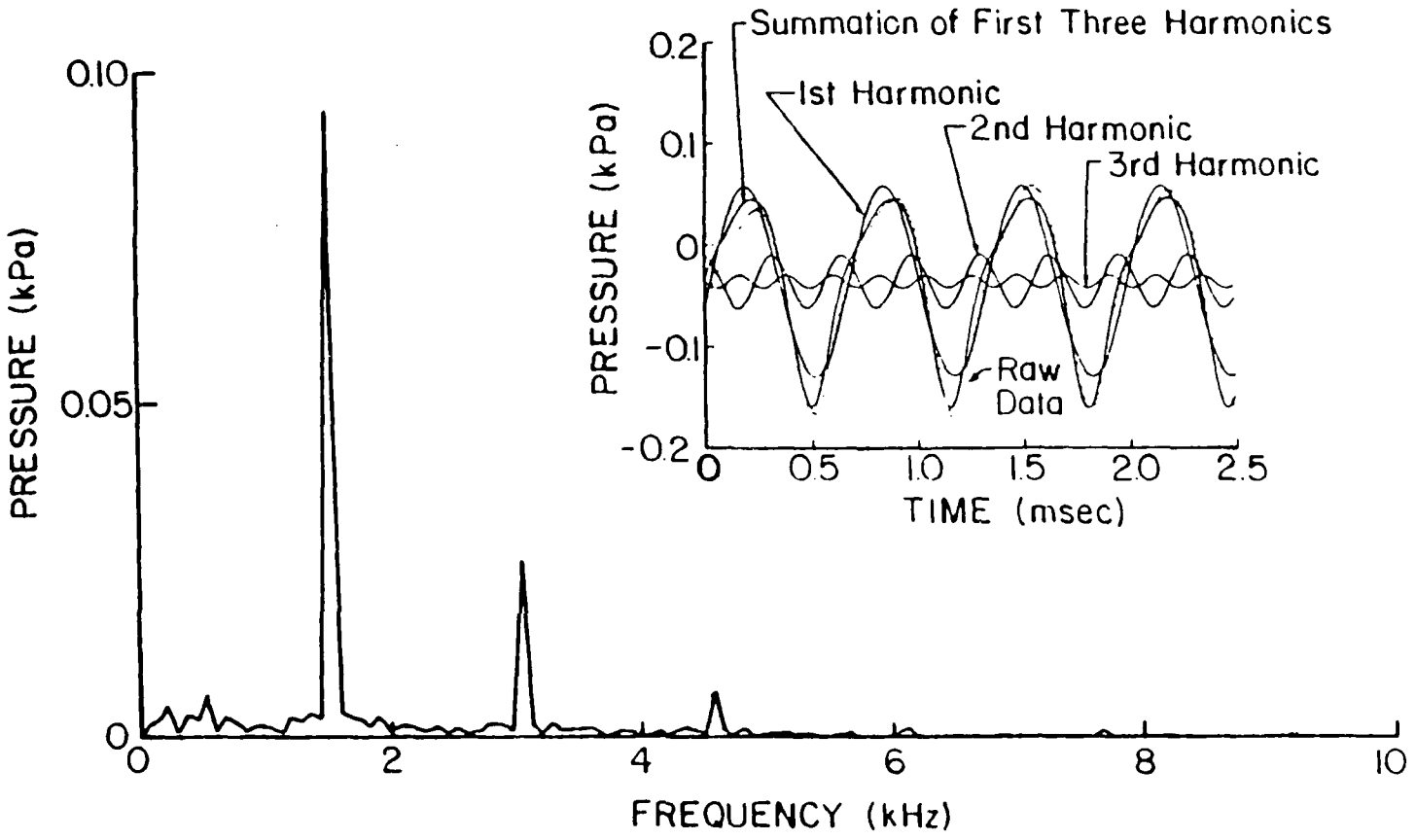

Figure 3. Fourier decomposition of averaged pressure signal

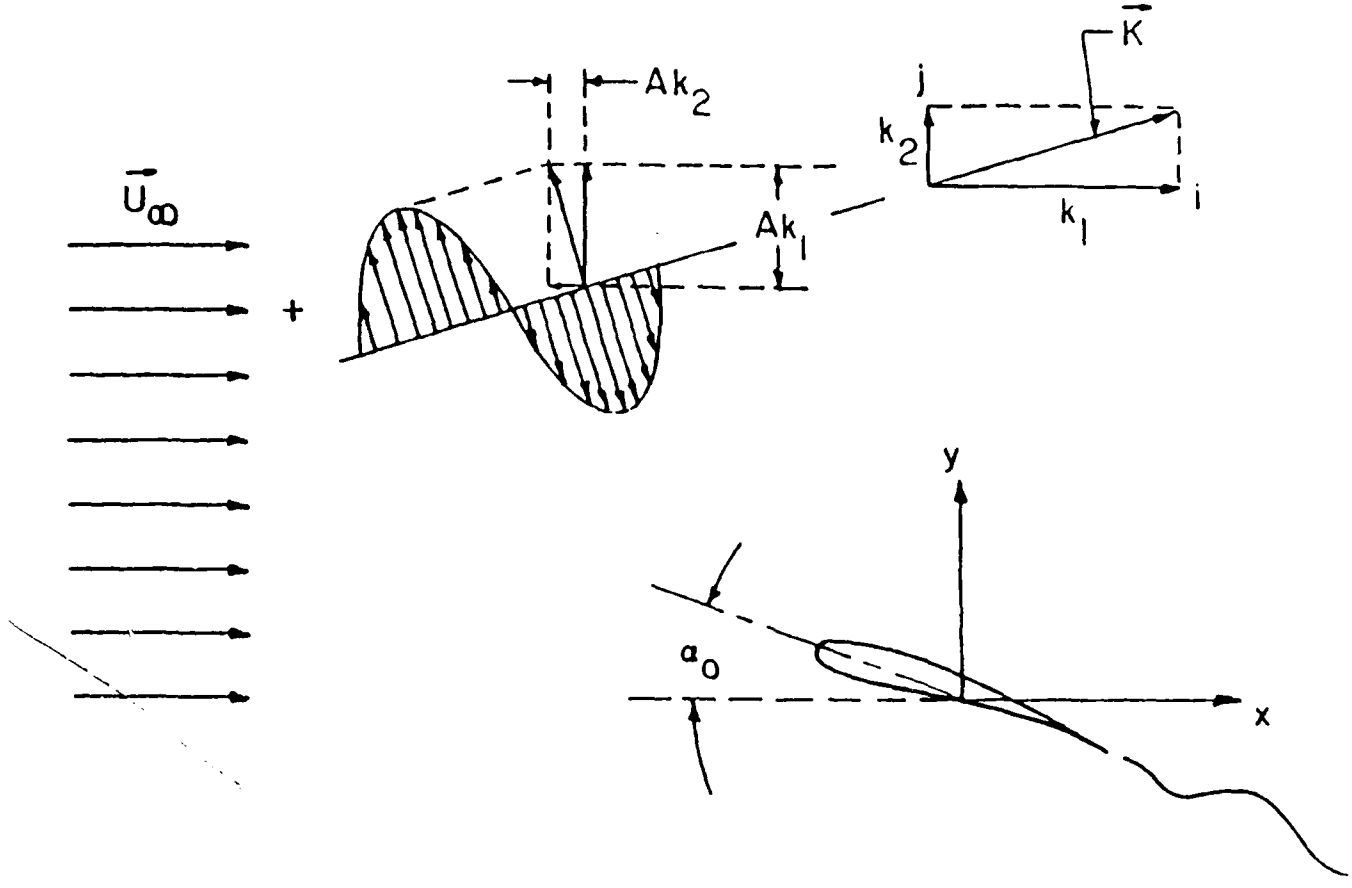

Figure 4. Flow of a two-dimensional gust past a cambered airfoil at angle of attack

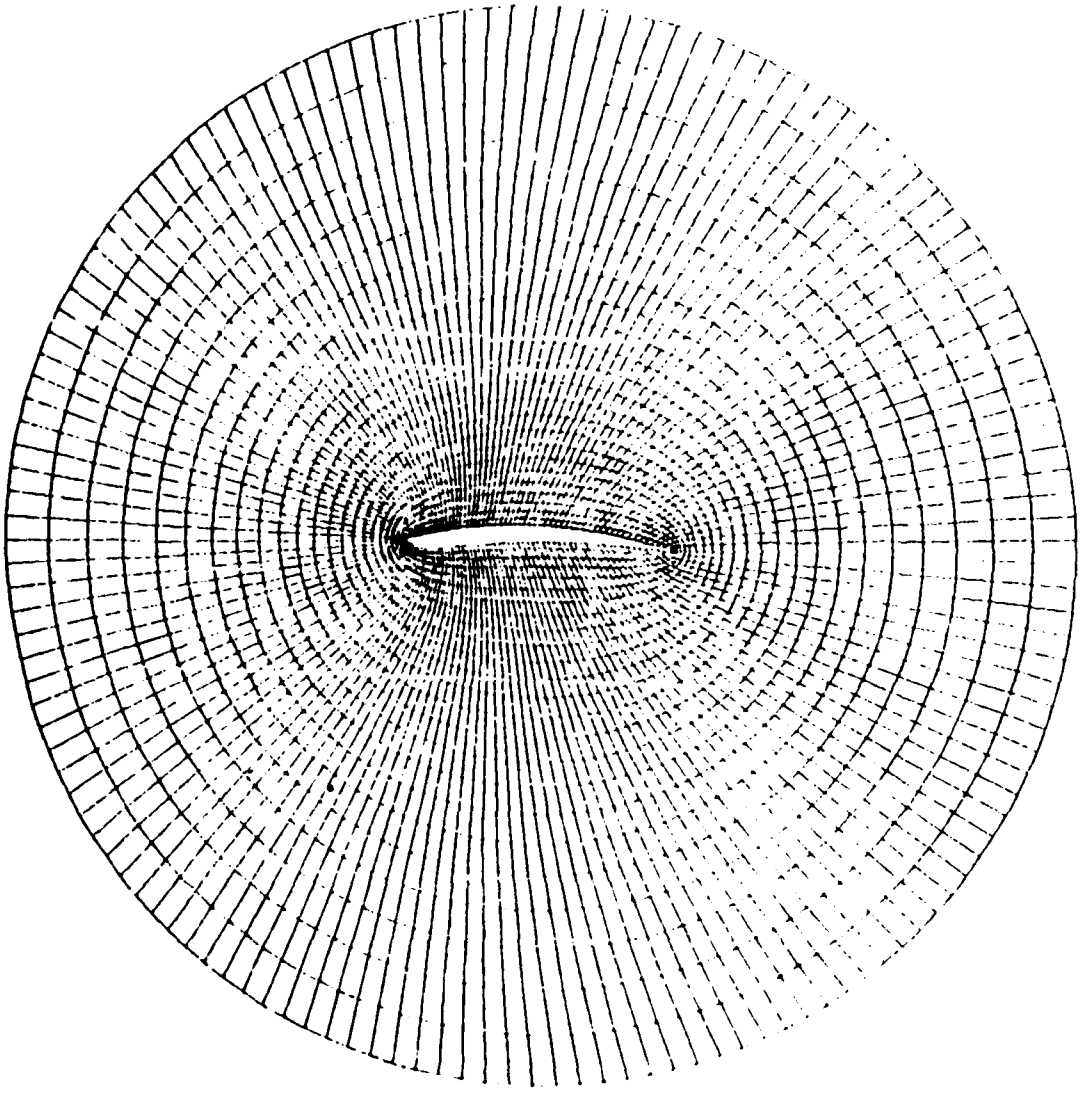

Figure 5. Airfoil profile and computational grid

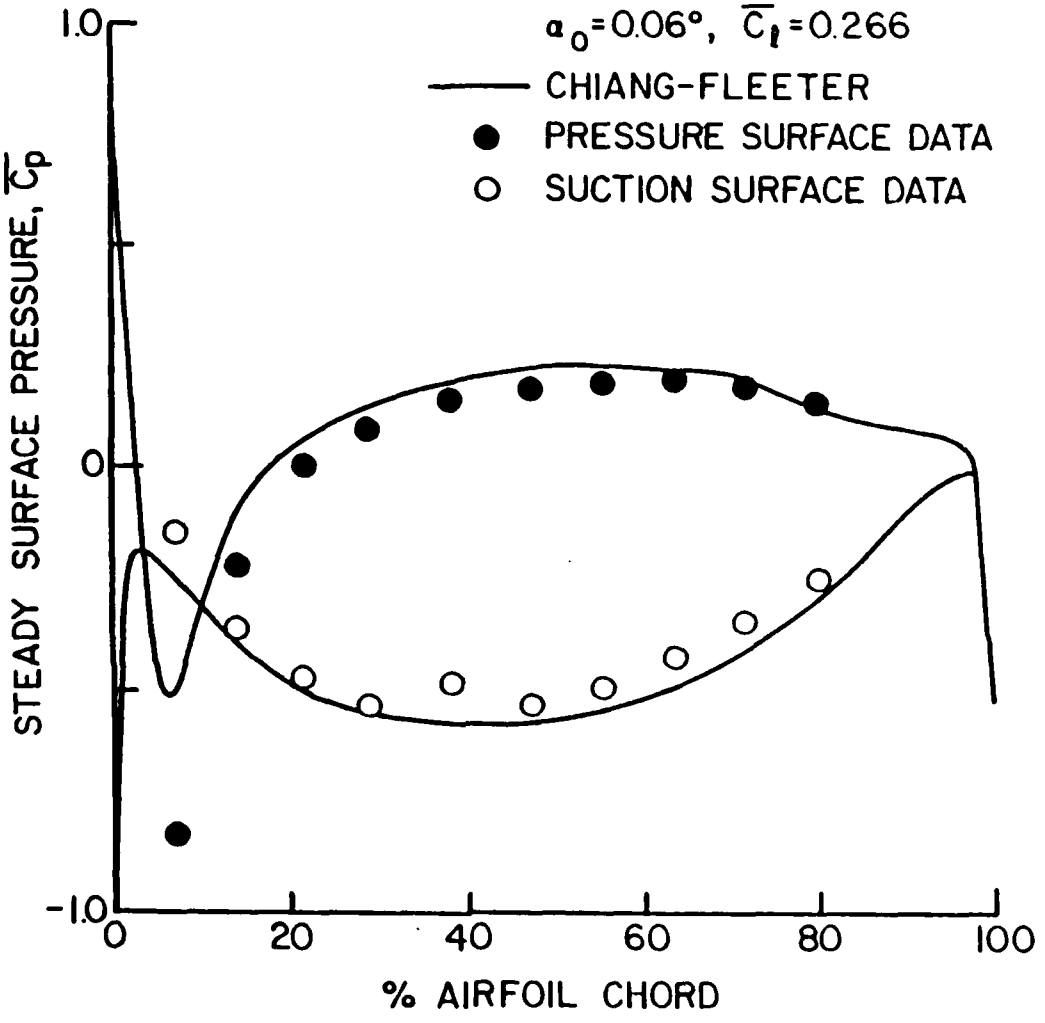

Figure 6. Steady airfoil surface static pressure distributions at low loading

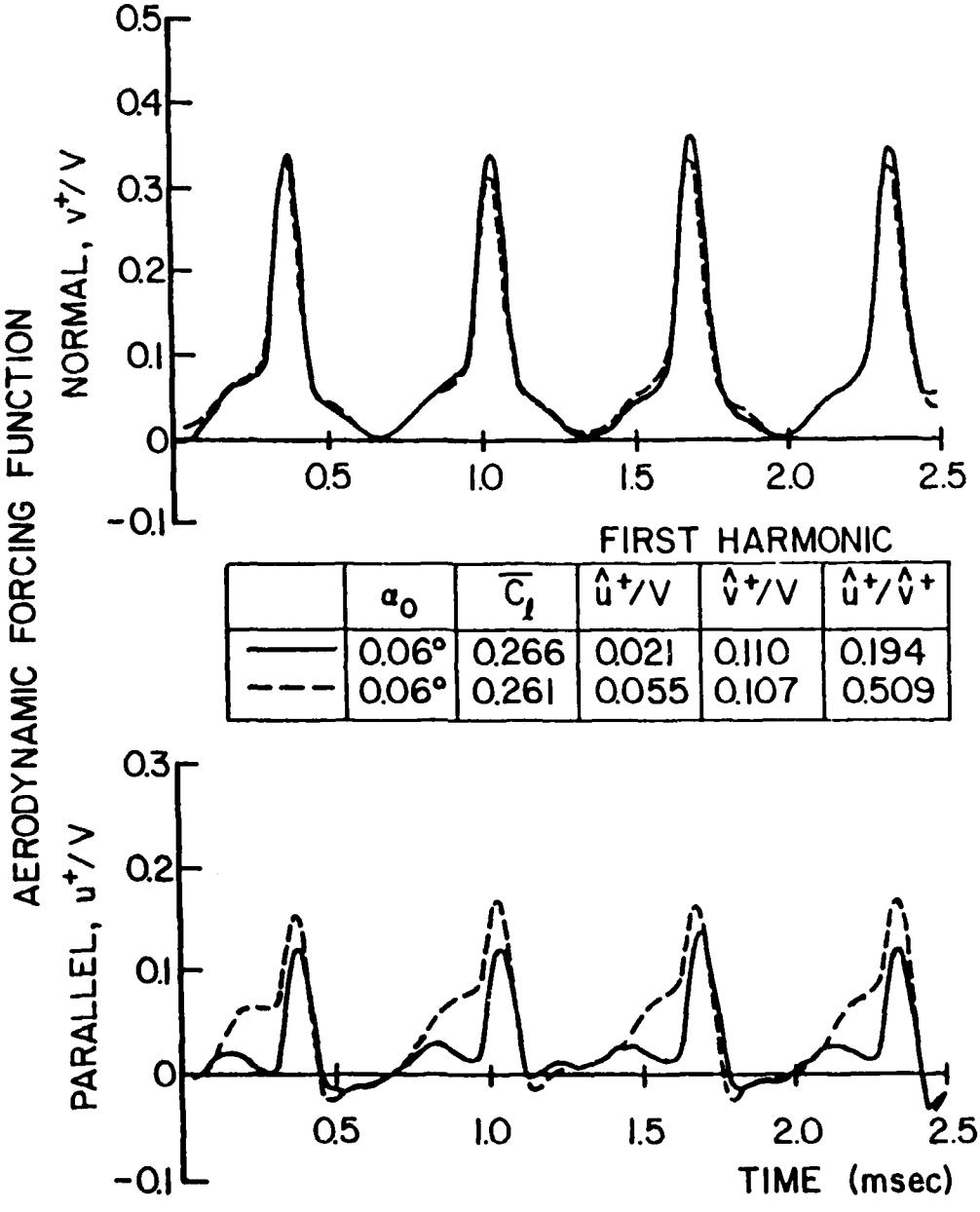

	α_0	$\overline{C_l}$	$\hat{u}^+/V$	$\hat{v}^+/V$	$\hat{u}^+/\hat{v}^+$
———	0.06°	0.266	0.021	0.110	0.194
- - -	0.06°	0.261	0.055	0.107	0.509

Figure 7. Gust Aerodynamic forcing functions at low steady loading

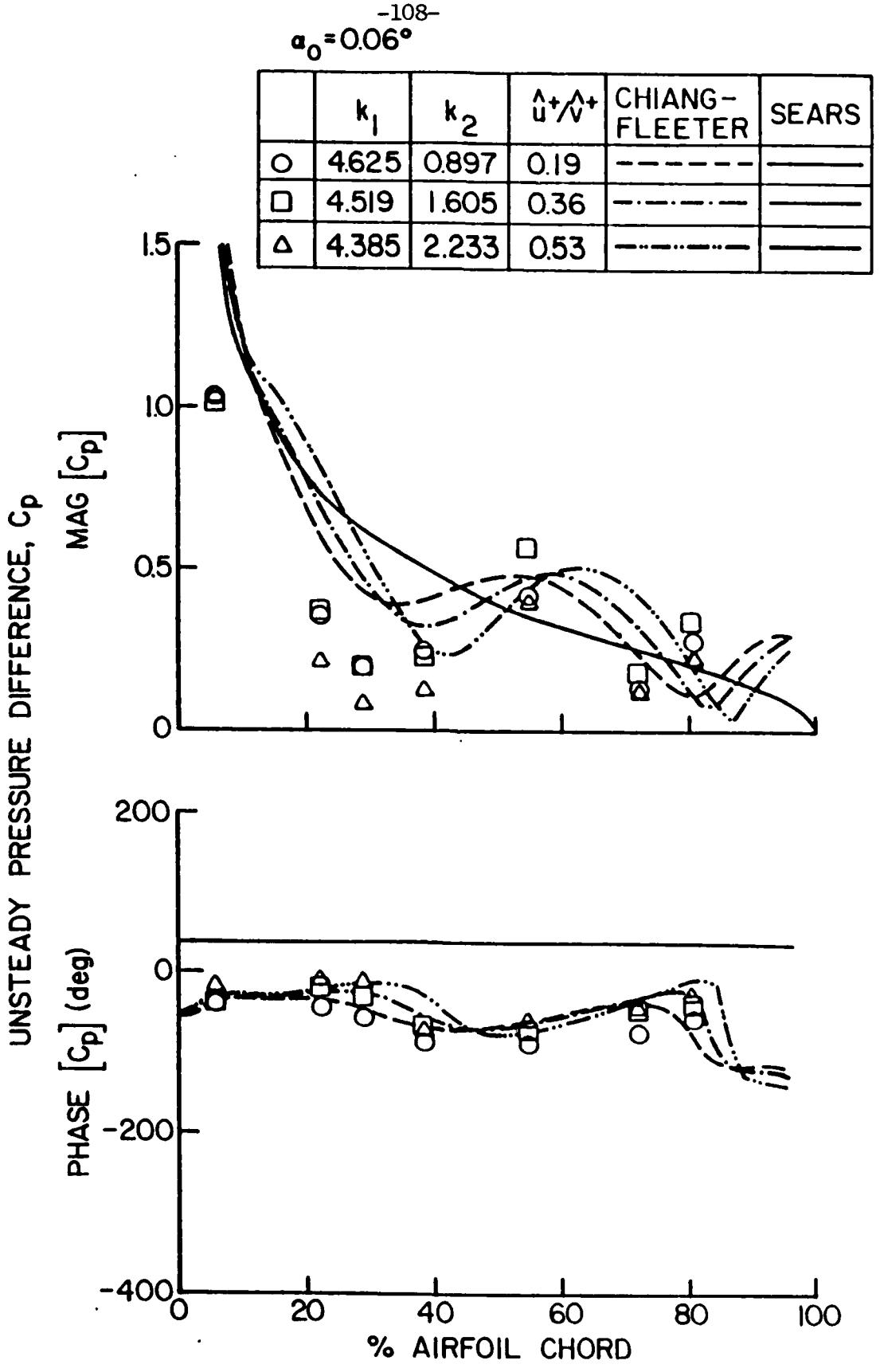

Figure 8. Effect of gust waveform on unsteady airfoil surface pressure difference at low steady loading

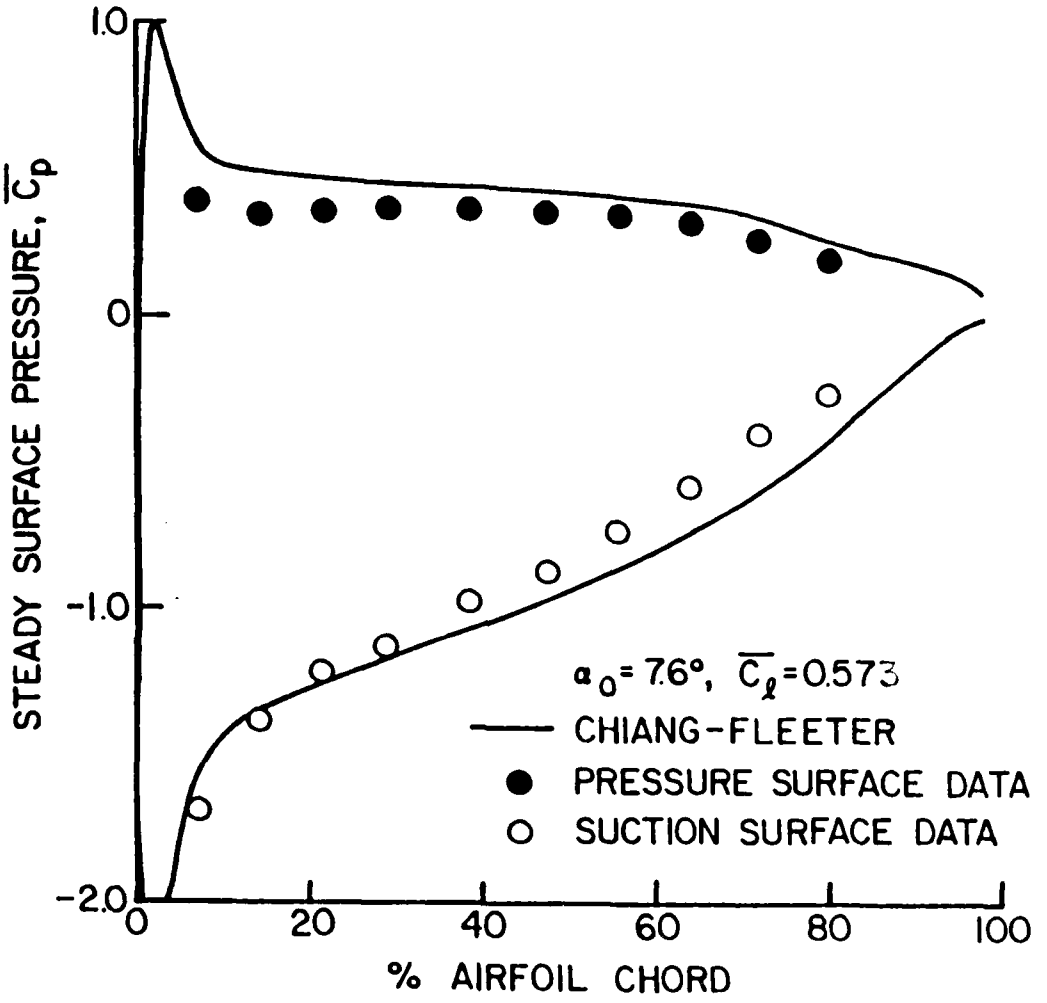

Figure 9. Steady airfoil surface static pressure distributions at intermediate loading

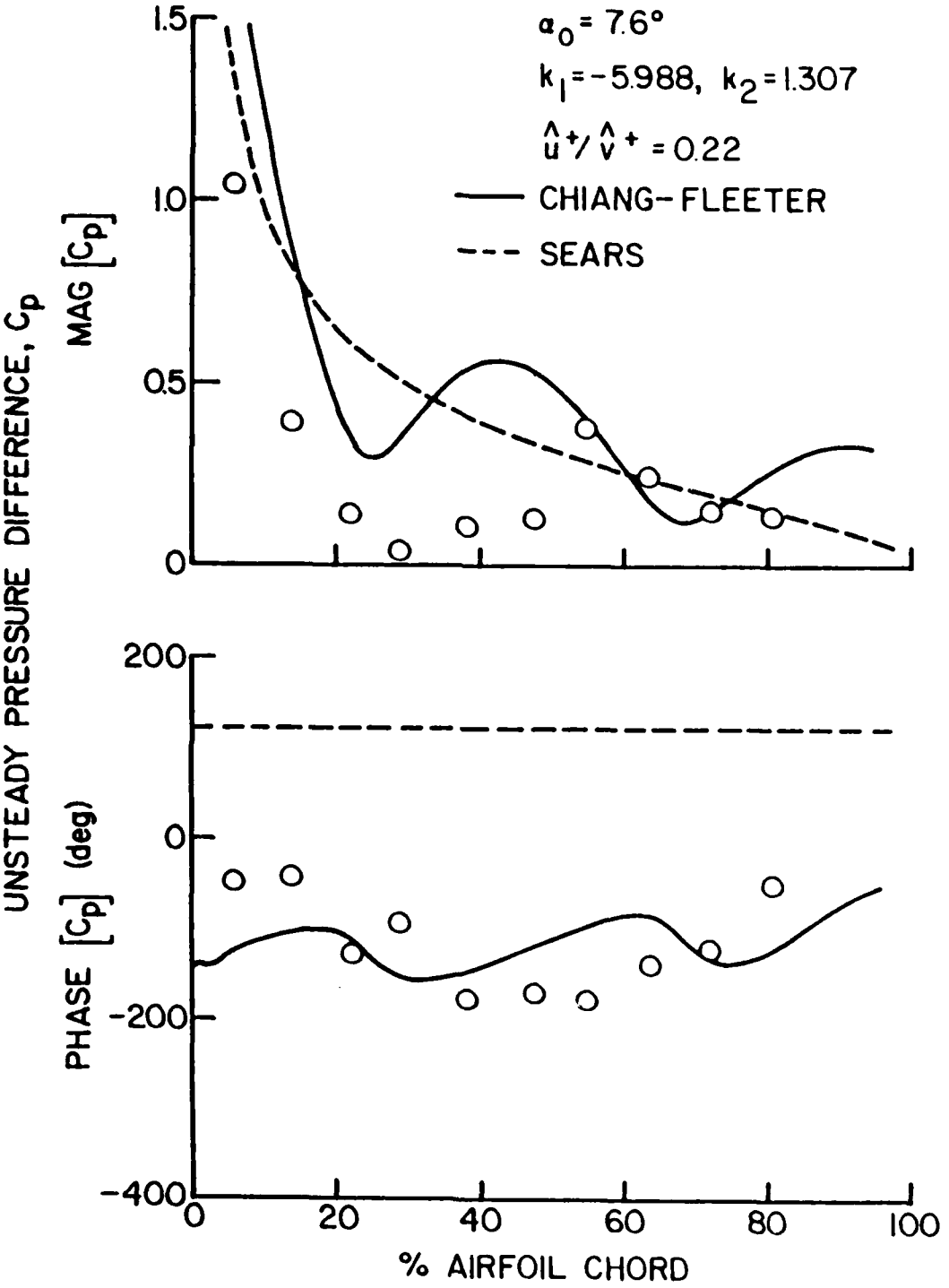

Figure 10. Unsteady airfoil surface pressure differences at intermediate loading with attached flow

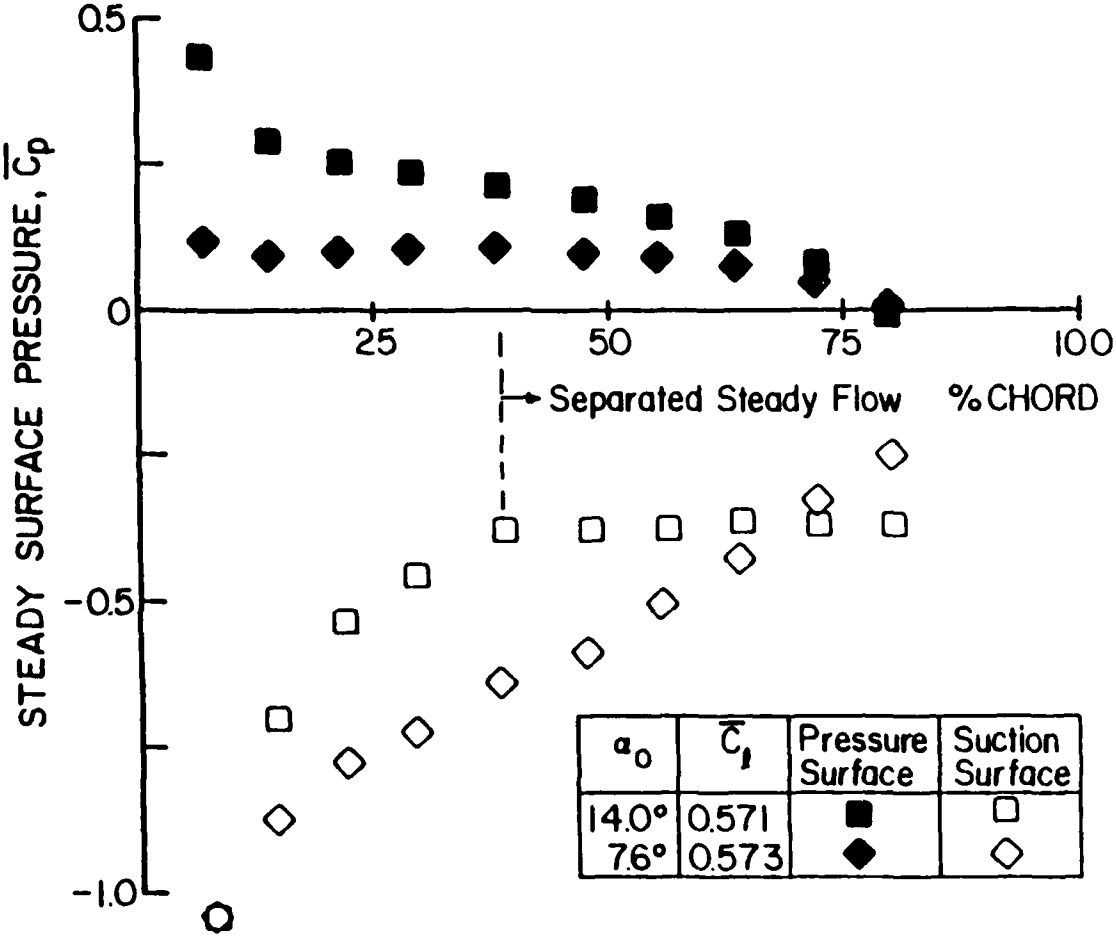

Figure 11. Effect of suction flow separation on steady surface static pressure distributions

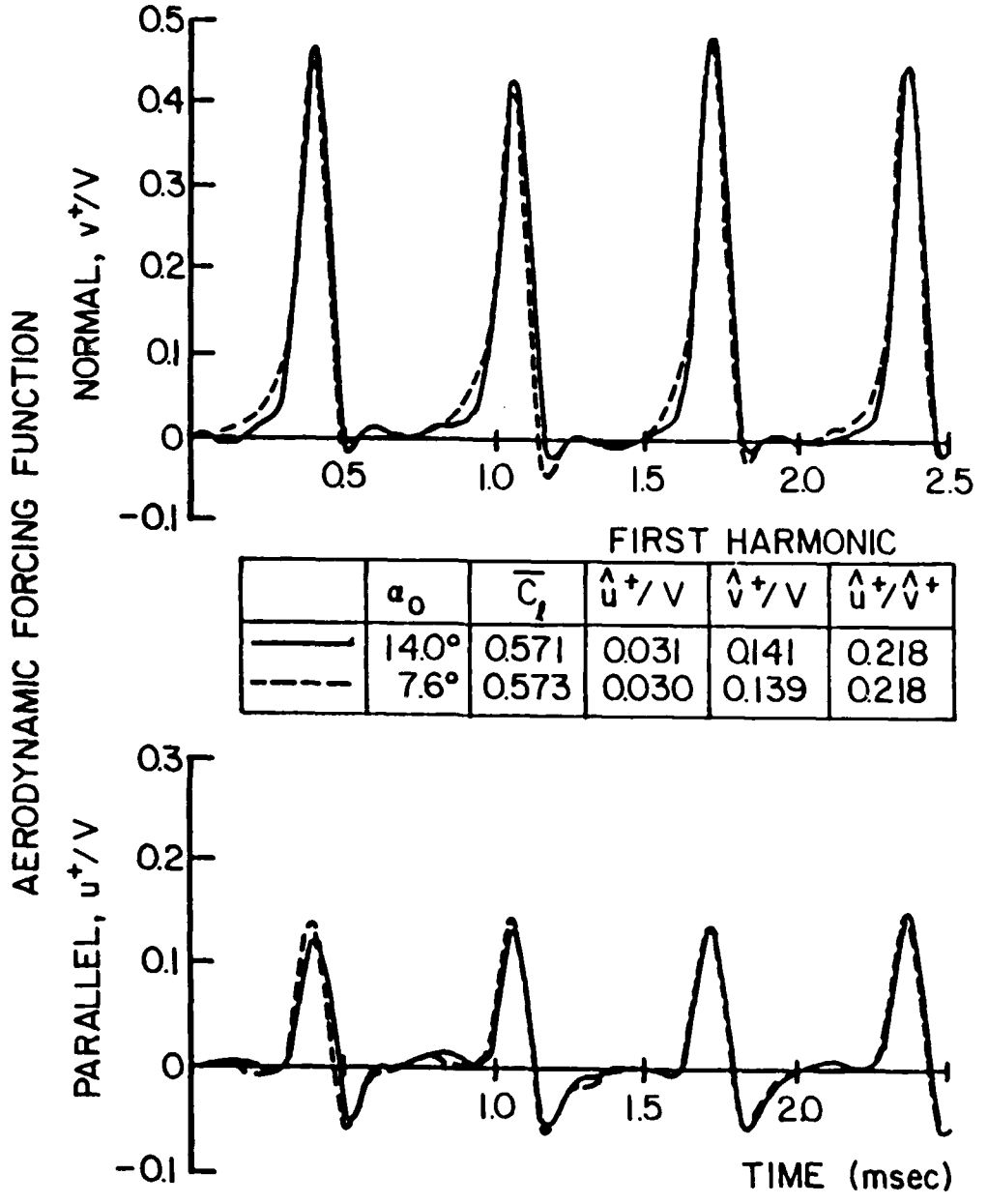

	α_0	$\overline{C_l}$	$\hat{u}^+/V$	$\hat{v}^+/V$	$\hat{u}^+/\hat{v}^+$
———	14.0°	0.571	0.031	0.141	0.218
- - - -	7.6°	0.573	0.030	0.139	0.218

Figure 12. Gust aerodynamic forcing function for attached and separated steady flows

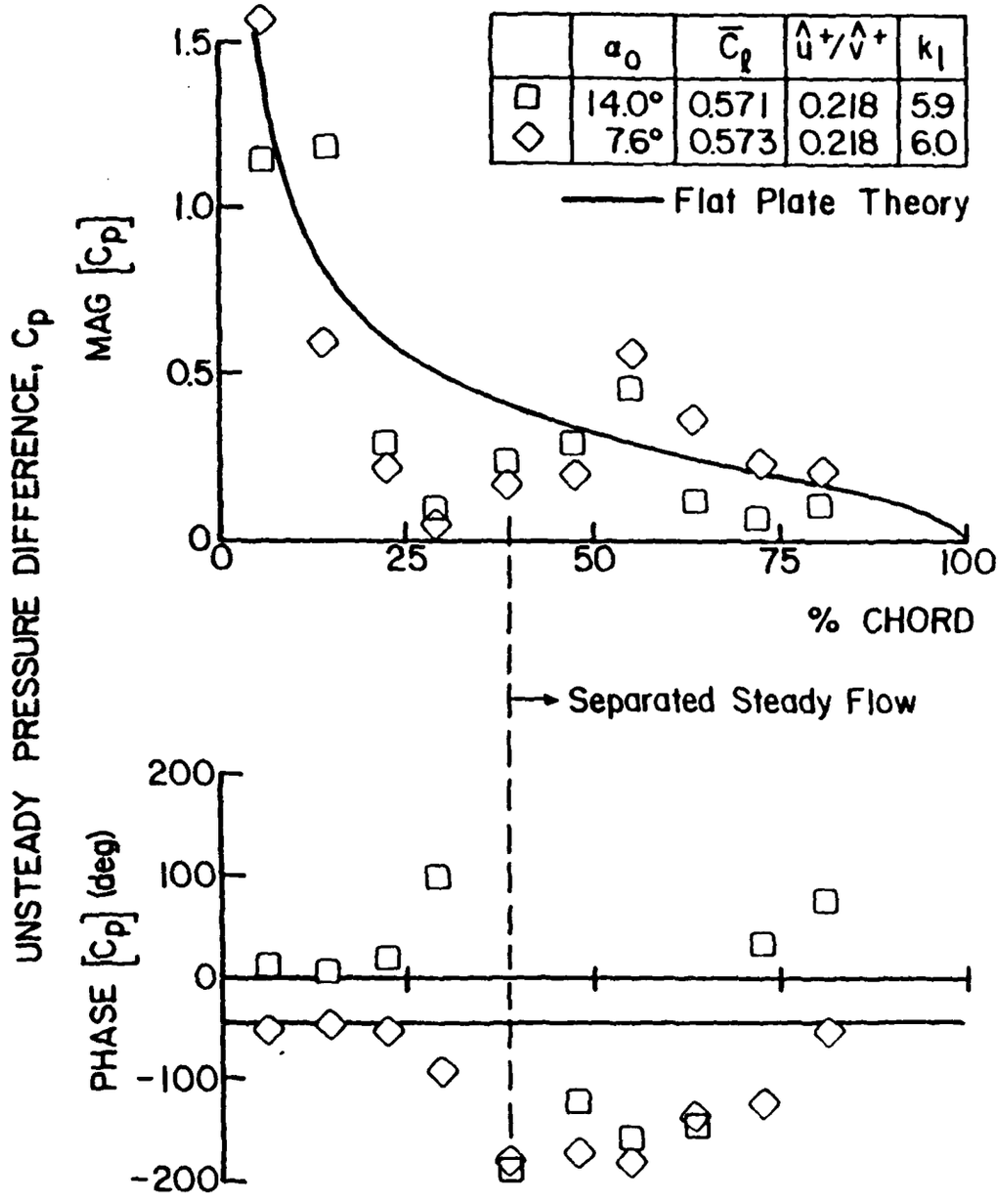

Figure 13. Effect of suction surface flow separation on unsteady surface pressure distributions

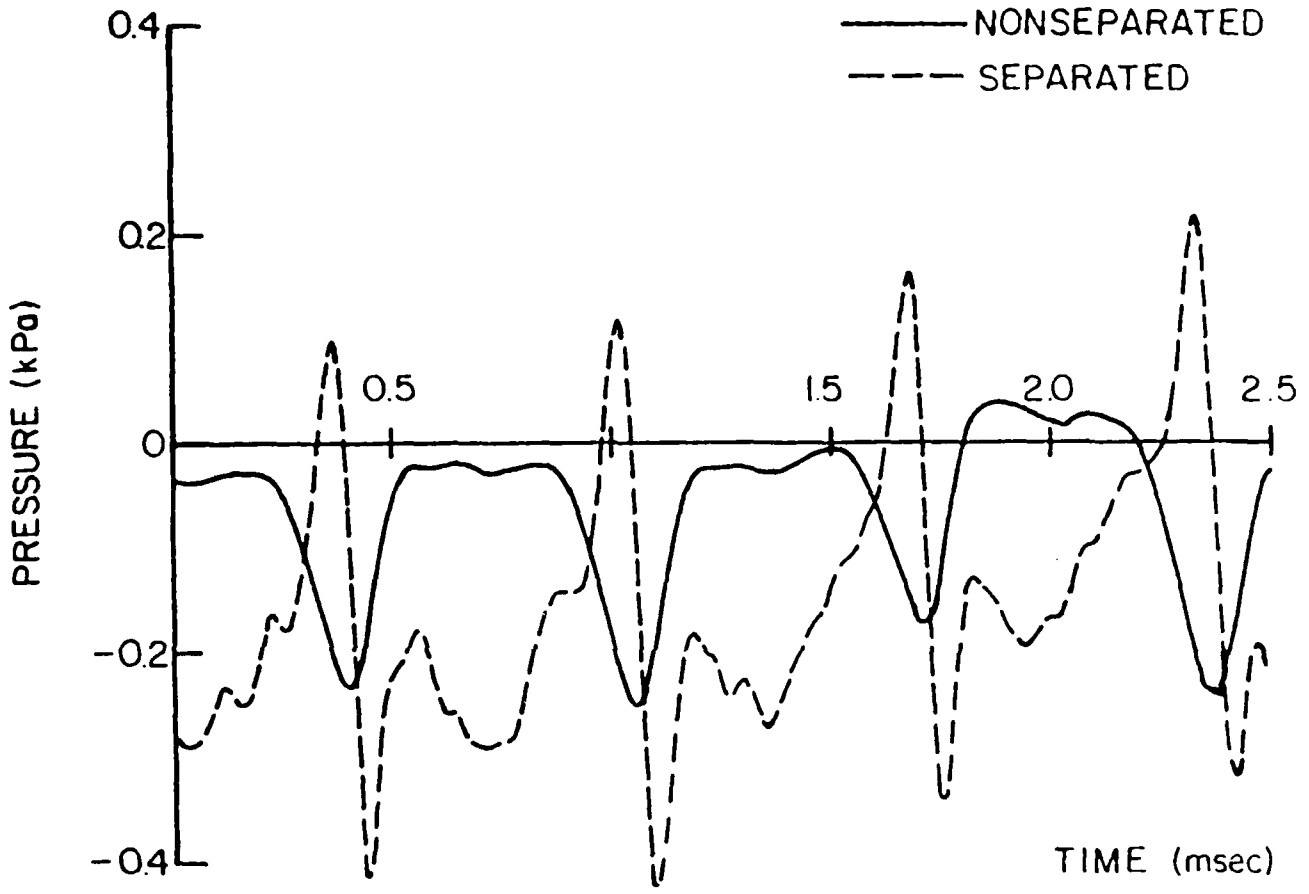

Figure 14. Unsteady separated and attached flow pressure signals upstream of separation point location

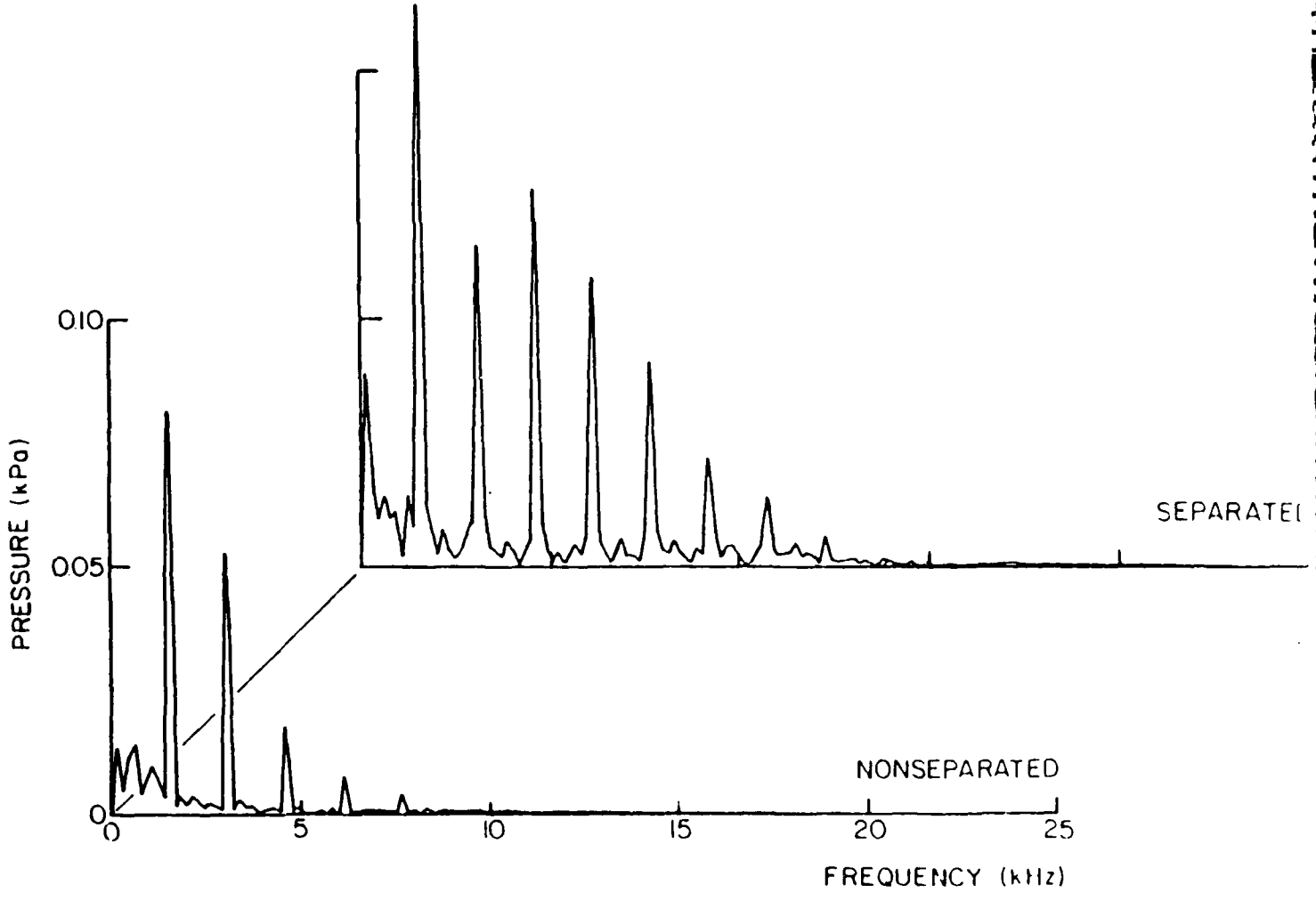

Figure 15. Fourier decomposition of unsteady separated and attached flow pressure signals upstream of separation point location

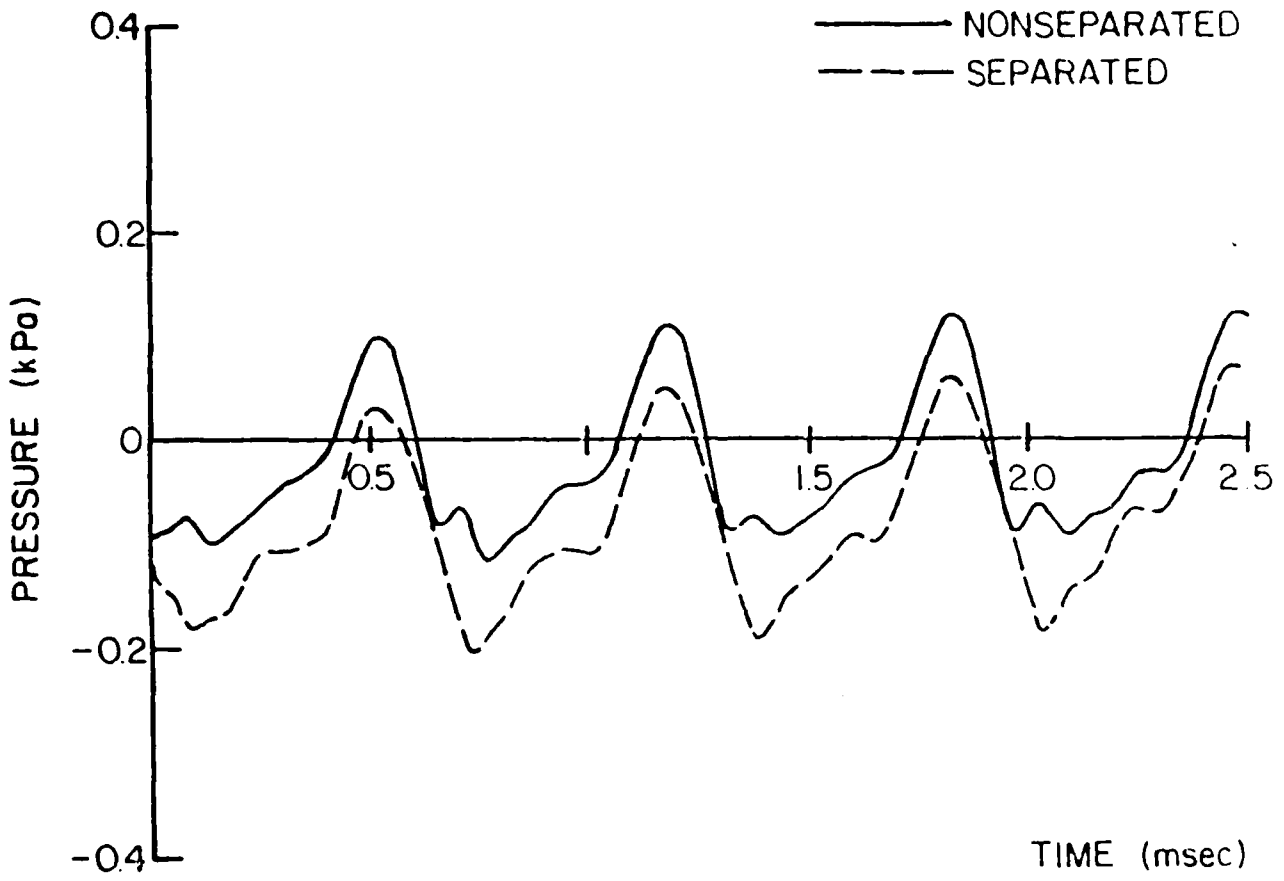

Figure 16. Unsteady separated and attached flow pressure signals within the separation region

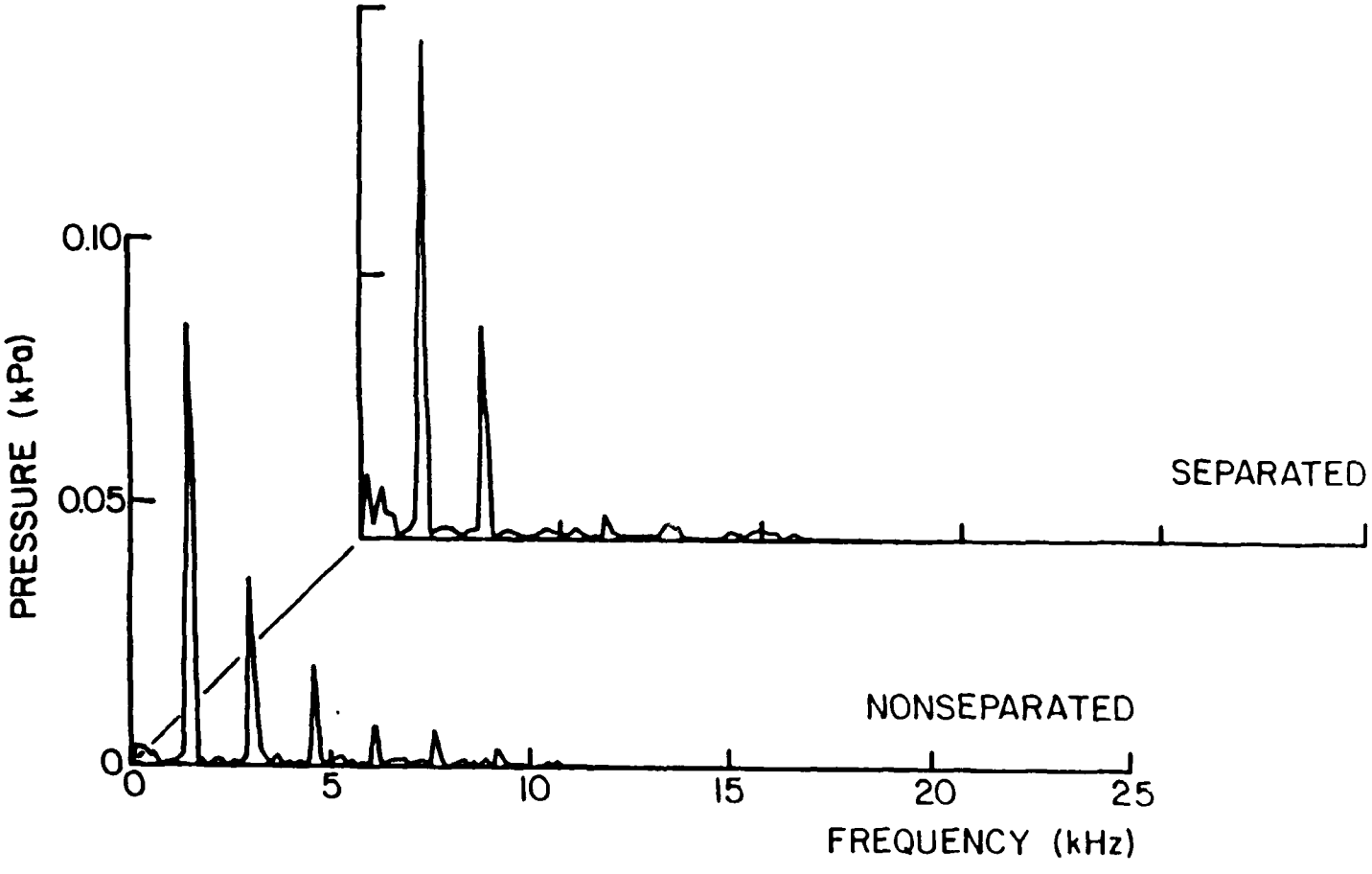

Figure 17. Fourier decomposition of unsteady separated and attached flow pressure signals within the separation region

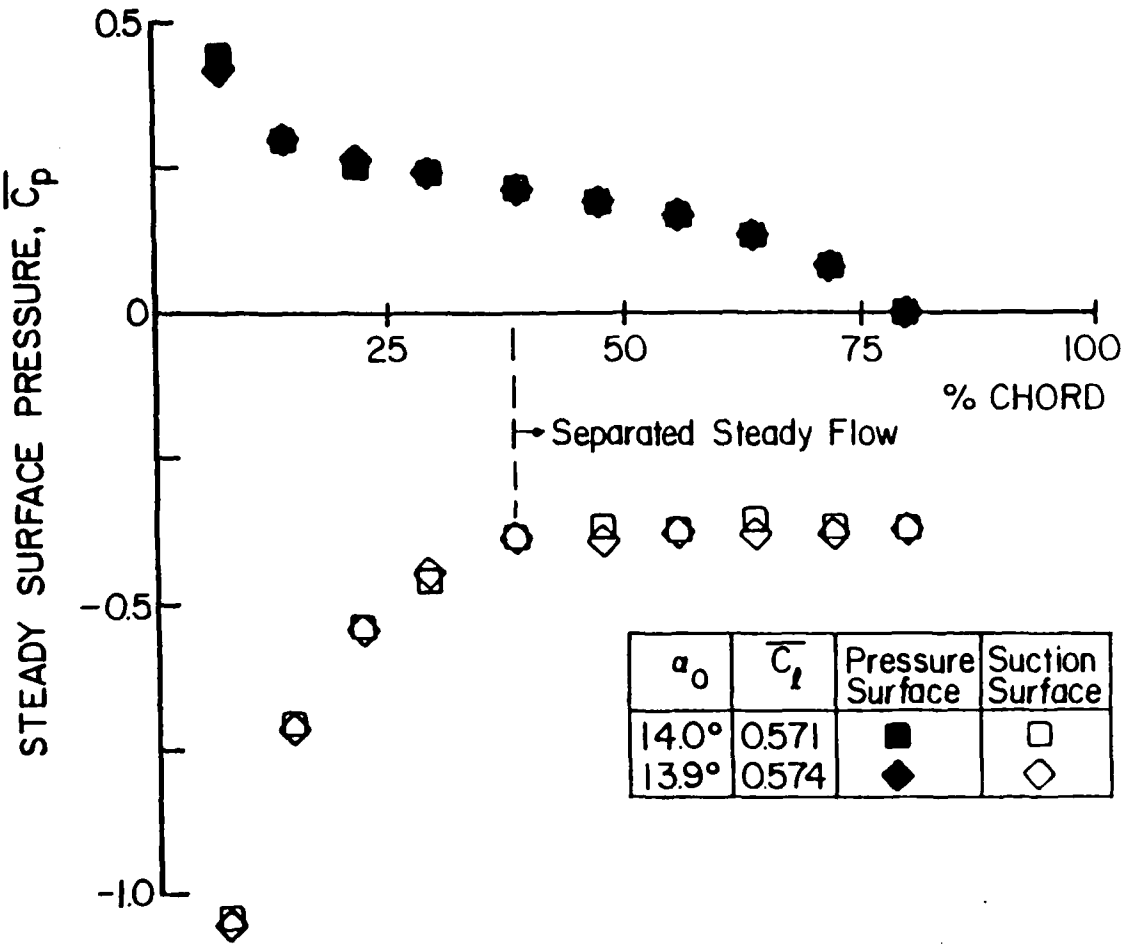

Figure 18. Effect of gust waveform on airfoil surface steady static pressure distributions

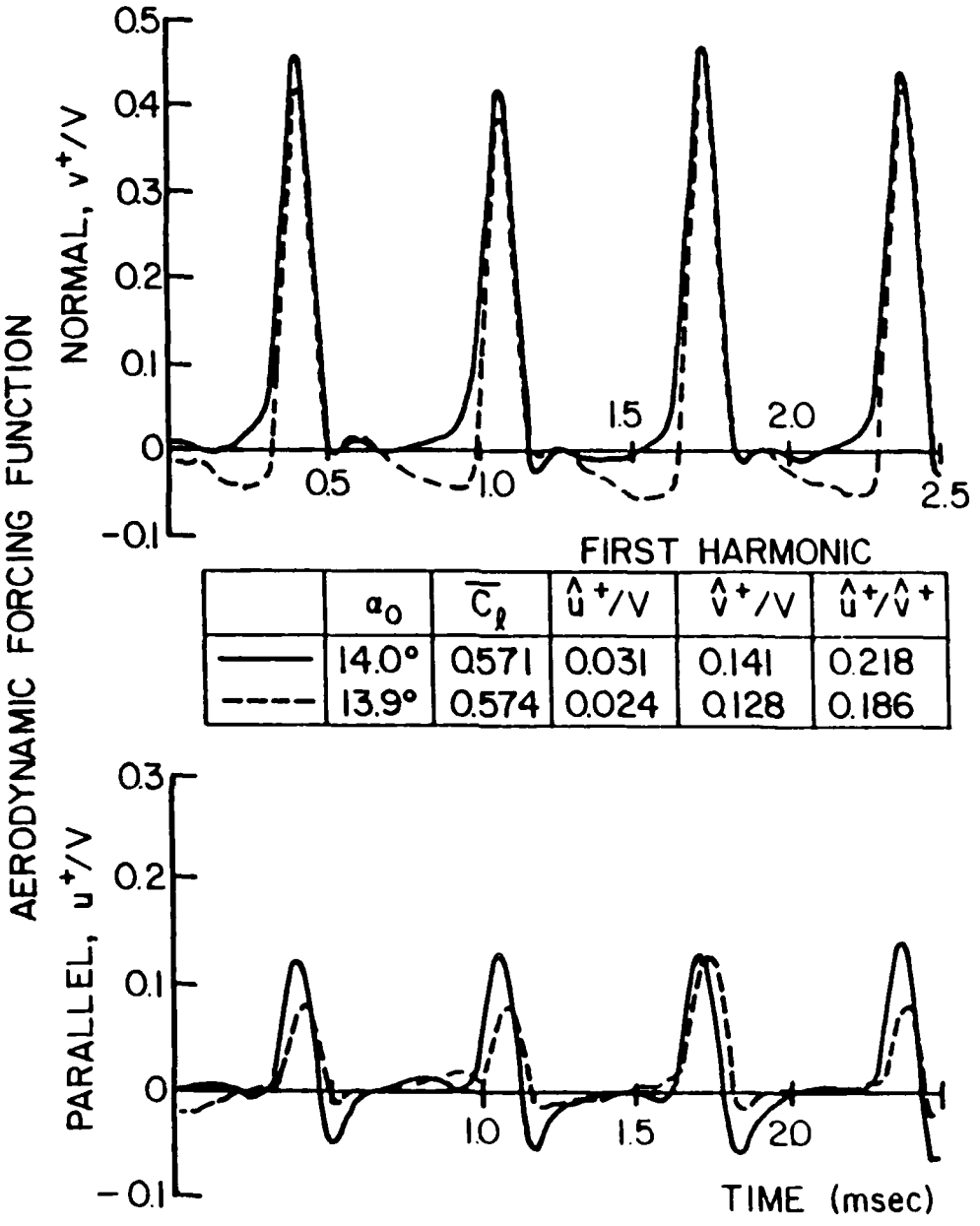

	α_0	$\overline{C_\ell}$	$\hat{u}^+/V$	$\hat{v}^+/V$	$\hat{u}^+/\hat{v}^+$
———	14.0°	0.571	0.031	0.141	0.218
- - - -	13.9°	0.574	0.024	0.128	0.186

Figure 19. Gust aerodynamic forcing function with suction surface flow separation

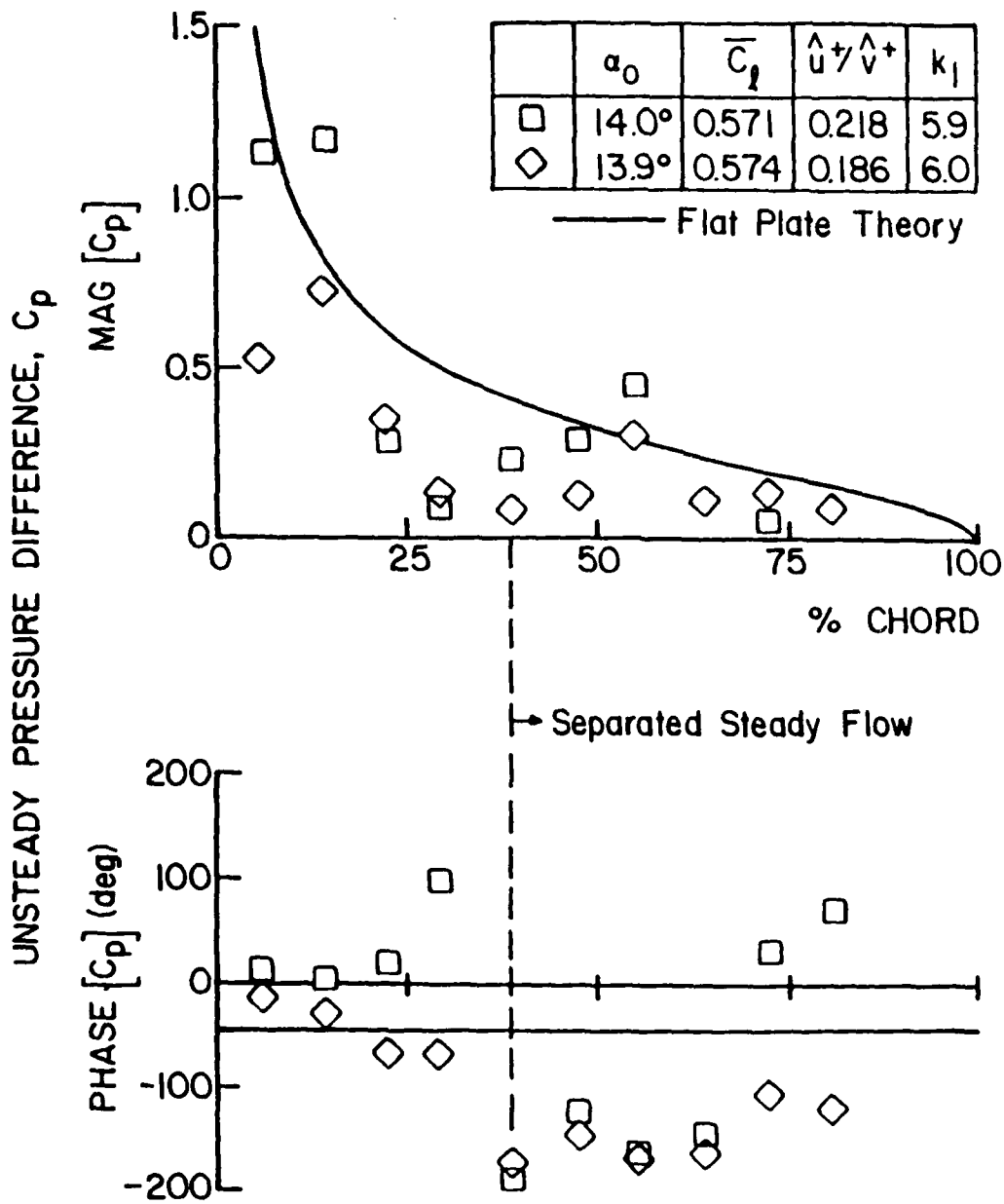

Figure 20. Effect of gust waveform on unsteady pressure differences with separated steady flow

APPENDIX VIII

LOCALLY ANALYTIC NUMERICAL METHOD AND APPLICATION TO VISCOUS INTERNAL AND EXTERNAL FLOWS

LOCALLY ANALYTIC NUMERICAL METHOD AND APPLICATION TO VISCOUS INTERNAL AND EXTERNAL FLOWS

Linda Schroeder and Sanford Fleeter

Thermal Sciences and Propulsion Center
School of Mechanical Engineering
Purdue University
West Lafayette, Indiana 47906

ABSTRACT

A locally analytic numerical method is developed to predict the two-dimensional internal and external steady laminar flow of an incompressible viscous fluid. In this method, analytic solutions of locally linearized partial differential equations are incorporated into the numerical solution. This is accomplished by dividing the flow field into computational grid elements. In each individual element, the nonlinear convective terms of the Navier Stokes equations are locally linearized, with analytic solutions then determined. The solution for the complete flow field is obtained by the assembly of these locally analytic solutions. The nonlinear character of the complete flow field is preserved as the flow is only locally linearized, i.e., independently linearized solutions are obtained in individual grid elements. This locally analytic numerical solution method is used to analyze the viscous flow in several internal and external flow configurations, with the prediction of flow development, reversal, separation, and reattachment demonstrated over a range of moderate values of the Reynolds number. In particular, three internal and one exernal flow configurations are investigated, with predictions obtained for entrance flow development in a straight channel, the flow through a sudden expansion, i.e., over a backward step, the flow in a diffuser, and the flow past a flat plate airfoil over a range of mean flow incidence angle values.

NOMENCLATURE

a,b,c,d	boundary constants
A	local grid velocity constant
B	local grid velocity constant
h	step height
H	channel half-height
L	reattachment length
P	dimensionless pressure
R_e	Reynolds number
U	nondimensional velocity in X direction
V	nondimensional velocity in Y direction
X	coordinate in mean flow direction
Y	coordinate in normal flow direction
ΔX	step size in X direction
ΔY	step size in Y direction
(X_o, Y_o)	center of grid element
Ψ	stream function
ξ	vorticity

Superscripts

Ψ	stream function
ξ	vorticity

Subscripts

(i,j)	nodal point
p	particular solution

INTRODUCTION

The steady laminar flow of an incompressible viscous fluid is described by the Navier-Stokes equations. Solutions to these coupled nonlinear partial differential equations are difficult to determine, with exact solutions existing only for very idealized flow situations. As a result, numerical solution techniques are being developed. However, when the nonlinear convective terms are significant, difficulties such as numerical instability and slow convergence are often encountered.

The various numerical methods differ in the means used to derive the corresponding algebraic representation of the differential equations. In finite difference methods, Taylor series expansion and control volume formulations are typically used, with numerical instability problems overcome by utilizing central differences for the diffusion terms and upwind, or backward, differences for the convective terms. In finite element methods, variational formulations and the method of weighted residuals are employed, with analogous upwind schemes utilized. In the locally analytic numerical method, analytic solutions to locally linearized differential equations are incorporated into the numerical method.

The concept of locally linearized solutions of nonlinear flow problems was developed and used to predict the steady inviscid transonic flow past a thin airfoil by Spreiter et al., references 1, 2, and 3, and subsequently extended to oscillating airfoils in transonic flow by Stahara and Spreiter, reference 4. Also, Dowell [5] developed a rational approximate method for unsteady transonic flow which is

broadly related to the local linearization concept. The locally analytic numerical technique which is based on the locally linearized solution approach, was initially developed by Chen et al., references 6 through 9, for steady two-dimensional fluid flow and heat transfer problems. They have shown that this method has several advantages over finite difference and finite element methods. It is less dependent on grid size and the system of algebraic equations are relatively stable. Also, since the solution is analytic, it is differentiable and is a continuous function in the solution domain. The disadvantage of the locally analytic numerical method is that, as will be seen, a great deal of mathematical analysis is required.

In this paper, the two-dimensional steady laminar flow of an incompressible viscous fluid in both internal and external flow configurations are predicted by developing a locally analytic numerical solution method. The flow field is first divided into computational grid elements. In each individual element, the nonlinear convective terms of the Navier-Stokes equations are locally linearized, with analytic solutions then determined. The solution for the complete flow field is obtained by assembly of these locally analytic solutions. The nonlinear character of the complete flow field is preserved as the flow is only locally linearized, i.e., independently linearized solutions are obtained in individual grid elements. The ability of the locally analytic numerical method to predict viscous flow development, reversal, separation, and reattachment, is then demonstrated at moderate values of the Reynolds number by considering several steady internal and external flow configurations.

MATHEMATICAL MODEL

The two-dimensional steady laminar flow of an incompressible viscous fluid is described by the nondimensional continuity and Navier-Stokes equations.

$$\frac{\partial U}{\partial X} + \frac{\partial V}{\partial Y} = 0 \tag{1a}$$

$$U \frac{\partial U}{\partial X} + V \frac{\partial U}{\partial Y} = - \frac{\partial P}{\partial X} + \frac{1}{R_e} \left[\frac{\partial^2 U}{\partial X^2} + \frac{\partial^2 U}{\partial Y^2} \right] \tag{1b}$$

$$U \frac{\partial V}{\partial X} + V \frac{\partial V}{\partial Y} = - \frac{\partial P}{\partial Y} + \frac{1}{R_e} \left[\frac{\partial^2 V}{\partial X^2} + \frac{\partial^2 V}{\partial Y^2} \right] \tag{1c}$$

where X and Y are the independent variables parallel and normal to the mean flow direction, U and V are the corresponding dimensionless velocity components, P is the dimensionless pressure, and R_e denotes the Reynolds number.

The boundary conditions specify that there is no slip between the fluid and the solid surfaces and that the normal velocity of the fluid is zero on these surfaces.

$$U = 0 \; ; \; V = 0 \quad \text{on surfaces} \tag{2}$$

There are three dependent variables, the two velocity components and the pressure. To reduce the number of dependent variables, the continuity and Navier-Stokes equations are rewritten in terms of the vorticity, ξ, and the stream function, Ψ , Equations 3 and 4.

$$\nabla^2\xi = R_e\left[U\frac{\partial\xi}{\partial X} + V\frac{\partial\xi}{\partial Y}\right] \tag{3a}$$

$$\xi = -\frac{\partial U}{\partial Y} = -\frac{\partial^2\Psi}{\partial Y^2} \quad \text{on boundaries} \tag{3b}$$

$$\nabla^2\Psi = \xi \tag{4a}$$

$$\Psi = 0 \ \text{on boundaries} \tag{4b}$$

where $\xi = \frac{\partial V}{\partial X} - \frac{\partial U}{\partial Y}$; $U = \frac{\partial\Psi}{\partial Y}$; $V = -\frac{\partial\Psi}{\partial X}$.

The vorticity equation is nonlinear, with the stream function described by a Poisson equation which is linear and coupled to the vorticity equation through the vorticity source term.

LOCALLY ANALYTIC NUMERICAL METHOD

In the locally analytic numerical method, analytic solutions of locally linearized partial differential equations are incorporated into the numerical solution. This is accomplished by dividing the flow field into computational grid elements and linearizing the nonlinear convective terms of the vorticity equation in each individual grid element. Analytic solutions to the linear equations describing the vorticity and the stream function in each element are then determined. The solution for the complete flow field is obtained through the application of the global boundary conditions and the assembly of the locally analytic solutions in the

individual grid elements.

Typical Grid Element

The vorticity and stream function equations are elliptic. Thus, to obtain unique analytic solutions in the typical grid element schematically depicted in Figure 1, continuous boundary conditions are required on all four boundaries. However, the element boundary conditions specify the values of the vorticity and the stream function only at the eight nodal boundary points. The requirement for continuous element boundary conditions is achieved herein by expressing the nodal boundary values in an implicit form as a second order polynomial in terms of the three known nodal values on each element boundary, Equation 5.

$$\xi(X,Y_o + \Delta Y) = a_1^{\xi} + a_2^{\xi} X + a_3^{\xi} X^2 \tag{5a}$$

$$\xi(X,Y_o - \Delta Y) = b_1^{\xi} + b_2^{\xi} X + b_3^{\xi} X^2 \tag{5b}$$

$$\xi(X_o + \Delta X,Y) = c_1^{\xi} + c_2^{\xi} Y + c_3^{\xi} Y^2 \tag{5c}$$

$$\xi(X_o - \Delta X,Y) = d_1^{\xi} + d_2^{\xi} Y + d_3^{\xi} Y^2 \tag{5d}$$

$$\psi(X,Y_o + \Delta Y) = a_1^{\psi} + a_2^{\psi} X + a_3^{\psi} X^2 \tag{5e}$$

$$\psi(X,Y_o - \Delta Y) = b_1^{\psi} + b_2^{\psi} X + b_3^{\psi} X^2 \tag{5f}$$

$$\psi(X_o + \Delta X,Y) = c_1^{\psi} + c_2^{\psi} Y + c_3^{\psi} Y^2 \tag{5g}$$

$$\psi(X_o - \Delta X, Y) = d_1^{\psi} + d_2^{\psi}\, Y + d_3^{\psi}\, Y^2 \tag{5h}$$

where the a_i, b_i, c_i, and d_i terms are constants determined from the three nodal points on each element side.

Vorticity Solution

The vorticity equation is nonlinear because of the inertia terms $U\frac{\partial \xi}{\partial X}$ and $V\frac{\partial \xi}{\partial Y}$. These terms are locally linearized by assuming that the velocity component coefficients U and V are constant in each individual grid element, i.e., locally constant, Equation 6.

$$U = \frac{A}{R_e} \;;\; V = \frac{B}{R_e} \tag{6}$$

where A and B are constant in an individual grid element, taking on different values in each element.

The resulting locally linearized vorticity equation is given in Equation 7.

$$\frac{\partial^2 \xi}{\partial X^2} + \frac{\partial^2 \xi}{\partial Y^2} = A\,\frac{\partial \xi}{\partial X} + B\,\frac{\partial \xi}{\partial Y} \tag{7}$$

The analytic solution for the vorticity subject to the appropriate boundary conditions is obtained utilizing the superposition principle. The vorticity is decomposed into two components, each having only two nonhomogeneous boundary conditions.

$$\xi = \xi^a + \xi^b \tag{8}$$

$$\frac{\partial^2 \xi^a}{\partial X^2} + \frac{\partial^2 \xi^a}{\partial Y^2} = A \frac{\partial \xi^a}{\partial X} + B \frac{\partial \xi^a}{\partial Y} \tag{9}$$

where:

$$\xi^a(X, Y_o + \Delta Y) = \overline{e}^{(A X + B \Delta Y)}[a_1^\xi + a_2^\xi X + a_3^\xi X^2]$$

$$\xi^a(X, Y_o - \Delta Y) = \overline{e}^{(A X - B \Delta Y)}[b_1^\xi + b_2^\xi X + b_3^\xi X^2]$$

$$\xi^a(X_o + \Delta X, Y) = 0$$

$$\xi^a(X_o - \Delta X, Y) = 0$$

$$\frac{\partial^2 \xi^b}{\partial X^2} + \frac{\partial^2 \xi^b}{\partial Y^2} = A \frac{\partial \xi^b}{\partial X} + B \frac{\partial \xi^b}{\partial Y} \tag{10}$$

where:

$$\xi^b(X, Y_o + \Delta Y) = 0$$

$$\xi^b(X, Y_o - \Delta Y) = 0$$

$$\xi^b(X_o + \Delta X, Y) = \overline{e}^{(A \Delta X + B Y)}[c_1^\xi + c_2^\xi Y + c_3^\xi Y^2]$$

$$\xi^b(X_o - \Delta X, Y) = e^{(A \Delta X - B Y)}[d_1^\xi + d_2^\xi Y + d_3^\xi Y^2]$$

The general analytic solutions for ξ^a and ξ^b are found by the separation of variables technique. After application of the boundary conditions for each component, the analytic solution for the vorticity, Equation 11, is determined by combining the two component solutions.

$$\xi(X,Y)=e^{(AX+BY)}\sum_{n=1}^{\infty}\left\{\left[C_{1n}\sinh(D_{1n}X)+C_{2n}\cosh(D_{1n}X)\right]\sin(\lambda_{1n}^{\xi}(Y+\Delta Y))\right.$$

$$\left.+\left[C_{3n}\sinh(D_{2n}Y)+C_{4n}\cosh(D_{2n}Y)\right]\sin(\lambda_{2n}^{\xi}(X+\Delta X))\right\} \quad (11)$$

The final algebraic form of the vorticity solution specifies the value of the vorticity at the center of the element as a function of the neighboring eight nodal values, Equation 12.

$$\begin{aligned}\xi(X_o,Y_o) = {} & Z_1\xi(x_o+\Delta X,Y_o+\Delta Y)+Z_2\xi(X_o+\Delta X,Y_o) \\ & +Z_3\xi(X_o+\Delta X,Y_o-\Delta Y)+Z_4\xi(X_o,Y_o-\Delta Y) \\ & +Z_5\xi(X_o-\Delta X,Y_o-\Delta Y)+Z_6\xi(X_o-\Delta X,Y_o) \\ & +Z_7\xi(X_o-\Delta X,Y_o+\Delta Y)+Z_8\xi(X_o,Y_o+\Delta Y)\end{aligned} \quad (12)$$

where:

$$Z_1 = \frac{1}{2\Delta Y}(I_1 + \frac{I_3}{\Delta Y})\, E^{\xi}_{1n} + \frac{1}{2\Delta X}(\bar{I}_2 + \frac{\bar{I}_2}{\Delta X})E^{\xi}_{3n}$$

$$Z_2 = (I_1 - \frac{I_3}{\Delta Y^2})\, E^{\xi}_{1n}$$

$$Z_3 = \frac{1}{2\Delta Y}(-I_2 + \frac{I_3}{\Delta Y})E^{\xi}_{1n} + \frac{1}{2\Delta X}(\bar{I}_2 + \bar{I}_3)E^{\xi}_{4n}$$

$$Z_4 = (\bar{I}^{\xi}_1 - \frac{\bar{I}^{\xi}_3}{\Delta X^2})E^{\xi}_{4n}$$

$$Z_5 = \frac{1}{2\Delta Y}(\, -I^{\xi}_2 + \frac{I^{\xi}_3}{\Delta Y})E^{\xi}_{2n} + \frac{1}{2\Delta X}(-\bar{I}^{\xi}_2 + \frac{\bar{I}^{\xi}_3}{\Delta X})E^{\xi}_{4n}$$

$$Z_6 = (I^{\xi}_1 - \frac{I^{\xi}_3}{\Delta Y^2})E^{\xi}_{2n}$$

$$Z_7 = \frac{1}{2\Delta Y}(I^{\xi}_2 + \frac{I^{\xi}_3}{\Delta Y})E^{\xi}_{2n} + \frac{1}{2\Delta X}(-\bar{I}^{\xi}_2 + \frac{\bar{I}^{\xi}_3}{\Delta X})E^{\xi}_{3n}$$

$$Z_8 = (\bar{I}^{\xi}_1 - \frac{\bar{I}^{\xi}_3}{2})E^{\xi}_{3n}$$

$$E_{1n}^{\xi} = \frac{e^{-A\Delta X}}{2\Delta Y} \sum_{n=1}^{\infty} \frac{\sin(\lambda_{1n}\Delta Y)}{\cosh(D_{1n}\Delta X)}$$

$$E_{2n}^{\xi} = \frac{e^{A\Delta X}}{2\Delta Y} \sum_{n=1}^{\infty} \frac{\sin(\lambda_{1n}\Delta Y)}{\cosh(D_{1n}\Delta X)}$$

$$E_{3n}^{\xi} = \frac{e^{-B\Delta Y}}{2\Delta X} \sum_{n=1}^{\infty} \frac{\sin(\lambda_{2n}\Delta X)}{\cosh(D_{2n}\Delta Y)}$$

$$E_{3n}^{\xi} = \frac{e^{B\Delta Y}}{2\Delta X} \sum_{n=1}^{\infty} \frac{\sin(\lambda_{2n}\Delta X)}{\cosh(D_{2n}\Delta Y)}$$

$$\lambda_{1n}^{\xi} = \frac{n\pi}{2\Delta X}$$

$$\lambda_{2n}^{\xi} = \frac{n\pi}{2\Delta Y}$$

$$D_{1n} = (A^2 + B^2 + \lambda_{1n}^2)^{\frac{1}{2}}$$

$$D_{2n} = (A^2 + B^2 + \lambda_{2n}^2)^{\frac{1}{2}}$$

$$I_1^{\xi} = {}_{-\Delta Y}\int^{\Delta Y} e^{-BY}\sin(\lambda_{2n}(Y+\Delta Y))dY$$

$$I_2^{\xi} = {}_{-\Delta Y}\int^{\Delta Y} Ye^{-BY}\sin(\lambda_{2n}(Y+\Delta Y))dY$$

$$I_3^{\xi} = {}_{-\Delta Y}\int^{\Delta Y} Y^2e^{-BY}\sin(\lambda_{2n}(Y+\Delta Y))dY$$

$$\bar{I}_1^{\xi} = {}_{-\Delta X}\int^{\Delta X} e^{-AX}\sin(\lambda_{2n}(X+\Delta X))dX$$

$$\bar{I}_2^{\xi} = {}_{-\Delta X}\int^{\Delta X} Xe^{-AX}\sin(\lambda_{2n}(X+\Delta X))dX$$

$$\bar{I}_3^{\xi} = {}_{-\Delta X}\int^{\Delta X} X^2e^{-AX}\sin(\lambda_{2n}(X+\Delta X))dX$$

Stream Function Solution

The stream function is described by a Poisson equation which is linear and coupled to the vorticity through the source term, Equation 4. The locally analytic solution for the stream function is obtained in a manner analogous to that used to solve for the vorticity. In particular, the superposition principle is utilized to decompose the stream function into two components, Equation 13. One component is described by a homogeneous Laplace equation with nonhomogeneous boundary conditions, Equation 14. The second component consists of a nonhomogeneous Poisson equation but with homogeneous boundary conditions, Equation 15.

$$\Psi = \Psi^a + \Psi^b \tag{13}$$

$$\nabla^2 \Psi^a = 0 \tag{14}$$

where:

$$\begin{aligned}
\Psi^a(X, Y_o + \Delta Y) &= a_1^\Psi + a_2^\Psi X + a_3^\Psi X^2 \\
\Psi^a(X, Y_o - \Delta Y) &= b_1^\Psi + b_2^\Psi X + b_3^\Psi X^2 \\
\Psi^a(X_o + \Delta X, Y) &= c_1^\Psi + c_2^\Psi Y + c_3^\Psi Y^2 \\
\Psi^a(X_0 - \Delta X, Y) &= d_1^\Psi + d_2^\Psi Y + d_3^\Psi Y^2
\end{aligned}$$

$$\nabla^2\Psi^b = -\xi \tag{15}$$

$$\Psi^b(X,Y_o + \Delta Y) = 0$$

$$\Psi^b(X,Y_o - \Delta Y) = 0$$

$$\Psi^b(X_o + \Delta X,Y) = 0$$

$$\Psi^b(X_o - \Delta X,Y) = 0$$

The mathematical problem for Ψ^a specified in Equation 14 corresponds directly to that for the vorticity. Thus, the separated variables solution for Ψ^a is obtained in an analogous manner to that previously described for ξ .

The solution for Ψ^b is somewhat more complex in that it is described by a nonhomogeneous Poisson equation. The homogeneous solution for Ψ^b is defined by a Laplace equation, and is thus also determined by separation of variables. However, the nonhomogeneous source term for the particular solution is the vorticity, ξ , which itself satisfies a Laplace equation. Thus, the particular solution, Ψ_p^b , is determined by assuming a separated variables Fourier series solution form, Equation 16.

$$\Psi_p^b(X,Y) = \sum_{n=1}^{\infty} F_n(Y)\sin[\lambda_{1n}^{\Psi}(X+\Delta X)] \tag{16}$$

where λ_{1n}^{Ψ} are the eigenvalues of the homogeneous solutions and the function $F_n(Y)$ is unknown.

The particular solution is determined by finding the unknown function $F_n(Y)$. This is accomplished by first expanding the previously determined nonhomogeneous

vorticity term, specified in Equation 11, in an analogous Fourier series.

$$\xi(X,Y)= \sum_{n=1}^{\infty} G_n(Y)\sin[\lambda_{1n}^{\Psi}(X+\Delta X)] \tag{17}$$

These Fourier series for Ψ_p^b and ξ are then substituted into Equation 15 which defines Ψ^b. This leads to the following nonhomogeneous second order ordinary differential equation for the unknown function $F_n(Y)$.

$$\frac{d^2F_n}{dY^2} - \lambda_{1n}^{\Psi} F_n = G_n \tag{18}$$

This equation is easily solved for $F_n(Y)$, thereby determining the particular solution, Ψ_p^b .

The complete solution for the stream function, $\Psi(X,Y)$, given in Equation 19, is obtained by the superposition of the two component solutions, Ψ^a and Ψ^b after application of the appropriate boundary conditions.

$$\Psi(X,Y) = \sum_{n=1}^{\infty} \Big\{ [H_{1n} \sinh(\lambda_{1n}^{\Psi} X) + H_{2n} \cosh(\lambda_{1n}^{\Psi} X)] \sin[\lambda_{1n}^{\Psi}(Y + \Delta Y)]$$

$$+ H_{3n} \sinh(\lambda_{2n}^{\Psi} Y) + H_{un} \cosh(\lambda_{2n}^{\Psi} Y)] \sin[\lambda_{2n}^{\Psi}(X + \Delta X)]$$

$$+ [H_{5n}(\lambda_{1n}^{\Psi} Y) + H_{6n}\cosh(\lambda_{1n}^{\Psi} Y) + H_{7n} + H_{8n} Y \qquad (19)$$

$$+ H_{9n} Y^2] \sin[\lambda_{1n}^{\Psi}(X + \Delta X)] \Big\}$$

The final algebraic form of the stream function specifies the value of the stream function at the center of the element as a function of the neighboring eight nodal values, Equation 20.

$$\Psi(X_0,Y_o) = P_1\Psi(X_o + \Delta X, Y_o + \Delta Y) + P_2\Psi(X_o + \Delta X, Y_o) \qquad (20)$$
$$+ P_3\Psi(X_o + \Delta X, Y_o - \Delta Y) + P_4\Psi(X_o, Y_o - \Delta Y)$$
$$+ P_5\Psi(X_o - \Delta X, Y_o - \Delta Y) + P_6\Psi(X_o - \Delta X, Y_o)$$
$$+ P_7\Psi(X_o - \Delta X, Y_o + \Delta Y) + P_8\Psi(X_o, Y_o + \Delta Y)$$
$$+ Q_1\xi(X_o + \Delta X, Y_o + \Delta Y) + Q_2\xi(X_o + \Delta X, Y_o)$$
$$+ Q_3\xi(X_o + \Delta X, Y_o - \Delta Y) + Q_4\xi(X_o, Y_o - \Delta Y)$$
$$+ Q_5\xi(X_o - \Delta X, Y_o - \Delta Y) + Q_6\xi(X_o - \Delta X, Y_o)$$
$$+ Q_7\xi(X_o - \Delta X, Y_o + \Delta Y) + Q_8\xi(X_o, Y_o + \Delta Y)$$
$$+ Q_9\xi(X_o, Y_o)$$

where:

$$P_1 = \frac{1}{2\Delta X}(I_2^{\Psi} + \frac{I_3^{\Psi}}{\Delta Y})E_{1n}^{\Psi} + \frac{1}{2\Delta X}(\bar{I}_2^{\Psi} + \frac{\bar{I}_3^{\Psi}}{\Delta X})E_{2n}^{\Psi}$$

$$P_2 = (I_1^{\Psi} - \frac{I_3^{\Psi}}{\Delta Y^2})E_{1n}^{\Psi}$$

$$P_3 = -\frac{1}{2\Delta Y}(I_2^{\Psi} - \frac{I_3^{\Psi}}{\Delta Y})E_{1n}^{\Psi} + \frac{1}{2\Delta X}(\bar{I}_2^{\Psi} + \frac{\bar{I}_3^{\Psi}}{\Delta X})E_{2n}^{\Psi}$$

$$P_4 = (\bar{I}_1^{\Psi} - \frac{\bar{I}_3^{\Psi}}{\Delta X^2})E_{2n}^{\Psi}$$

$$P_5 = -\frac{1}{2\Delta Y}(I_2^{\Psi} - \frac{I_3^{\Psi}}{\Delta Y})E_{1n}^{\Psi} - \frac{1}{2\Delta X}(\bar{I}_2^{\Psi} - \frac{\bar{I}_3^{\Psi}}{\Delta X})E_{2n}^{\Psi}$$

$$P_6 = (I_1^{\Psi} - \frac{I_3^{\Psi}}{\Delta Y^2})E_{1n}^{\Psi}$$

$$P_7 = \frac{1}{2\Delta Y}(I_2^{\Psi} + \frac{I_3^{\Psi}}{\Delta Y})E_{1n}^{\Psi} - \frac{1}{2\Delta X}(\bar{I}_2^{\Psi} - \frac{\bar{I}_3^{\Psi}}{\Delta X})E_{2n}^{\Psi}$$

$$P_8 = (\bar{I}_1^{\Psi} - \frac{\bar{I}_2^{\Psi}}{\Delta X^2})E_{2n}^{\Psi}$$

$$Q_1 = \frac{E_{4n}^{\Psi}}{4\Delta X\Delta Y^2}(I_2^{\Psi} + \frac{I_3^{\Psi}}{\Delta X}E_{1n}^{\Psi}$$

$$Q_2 = (E_{3n}^{\Psi} - \frac{E_{4n}^{\Psi}}{\Delta Y^2})(\frac{I_2^{\Psi}}{2\Delta X} + \frac{I_3^{\Psi}}{2\Delta X^2})E_{1n}^{\Psi}$$

$$Q_3 = \frac{E_{4n}^{\Psi}}{4\Delta X\Delta Y^2}(I_2^{\Psi} + \frac{I_3^{\Psi}}{\Delta X})E_{1n}^{\Psi}$$

$$Q_4 = \frac{E_{4n}^{\Psi}}{2\Delta Y^2}(I_1^{\Psi} - \frac{I_3^{\Psi}}{\Delta X^2})E_{1n}^{\Psi}$$

$$Q_5 = \frac{E_{4n}^{\Psi}}{4\Delta X\Delta Y^2}(-I_2^{\Psi} + \frac{I_3^{\Psi}}{\Delta X})E_{1n}^{\Psi}$$

$$Q_6 = (E_{3n}^{\Psi} - \frac{E_{4n}^{\Psi}}{\Delta Y^2})(-\frac{I_2^{\Psi}}{2\Delta X} + \frac{I_3^{\Psi}}{2\Delta X^2})E_{1n}^{\Psi}$$

$$Q_7 = \frac{E_{4n}^{\Psi}}{4\Delta X\Delta Y^2}(-I_2^{\Psi} + \frac{I_3^{\Psi}}{\Delta X})E_{1n}^{\Psi}$$

$$Q_8 = \frac{E_{4n}^{\Psi}}{2\Delta Y^2}(I_1^{\Psi} - \frac{I_3^{\Psi}}{\Delta X^2})E_{1n}^{\Psi}$$

$$Q_9 = (E_{3n}^{\Psi} - \frac{E_{4n}^{\Psi}}{\Delta Y^2})(I_1^{\Psi} - \frac{I_3^{\Psi}}{2\Delta X^2})E_{1n}^{\Psi}$$

$$E_{1n}^{\Psi} = \frac{\sin(\lambda_{1n}\Delta Y)}{2\Delta Y\cosh\lambda_{1n}\Delta X}$$

$$E_{2n}^{\Psi} = \frac{\sin(\lambda_{2n}\Delta X)}{2\Delta X\cosh\lambda_{2n}\Delta Y}$$

$$E_{3n}^{4} = \frac{-1 + \cosh(\lambda_{1n}\Delta Y)}{\lambda_{1n}2_{\Delta}X\cosh(\lambda_{1n}\Delta Y)}$$

$$E_{4n}^{\Psi} = \frac{-2-\lambda_{1n}^2\Delta Y^2 + 2\cosh(\lambda_{1n}\Delta Y)}{\Delta X\lambda_{1n}^4\cosh(\lambda_{1n}\Delta Y)}$$

Computational Procedure

The above technique is applied to adjacent grid elements with the boundary nodal point considered as the interior point. For a general grid element with center at (i,j), the resulting algebraic equations which relate the values of the vorticity and the stream function at the center with their corresponding known values at the eight surrounding nodes are given in Equations 21 and 22.

$$\psi(i,j) = P_{i+1,j+1}\psi(i+1,j+1) + P_{i+1,j}\psi(i+1,j) \tag{21}$$
$$+ P_{i+1,j-1}\psi(i+1,j-1) + P_{i,j-1}\psi(i,j-1)$$
$$+ P_{i-1,j-1}\psi(i-1,j-1) + P_{i-1,j}\psi(i-1,j)$$
$$+ P_{i-1,j+1}\psi(i-1,j+1) + P_{i,j+1}\psi(i,j+1)$$
$$+ Q_{i+1,j+1}\xi(i+1,j+1) + Q_{i+1,j}\xi(i+1,j)$$
$$+ Q_{i+1,j-1}\xi(i+1,j-1) + Q_{i,j-1,}\xi(i,j-1)$$
$$+ Q_{i-1,j-1}\xi(i-,j-) + Q_{i-1,j}\xi(i-1,j)$$
$$+ Q_{i-1,j+1}\xi(i-1,j+1) + Q_{i,j+1}\xi(i,j+1) + Q_{i,j}\xi(i,j)$$

$$\xi(i,j) = Z_{i+1,j+1}\xi(1+1,j+1) + Z_{i+1,j}\xi(i+1,j) \tag{22}$$
$$+ Z_{i+1,j-1}\xi(i+1,j-1) + Z_{i,j-1}\xi(i,j-1)$$
$$+ Z_{i-1,j-1}\xi(i-1,j-1) + Z_{i-1,j}\xi(i-1,j)$$
$$+ Z_{i-1,j+1}\xi(i-1,j+1) + Z_{i,j+1}\xi(i,j+1)$$

These algebraic solutions for the vorticity and stream function are coupled and, thus, must be solved iteratively. With global boundary conditions applied, the above interior point solution leads to a system of algebraic equations. These are given in Equations 23 and 24 for a fixed value of j.

$$
\begin{aligned}
&- P_{i-1,j}\psi(i-1,j) + \psi(i,j) - P^{\psi}_{i+1,j}(i+1,j) \qquad (23)\\
&= P_{i+1,j+1}\psi(i+1,j+1) + P_{i+1,j-1}\psi(i+1,j-1) + P_{i,j-1}\psi(i,j-1)\\
&\quad + P_{i-1,j-1}\psi(i-1,i-j) + P_{i-1,j+1}\psi(i-1,j+1)\\
&\quad + P_{i,j+1}\psi(i,j+1) + Q_{i+1,j+1}\xi(i+1,j+1) + Q_{i+1,j}\xi(i+1,j)\\
&\quad + Q_{i+1,j-1}\xi(i+1,j-1) + Q_{i,j-1}\xi(i,j-1)\\
&\quad + Q_{i-1,j-1}\xi(i-1,j-1) + Q_{i-1,j}\xi(i-1,j)\\
&\quad + Q_{i-1,j+1}\xi(i-1,j+1) + Q_{i,j+1}\xi(i,j+1) + Q_{i,j}\xi(i,j)
\end{aligned}
$$

$$
\begin{aligned}
&- Z_{i-1,j}\xi(i-1,j) + \xi(i,j) - Z_{i+1,j}\xi(i+1,j) \qquad (24)\\
&= Z_{i+1,j+1}\xi(i+1,j+1) + Z_{i+1,j-1}\xi(i+1,j-1)\\
&\quad + Z_{i,j-1}\xi(i,j-1) + Z_{i-1,j-1}\xi(i-1,j-1)\\
&\quad + Z_{i-1,j+1}\xi(i-1,j+1) + Z_{i,j+1}\xi(i,j+1)
\end{aligned}
$$

The right hand sides of these two equations are known, i.e., the (j-1) terms are known from the boundary conditions or the last sweep, with the (j+1) terms determined from the boundary conditions or the previous iteration. They can be written as tridiagonal matrices and then solved by Thomas algorithm for all j values.

To begin the solution process, the stream function solution is first determined from Equation 23. The constants in this equation, P_{ij} and Q_{ij}, are calculated for each nodal point. These need only be calculated once as they are the same for all grid elements and all iterations. This equation is then solved line by line by sweeping in the j direction and using the tridiagonal matrix solver with each j held constant.

The vorticity is then determined from Equation 24 using the tridiagonal matrix solver. After internal convergence is achieved, successive over relaxation is used for the stream function and the vorticity to expedite the external iterative process. This whole procedure is repeated until overall convergence is achieved.

RESULTS

This locally analytic numerical solution method is used to analyze the internal and external two-dimensional laminar flow of an incompressible viscous fluid, with the prediction of flow development, reversal, separation, and reattachment demonstrated for moderate values of the Reynolds number. In particular, three internal and one external flow configurations are investigated, with predictions obtained for entrance flow development in a straight channel, the flow through a sudden expansion, i.e., over a backward step, the flow in a diffuser, and the flow past a flat plate airfoil over a range of mean flow incidence angle values.

Entrance Region Flow Development

The predicted development of a uniform inlet flow as it progresses downstream in a channel comprised of two parallel plates is presented in Figure 2 for a Reynolds number of 10. These predictions were obtained on a 31 x 11 computational grid with $\Delta X = \Delta Y = 0.1$ and internal and external tolerances for the stream function and vorticity of 10^{-6} and 10^{-4}, respectively. On a Cyber 205 vector processing computer, 79 overall iterations were required, taking 41.5 CPU seconds. The velocity profiles show the boundary layer development along the length of the plate, with the boundary layer thickness increasing with distance

from the entrance. Also, presented are the classical fully developed results from reference 10. As seen, excellent agreement is obtained.

Sudden Expansion (Backward Step)

This example considers the viscous flow in a channel of height 2H which undergoes a sudden expansion to a channel of height 2(H+h). As the flow configuration is symmetric about the centerline, the solution is obtained by considering one half of the channel, i.e., the flow over a backward step. The abrupt geometry of the step results in the flow separating from the step and reattaching on the bottom of the flow channel. These separation and reattachment locations are predicted as follows. The vorticity is defined as $\xi = \frac{\partial U}{\partial X} - \frac{\partial V}{\partial Y}$. Flow separation from a boundary occurs when $\frac{\partial V}{\partial Y} = 0$. As the normal velocity is always zero on the boundaries, $\frac{\partial U}{\partial X} = 0$. Thus separation from a boundary is predicted when $\xi = 0$.

Figures 3 and 4 present the predicted stream function contours for the flow through channels with inlet to exit flow area ratios of 3:1 and 2:1, h/H = 2 and 1, respectively, at Reynolds numbers between 10 and 80. These predictions were obtained on a 71 x 16 grid with $\Delta X = \Delta Y = 0.05$. The internal and external convergence criteria were 10^{-5} for the stream function while the internal and external tolerances for the vorticity were 10^{-2} and $5x10^{-2}$, respectively. Computational time averaged about 310 CPU seconds on the Cyber 205 for all cases, with an average of 70 overall iterations.

The stream function contour plots show the flow separation from the side of the step, Point A, and the reattachment on the bottom of the flow channel, Point B. Also, the recirculation zone at the base of the step is clearly defined, with a vortex formed due to the reverse flow. Note that as the Reynolds number is increased, the separation point moves upward on the step and also reattaches at a point further downstream. With the predicted locations of the separation and reattachment points known, the relationship between these two locations can be determined. In particular, a linear relation between the nondimensional reattachment length from the step, L/H, and the Reynolds number for these two step geometries is predicted, Figure 5. This is in agreement with the experimental results of Goldstein et. al. [11] and also the Navier Stokes numerical solutions of Morihara [12].

Diffuser

The predicted stream function contours for the flow through a diffusing channel with a 45^{o} angle of divirgence at Reynolds numbers of 10 and 15 are presented in Figure 6. The tolerances for the stream function and vorticity were 10^{-4} and 10^{-2}, respectively, requiring 52 overall iterations and 64.8 CPU seconds. This internal flow configuration demonstrates flow separation and reattachment resulting from the strong adverse pressure gradient in this highly divergent channel. The separation and recirculation regions are predicted, with the separation location moving downstream as the Reynolds number is decreased.

Flat Plate Airfoil

Predictions of the flow past a flat plate airfoil at mean flow incidence angles of 0°, 12°, and 18°, and Reynolds numbers between 100 and 1,000 are presented in Figures 7 through 13. In these figures, the overall features of the flow field are shown in the form of stream function contours, with vorticity distributions on the airfoil surfaces used to quantify the regions of flow separation. In particular, the stream function contours qualitatively show the separation region with the vorticity distributions on the upper and lower surfaces of the airfoil showing the exact locations of the flow separation and reattachment. When the vorticity is zero, the flow separates from the airfoil surface, with reattachment predicted when the vorticity again takes on a zero value.

For these predictions, a 45 x 35 grid with $\Delta X = \Delta Y = 0.025$ was utilized. The convergence criteria for the stream function was 10^{-4} while the internal tolerance for the vorticity was 10^{-2} and the external convergence criteria was $5x10^{-2}$. Computational time on the Cyber 205 ranged from 565.6 CPU seconds for a Reynolds number of 100 at 0° of incidence, requiring 163 stream function - vorticity iterations, to 1105.6 CPU seconds requiring 321 iterations for a Reynolds number of 1000 at an incidence angle of 12°.

At each incidence angle, the thickness of the boundary layer decreases as the Reynolds number increases, as expected. Also, at 0° of incidence, the flow does not separate from the airfoil, as seen in Figures 7 and 8 for Reynolds numbers of 100 and 1,000, respectively. However, as the incidence angle is increased, regions of separated flow are predicted, with the characteristics of the separation at each

incidence angle a function of the Reynolds number.

At 12° of incidence, no flow separation is found at a Reynolds number of 100, Figure 9. However, increasing the value of the Reynolds number is seen to result in separation. At a Reynolds number of 500, Figure 10 shows that the flow separates from the airfoil at approximately 40% of the chord and reattaches near the trailing edge. Increasing the Reynolds number to 1,000 results in the flow separation position moving forward to approximately 25% of the airfoil chord and the reattachment point moving just slightly forward, Figure 11.

The effect of Reynolds number on flow separation and reattachment on the airfoil is further demonstrated at an incidence angle of 18°. At a Reynolds number of 100, Figure 12 shows that the flow separates from the airfoil near midchord, with reattachment indicated at approximately 80% of the chord. Increasing the Reynolds number to 500, results in moving the separation point forward to 10% of the chord, with reattachment moving rearward to approximately 95% of the chord, Figure 13.

SUMMARY AND CONCLUSIONS

A locally analytic numerical method has been developed to predict the two-dimensional internal and external steady laminar flow of an incompressible viscous fluid. In this numerical method, analytic solutions of locally linearized partial differential equations are incorporated into the solution. This is accomplished by dividing the flow field into computational grid elements. In each individual element, the nonlinear convective terms of the Navier-Stokes equations are locally

linearized, with analytic solutions then determined. The solution for the complete flow field solution is obtained by the assembly of these locally analytic solutions.

The ability of this locally analytic numerical solution to predict flow development, reversal, separation, and reattachment at moderate values of the Reynolds number for both internal and external flow configurations was then demonstrated. This was accomplished by utilizing this numerical solution technique to predict the developing flow in a straight channel, the flow through a sudden expansion, i.e., over a backward step, the flow in a diffuser, and the flow past a flat plate airfoil over a range of mean flow incidence angle values.

ACKNOWLEDGEMENT

This research was sponsored, in part, by the Air Force Office of Scientific Research.

REFERENCES

1. Spreiter, J.R. and Alksne, A.Y., "Thin Airfoil Theory Based on Approximate Solution of the Transonic Flow Equation," *NACA-TR-1959*, 1958.

2. Spreiter, J.R., "Aerodynamics of Wings and Bodies at Transonic Speeds," *Journal of the Aerospace Sciences*, Volume 26, Number 8, pp 465-487, August 1959.

3. Spreiter, J.R., "The Local Linearization Method in Transonic Flow Theory," *Symposium Transsonicum*, K. Oswatitsch, editor, Springer-Verlag, Berlin-Gottingen-Heidelberg, pp 92-109, 1964.

4. Stahara, S.S., and Spreiter, J.R., "Development of a Nonlinear Unsteady Transonic Flow Theory," *NASA CR-2258*, June 1973.

5. Dowell, E.H., "A Simplified Theory of Oscillating Airfoils in Transonic Flow," *Proceedings of Symposium on Unsteady Aerodynamics*, Kinney, R.B., editor, University of Arizona, Tucson, pp 655-679, July 1975.

6. Chen, C.J., Naseri-Neshat, H. and Ho, K.S., "Finite Analytic Numerical Solution of Heat Transfer in Two-Dimensional Cavity Flow," *Journal of Numerical Heat Transfer*, Vol. 4, pp 179-197, 1981.

7. Chen, C.J., and Yoon, Y.H., "Finite Analytic Numerical Solution of Axisymmetric Navier-Stokes and Energy Equations," *Journal of Heat Transfer*, Vol. 105, pp 639-645, August 1983.

8. Chen, C.J. and Li, P., "Finite Differential Methods in Heat Conduct - Application of Analytic Solution Techniques, *ASME Paper 79-WA/HT-50*, December 1979.

9. Chen, C.J., and Li, P., "The Finite Analytic Method for Steady and Unsteady Heat Transfer Problems" *ASME Paper 80-HT-86*, 1980.

10. Schlichting, H., "Boundary Layer Theory," McGraw-Hill Book Company, copyright 1960.

11. Goldstein, R.J., Eriksen, V.L. Olson, R.M., and Eckert, E.R.G., "Laminar Separation, Reattachment, and Transition of the Flow over a Downstream-Facing Step," *Journal of Basic Engineering*, Vol. 92, 1970 pp 732-741.

12. Moriharo, H. "Numerical Integration of the Navier-Stokes Equations". Ph.D. Dissertation, State University of New York at Buffalo 1972.

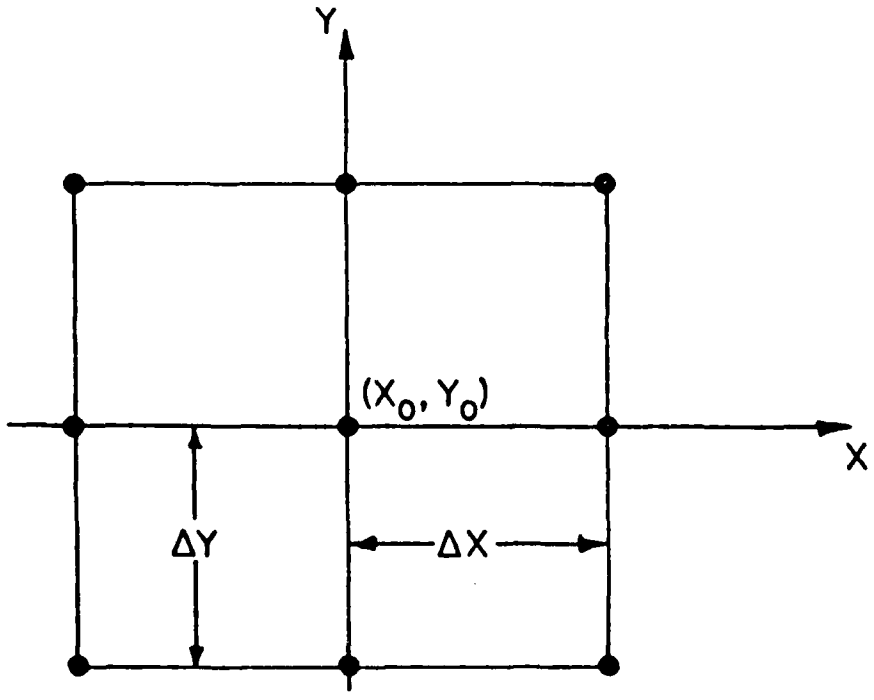

Figure 1. Typical computational grid element

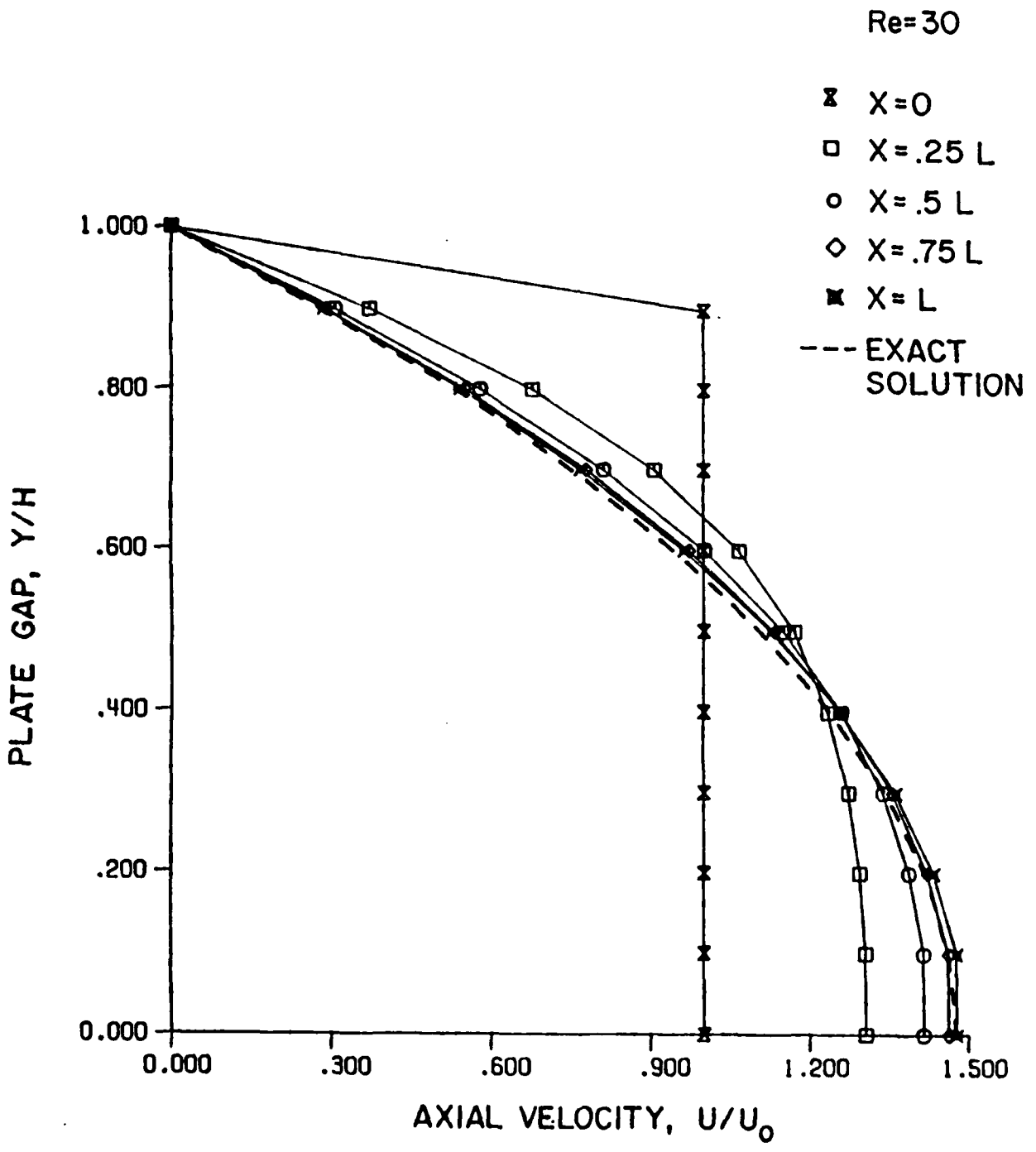

Figure 2. Flow development between two parallel flat plates

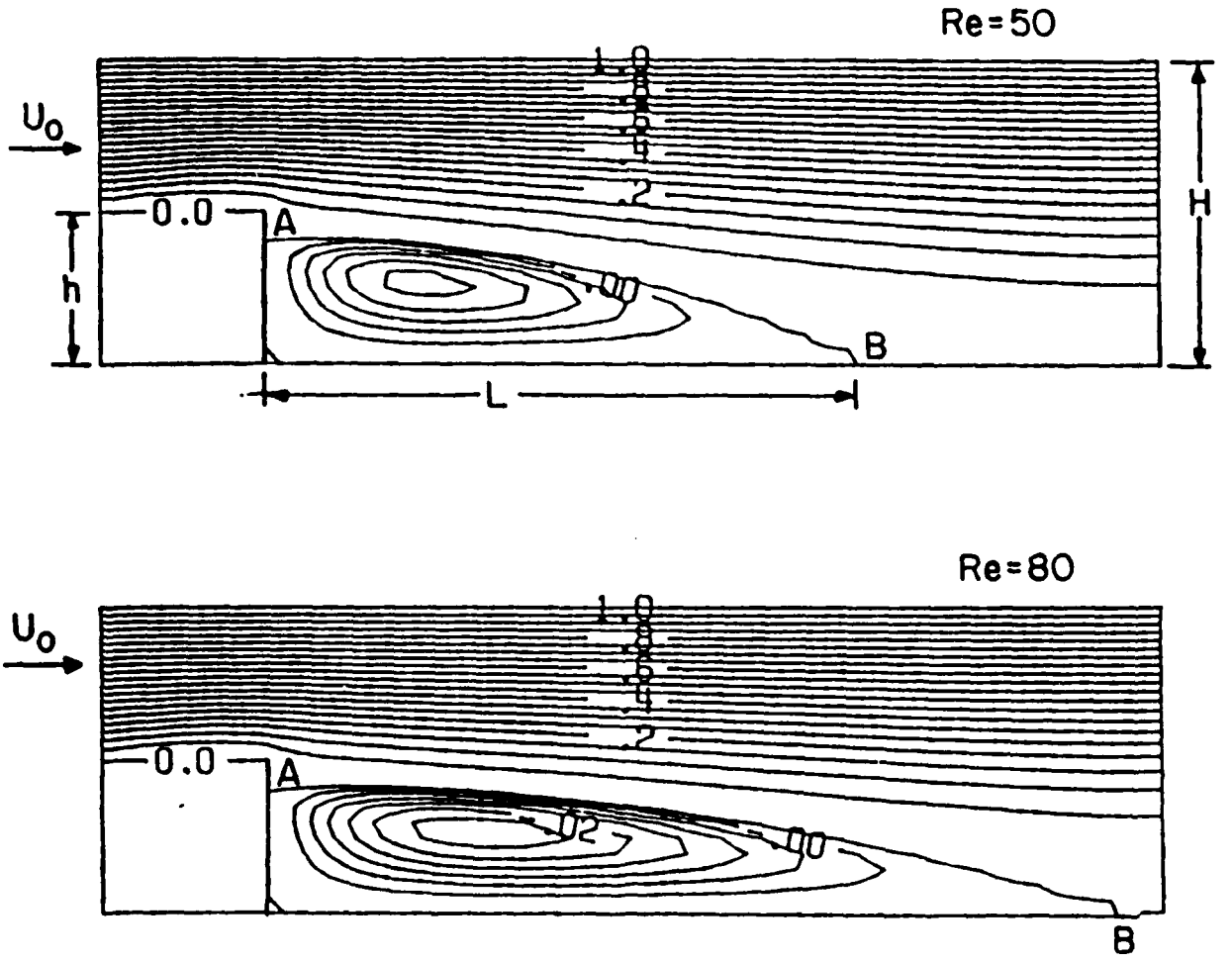

Figure 3. Stream function contours for the flow in a channel with a sudden expansion of area ratio 3:1

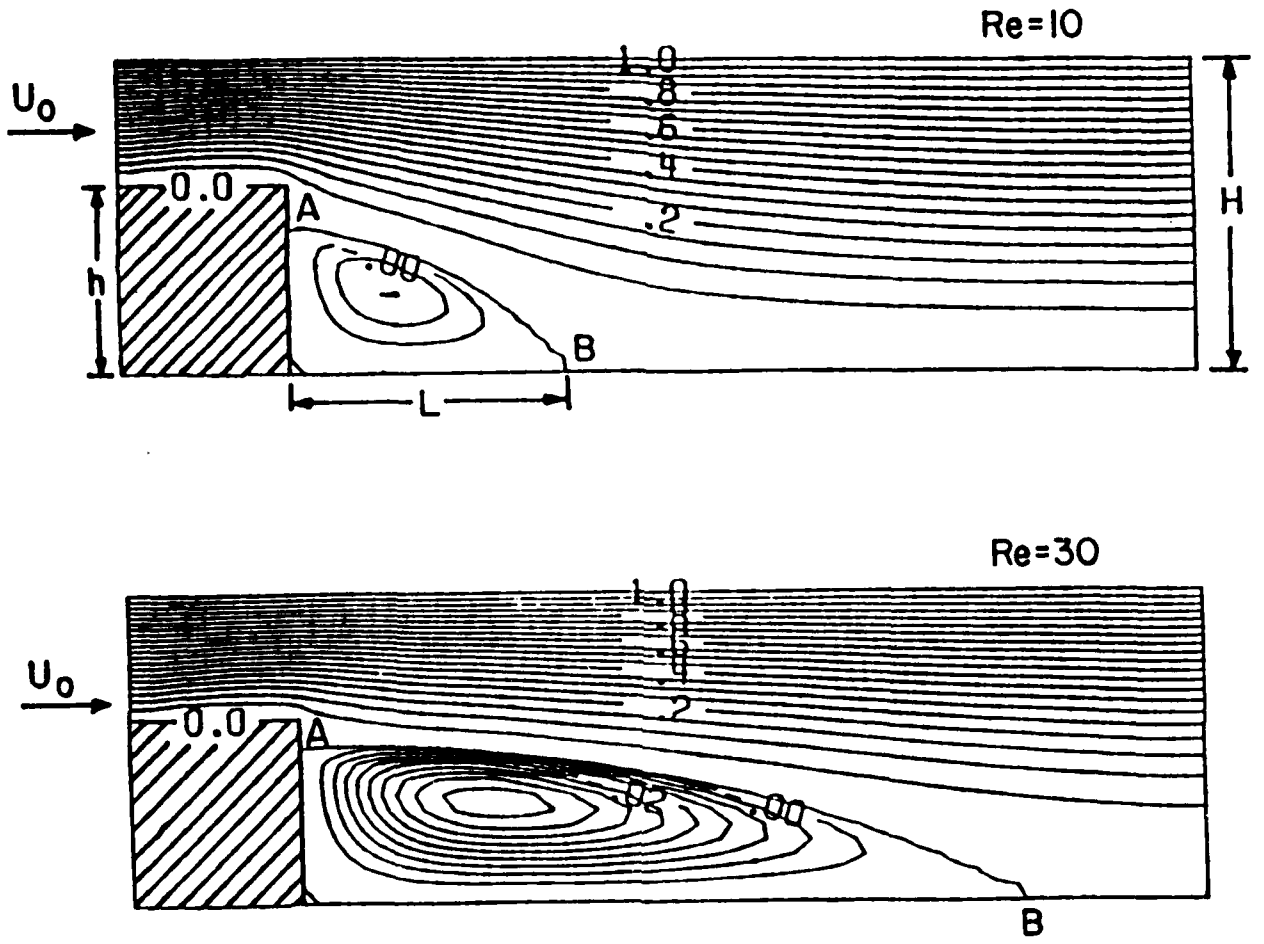

Figure 4. Stream function contours for the flow in a channel with a sudden expansion of area ratio 2:1

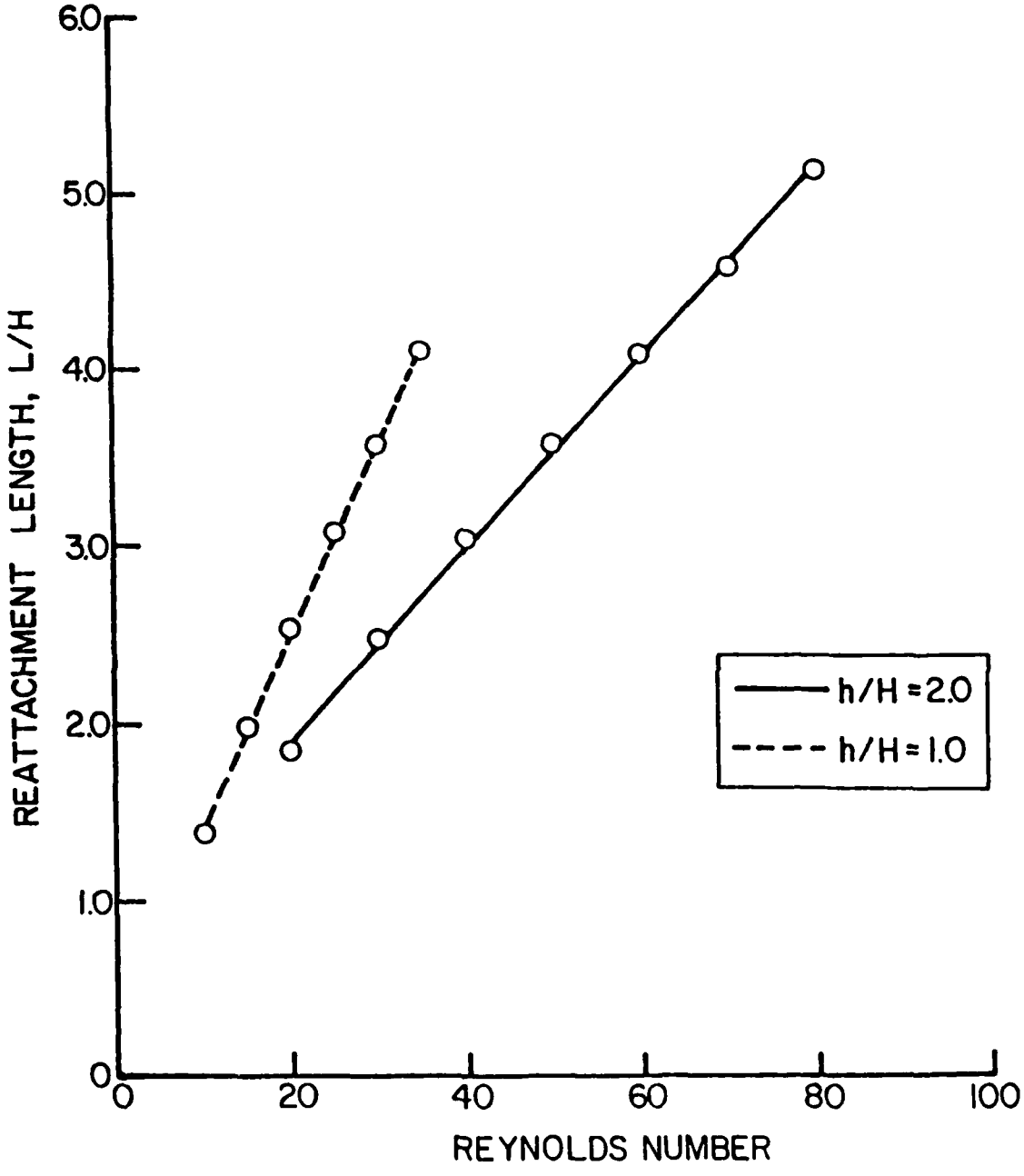

Figure 5. Reattachment length in the sudden expansion as a function of the Reynolds number

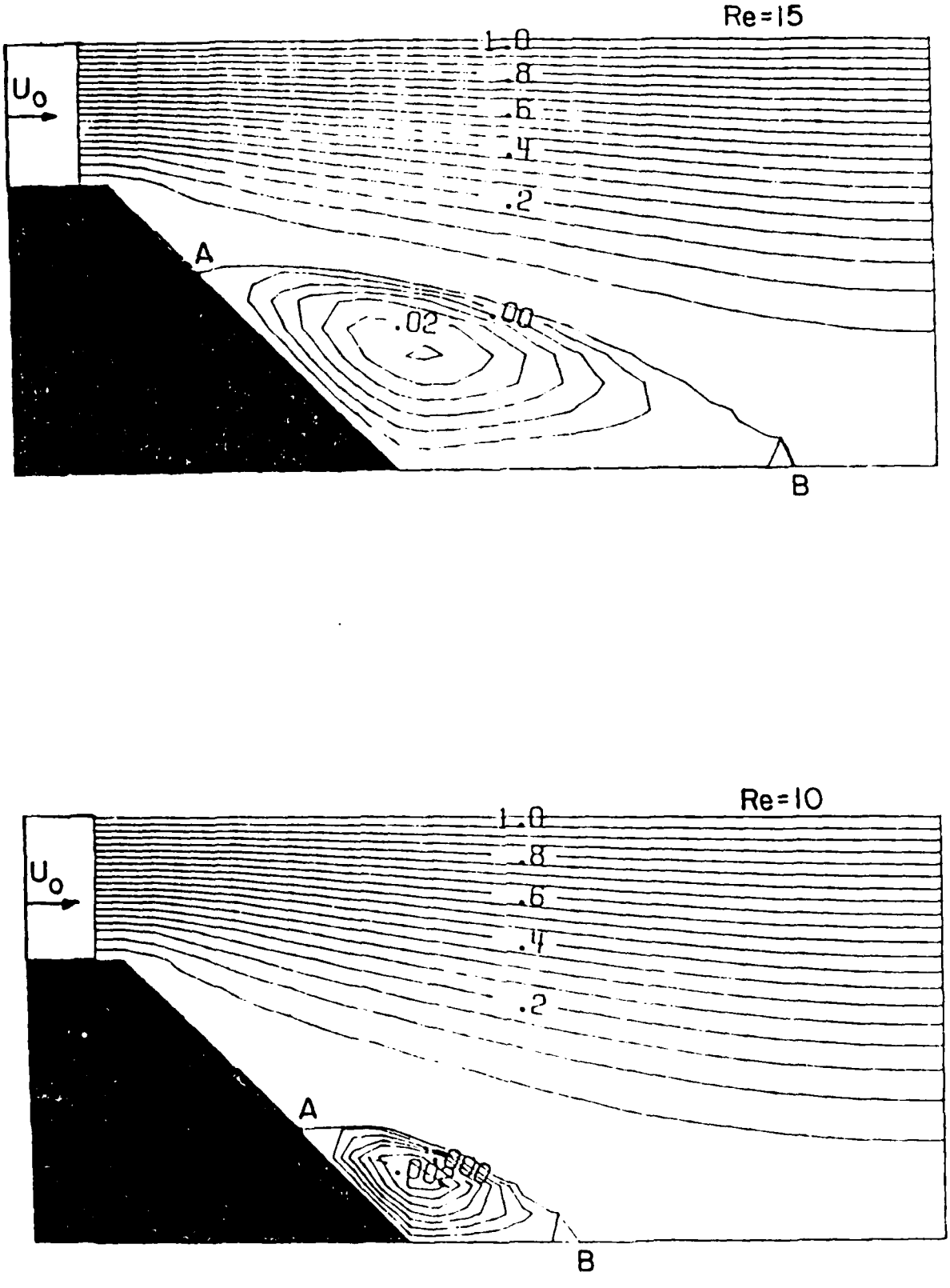

Figure 6. Stream function contours in a diffusing channel

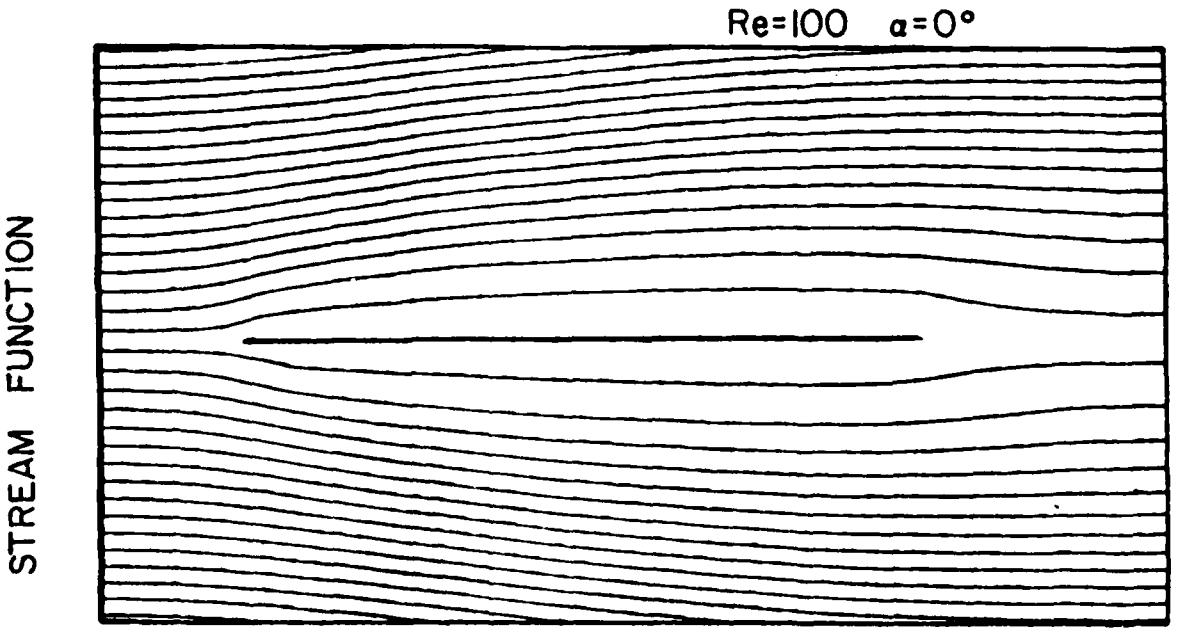

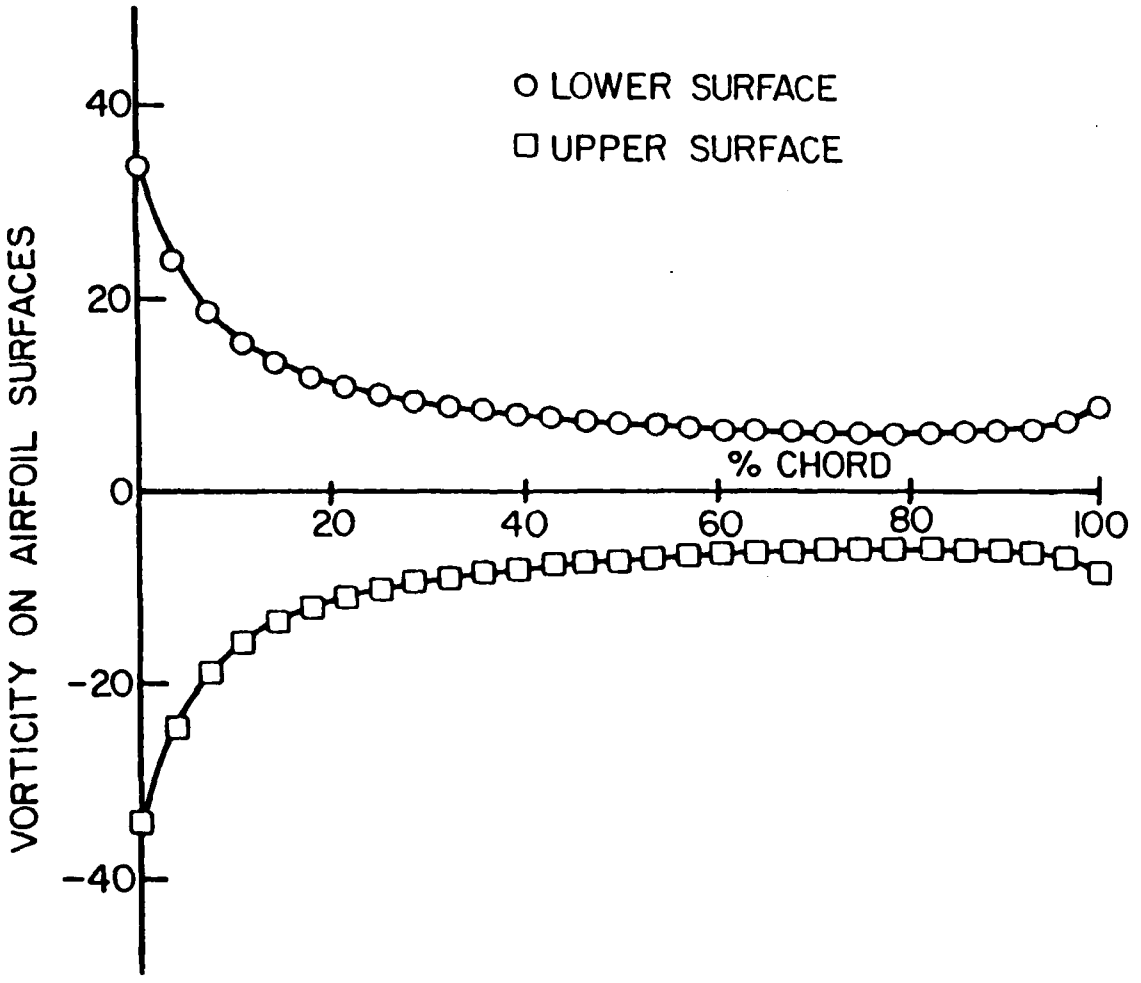

Figure 7. Stream function and airfoil surface vorticity distributions for flow past an airfoil at 0° of incidence and a Reynolds number of 100

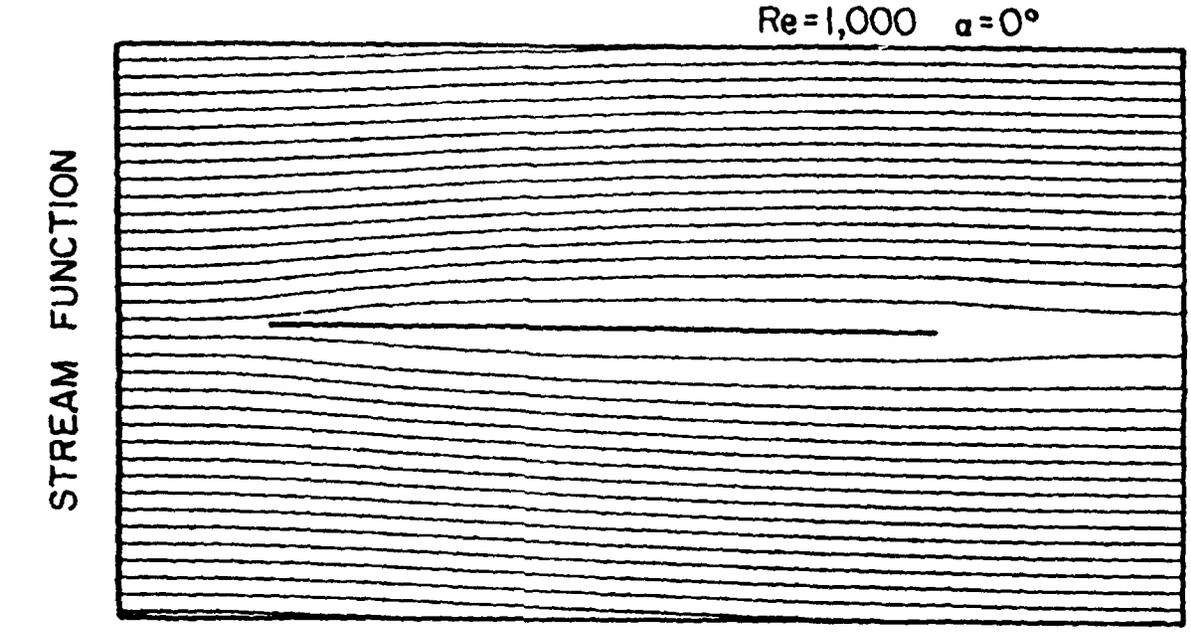

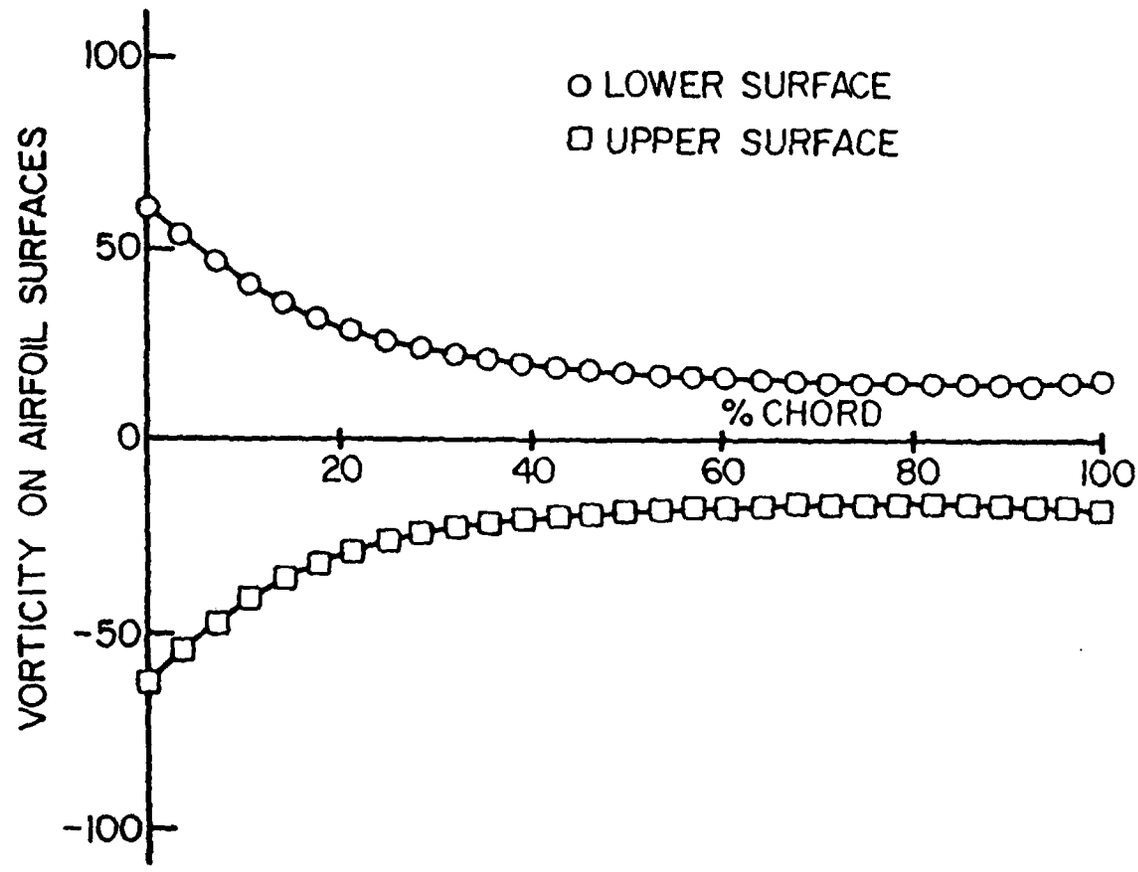

Figure 8. Stream function and airfoil surface vorticity distributions for flow past an airfoil at 0° of incidence and a Reynolds number of 1000

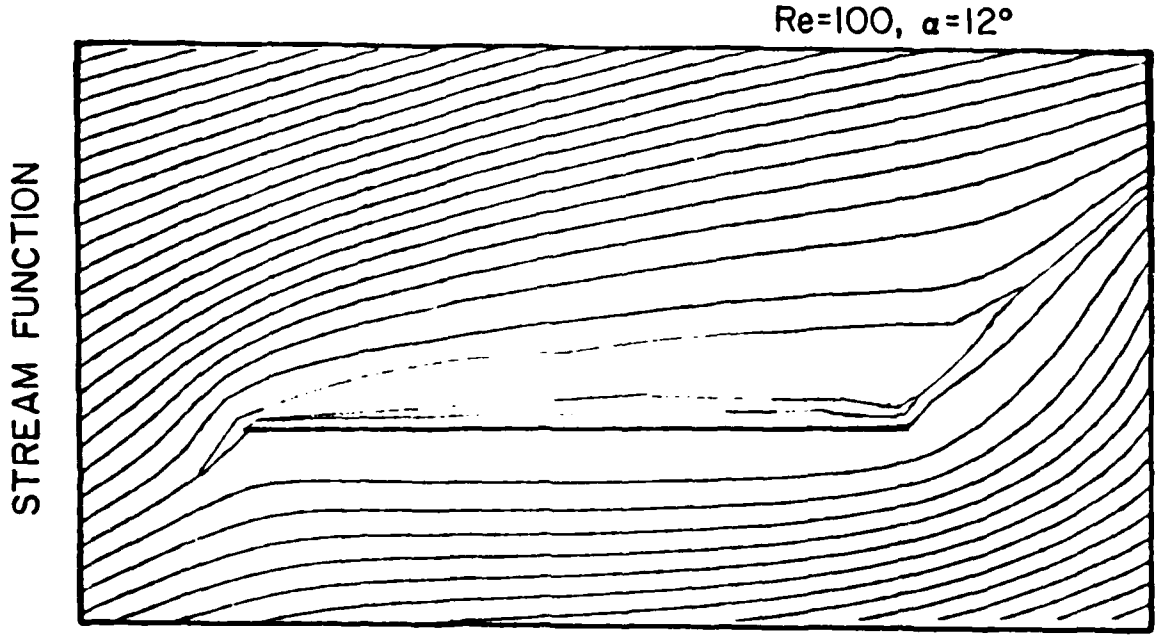

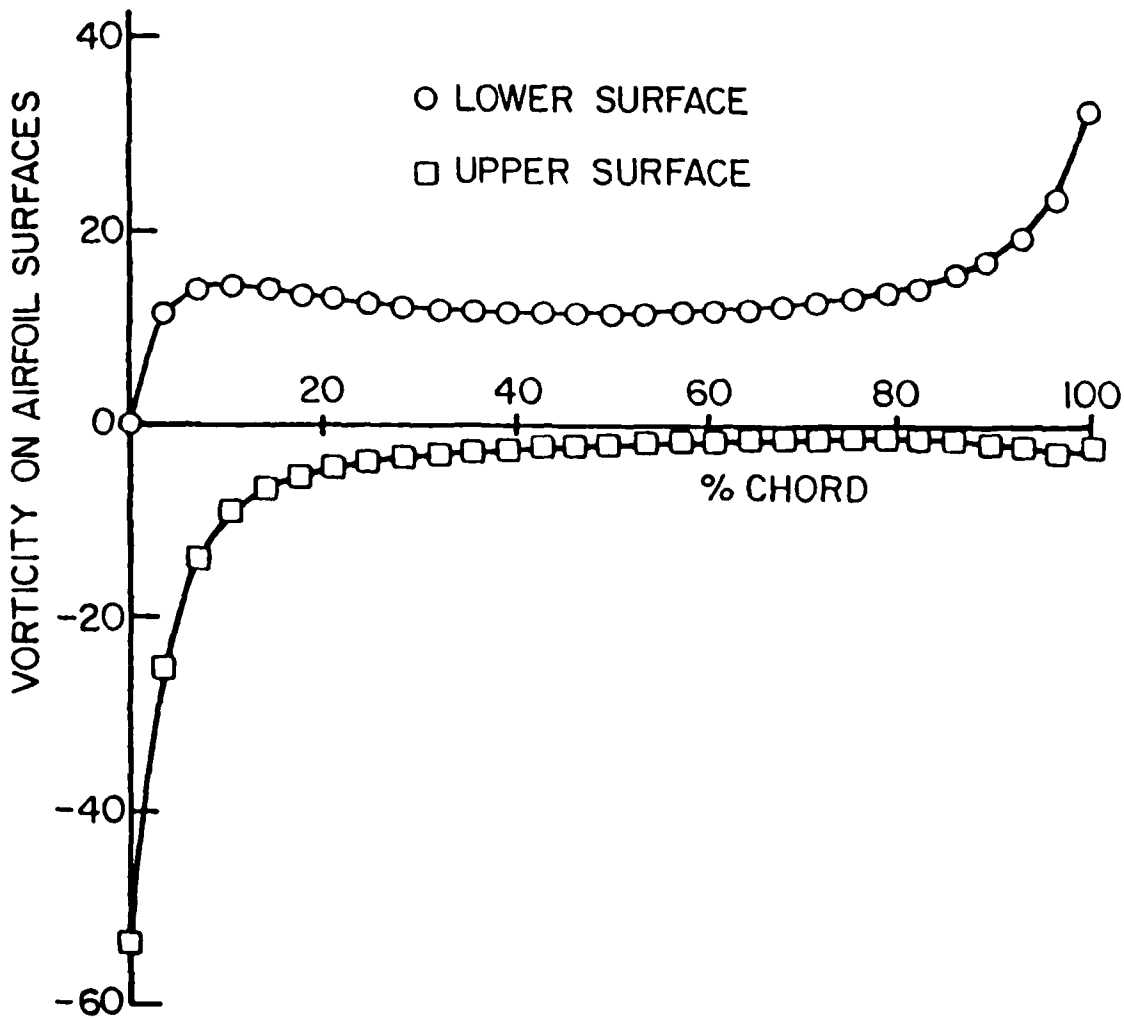

Figure 9. Stream function and airfoil surface vorticity distributions for flow past an airfoil at 12° of incidence and a Reynolds number of 100

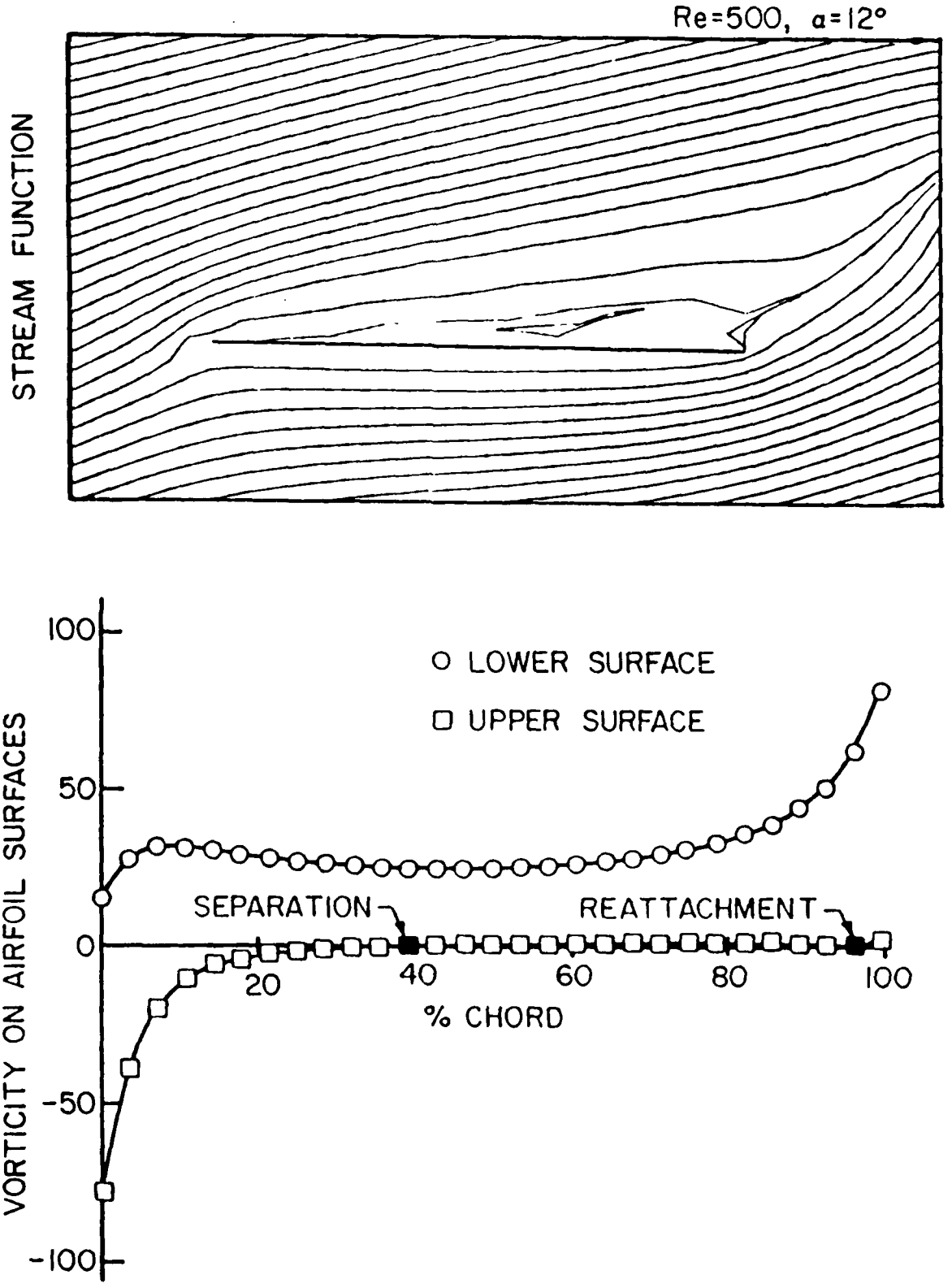

Figure 10. Stream function and airfoil surface vorticity distributions for flow past an airfoil at 12° of incidence and a Reynolds number of 500

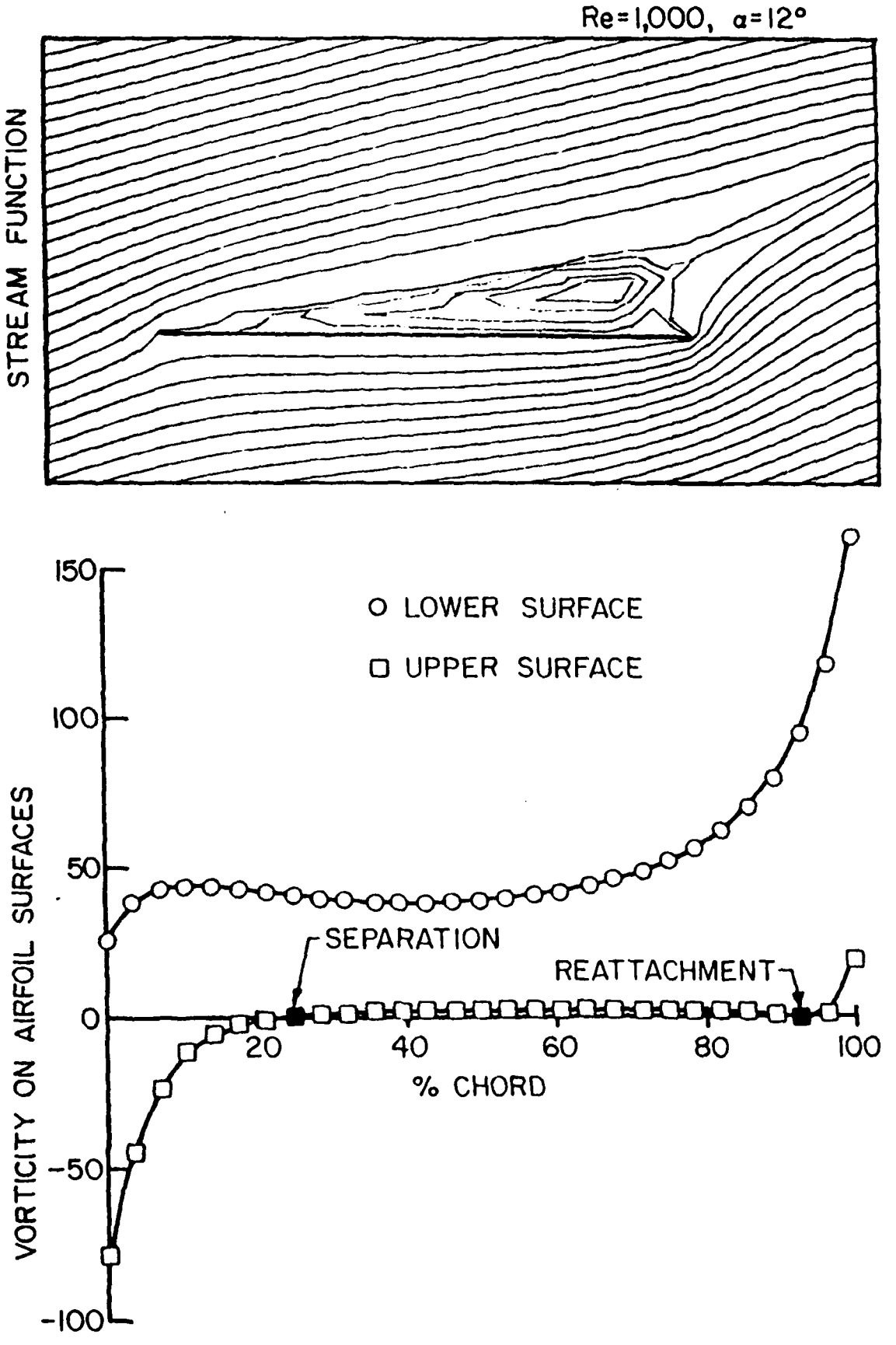

Figure 11. Stream function and airfoil surface vorticity distributions for flow past an airfoil at 12° of incidence and a Reynolds number of 1000

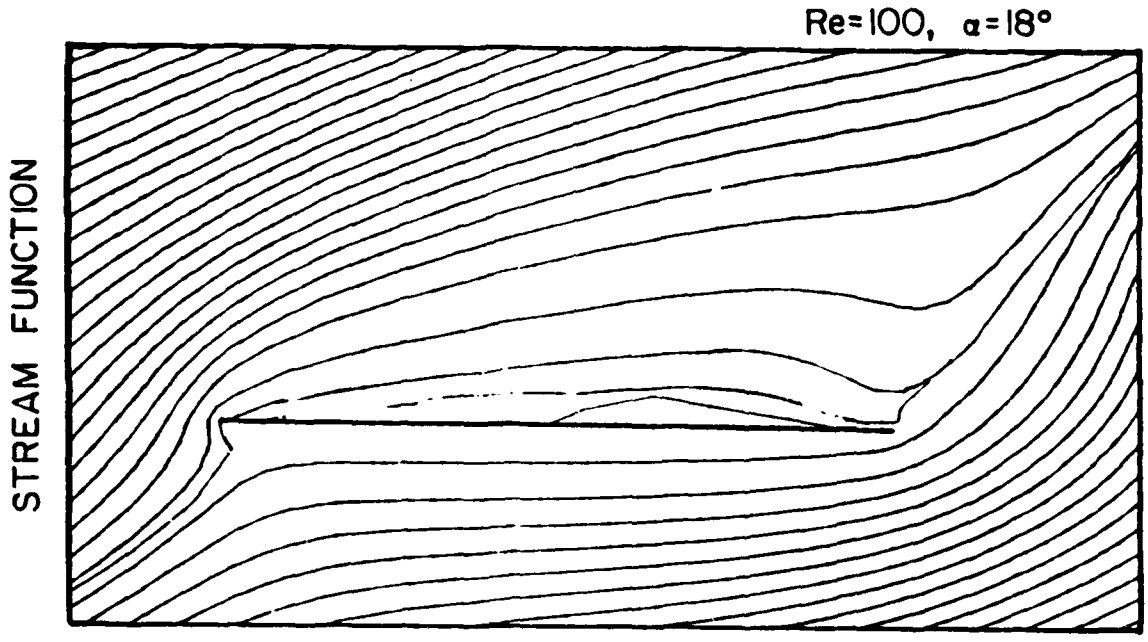

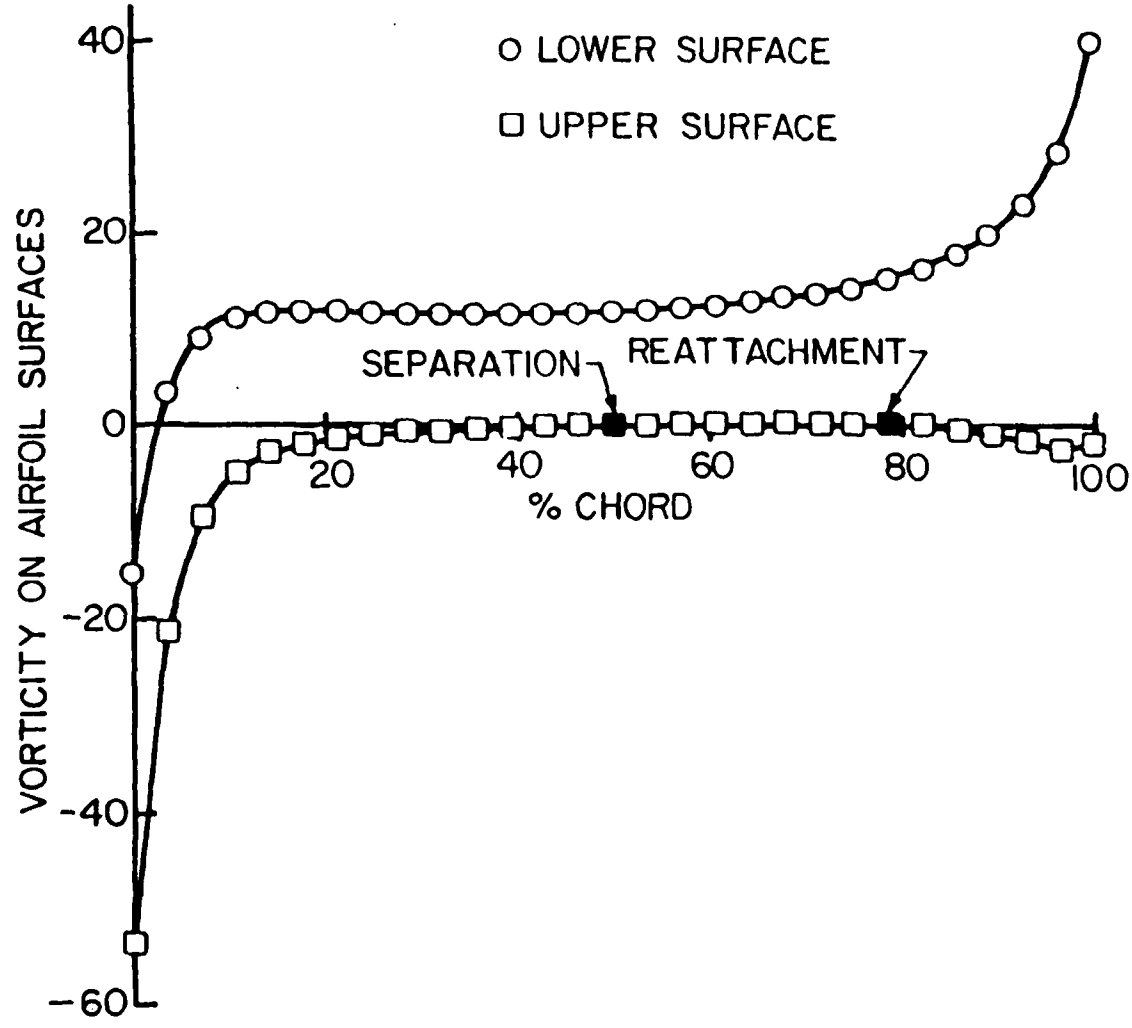

Figure 12. Stream function and airfoil surface vorticity distributions for flow past an airfoil at 18° of incidence and a Reynolds number of 100.

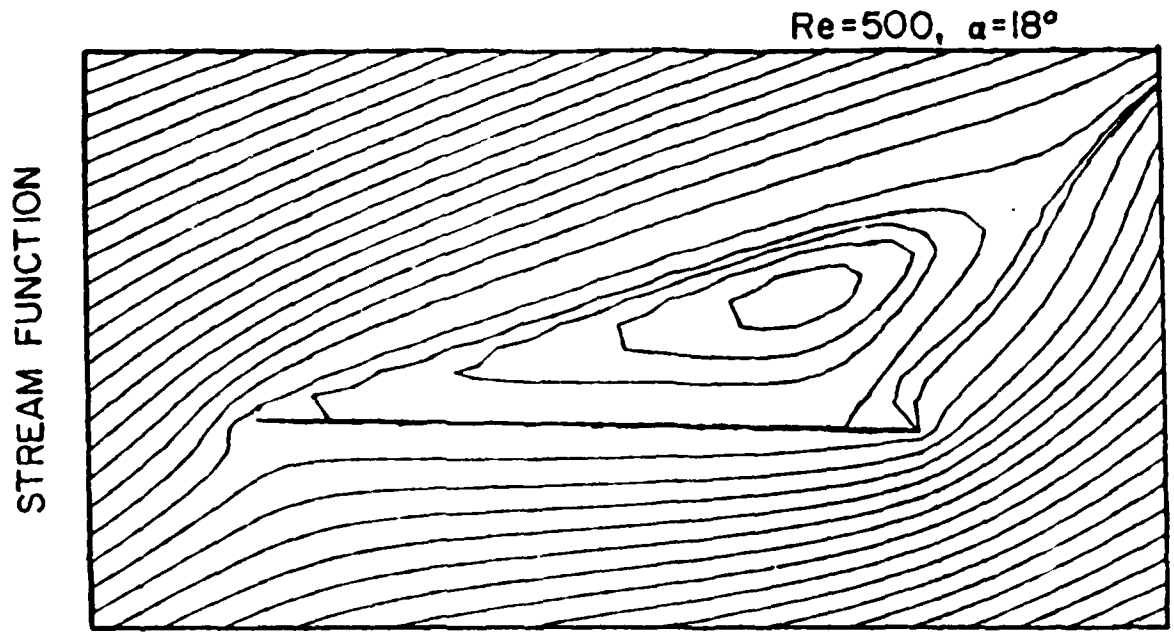

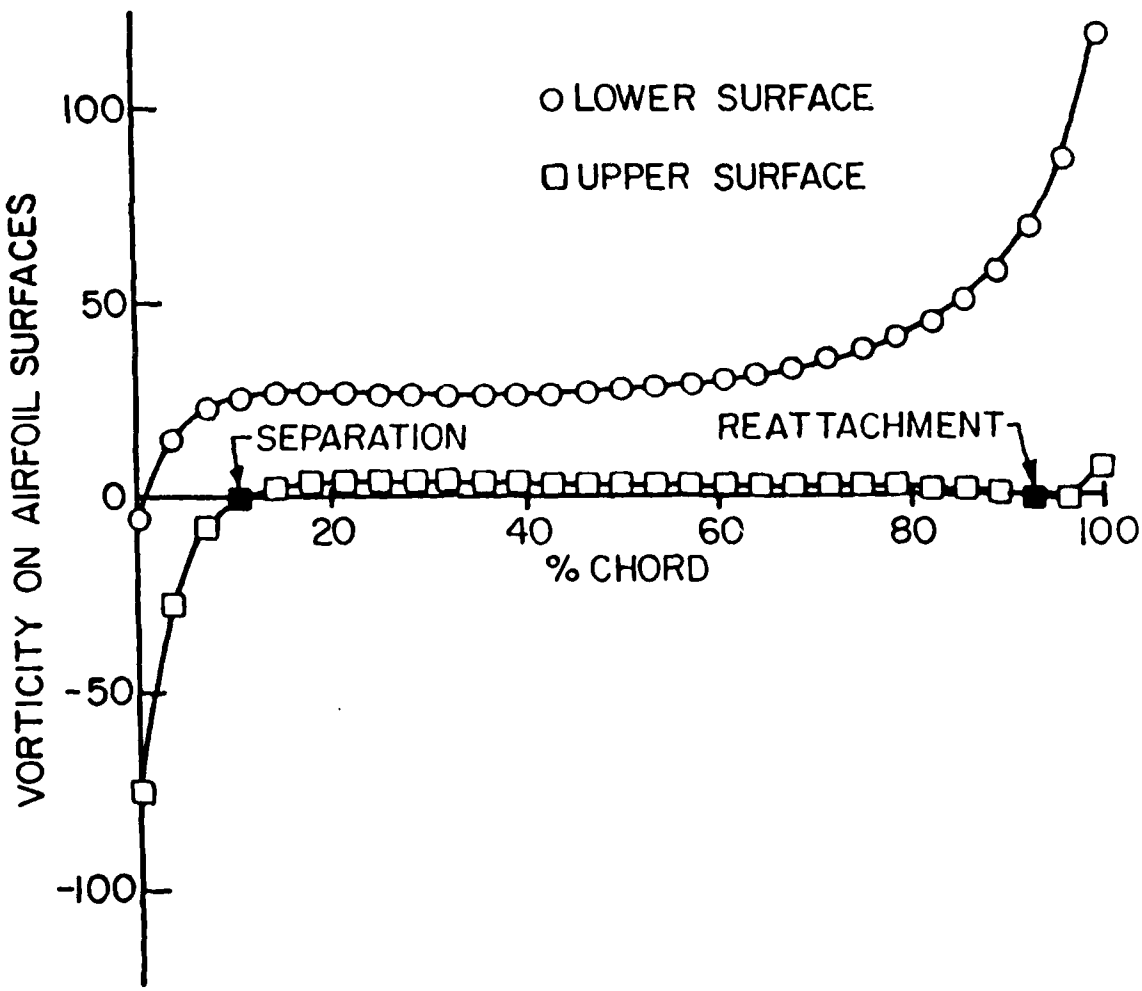

Figure 13. Stream function and airfoil surface vorticity distributions for flow past an airfoil at 18° of incidence and a Reynolds number of 500

APPENDIX IX

PREDICTION OF LOADED AIRFOIL UNSTEADY AERODYNAMIC GUST RESPONSE

INTERNATIONAL JOURNAL OF MATHEMATICAL MODELING

PREDICTION OF LOADED AIRFOIL UNSTEADY AERODYNAMIC GUST RESPONSE BY A LOCALLY ANALYTICAL METHOD

Hsiao-Wei D. Chiang and Sanford Fleeter

Thermal Sciences and Propulsion Center
School of Mechanical Engineering
Purdue University
West Lafayette, Indiana 47907

ABSTRACT

A complete first order model is formulated to analyze the effects of steady loading on the incompressible unsteady aerodynamics generated by a two-dimensional gust convected with the steady mean flow past an arbitrary airfoil at finite nonzero angle of attack. A locally analytical solution is then developed in which the discrete algebraic equations which represent the flow field equations are obtained from analytical solutions in individual grid elements. The unsteady flow field is rotational, and is linearized about the full potential steady flow past the airfoil. Thus, the effects of airfoil geometry and angle of attack are completely accounted for through the mean potential flow field. The steady flow is independent of the unsteady flow. However, the strong dependence of the unsteady flow on the steady effects of airfoil geometry and finite angle of attack are manifested in the unsteady boundary conditions which are coupled to the steady flow. A body fitted computational grid is utilized. Analytical solutions to the transformed flow equations in individual grid elements are then developed, with the complete solution obtained by assembling these locally analytical solutions. This model and locally analytical solution are then applied to a series of airfoil and flow configurations. The results demonstrate that accurate predictions for the unsteady aerodynamic gust response are obtained only by including the coupled steady flow effects on the unsteady aerodynamics. Thus for cambered, or cambered and thick airfoils at zero or finite angle of attack, or a thin flat plate airfoil at a nonzero angle of attack, the model and solution developed herein accurately predict the gust response. It was also demonstrated that the classical small perturbation combined transverse and chordwise gust models yield accurate predictions only for the special case of a thin flat plate airfoil at zero angle of attack, i.e., only when the chordwise gust is zero.

NOMENCLATURE

b	airfoil semi-chord, $c/2$
c	airfoil chord
α_o	angle of attack
$\mathcal{U}_\infty$	far field uniform mean flow
U_∞	far field uniform mean flow velocity
A	gust amplitude
ω	gust harmonic frequency
$\mathcal{K}$	gust propagation direction vector
k_1	reduced frequency, $\omega b/U_\infty$
k_2	transverse gust wave number
$\mathcal{Q}$	complete flow field
$\mathcal{Q}_o$	steady mean flow
$\mathcal{Q}_G$	harmonic gust generated unsteady flow
Φ_o	steady velocity potential
x	nondimensional chordwise coordinate, x/b
y	nondimensional normal coordinate, y/b
θ	polar coordinate
Γ	steady flow circulation
$\hat{n}$	surface unit normal
$\mathcal{Q}_R$	rotational unsteady flow field
$\mathcal{Q}_p$	potential unsteady flow field
P_R	unsteady pressure associated with rotational flow
u^+	chordwise gust component
v^+	transverse gust component

Φ'_G	unsteady harmonic gust potential
Φ'_C	circulatory gust velocity potential
Φ'_{NC}	non-circulatory gust velocity potential
Γ'	unsteady circulation
W'	airfoil upwash
f	function describes airfoil profile
P_p	unsteady pressure associated with potential flow
P'_G	total unsteady pressure
ξ	transformed chordwise coordinate
η	transformed normal coordinate
α,β,γ	transformed coordinate functions
F	source term contains the cross derivative term, $\partial^2\bar{\phi}/\partial\xi\partial\eta$.
$\bar{\phi}$	shorthand representation for velocity potential $\Phi_o,\Phi'_{NC},\Phi'_C$.
ϕ	transformed velocity potential

SUPERSCRIPTS

+	upper surface
-	lower surface

INTRODUCTION

The aerodynamic response of an airfoil to a gust is of significance to unsteady aerodynamics, aeroelasticity, and acoustics. However, unsteady aerodynamic gust models have typically been restricted to thin airfoil theory, with the unsteady gust disturbance assumed to be small as compared to the mean steady potential flow field. In addition, the airfoil is considered to be a flat plate at zero incidence. Thus, the unsteady aerodynamics become uncoupled from the steady flow, leading to a model wherein the flow is linearized about a uniform parallel flow. Such models have considered convected gusts transported with the mean velocity of the flow, including both transverse gusts, Sears [1], and linearly combined transverse and chordwise gusts, Horlock [2], with the application of isolated airfoil theories to turbomachines discussed by Horlock and Naumann and Yeh [3]. Unfortunately, these linearized models are only approximate, having neglected second order terms. Thus, they cannot be extended to finite angles of attack or realistic cambered profiles, i.e., loaded airfoil designs.

In many applications, for example aircraft wings and turbomachines, airfoils with arbitrary shape, large camber, and finite angles of attack are required. It is quite apparent that the thin airfoil approach is not adequate for such applications. In this regard, Goldstein and Atassi [4] developed a theory for the inviscid incompressible flow past an oscillating airfoil or an airfoil subject to an interacting periodic gust. The theory assumes that the fluctuating flow velocity is small compared to the mean velocity, with the unsteady flow linearized about the full potential steady flow past the airfoil which accounts for the effects of airfoil geometry and angle of attack.

All of the above noted unsteady aerodynamic models utilize classical airfoil techniques, resulting in analytical solutions. Thus, solutions in the form of integral equations are obtained for the unsteady lift, not the unsteady pressure distribution on the airfoil surfaces which is the fundamental dependent variable. Although such

classical models and integral solution techniques are certainly important, the development and use of computers and numerical methods enables the mathematical modeling to be extended and enhanced. For example, the results presented by Goldstein and Atassi are limited to zero thickness airfoils which have analytical solutions for the steady flow field. However, numerical methods require that the flow field equations be approximated by a set of finite difference equations determined from expansions of appropriate variables. Thus, truncation errors are introduced into the numerical solutions.

In this paper, a complete first order model is formulated, i.e., the thin airfoil approximation is not used, to analyze the effects of steady loading on the incompressible unsteady aerodynamics generated by a two-dimensional gust convected with the steady mean flow past an arbitrary thick, cambered, airfoil at non-zero angle of attack. The unsteady flow field is considered to be rotational, and is linearized about the full steady potential flow past the airfoil. Thus, the effects of airfoil thickness and camber as well as mean flow angle of attack are completely accounted for through the mean potential flow field. The steady potential flow field and the unsteady potential flow component are individually described by Laplace equations, with the unsteady potential decomposed into circulatory and noncirculatory parts. The steady velocity potential is independent of the unsteady flow field. However, the strong dependence of the unsteady aerodynamics on the steady effects of airfoil geometry and angle of attack are manifested in the coupling of the unsteady and steady flow fields through the unsteady boundary conditions.

A locally analytical solution is developed. In this method, the discrete algebraic equations which represent the flow field equations are obtained from analytical solutions in individual grid elements. Thus, this locally analytical method relates classical fluid mechanics and modern computational techniques. A body fitted computational grid is utilized. General analytical solutions to the transformed Laplace equations are

developed by applying these solutions to individual grid elements, i.e., the integration and separation constants are determined from the boundary conditions in each grid elements. The complete flow field is then obtained by assembling these locally analytical solutions.

The concept of locally linearized solutions was applied to the problem of the steady inviscid transonic flow past thin airfoils by Spreiter et al, references 5, 6, and 7, and subsequently extended to oscillating airfoils in transonic flow by Stahara and Spreiter, reference 8. Also, Dowell developed a rational approximate method for unsteady transonic flow which is broadly related to the local linearization concept, reference 9. The locally analytic numerical method for steady two-dimensional fluid flow and heat transfer problems was initially developed by Chen et. al., reference 10 through 12. They have shown that this method has several advantages over the finite difference and finite element methods. In particular, it is more accurate as no truncation errors are introduced, less dependent on grid size and the system of algebraic equations are relatively stable. Also, since the solution is analytical, it is differentiable and is a continuous function in the solution domain. The disadvantage is that a great deal of mathematical analysis is required before programming.

MATHEMATICAL MODEL

The flow of a two-dimensional unsteady aerodynamic gust past a thick, cambered, airfoil at finite angle of attack α_o with respect to the far field uniform mean flow, $\mathcal{U}_\infty = U_\infty \hat{i}$, is depicted schematically in Figure 1 together with the dimensionless cartesian coordinate system. The periodic gust amplitude and harmonic frequency are denoted by A and ω, respectively. The two-dimensional gust propagates in the direction $\mathcal{K} = k_1\hat{i} + k_2\hat{j}$, where k_1 is the reduced frequency and k_2 is the transverse gust wave number, i.e., the transverse component of the gust propagation direction vector.

The complete flow field, $\mathcal{Q}$ (x, y, t), is assumed to be comprised of a steady mean

flow and an harmonic gust generated unsteady flow field.

$$\mathcal{Q}(x, y, t) = \mathcal{Q}_o(x, y) + \mathcal{Q}_G(x, y) \exp[ik_1 t] \quad (1)$$

STEADY FLOW FIELD

The model for the steady flow field analyzes the incompressible flow past a thick, cambered, airfoil at finite angle of attack. As the steady flow is assumed to be a potential flow, it is described by the following Laplace equation.

$$\nabla^2 \Phi_o(x, y) = 0 \quad (2)$$

The boundary conditions require that the far field steady flow is uniform and that the normal velocity is zero on the airfoil surfaces.

$$\Phi_o|_{farfield} = U_\infty x + \frac{\Gamma \theta}{2\pi} \quad (3a)$$

$$\frac{\partial \Phi_o}{\partial n}|_{airfoil} = 0 \quad (3b)$$

where U_∞ is the magnitude of the far field uniform flow, Γ is the steady flow circulation, θ is the standard polar coordinate, and $\hat{n}$ denotes the surface unit normal.

The Kutta condition is also applied. It is satisfied by requiring the velocities on the upper and lower airfoil surfaces to be equal in magnitude at the trialing edge.

$$|\mathcal{Q}_o|^+_{TE} = |\mathcal{Q}_o|^-_{TE} \quad (4)$$

where TE, + and - denote the airfoil trailing edge and the upper and lower airfoil surfaces, respectively.

The steady circulation, Γ, is determined from the velocity potential discontinuity along the airfoil wake dividing streamline.

$$\Delta \Phi_o|_{wake} = \Phi_o^+ - \Phi_o^- = \Gamma = \Delta \Phi_o|_{TE} \quad (5)$$

UNSTEADY FLOW FIELD

The harmonic unsteady flow field is determined by decomposing the gust generated unsteady flow field into harmonic rotational, $\mathcal{Q}_R$, and potential, $\mathcal{Q}_P$, components.

$$\mathcal{Q}_G = \mathcal{Q}_R + \mathcal{Q}_P \tag{6}$$

The two-dimensional gust is defined by the rotational component. Thus, the unsteady rotational flow is independent of the unsteady potential flow component. However, the unsteady potential component is coupled to the rotational component. As a result, the unsteady rotational flow field defined by the gust must be determined first.

Unsteady Rotational Flow Field

Rotational flows are described by the Euler equations. In this case, the unsteady rotational flow field is determined from the following set of linearized unsteady Euler equations, determined by linearizing the unsteady flow about the steady flow field.

$$\nabla \cdot \mathcal{Q}_R = 0 \tag{7a}$$

$$\frac{D_o}{Dt} \mathcal{Q}_R + \mathcal{Q}_R \cdot \nabla(\nabla \Phi_o) = -\frac{1}{\rho} \nabla P_R \tag{7b}$$

where $\frac{D_o}{Dt}( ) = \frac{\partial}{\partial t}( ) + \mathcal{Q}_o \cdot \nabla( )$ and P_R is the unsteady pressure associated with the rotational gust flow field.

The gust is assumed to be convected with the steady mean flow past the airfoil and, therefore, does not interact with the airfoil. The following solution for the rotational gust is thus determined by solving the linearized Euler equations in the far upstream where the steady flow field is uniform.

$$\mathcal{Q}_R = u^+ \hat{i} + v^+ \hat{j} \tag{8}$$

where $u^+ = -A\, k_2 \exp[ik_1(t-x) - ik_2 y]$ and $v^+ = A\, k_1 \exp[ik_1(t-x) - ik_2 y]$.

It should be noted that in this gust solution, the components u^+ and v^+ are coupled, with the ratio of their amplitudes being $u^+/v^+ = -k_2/k_1$. Also, this solution corresponds exactly to the Sears transverse gust when $k_2 = 0$, i.e., $u^+ = 0$ and $v^+ = A\, k_1\, [\exp ik_1(t-x)]$. However, this gust solution differs from that used in the Horlock and Naumann and Yeh models in which: (1) the two gust components are uncoupled, $u^+ = \bar{u}^+ \exp [ik_1(t-x)]$ and $v^+ = \bar{v}^+ \exp [ik_1(t-x)]$ where $\bar{u}^+$ and $\bar{v}^+$ denote the individual amplitudes of the two gust components; (2) the gust and resulting unsteady aerodynamics are independent of the transverse component of the gust propagation direction vector $\mathcal{K} = k_1\hat{i} + k_2\hat{j}$.

With the unsteady rotational flow field determined, Equation 8, the resulting unsteady pressure due to the rotational gust flow field is determined in terms of the steady flow field from the following form of Equation 7b, the linearized unsteady momentum equation.

$$\nabla P_R = -\rho \left[\nabla(\mathcal{Q}_o \cdot \mathcal{Q}_R) + \frac{\partial \mathcal{Q}_R}{\partial t} - \mathcal{Q}_o \times (\nabla \times \mathcal{Q}_R) \right] \qquad (9)$$

Potential Unsteady Flow Field

The unsteady harmonic gust potential flow component, Φ'_G, is described by a Laplace equation. The solution is determined by decomposing this potential function into circulatory and noncirculatory components, $\Phi'_C(x,y)$ and $\Phi'_{NC}(x,y)$, each of which is individually described by a Laplace equation.

$$\mathcal{Q}_p = \frac{\partial \Phi'_G}{\partial x}\,\hat{i} + \frac{\partial \Phi'_G}{\partial y}\,\hat{j} \qquad (10a)$$

$$\Phi'_G = \Phi'_C + \Gamma' \Phi'_{NC} \qquad (10b)$$

$$\nabla^2 \Phi'_C = 0 \;;\; \nabla^2 \Phi'_{NC} = 0 \qquad (10c)$$

where Γ' is the unsteady circulation.

Boundary conditions must be specified in the far field, on the airfoil surfaces, and on the wake dividing streamline for the circulatory and noncirculatory components.

In the far field, the potential part of the unsteady flow vanishes.

$$\Phi'_C|_{\text{farfield}} = 0 \tag{11a}$$

$$\Phi'_{NC}|_{\text{farfield}} = 0 \tag{11b}$$

The airfoil surface boundary conditions specify that the normal velocity of the flow field is equal to that of the airfoil.

$$\frac{\partial \Phi'_C}{\partial n}|_{\text{airfoil}} = 0 \tag{12a}$$

$$\frac{\partial \Phi'_{NC}}{\partial n}|_{\text{airfoil}} = W'(x,y) = \text{Upwash} \tag{12b}$$

The gust generated unsteady rotational and potential flow fields are coupled through the boundary conditions on the noncirculatory unsteady potential. In particular, the airfoil is stationary, with the rotational gust defined in Equation 8 convected with the mean steady flow field. Thus the upwash on the airfoil, $W'(x,y)$, is determined by requiring the normal component of the unsteady flow field to be zero on the airfoil.

$$\frac{\partial \Phi'_{NC}}{\partial n}|_{\text{airfoil}} = W'(x,y) = \hat{n} \cdot \mathcal{Q}_R$$

or

$$W'(x,y) = A\left(\frac{\partial f}{\partial x} k_2 + k_1\right) \exp[-i(k_1 x + k_2 y)] \tag{13}$$

where $f(x)$ specifies the airfoil profile.

The boundary conditions along the airfoil wake dividing streamline are specified in Equation 14. The noncirculatory velocity potential is continuous. The circulatory

component is discontinuous, with this discontinuity specified by requiring the pressure to be continuous across the wake and then utilizing the unsteady Bernoulli equation to relate the velocity potential and the pressure.

$$\Delta\Phi'_C\,|_{wake} = \exp[-ik_1(x-1)] \tag{14a}$$

$$\Delta\Phi'_{NC}\,|_{wake} = 0 \tag{14b}$$

The Kutta condition is also imposed on the unsteady potential flow field by requiring no unsteady pressure difference across the airfoil chordline at the trailing edge. The corresponding relation for the trailing edge unsteady velocity potential difference is then determined from the unsteady Bernoulli equation.

$$\Delta P_p\,|_{TE} = P_p^+|_{TE} - P_p^-|_{TE} = 0 \tag{15a}$$

$$[\nabla\Phi_o\cdot\nabla\Phi'_G + ik_1\Phi'_G]^+|_{TE} = [\nabla\Phi_o\cdot\nabla\Phi'_G + ik_1\Phi'_G]^-\,|_{TE} \tag{15b}$$

where P_p is the unsteady pressure associated with the unsteady potential flow field.

The unsteady dependent variable of primary interest is the unsteady pressure P'_G, from which the unsteady aerodynamic lift on the airfoil is calculated. It is determined from the solution for the steady and unsteady velocity potentials, the unsteady Bernoulli equation, and the unsteady rotational gust pressure P_R, specified in Equation 9.

$$P'_G = -\nabla\Phi_o\cdot\nabla\Phi'_G - ik_1\Phi'_G + P_R \tag{16}$$

COMPUTATIONAL DOMAIN

Computational Grid

The boundary fitted computational grid developed by Thompson, Thames, and Mastin, reference 13, is utilized for the numerical solution because of its general availability. This method permits grid points to be specified along the entire boundary

of the computational plane. As depicted in Figure 2, the boundary in the physical plane is denoted by the curve a-b-c-d-e-f-g-h-i-a and encompasses the airfoil, its wake, and the far field. The application of this grid generation technique results in a smoothly spaced, nonoverlapping grid at the interior points in the transformed (ξ,η) plane. A typical boundary fitted grid for a Joukowski airfoil is shown in Figure 3.

The complete flow field is described by the steady velocity potential, $\Phi_o(x,y)$, and the gust generated unsteady velocity potential which has two components, $\Phi'_{NC}(x,y)$ and $\Phi'_C(x,y)$. These three velocity potentials are each individually described by Laplace equations, as specified in Equations 2 and 10. In the transformed (ξ,η) coordinate system, these Laplace equations have the following nonhomogeneous form.

$$\frac{\partial^2\bar{\phi}}{\partial\xi^2} + \alpha\frac{\partial^2\bar{\phi}}{\partial\eta^2} - 2\,\alpha\beta\,\frac{\partial\bar{\phi}}{\partial\eta} - 2\,\gamma\,\frac{\partial\bar{\phi}}{\partial\xi} = F(\xi,\eta) \qquad (17)$$

where $\bar{\phi}$ is a shorthand method of writing these three velocity potentials in the transformed plane, i.e., $\bar{\phi}$ denotes $\Phi_o(\xi,\eta)$, $\Phi'_{NC}(\xi,\eta)$ or $\Phi'_C(\xi,\eta)$; $F(\xi,\eta)$ contains the cross derivative term $\partial^2\bar{\phi}/\partial\xi\partial\eta$, and the coefficients α, β, and γ are functions of the transformed coordinates ξ and η and are treated as constants in each individual grid element.

Analytical Solution

To obtain the analytical solution to the transformed Laplace equation, it is first rewritten as a homogeneous equation by defining a new dependent variable $\hat{\phi}(\xi,\eta)$.

$$\frac{\partial^2\hat{\phi}}{\partial\xi^2} + \alpha\,\frac{\partial^2\hat{\phi}}{\partial\eta^2} - (\gamma^2 + \alpha\beta^2)\,\hat{\phi} = 0 \qquad (18)$$

where $\bar{\phi} = \hat{\phi}\,\exp\left[\gamma\xi + \beta\eta\right] - \dfrac{F(\gamma\xi + \beta\eta)}{2(\gamma^2 + \alpha\beta^2)}$

The general solution for $\hat{\phi}$ is determined by separation of variables.

$$\phi(\xi,\eta) = [A_1 \cos(\lambda\xi) + A_2 \sin(\lambda\xi)] \times [B_1 \cosh(\mu\eta) + B_2 \sinh(\mu\eta)] \quad (19)$$

where $\mu = [(\gamma^2 + \alpha\beta^2 + \lambda^2)/\alpha]^{1/2}$ and λ, A_1, A_2, B_1, and B_2 are constants to be determined from the boundary conditions.

LOCALLY ANALYTICAL SOLUTION

Analytical solutions in individual computational grid elements are determined by applying proper boundary conditions on each element to evaluate the unknown constants in the general velocity potential solution, Equation 19. The solution of the global problem is then determined through the application of the global boundary conditions and the assembly of the locally analytical solutions.

Grid Element Boundary Conditions

A typical computational grid element is schematically depicted in Figure 4. The local element boundary conditions specify the values of the various velocity potentials at the eight boundary nodal points. However, to obtain unique analytical solutions to the Laplace equation in this element, i.e., determine the values of the integration constants in the general solution for each element, continuous boundary conditions are required on all four boundaries. For numerical purposes, these boundary conditions are expressed in an implicit formulation in terms of the three known nodal values on each element boundary. In particular, a combination of a linear and exponential function are utilized on each boundary as they satisfy the Laplace equation.

$$\phi(\xi,1) = a_1^{(1)} e^{\xi} + a_2^{(1)} \xi + a_3^{(1)} \quad (20a)$$

$$\phi(1,\eta) = a_1^{(2)} e^{\eta} + a_2^{(2)} \eta + a_3^{(2)} \quad (20b)$$

$$\phi(\xi,-1) = a_1^{(3)} e^{\xi} + a_2^{(3)} \xi + a_3^{(3)} \quad (20c)$$

$$\phi(-1,\eta) = a_1^{(4)} e^{\eta} + a_2^{(4)} \eta + a_3^{(4)} \quad (20d)$$

where the constants $a_1^{(i)}$, $a_2^{(i)}$ and $a_3^{(i)}$ are determined from the known values at the three nodal points on each boundary.

Grid Element Analytical Solutions

The general analytical solution to the Laplace equation given in Equation 19 is valid in individual grid elements as well as over the complete flow region. To determine the relationship between the velocity potential at the center of the typical grid element, Figure 4, and its surrounding values, the superposition principle is used to decompose the solution for ϕ into four components, each having only one nonhomogeneous boundary condition.

$$\phi(\xi,\eta) = \sum_{n=1}^{\infty} \Big\{ A_{n_1} \sinh(\mu_n(\eta+1)) \sin(\lambda_n(\xi+1)) \tag{21}$$
$$+ A_{n_2} \sinh(\mu_n(\eta-1)) \sin(\lambda_n(\xi+1))$$
$$+ A_{n_3} \sinh(\mu_n'(\xi+1)) \sin(\lambda_n(\eta+1))$$
$$+ A_{n_4} \sinh(\mu_n'(\xi-1)) \sin(\lambda_n(\eta+1)) \Big\}$$

where $\lambda_n = \frac{n\pi}{2}$; $\mu_n = ((\gamma^2 + \beta^2\alpha + \lambda_n^2)/\alpha)^{1/2}$; $\mu_n' = (\gamma^2 + \beta^2\alpha + \lambda_n^2\alpha)^{1/2}$

The application of the local boundary conditions, Equation 20, together with the orthogonality of the Fourier series leads to the following values for A_{n_i}.

$$A_{n_i} = C_{1ni}\,\phi(1,1) + C_{2ni}\,\phi(1,0) + C_{3ni}\,\phi(1,-1) \tag{22}$$
$$+ C_{4ni}\,\phi(0,-1) + C_{5ni}\,\phi(-1,-1) + C_{6ni}\,\phi(-1,0)$$
$$+ C_{7ni}\,\phi(-1,1) + C_{8ni}\,\phi(0,1)$$

where the constants C_{1ni} ....., C_{8ni} are functions of the $a_1^{(i)}$, $a_2^{(i)}$ and $a_3^{(i)}$ boundary constants.

With the analytical solution in an individual grid element thus specified, Equations

21 and 22, the value of $\tilde{\phi}$ at the center of the element can be written as follows.

$$\tilde{\phi}(0,0) = \sum_{n=1}^{\infty} \left\{ [(A_{n_1} - A_{n_2}) \sinh(\mu_n) + (A_{n_3} - A_{n_4}) \sinh(\mu_n')] \sin(\lambda_n) \right\} \tag{23}$$

Substituting for the A_{n_i} terms from Equation 22 leads to the following.

$$\begin{aligned}\tilde{\phi}(o,o) = {} & C_1' \tilde{\phi}(1,1) + C_2' \tilde{\phi}(1,0) + C_3' \tilde{\phi}(1,-1) + C_4' \tilde{\phi}(0,-1) \\ & + C_5' \tilde{\phi}(-1,-1) + C_6' \tilde{\phi}(-1,0) + C_7' \tilde{\phi}(-1,1) + C_8' \tilde{\phi}(0,1)\end{aligned} \tag{24}$$

where the constants C_1', C_2', ..., C_8' are functions of the $a_1^{(i)}$, $a_2^{(i)}$, and $a_3^{(i)}$ boundary constants as well as the transformed coordinate functions α, β, and γ.

This solution for $\tilde{\phi}$ at the center point is rewritten in terms of the original dependent variable $\bar{\phi}$, in Equation 25.

$$\begin{aligned}\bar{\phi}(0,0) = {} & C_1 \bar{\phi}(1,1) + C_2 \bar{\phi}(1,0) + C_3 \bar{\phi}(1,-1) \\ & + C_4 \bar{\phi}(0,-1) + C_5 \bar{\phi}(-1,-1) + C_6 \bar{\phi}(-1,0) \\ & + C_7 \bar{\phi}(-1,1) + C_8 \bar{\phi}(0,1)\end{aligned} \tag{25}$$

where the constants C_1, C_2,...., C_8 are again functions of the $a_1^{(i)}$, $a_2^{(i)}$, and $a_3^{(i)}$ boundary constants as well as the transformed coordinate function α, β, and γ.

Thus, the local analytical algebraic equation relating the value of the velocity potential at the center of the computational element to its neighboring eight known nodal values has been completely determined.

Computational Procedure

The above technique is applied to adjacent grid elements, with the boundary nodal point considered as the interior point. For a general grid element with center at (i, j),

the resulting algebraic relation between the center value of the velocity potential and its eight surrounding nodal values is given in Equation 26.

$$\begin{aligned}\bar{\phi}(i,j) = {} & C_{i+1,j+1}\bar{\phi}(i+1, j+1) + C_{i+1,j}\,\bar{\phi}(i+1,j) \\ & + C_{i+1,j-1}\,\bar{\phi}(i+1, j-1) + C_{i,j-1}\,\bar{\phi}(i,j-1) \\ & + C_{i-1,j-1}\,\bar{\phi}(i-1, j-1) + C_{i-1,j}\,\bar{\phi}(i-1,j) \\ & + C_{i-1,j+1}\,\bar{\phi}(i-1, j+1) + C_{i,j+1}\,\bar{\phi}(i,j+1)\end{aligned} \tag{26}$$

where $2 \leq i \leq i_{max} - 1$, $2 \leq j \leq j_{max} - 1$ and c_{ij} are functions of the $a_1^{(i)}$, $a_2^{(i)}$, and $a_3^{(i)}$ boundary constants as well as the transformed coordinate functions α, β, and γ.

The global boundary conditions are specified in Equation 27.

$$\bar{\phi}(i,1)\,|_{\text{airfoil surface}} = \text{Upwash} \quad 1 \leq i \leq i_{max} \tag{27a}$$

$$\bar{\phi}(i,j_{max})\,|_{\text{farfield}} = \text{Free Stream} \quad 1 \leq i \leq i_{max} \tag{27b}$$

$$\bar{\phi}(i_{max},j)\,|_{\text{wake}} = \text{Upper Wake} \quad 1 < j < j_{max} \tag{27c}$$

$$\bar{\phi}(1,j)\,|_{\text{wake}} = \text{Lower Wake} \quad 1 < j < j_{max} \tag{27d}$$

These global boundary conditions together with the interior point solution specified in Equation 26 for $\bar{\phi}\,(i,j)$, where $2 \leq i \leq i_{max} - 1$, and $2 \leq j \leq j_{max} - 1$, lead to a system of algebraic equations. For a fixed j value:

$$\begin{aligned}-C_{i-1,j}\,\bar{\phi}(i-1,j) + \bar{\phi}(i,j) - C_{i+1,j}\,\bar{\phi}(i+1,j) = {} & \\ C_{i+1,j+1}\bar{\phi}(i+1,j+1) + C_{i-1,j+1}\bar{\phi}(i-1,j+1) + C_{i,j+1}\bar{\phi}(i,j+1) & \\ + C_{i+1,j-1}\bar{\phi}(i+1,j-1) + C_{i-1,j-1}\bar{\phi}(i-1,j-1) + C_{i,j-1}\bar{\phi}(i,j-1) &\end{aligned} \tag{28}$$

The right hand side of this equation is comprised of known quantities, i.e., the (j-1) terms are known from the boundary conditions (j=2) or the last sweep, with the (j+1) terms determined from the boundary condition ($j=j_{max} - 1$) or the previous iteration.

Equation 28 can be written as a tridiagonal matrix, with the matrix solved by Thomas algorithm for all j values ($2 \leq j \leq j_{max} - 1$). This procedure is then iterated by successive over relaxation until the entire solution converges.

MODEL & SOLUTION TECHNIQUE VERIFICATION

To verify this development of the mathematical model as well as the locally analytical solution technique, predictions from this model are correlated with classical zero angle of attack gust analyses. As these classical solutions are integral solutions, the unsteady aerodynamic lift is considered.

The transverse gust solution of Sears [1] is obtained by setting $k_2 = 0$, per Figure 1. As seen in Figure 5 which presents the real and imaginary parts of the unsteady lift with the reduced frequency as parameter, excellent correlation is obtained.

The Horlock [2] and Naumann and Yeh [3] analyses consider noninteracting linearly combined transverse and chordwise gusts convected past flat plate and constant slightly cambered airfoils, respectively. However, the model developed herein considers two-dimensional interacting gust components, Equation 8. Thus, for the purpose of this model and solution technique verification, the interacting gust components specified in Equation 8 are modified as follows to correspond to the noninteracting chordwise gust.

$$u^+ = \bar{u}^+ \exp\left\{ik_1(t-x)\right\} \tag{29a}$$

$$v^+ = 0 \tag{29b}$$

where $\bar{u}^+$ denotes the amplitude of the chordwise gust components.

The excellent correlation of the predictions for the unsteady aerodynamic lift obtained from the model with appropriately modified boundary conditions and locally analytical solution developed herein and both the Horlock [2] flat plate and the Naumann and Yeh [3] constant slightly cambered airfoils solutions is demonstrated in Figures 6 and 7, respectively.

RESULTS

This complete first order flow model for the unsteady aerodynamic response of an arbitrary airfoil due to a two-dimensional gust and locally analytical solution are utilized to demonstrate the important effect of the coupling between the steady and the unsteady flow fields. Also, the limited application range of the flat plate Horlock [2] and small cambered airfoil Naumann and Yeh [3] combined transverse and chordwise gust models is also shown. This is accomplished by: (1) utilizing the model and solution developed herein to predict the unsteady lift due to the two-dimensional gust on a series of flat plate and cambered airfoils for both zero and non-zero angles of attack over a large range of reduced frequency values; (2) correlating these predictions with ones obtained from the corresponding appropriate Horlock and Naumann and Yeh models. These results are presented in Figures 8 through 12 in the format of the real versus the imaginary components of the unsteady lift with the reduced frequency as parameter.

The effects of thickness and finite angle of attack on the unsteady response of a flat plate airfoil to a 45° gust are shown in Figures 8 and 9, respectively. Airfoil thickness is seen to be significant with regard to the unsteady lift only at relatively small values of the reduced frequency, i.e., thickness affects only the quasi-steady and steady aerodynamics. Also, at zero angle of attack the Horlock, which reduces to the Sears transverse gust model, yields accurate predictions of the unsteady lift. However, increasing the angle of attack to a finite nonzero value has an effect on the predicted unsteady lift, seen by comparing the 0° and 10° angle of attack results. Also, the correlation of the predictions from the model developed herein with the corresponding chordwise gust Horlock model is not very good. This is due to the coupling of the steady and unsteady flow fields at non-zero angle of attack and of the coupled two-dimensional gust included in the flow model developed herein but not in the Horlock model.

Figure 10 shows that both airfoil camber and non-zero finite angle of attack have a significant effect on the unsteady gust response of a zero thickness airfoil over a wide range of reduced frequency values. Also, the correlations of the predictions from the model developed herein with the corresponding ones from the chordwise gust Naumann and Yeh model are poor. Again, this is due to the coupling between the steady and unsteady flow fields for cambered airfoils and non-zero finite angle of attack and of the gust included in the flow model developed herein but neglected in the Naumann and Yeh model.

The combined effects of airfoil camber and thickness and non-zero finite angle of attack are demonstrated in Figure 11. As expected based on the previous results, these combined effects are important, with the small camber predictions of Naumann and Yeh resulting in relatively large errors in the predicted unsteady lift. These are due to the coupling between the steady and unsteady flow fields for cambered airfoils and non-zero finite angle of attack and of the gust included in the flow model developed herein.

Figure 12 demonstrates that the two-dimensionality of the gust has a significant effect on the resulting unsteady lift on the airfoil. In particular, over the range of reduced frequency values considered, altering the gust direction from 15° to 90° results in relatively large differences in the unsteady aerodynamic response of the airfoil.

SUMMARY AND CONCLUSIONS

A complete first order model was formulated to analyze the effects of steady loading on the incompressible unsteady aerodynamics generated by a two-dimensional gust convected with the steady mean flow past an arbitrary thick, cambered, airfoil at finite nonzero angle of attack. A locally analytical solution was then developed in which the discrete algebraic equations which represent the flow field equations were obtained from analytical solutions in individual grid elements.

The steady flow field was found to be independent of the unsteady flow field. However, the dependence of the unsteady aerodynamics on the steady effects of airfoil geometry and finite non-zero angle of attack were manifested in the coupling of the unsteady and steady flow fields through the unsteady boundary conditions. A body fitted computational grid was utilized. General analytical solutions to the transformed flow field equations were then developed by applying these solutions to individual grid elements, with the complete flow field solution obtained by assembling these locally analytical solutions.

This model and locally analytical solution were then applied to a series of airfoil and flow configurations. The results demonstrated that accurate predictions for the unsteady aerodynamic gust response are obtained only by including the coupled steady flow effects on the unsteady aerodynamics. Thus for cambered, or cambered and thick airfoils at zero or finite angle of attack, or a thin flat plate airfoil at a non-zero angle of attack, the model and solution developed herein accurately predict the gust response. It was also demonstrated that the classical small perturbation combined transverse and chordwise gust models yield accurate predictions only for the special case of a thin flat plate airfoil at zero angle of attack, i.e., only when the chordwise gust is zero.

ACKNOWLEDGEMENT

This research was sponsored in part by the Air Force Office of Scientific Research and the NASA-Lewis Research Center.

REFERENCES

1. Sears, W.R., "Some Aspects of Nonstationary Airfoil Theory and its Practical Applications," *Journal of the Aeronautical Sciences*, Vol. 8, No. 3, pp. 104-108, January 1941.
2. Horlock, J.H., "Fluctuating Lift Forces on Airfoils Moving Through Transverse and Chordwise Gusts," *ASME Journal of Basic Engineering*, Series D, Vol. 90, No. 4, pp. 494-500, December 1968.
3. Naumann, H. and Yeh, H.J., "Lift and Pressure Fluctuations of a Cambered Airfoil Under Periodic Gusts and Applications to Turbomachinery," *ASME Paper 72-GT-30*, 1972.

4. Goldstein, M.E., and Atassi, H., "A Complete Second Order Theory for the Unsteady Flow About an Airfoil Due to a Periodic Gust," *Journal of Fluid Mechanics*, Vol. 74, pp. 741-766, 1976.

5. Spreiter, J.R., and Alksne, A.Y., "Thin Airfoil Theory Based on Approximate Solution of the Transonic Flow Equation," *NACA-TR-1959*, 1958.

6. Spreiter, J.R., "Aerodynamics of Wings and Bodies at Transonic Speeds," *Journal of Aerospace Sciences*, Vol. 26, No. 8, pp. 465-487, August 1959.

7. Spreiter, J.R., "The Local Linearization Method in Transonic Flow Theory," *Symposium Transsonicum*, K. Oswatitsch, editor, Springer-Verlag, Berling-Bottingen-Heidelberg, pp. 91-109, 1964.

8. Stahara, S.S., and Spreiter, J.R., "Development of a Nonlinear Unsteady Transonic Flow Theory," *NASA CR-2258*, June 1973.

9. Dowell, E.H., "A Simplified Theory of Oscillating Airfoils in Transonic Flow," *Proceedings of Symposium on Unsteady Aerodynamics*, Kinney, R.B., editor, University of Arizona, Tucson, pp. 655-679, July 1975.

10. Chen, C.J., Naresi-Neshat, H., and Ho, K.S., "Finite Analytic Numerical Solution of Heat Transfer in Two-Dimensional Cavity Flow," *Journal of Numerical Heat Transfer*, Vol. 4, pp. 179-197, 1981.

11. Chen, C.J., and Yoon, Y.H., "Finite Analytic Numerical Solution of Axisymmetric Navier-Stokes and Energy Equations," *Journal of Heat Transfer*, Vol. 105, p. 639-645, August 1983.

12. Chen, C.J., and Li, P., "Finite Differential Methods in Heat Conduction - Application of Analytic Solution Techniques," *ASME Paper 79-WA/HT-50*, December 1979.

13. Thompson, J.F., Thames, F.C. and Mastin, C.W., "Boundary Fitted Curvilinear Coordinate Systems for Solution of Partial Differential Equations on Fields Containing Any Number of Arbitrary Two-Dimensional Bodies," *NASA-CR-2729*, 1977.

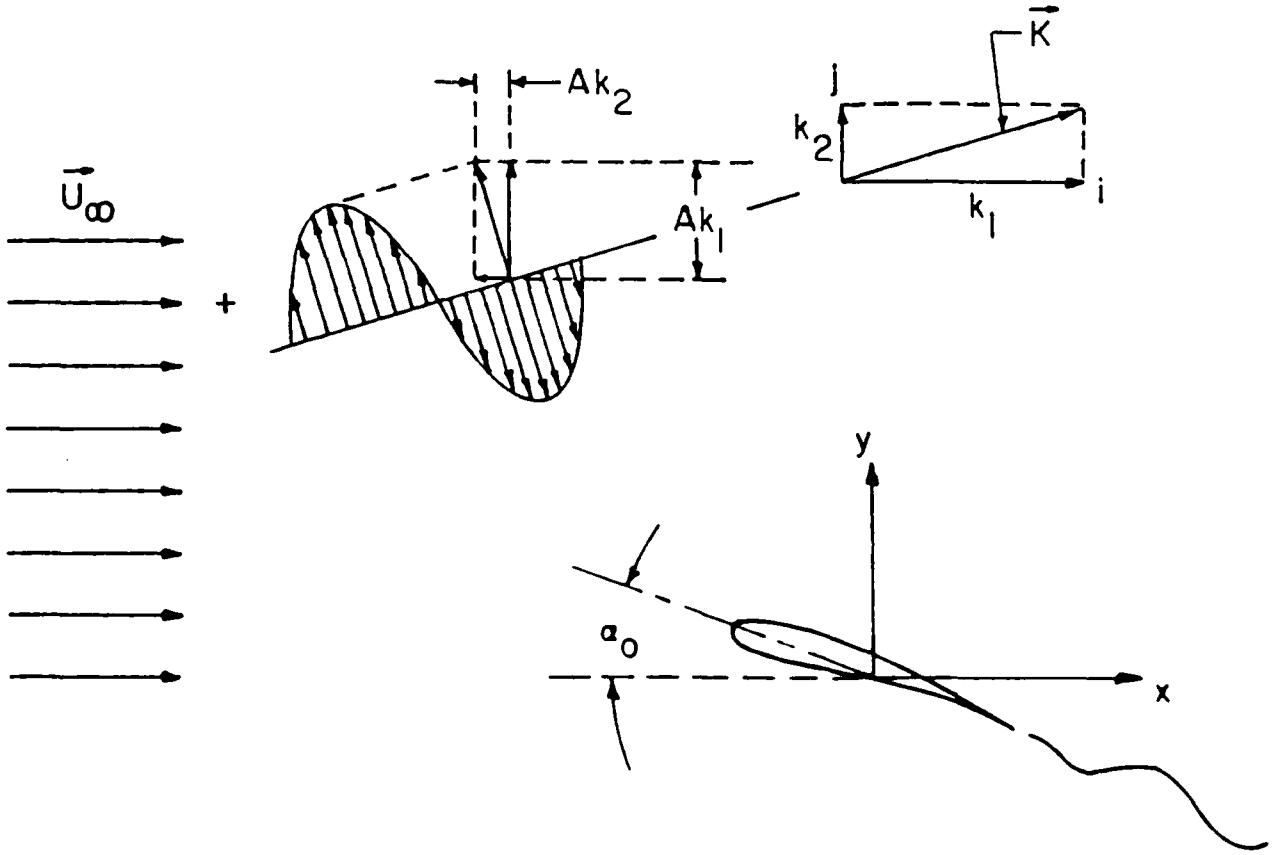

Figure 1. Flow of a Two-Dimensional Gust Past a Thick, Cambered, Airfoil at Angle of Attack

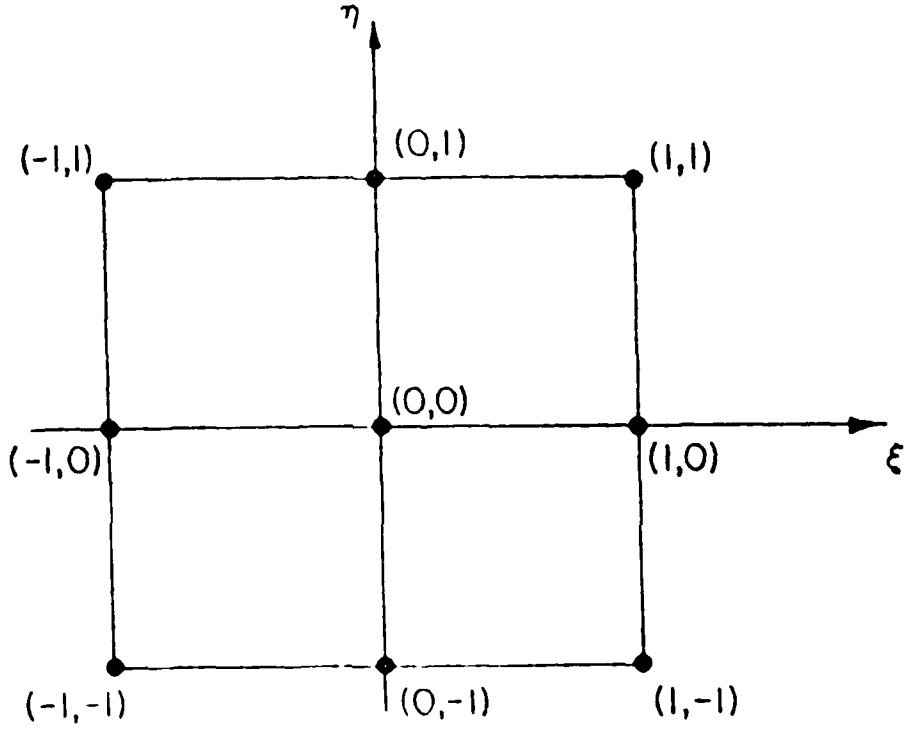

Figure 2. Body-Fitted Coordinate Transformation

AD-A192 169 RESEARCH ON AERO-THERMODYNAMIC DISTORTION INDUCED STRUCTURAL DYNAMIC RESP..(U) PURDUE UNIV LAFAYETTE IND THERMAL SCIENCES AND PROPULSION CEN.. S FLEETER

UNCLASSIFIED 15 JAN 88 ME-TSPC-TR-88-10 AFOSR-TR-88-0045 F/G 1/1 NL

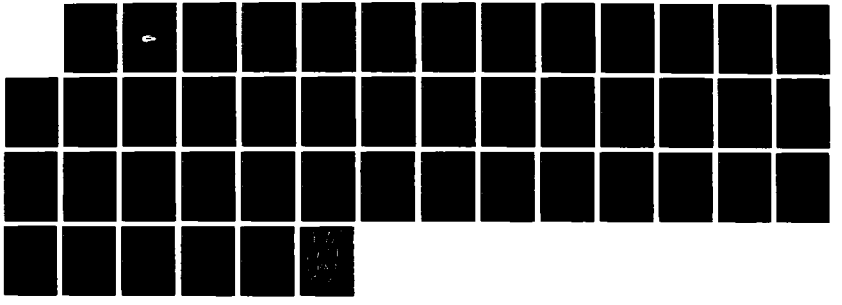

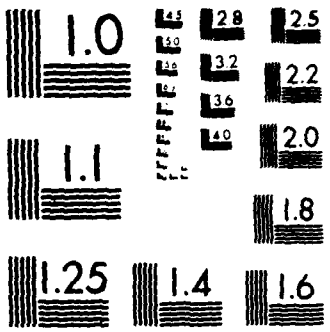

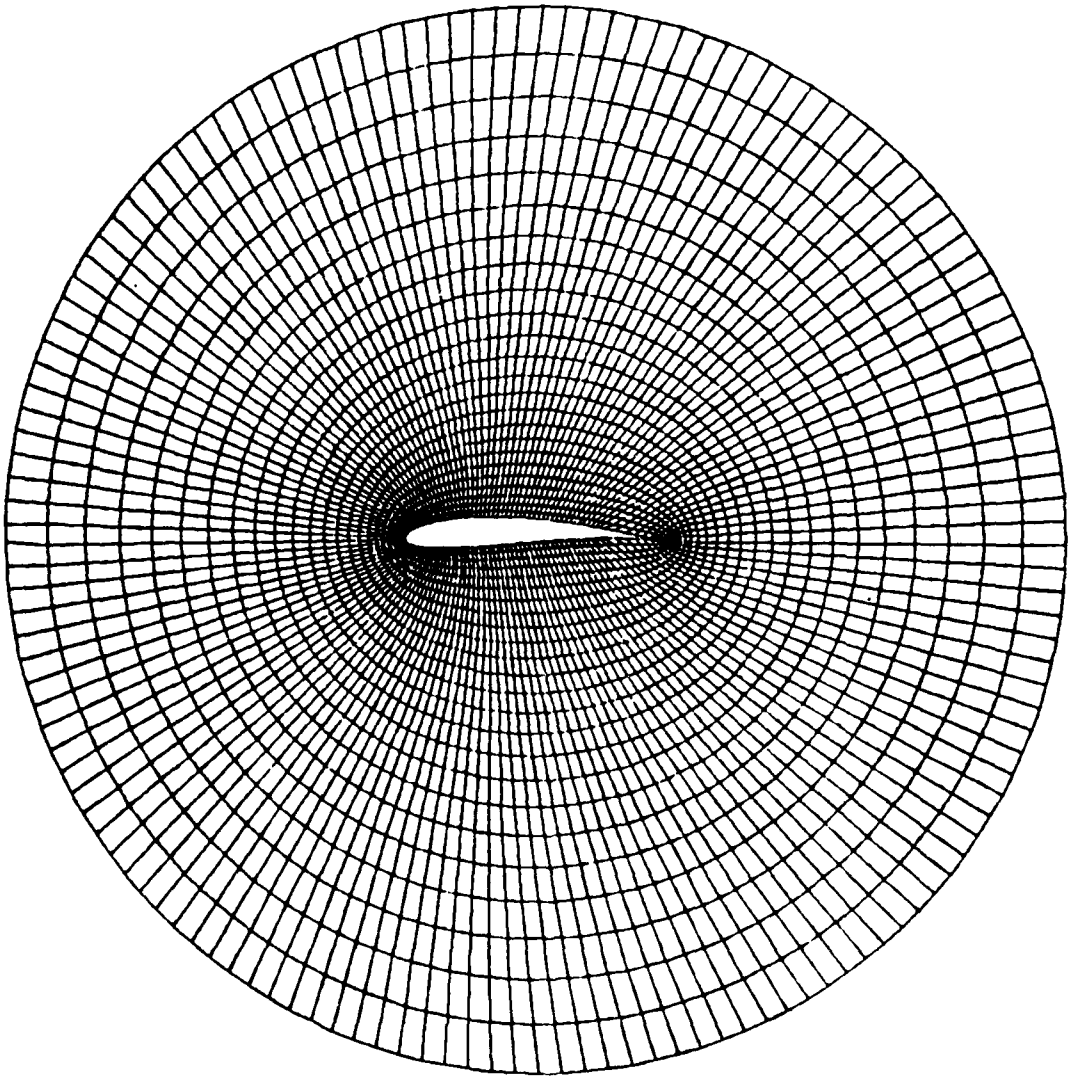

Figure 3. Boundary-Fitted Grid for a Joukowski Airfoil

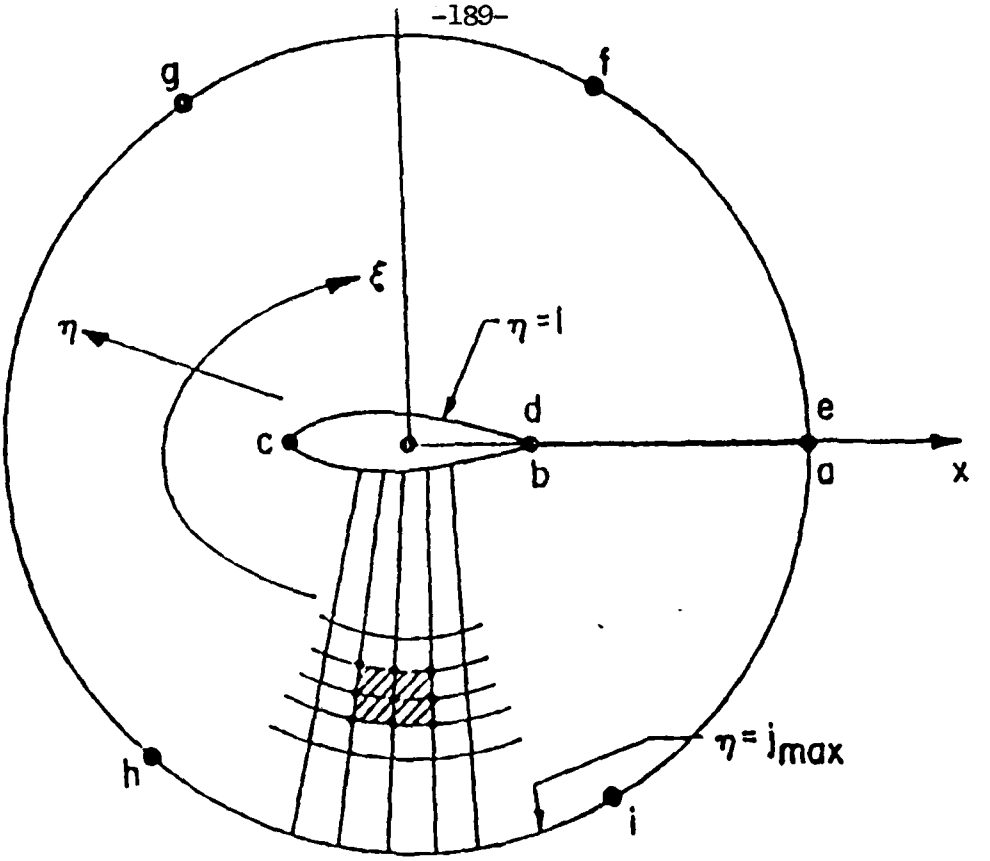

(a) Physical Plane

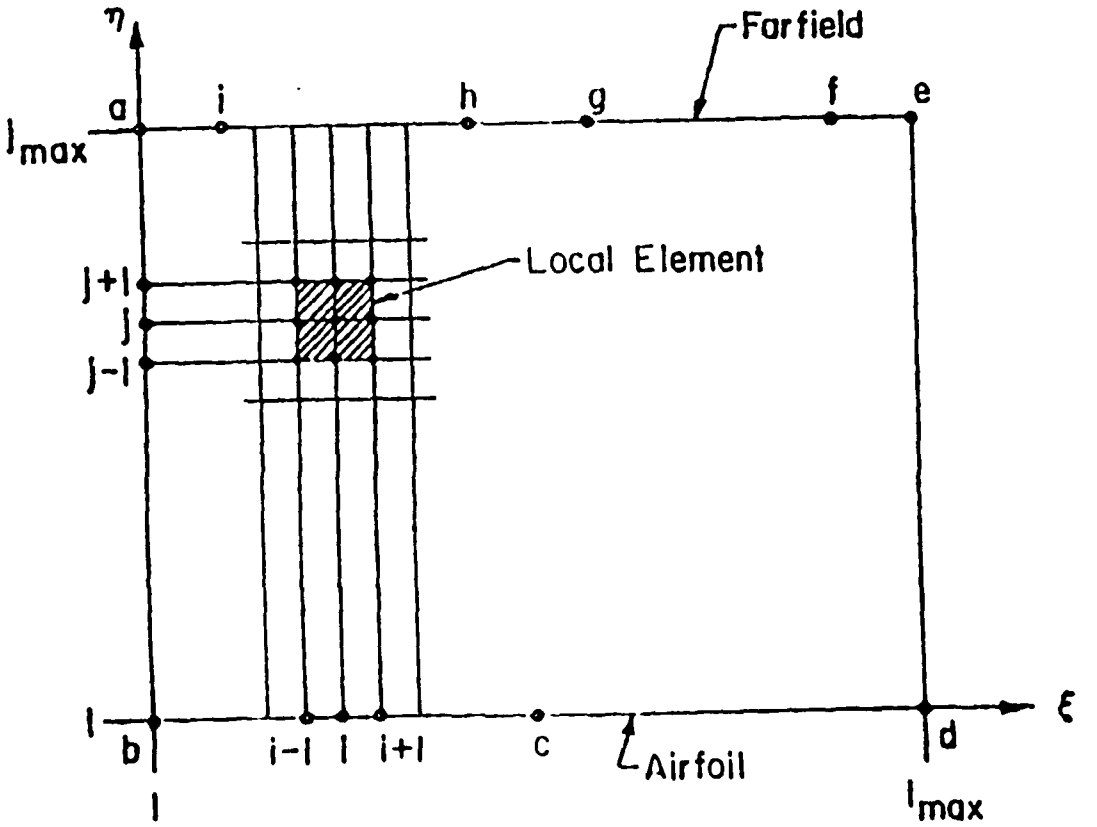

(b) Transformed Plane

Figure 4. Local Computational Grid Element

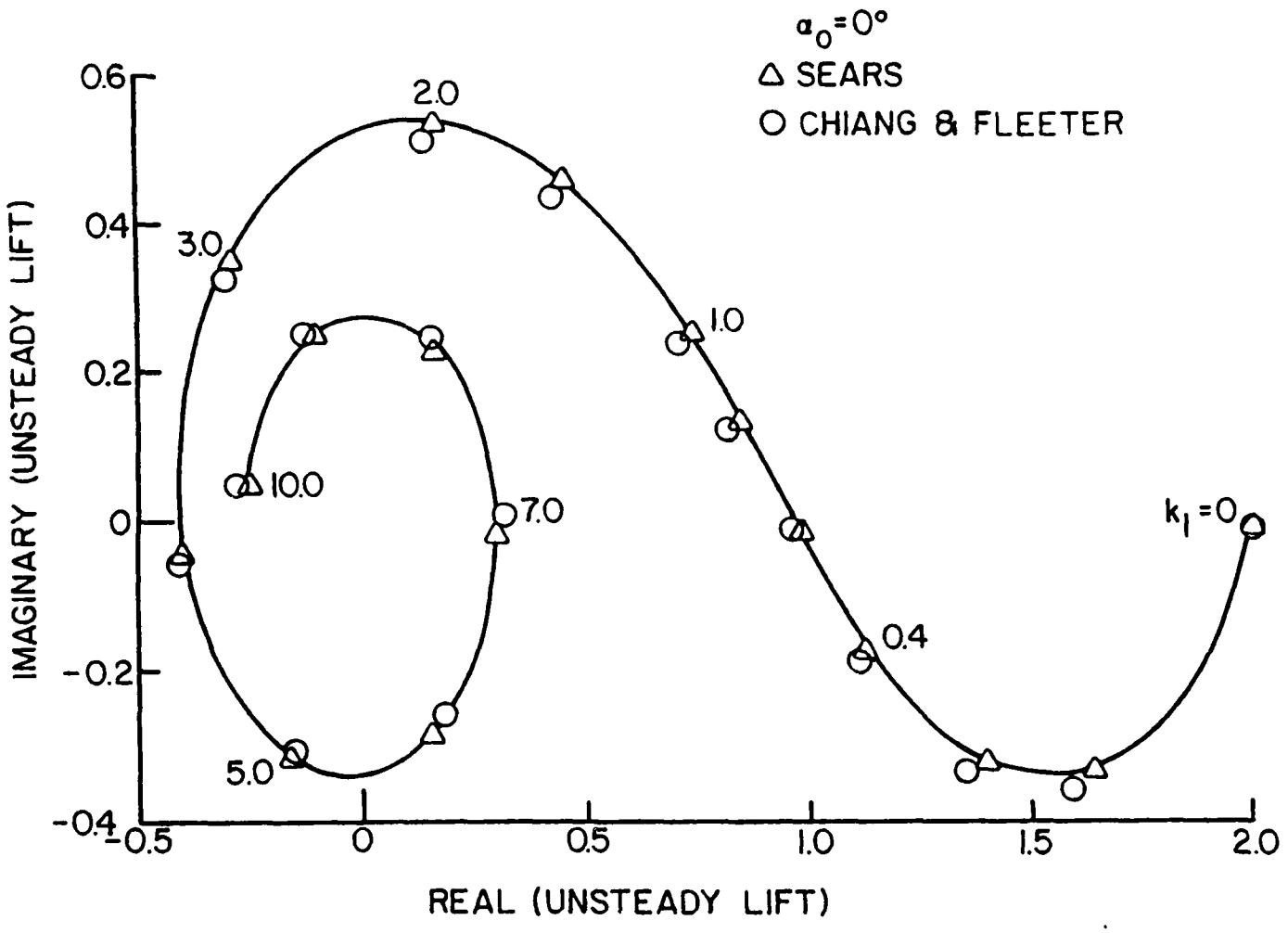

Figure 5. Correlation of Predicted Unsteady Lift with Sears Transverse Gust Flat Plate Model

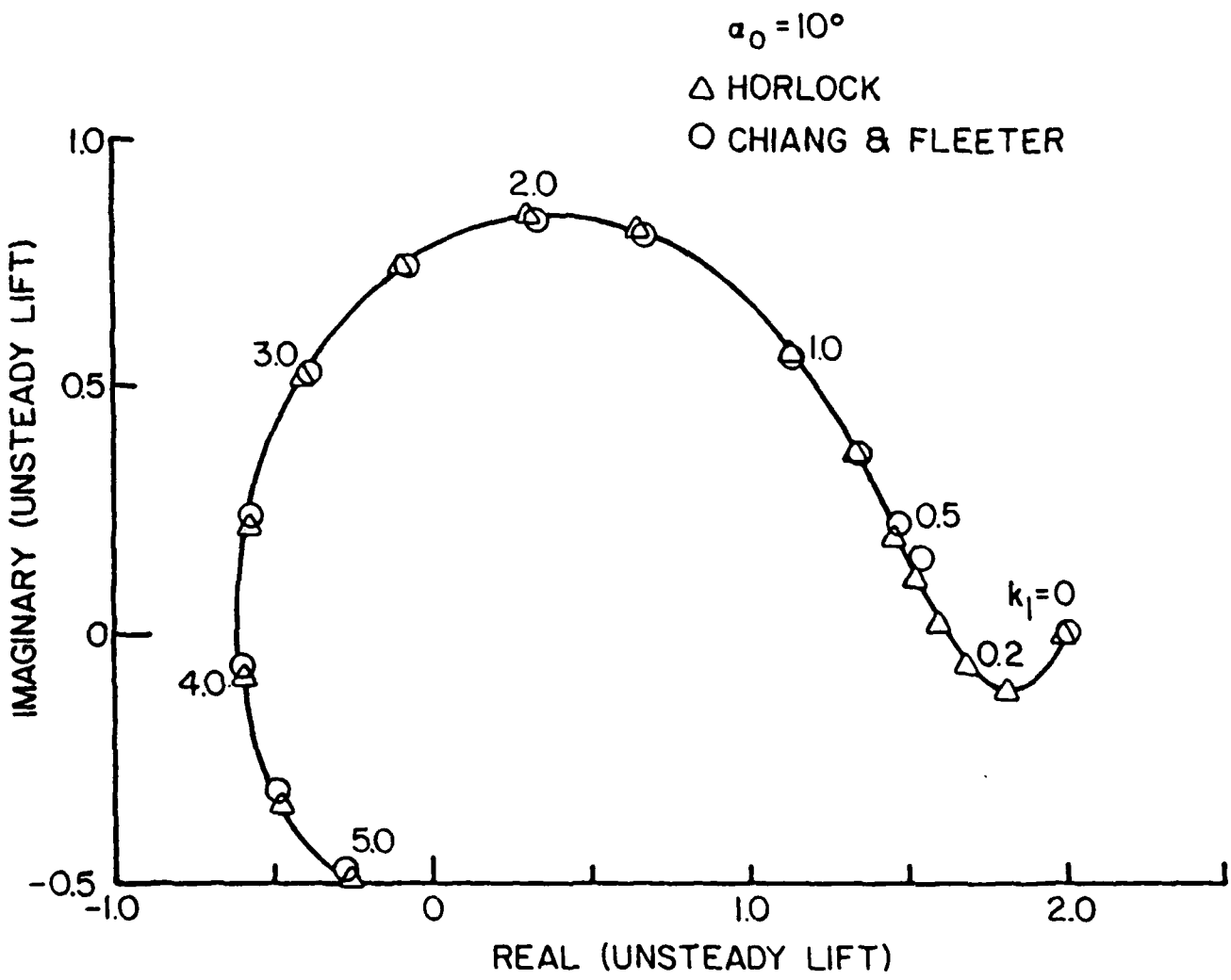

Figure 6. Correlation of Predicted Unsteady Lift with Horlock's Flat Plate Chordwise Gust Model

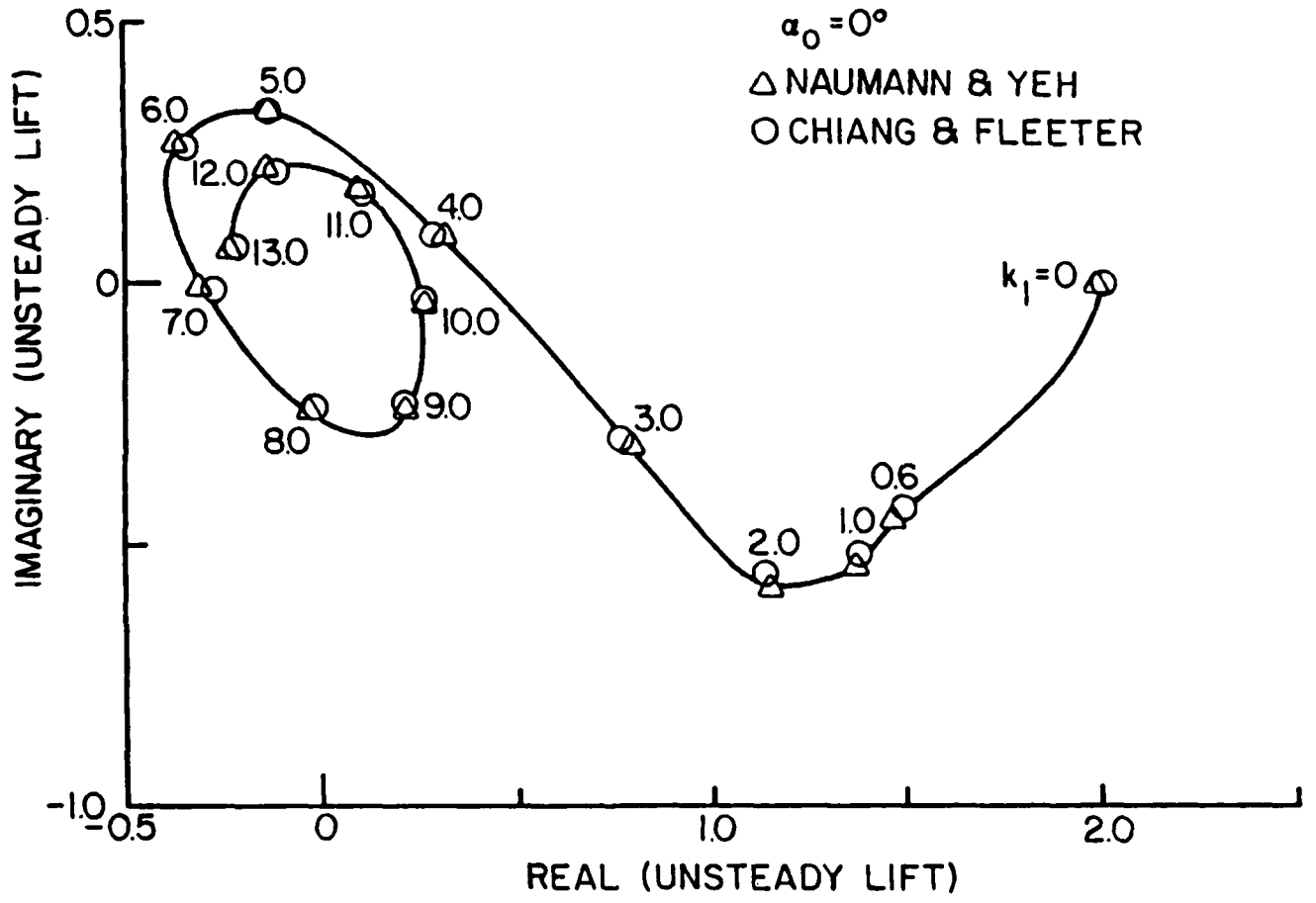

Figure 7. Correlation of Predicted Unsteady Lift with Naumann and Yeh's Small Cambered Airfoil Chordwise Gust Results

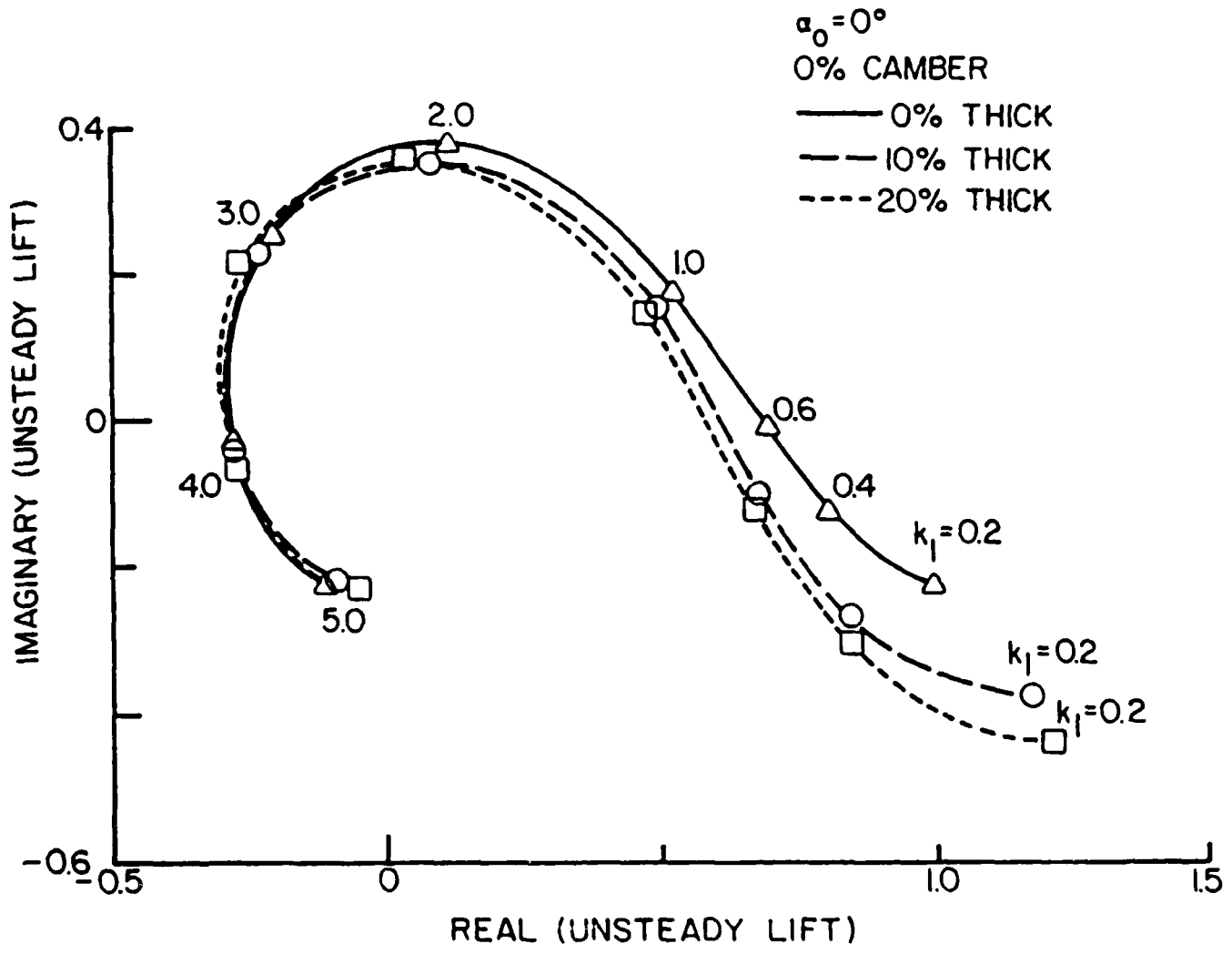

Figure 8. Thickness Effect on the Unsteady Lift of a Flat Plate Airfoil at Zero Angle of Attack due to a 45° Gust

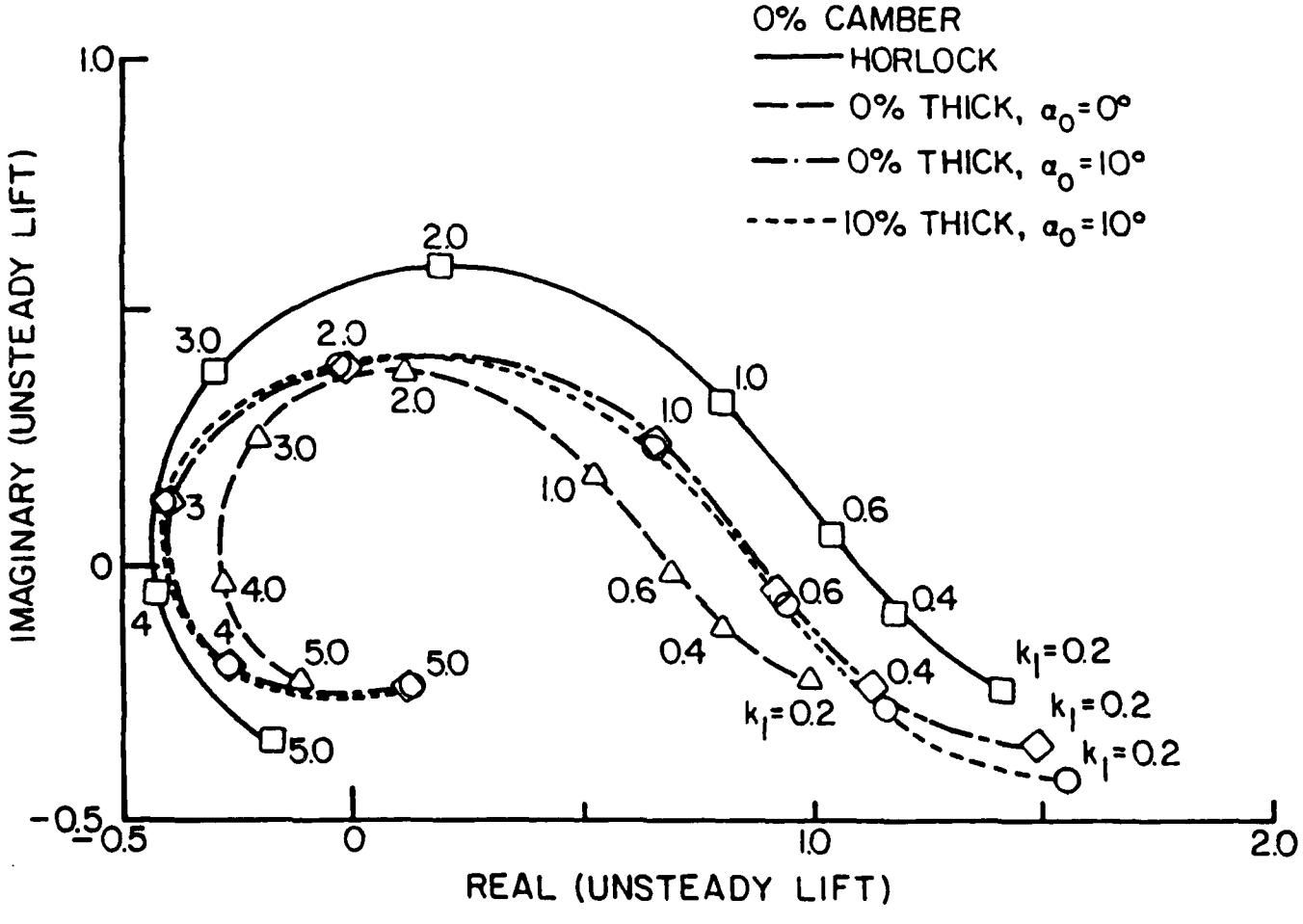

Figure 9. Thickness Effect on the Unsteady Lift of a Flat Plate Airfoil at Nonzero angle of Attack due to a 45° Gust

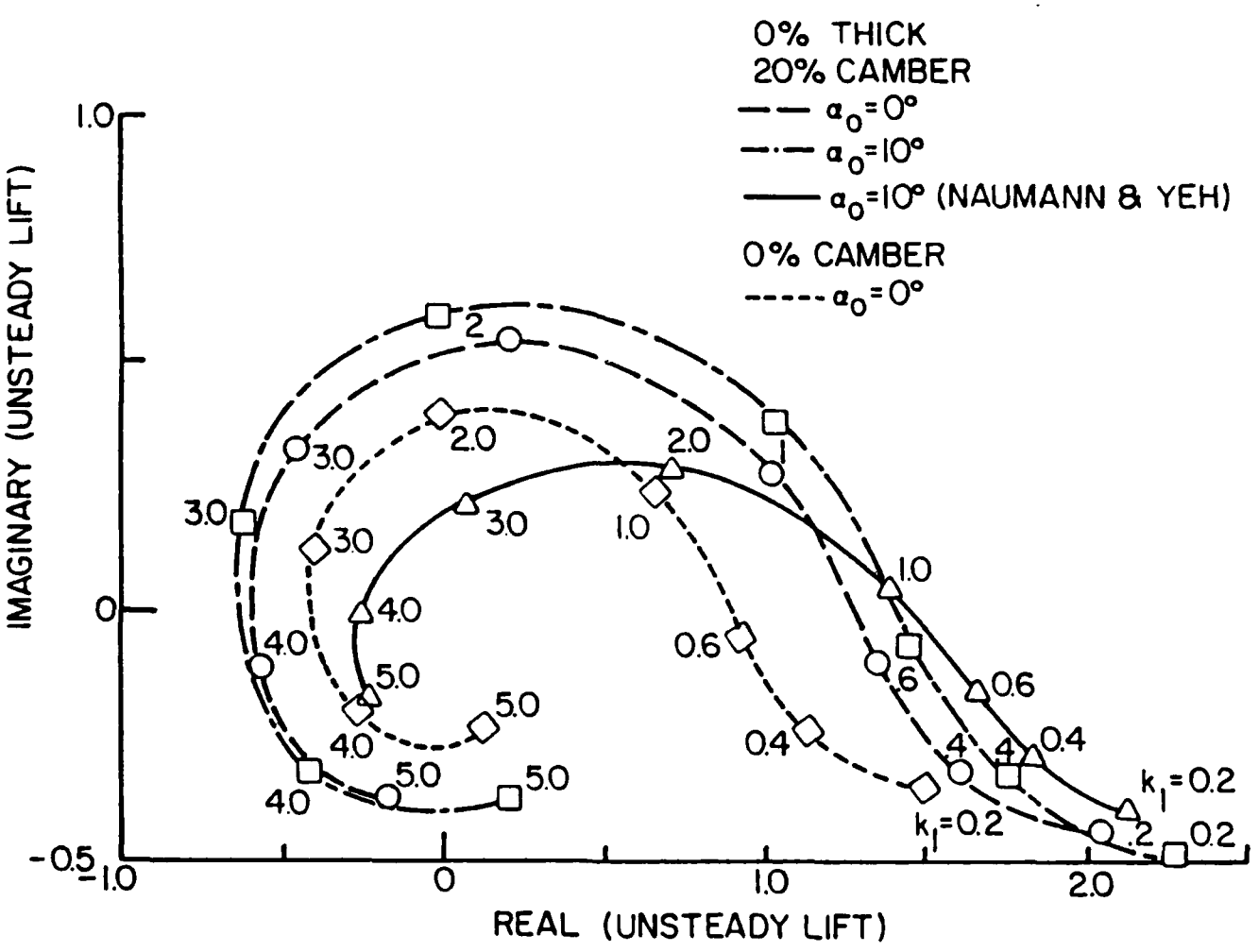

Figure 10. Effect of Camber and Angle of Attack on the Unsteady Lift of a Zero Thickness Airfoil due to a 45° Gust

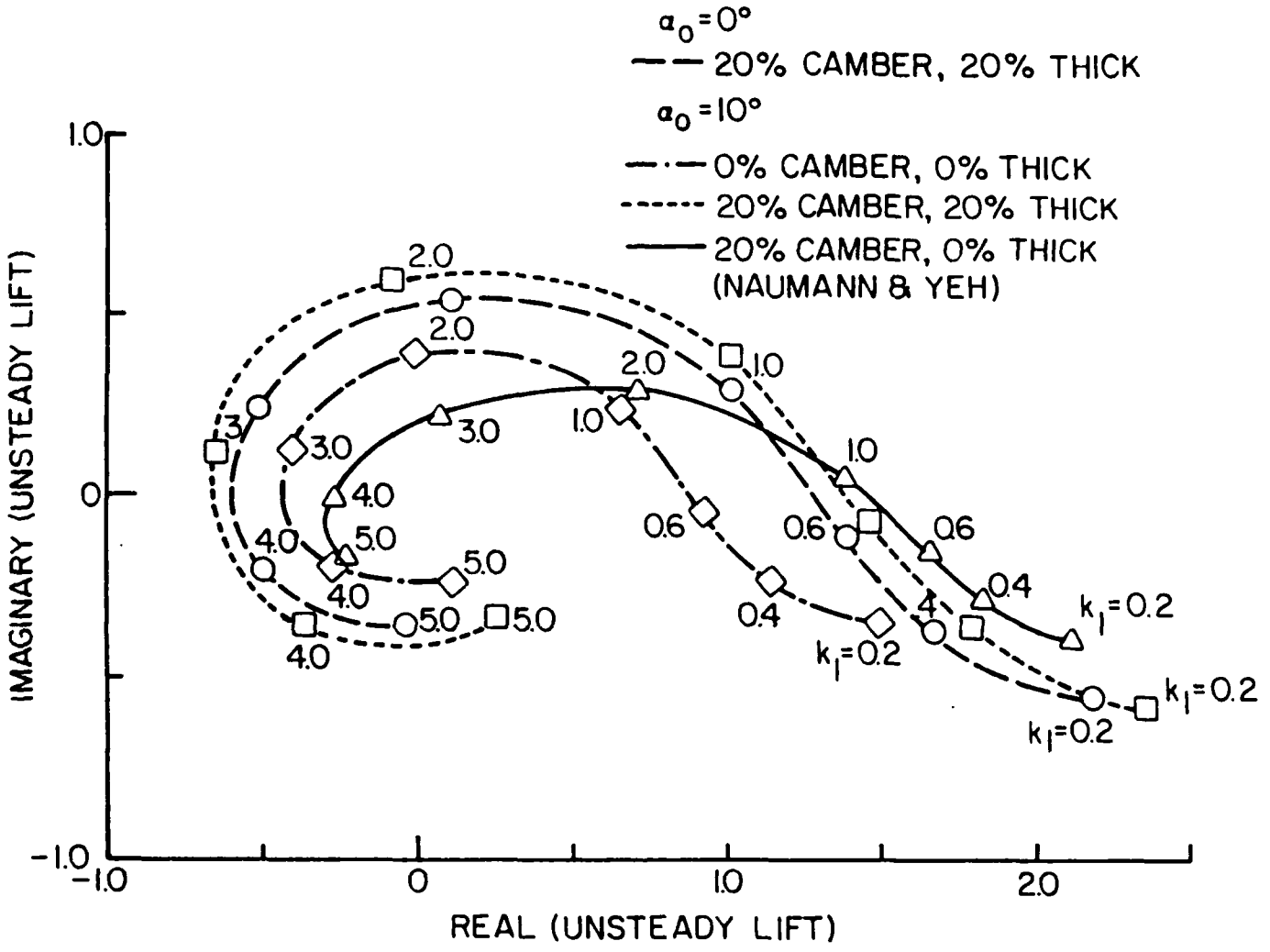

Figure 11. Effect of Thickness and Camber on the Unsteady Lift of an Airfoil at 10° Angle of Attack due to a 45° Gust

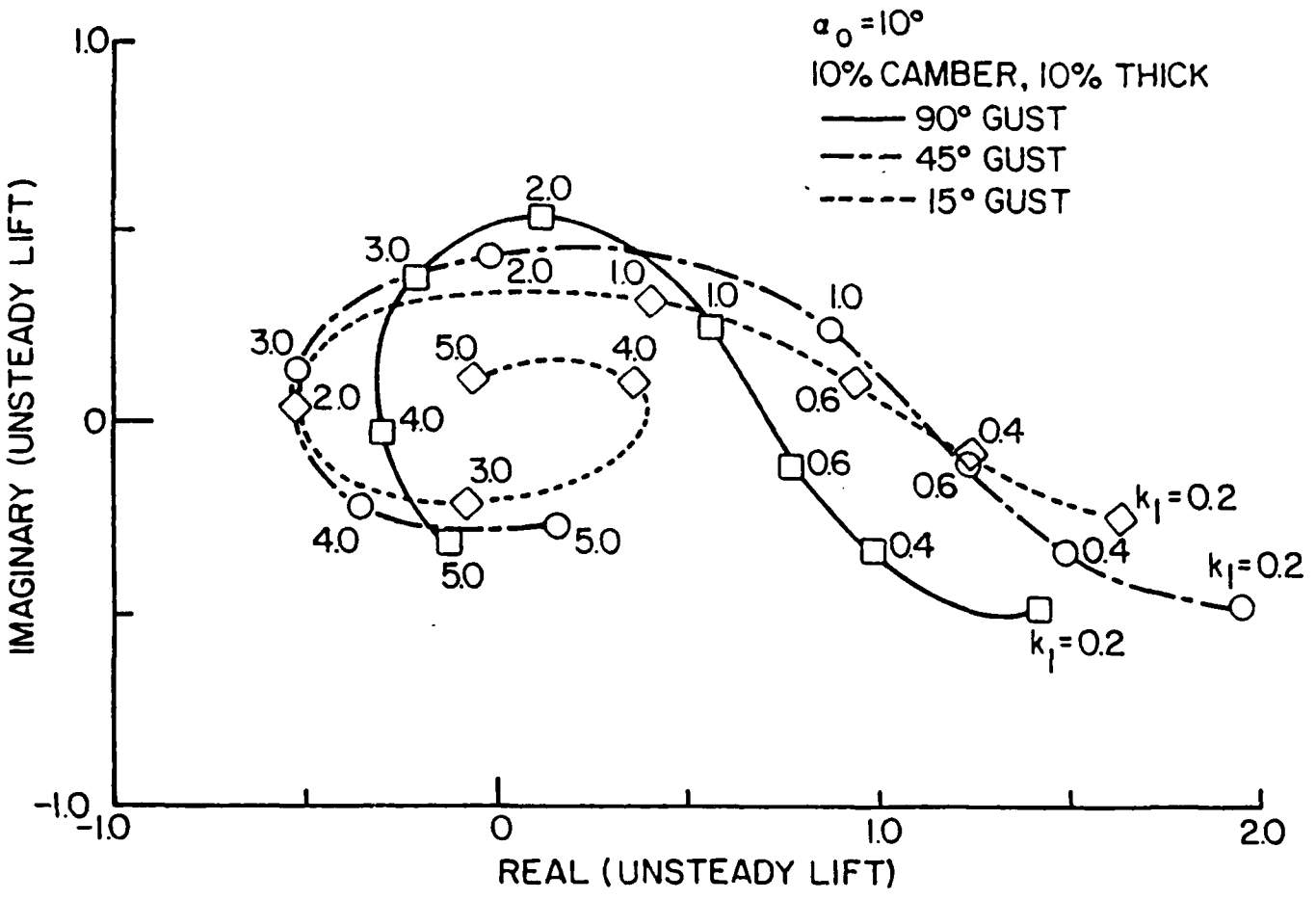

Figure 12. Gust Direction Effect on the Unsteady Lift of a 10% Thick, 10% Camber, Airfoil at 10° Angle of Attack

APPENDIX X

VISCOUS AERODYNAMIC ANALYSIS OF AN OSCILLATING FLAT PLATE AIRFOIL WITH A LOCALLY ANALYTICAL SOLUTION

AIAA PAPER 88-0130

VISCOUS AERODYNAMIC ANALYSIS OF AN OSCILLATING FLAT PLATE AIRFOIL WITH A LOCALLY ANALYTICAL SOLUTION

Linda M. Schroeder[+] and Sanford Fleeter[*]
Thermal Sciences and Propulsion Center
School of Mechanical Engineering
Purdue University
West Lafayette, Indiana 47907

Abstract

A mathematical model is developed to predict the unsteady aerodynamics of a flat plate airfoil executing harmonic torsional motion in an incompressible laminar flow at moderate values of the Reynolds numbers. The unsteady viscous flow is assumed to be a small perturbation to the steady viscous flow described by the Navier-Stokes equations. Solutions for both the steady and the unsteady viscous flow fields are obtained by developing a locally analytical solution. This model is then utilized to demonstrate the effects of Reynolds number, mean flow incidence angle, and reduced frequency on the complex unsteady airfoil surface pressure distributions as well as airfoil stability.

Nomenclature

C_{Li}	imaginary component of lift coefficient
C_{Lr}	real component of lift component
C_{Mi}	imaginary component of moment coefficient
C_{Mr}	real component of moment coefficient
k	reduced frequency
p	dimensionless unsteady pressure
P	dimensionless steady pressure
Re	Reynolds number
u	nondimensional unsteady velocity in x direction
U	nondimensional steady velocity in x direction
U_∞	magnitude of free-stream velocity
v	nondimensional unsteady velocity in y direction
x_{ea}	elastic axis location
x	coordinate in mean flow direction
y	coordinate in normal flow direction
Δx	step size in x direction
Δy	step size in y direction
α'	amplitude of airfoil oscillation
ψ	nondimensional unsteady stream function
Ψ	nondimensional steady stream function
ξ	nondimensional unsteady vorticity
ς	nondimensional steady vorticity
ω	frequency of oscillation

Introduction

Considerable progress has been made in the prediction of the unsteady aerodynamics of oscillating airfoils. These analyses are typically limited to inviscid potential flows, with the unsteady flow assumed to be a small perturbation to a uniform mean flow and the Kutta condition imposed on the unsteady flow field. By considering the airfoils to be zero thickness flat plates at zero mean incidence, the steady and unsteady flow fields are uncoupled, with the steady flow being uniform and parallel.

Unsteady aerodynamic analyses have been developed which include the effects of viscosity, thereby removing the need for the Kutta condition. Yates [1] formulated an incompressible viscous flat plate airfoil theory with a zero thickness boundary layer. Also, the low Reynolds number incompressible Oseen flow model has been used to calculate zero incidence oscillating flat plate aerodynamics [2,3]. These analyses utilize classical aerodynamic solution techniques, resulting in integral equation solutions. Although such classical models and solution techniques are of value, advanced numerical techniques permit the flow physics modeling to be extended. In this regard, unsteady viscous flow models are being developed which march in time, with one primary interest being the patterns of the unsteady flow, for example, Mehta and Lavan [4], Thompson et. al. [5], and Wu and Sampath [6].

In this paper, an analysis is developed which models the unsteady aerodynamics of an harmonically oscillating flat plate airfoil, including the effects of mean flow incidence angle, in an incompressible laminar flow at moderate values of the Reynolds number. The unsteady viscous flow is assumed to be a small perturbation to the steady viscous flow field. Hence, the Kutta condition is not appropriate for either the steady or the unsteady flow fields. The steady flow field is described by the Navier-Stokes equations. It is thus nonuniform and nonlinear. Also, the steady flow field is independent of the unsteady flow field. The small perturbation unsteady viscous flow is described by a system of linear partial differential equations that are coupled to the steady flow field, thereby modeling the strong dependence of the unsteady aerodynamics on the steady flow.

+ AFRAPT Trainee, currently Associate Aerodynamics Engineer, Sundstrand Turbomach, Member AIAA
* Professor and Director, Thermal Sciences and Propulsion Center, Associate Fellow AIAA

Solutions for both the steady and the unsteady viscous flow fields are obtained by developing a locally analytical method in which the discrete algebraic equations which represent the flow field equations are obtained from analytical solutions in individual local grid elements.

Mathematical Model

The two-dimensional flow past an isolated airfoil is schematically depicted in Figure 1, which also defines the cartesian x-y coordinate system. For harmonic time dependence at a frequency ω, the nondimensional forms of the continuity and Navier-Stokes equations are given in Equation 1.

$$\bar{u}_x + \bar{v}_y = 0 \tag{1a}$$

$$k\bar{u}_t + \bar{u}\bar{u}_x + \bar{v}\bar{u}_y = -\bar{p}_x + (\bar{u}_{xx} + \bar{u}_{yy})/Re \tag{1b}$$

$$k\bar{v}_t + \bar{u}\bar{v}_x + \bar{v}\bar{v}_y = -\bar{p}_y + (\bar{v}_{xx} + \bar{v}_{yy})/Re \tag{1c}$$

where $Re = U_\infty C/\nu$ denotes the Reynolds number, and $k = \omega C/U_\infty$ is the reduced frequency.

There are three dependent variables, the two velocity components and the pressure. To reduce the number of dependent variables, a vorticity, $\bar{\zeta}$, stream function, $\bar{\psi}$, formulation is utilized.

$$\nabla^2\bar{\zeta} = \bar{\zeta}_{xx} + \bar{\zeta}_{yy} = Re(k\bar{\zeta}_t + \bar{u}\,\bar{\zeta}_x + \bar{v}\,\bar{\zeta}_y) \tag{2a}$$

$$\nabla^2\bar{\psi} = -\bar{\zeta} \tag{2b}$$

where $\bar{\zeta} = \bar{v}_x - \bar{u}_y$ and $\bar{u} = \bar{\psi}_y$; $\bar{v} = -\bar{\psi}_x$

Unsteady Small Perturbation Model

For a flat plate airfoil executing small amplitude harmonic oscillations, the flow field is decomposed into steady and harmonic unsteady components, with the steady component assumed to be a small perturbation to the steady component.

$$\bar{\zeta}(x,y,t) = \zeta(x,y) + e^{it}\,\xi(x,y) \tag{3a}$$

$$\bar{\psi}(x,y,t) = \Psi(x,y) + e^{it}\,\psi(x,y) \tag{3b}$$

$$\bar{u}(x,y,t) = U(x,y) + e^{it}\,u(x,y) \tag{3c}$$

$$\bar{v}(x,y,t) = V(x,y) + e^{it}\,v(x,y) \tag{3d}$$

$$\bar{p}(x,y,t) = P(x,y) + e^{it}\,p(x,y) \tag{3e}$$

where

$$\xi \ll \zeta,\ \psi \ll \Psi,\ u \ll U,\ v << V,\ p \ll P$$

The equations describing the steady and unsteady viscous flow fields are determined by substituting Equation 3 into Equation 2, and grouping together the time independent and the time dependent terms. For the unsteady flow, the second order terms are neglected as small compared to the first order terms. Also, as the linearized unsteady flow is assumed to be harmonic, the exp(it) is dropped, for convenience.

The resulting coupled nonlinear partial differential equations describing the steady flow field, Equation 4, are independent of the unsteady flow. The vorticity equation is nonlinear, with the stream function described by a linear Poisson equation which is coupled to the vorticity equation through the vorticity source term. The pressure is also described by a linear Poisson equation, with the source terms dependent on the steady flow field.

$$\nabla^2\zeta = Re(U\zeta_x + V\zeta_y) \tag{4a}$$

$$\nabla^2\Psi = -\zeta \tag{4b}$$

$$\nabla^2 P = -2(U_x V_y - V_y U_x) \tag{4c}$$

The resulting coupled linear partial differential equations describing the unsteady harmonic flow field are given in Equation 5. The unsteady flow is coupled to the steady flow field. In particular, in both the unsteady vorticity transport and pressure equations, the variable coefficients are dependent on the steady flow field with the unsteady stream function coupled to the solution for the unsteady vorticity.

$$\nabla^2\xi = Re(ki\,\xi + U\xi_x + V\xi_y + u\zeta_x + v\zeta_y) \tag{5a}$$

$$\nabla^2\psi = -\xi \tag{5b}$$

$$\nabla^2 p = -2|(u_x V_y + v_y U_x) - (v_x U_y + u_y V_x)| \tag{5c}$$

Steady Flow Boundary Conditions

The steady flow boundary conditions specify no slip between the fluid and the surface and that the velocity normal to the surface is zero. In terms of the stream function and vorticity, these boundary conditions are specified in Equation 6.

$$\Psi = \text{constant} \quad \text{on solid surfaces} \tag{6a}$$

$$\zeta = -U_y = \Psi_{yy} \quad \text{on solid surfaces} \tag{6b}$$

Unsteady Flow Boundary Conditions

The unsteady boundary conditions require that the velocity of the fluid is equal to that of the surfaces. For a flat plate airfoil executing small amplitude harmonic torsion mode oscillations about an elastic axis located at x_{ea} measured from the leading edge, the linearized normal velocity boundary condition is applied on the mean position of the oscillating airfoil, and is given in Equation 7.

$$v(x,0) = \alpha'|ik(x - x_{ea})|e^{it} \tag{7}$$

where α' is the amplitude of oscillation.

The fluid is viscous. Thus the unsteady chordwise velocity component must satisfy the no-slip boundary condition.

$$u(x,0) = 0 \tag{8}$$

The corresponding unsteady stream function and vorticity boundary conditions are specified from their definitions and the above unsteady boundary conditions.

$$\psi(x,0) = -ik\,\alpha'\left(\frac{x^2}{2} - x_{ea}\right)xe^{it} \tag{9a}$$

$$\xi(x,0) = |\alpha' ik - u_y(x,0)|e^{it} \tag{9b}$$

Locally Analytical Solutions

The locally analytical solutions for the unsteady and steady viscous flow fields are now developed. In this method, the discrete algebraic equations which represent the aerodynamic equations are obtained from analytical solutions in individual local grid elements. This is accomplished by dividing the flow field into computational grid elements. In each individual element the nonlinear convective terms of the Navier-Stokes equations which describe the steady flow are locally linearized. The nonlinear character of the steady flow field is preserved as the flow is only locally linearized, that is, independently linearized in individual grid elements. Analytical solutions to the linear equations describing both the steady and the unsteady flow fields in each element are then determined. The solution for the complete flow field is obtained through the application of the global boundary conditions and the assembly of the locally analytic solutions in the individual grid elements.

Steady Vorticity

The steady vorticity transport is described by Equation 4a which is nonlinear because of the convective terms $U\zeta_x + V\zeta_y$. These terms are locally linearized by assuming that the velocity components U and V, which are the coefficients of the vorticity, are constant in each individual grid element, that is, locally linearized.

$$U = \frac{2A}{Re} \quad V = \frac{2B}{Re} \tag{10}$$

where A and B are constants in an individual grid element, taking on different values in each grid element. The resulting locally linearized vorticity equation is given in Equation 11.

$$2A\zeta_x + 2B\zeta_y = \zeta_{xx} + \zeta_{yy} \tag{11}$$

This locally linearized equation can be solved analytically to determine the vorticity, ζ, in a grid element, thereby providing the functional relationships between the vorticity, ζ, in an individual grid element and the boundary values specified on that grid element. This vorticity transport equation is elliptic. Therefore, to obtain a unique solution for the typical uniform grid element with center (x_o,y_o), Figure 2, boundary conditions must be specified on all four boundaries. These boundary conditions are expressed in an implicit formulation in terms of the nodal values of the vorticity along the boundaries of the element. A second-order polynomial is used to approximate the vorticity on each of the boundaries.

$$\zeta(x,y_o+\Delta y) = a_1^\zeta + a_2^\zeta x + a_3^\zeta x^2 \tag{12}$$

$$\zeta(x_o+\Delta x,y) = b_1^\zeta + b_2^\zeta y + b_3^\zeta y^2$$

$$\zeta(x,y_o-\Delta y) = c_1^\zeta + c_2^\zeta x + c_3^\zeta x^2$$

$$\zeta(x_o-\Delta x,y) = d_1^\zeta + d_2^\zeta y + d_3^\zeta y^2$$

where a_i^ζ, b_i^ζ, c_i^ζ, d_i^ζ are constants determined from the three nodal points on each boundary side and the x and y distances are all measured from the center of the element (x_o,y_o).

The analytical solution to Equation 11 subject to the boundary conditions specified in Equation 12 is determined by separation of variables.

$$\zeta(x,y) = e^{(Ax+By)}\sum_{n=1}^{n=\infty}\Big\{[B_{1n}^\zeta \sinh(E_{1n}x) + B_{2n}^\zeta \cosh(E_{1n}x)]\sin(\lambda_{1n}^\zeta(y+\Delta y)) + [B_{3n}^\zeta \sinh(E_{2n}y) + B_{4n}^\zeta \cosh(E_{2n}y)]\sin(\lambda_{2n}^\zeta(x+\Delta x))\Big\} \tag{13}$$

Steady Stream Function

The locally analytical solution for the stream function is obtained by a procedure analogous to that used for the vorticity. First, the flow region is subdivided into computational grid elements.

The stream function is described by a linear Poisson equation which is coupled to the vorticity, Equation 4b. This stream function Poisson equation also is elliptic. Therefore, to obtain a unique analytical solution for the typical grid element, continuous conditions must be specified on all four boundaries. As for the vorticity transport equation, continuous boundary conditions are represented in an implicit formulation in terms of the nodal values of the stream function by second-order polynomials in x or y as measured from the element center (x_o,y_o).

$$\Psi(x,yo+\Delta y) = a_1^\psi + a_2^\psi x + a_3^\psi x^2 \tag{14}$$

$$\Psi(xo+\Delta x,y) = b_1^\psi + b_2^\psi y + b_3^\psi y^2$$

$$\Psi(x,yo-\Delta y) = c_1^\psi + c_2^\psi x + c_3^\psi x^2$$

$$\Psi(xo-\Delta x,y) = d_1^\psi + d_2^\psi y + d_3^\psi y^2$$

where a_i^ψ, b_i^ψ, c_i^ψ, d_i^ψ are constants determined from the three nodal points on each boundary side.

The stream function equation is linear and possesses a nonhomogeneous term, $-\zeta(x,y)$, which couples the stream function to the vorticity. To solve Equation 4b subject to the boundary conditions specified in Equation 14, it is divided into two component problems. One problem has a homogeneous equation with nonhomogeneous boundary conditions, whereas the second problem has a nonhomogeneous equation with homogeneous boundary conditions.

$$\Psi = \Psi^a + \Psi^b \tag{15}$$

Problem 1:

$$\nabla^2\Psi^a = 0 \tag{16}$$

$$\Psi^a(x,yo+\Delta y) = a_1^\psi + a_2^\psi x + a_3^\psi x^2$$

$$\Psi^a(xo+\Delta x,y) = b_1^\psi + b_2^\psi y + b_3^\psi y^2$$

$$\Psi^a(x,yo-\Delta y) = c_1^\psi + c_2^\psi x + c_3^\psi x^2$$

$$\Psi^a(x-\Delta x,yo) = d_1^\psi + d_2^\psi y + d_3^\psi y^2$$

Problem 2:

$$\nabla^2\Psi^b = -\zeta(x,y) \tag{17}$$

$$\Psi^b(x_o+\Delta x,y) = 0$$

$$\Psi^b(x_o-\Delta x,y) = 0$$

$$\Psi^b(x,y_o+\Delta y) = 0$$

$$\Psi^b(x,y_o-\Delta y) = 0$$

The solutions for Ψ^a and Ψ^b are then determined by separation of variables. Steady Velocity and Pressure

$$\Psi(x,y) =$$

$$\sum_{n=1}^{n=\infty}\Big\{[B_{1n}^\psi\sinh(\lambda_{1n}^\psi x) + B_{2n}^\psi\cosh(\lambda_{1n}^\psi x)]\sin(\lambda_{1n}^\psi(y+\Delta y))$$

$$+ [B_{3n}^\psi\sinh(\lambda_{2n}^\psi y) + B_{4n}^\psi\cosh(\lambda_{2n}^\psi y)]\sin(\lambda_{2n}^\psi(x+\Delta x))$$

$$+ [G_{4n}^\psi\sinh(\lambda_{1n}^\psi y) + G_{5n}^\psi\cosh(\lambda_{1n}^\psi y) + G_{1n}^\psi + G_{2n}^\psi y$$

$$+ G_{3n}^\psi y^2]\sin(\lambda_{1n}^\psi(x + \Delta x))\Big\} \tag{18}$$

The stream function is continuously differentiable across the grid element. Hence the U and V velocity components can be obtained analytically by differentiating the stream function solution. The solutions for Ψ, ζ, U and V are then used to determine the pressure in the flow field and on the boundaries. Thus, the locally analytical solutions for the velocity components and the pressure are performed as post processes.

Unsteady Flow Field

Unsteady Vorticity

The unsteady vorticity is described by a linear partial differential equation with nonconstant coefficients, Equation 5a. In particular, the unsteady perturbation velocity coefficients u and v vary across the typical computational grid element. However, the steady velocity coefficients U and V are known from the previously determined steady state solution and are constant in the typical grid element, as specified in Equation 10.

To determine the locally analytical solution to the unsteady perturbation vorticity equation, it is approximated as a constant coefficient partial differential equation in individual grid elements. This is accomplished by assuming that the perturbation velocities u and v are constant in each element.

$$u = \frac{2A'}{Re} \quad v = \frac{2B'}{Re} \tag{19}$$

where A' and B' are constant in each individual grid element, taking on different values in different grid elements.

Thus, the following linear constant coefficient partial differential equation defines the unsteady perturbation vorticity in an individual computational grid element.

$$k\cdot i\cdot Re\ \xi + 2A\ \xi_x + 2B\ \xi_y + (2A'\zeta_x + 2B'\zeta_y) \tag{20}$$

$$= \xi_{xx} + \xi_{yy}$$

To determine the analytical solution in the typical grid element, Equation 20 is rewritten as follows.

$$-(2A\ \xi_x + 2B\ \xi_y) + \xi_{xx} + \xi_{yy} = S(x,y) \tag{21}$$

where

$$S(x,y) = (2A'\ \zeta_x + 2B'\ \zeta_y + k\cdot Re\cdot i\ \xi)$$

It is then transformed to an homogeneous equation by the following change in the dependent variable.

$$\bar{\xi}(x,y) = \xi(x,y) + \frac{S(Ax + \frac{B}{A}y)}{2(A^2 + \frac{B^2}{A})} \cdot .$$

The resulting homogeneous equation is given in Equation 22.

$$\nabla^2\bar{\zeta} = 2A\ \bar{\zeta}_x + 2B\ \bar{\zeta}_y \tag{22}$$

This equation is of the same form as that for the steady linearized vorticity, Equation 11. Thus, the solution for $\bar{\zeta}$ is obtained in a manner exactly analogous to that for the steady vorticity, ζ, and is given in Equation 23.

$$\bar{\xi}(x_o,y_o) = z_1(x_o+\Delta x,y_o+\Delta y)\bar{\xi}(x_o+\Delta x,y_o+\Delta y) \tag{23}$$

$$+ z_2(x_o+\Delta x,y_o)\bar{\xi}(x_o+\Delta x,y_o)$$

$$+ z_3(x_o+\Delta x,y_o-\Delta y)\bar{\xi}(x_o+\Delta x,y_o-\Delta y)$$

$$+ z_4(x_o,y_o-\Delta y)\bar{\xi}(x_o,y_o-\Delta y)$$

$$+ z_5(x_o-\Delta x,y_o-\Delta y)\bar{\xi}(x_o-\Delta x,y_o-\Delta y)$$

$$+ z_6(x_o-\Delta x,y_o)\bar{\xi}(x_o-\Delta x,y_o)$$

$$+ z_7(x_o-\Delta x,y_o+\Delta y)\bar{\xi}(x_o-\Delta x,y_o+\Delta y)$$

$$+ z_8(x_o,y_o+\Delta y)\bar{\xi}(0,\Delta y)$$

where the coefficients z_i are dependent on the steady state velocity components, U and V.

Unsteady Stream Function

The unsteady stream function is described by Equation 5b. This equation is identical to that for the steady stream function, Equation 4b. Hence, the solution procedure is identical to that for the steady stream function. As the coefficients for the stream function are only a function of their position in the

grid element, that is, Δx and Δy, the unsteady coefficients remain the same as those found previously for the steady stream function $\Psi(x_o,y_o)$. Thus, the solution for the unsteady stream function is determined from the steady stream function solution, Equation 18, by replacing Ψ by ψ and the steady vorticity ς by the unsteady vorticity ξ. The algebraic equation for the value of the unsteady stream function at the center of the typical element in terms of the values of the unsteady stream function and vorticity at its eight neighboring values is given in Equation 24.

$$\psi(x_o,y_o) = p_1^\psi \psi(x_o+\Delta x,y_o+\Delta y) + p_2^\psi \psi(x_o+\Delta x,y_o) \quad (24)$$
$$+ p_3^\psi \psi(x_o+\Delta x,y_o-\Delta y) + p_4^\psi \psi(x_o,y_o-\Delta y)$$
$$+ p_5^\psi \psi(x_o-\Delta x,y_o-\Delta y) + p_6^\psi \psi(x_o-\Delta x,y_o)$$
$$+ p_7^\psi \psi(x_o-\Delta x,y_o+\Delta y) + p_8^\psi \psi(x_o,y_o+\Delta y)$$
$$+ q_1^\psi \xi(x_o+\Delta x,y_o+\Delta y) + q_2^\psi \xi(x_o+\Delta x,y_o)$$
$$+ q_3^\psi \xi(x_o+\Delta x,y_o-\Delta y) + q_4^\psi \xi(x_o,y_o-\Delta y)$$
$$+ q_5^\psi \xi(x_o-\Delta x,y_o-\Delta y) + q_6^\psi \xi(x_o-\Delta x,y_o)$$
$$+ q_7^\psi \xi(x_o-\Delta x,y_o+\Delta y) + q_8^\psi \xi(x_o,y_o+\Delta y)$$
$$+ q_9^\psi \xi(x_o,y_o)$$

Unsteady Velocity and Pressure

The unsteady velocity components u and v are determined by differentiating the unsteady stream function, with the locally analytical solution for the unsteady pressure determined by a post process.

Results

The small perturbation unsteady viscous flow model and locally analytical solution are utilized to investigate the effects of Reynolds number, mean flow incidence angle, and reduced frequency on the unsteady aerodynamics of a harmonically oscillating airfoil. These results are presented in the form of the unsteady pressure distributions on the surfaces of the oscillating airfoil and the complex unsteady aerodynamic lift and moment coefficients, defined in Equation 25.

$$C_L = \frac{L}{\frac{1}{2}\rho c U^2 k^2 \pi} = \frac{\int_{c=0}^{c=1} (P_{lower} - P_{upper})dx}{\frac{1}{2}\rho c U^2 k^2 \pi} \quad (25)$$

$$C_M = \frac{M}{\frac{1}{2}\rho c^2 U^2 k^2 \pi} = \frac{\int_{c=0}^{c=1} (P_{lower} - P_{upper})(x - x_{ea})dx}{\frac{1}{4}\rho c^2 U^2 k^2 \pi}$$

Predictions are obtained on a 50 x 35 rectangular grid with $\Delta x = 0.025$ and $\Delta y = 0.025$. Twenty-one points are located on the flat plate airfoil. The convergence criteria for the internal and external iterations for the stream function are both 10^{-4}, with the vorticity tolerance being $5 \cdot 10^{-2}$. The tolerances for the pressure iterations are 10^{-6} and 10^{-5} for the internal and external iterations, respectively. The computational time averaged 440 CPU on the Cyber 205, with an average of 160 iterations for the solutions of the stream function and vorticity and an additional 160 iterations for the pressure solution.

The chordwise distributions of the complex unsteady pressure on the individual surfaces of an oscillating airfoil at zero, four, and eight degrees of incidence and Reynolds numbers of 500 and 1,000 are presented in Figures 3 through 7. The corresponding classical inviscid Theodorsen predictions [7] are also shown.

Viscosity has a large effect on the complex unsteady surface pressures, particularly the real part, over the front part of the airfoil. One difference between the two solutions is that the viscous solution is finite at the leading edge whereas the inviscid solution is singular. Also, the real part of the inviscid unsteady pressure is greatly increased in magnitude as compared to the viscous predictions over the front half of the airfoil, with the imaginary part of the viscous and inviscid solutions of approximately the same magnitude aft of the airfoil inviscid leading edge singularity. This is due to the differences in the viscous and inviscid normal velocity boundary conditions. Namely, the real part of this boundary condition is dependent on the steady flow axial velocity component, U, evaluated on the airfoil surface. In the inviscid model, this velocity is the nonzero axial freestream velocity. However, in the viscous flow model, this velocity is zero because of the no-slip airfoil surface boundary condition.

Increasing the Reynolds number from 500 to 1,000 results in a small increase in the absolute magnitude of the complex unsteady pressures on the airfoil surfaces. It also increases the leading and trailing edge unsteady surface pressure differences, with a somewhat larger effect on the imaginary component.

For nonzero incidence angle values, neither the real nor the imaginary components of the chordwise unsteady pressure distributions are symmetric, with this nonsymmetry increasing with increasing incidence angle, as expected. Also, as the incidence angle is increased, the trailing edge unsteady surface pressure difference is increased, particularly the imaginary part.

The torsion mode flutter stability of an airfoil is determined by the imaginary part of the unsteady aerodynamic moment if there is no mechanical damping. Thus, the effects of incidence angle, Reynolds number, and reduced frequency on the imaginary part of the moment coefficients are considered in Figures 8 through 11 together with Theodorsen's inviscid zero incidence results. In particular, these figures present the imaginary part of the unsteady aerodynamic moment coefficient as a function of the elastic axis location, with the reduced frequency as parameter at Reynolds numbers of 500 and 1,000 for incidence angles of 0 and 4 degrees. Also, the effects of Reynolds number and incidence angle on the complex unsteady aerodynamic lift and

moment on an airfoil with a quarter-chord elastic axis location are given in Table 1.

In an inviscid flow field, the minimum relative stability is found when the elastic axis is located in the midchord region of the airfoil. As the reduced frequency is increased from 1.0 to 2.4, the relative stability of the airfoil is decreased, with the location of the elastic axis for minimum relative stability moving aft with increasing values of the reduced frequency.

Viscous effects are seen to generally decrease the relative stability of the airfoil at all elastic axis locations at both zero and four degrees of incidence. The largest relative decrease in airfoil stability is associated with the lower reduced frequency value. Also, increasing the Reynolds number from 500 to 1,000 results in a decrease in the relative airfoil stability. In fact, at zero incidence, the airfoil becomes unstable for all reduced frequency values with an elastic axis located at 75% chord at a Reynolds number of 1,000. Increasing the value of the incidence angle results in an increase in the relative stability of the airfoil. However, at a Reynolds number of 1,000 with an elastic axis at 75% chord, the airfoil is still unstable at a reduced frequency value of 1.0, the lowest value considered.

Summary and Conclusions

A mathematical model has been developed to predict the unsteady aerodynamics of a flat plate airfoil executing harmonic torsional motions in an incompressible laminar flow at moderate values of the Reynolds numbers. The unsteady viscous flow is assumed to be a small perturbation to the steady viscous flow which is described by the Navier-Stokes equations. Thus, the steady flow is nonuniform and nonlinear and is also independent of the unsteady flow field. The small perturbation unsteady viscous flow field is described by a system of linear partial differential equations that are coupled to the steady flow field, thereby modeling the strong dependence of the unsteady aerodynamics on the steady flow.

Solutions for both the steady and the unsteady viscous flow fields are obtained by developing a locally analytical solution. In this approach, the discrete algebraic equations which represent the flow field equations are obtained from analytical solutions in individual local grid elements. The complete flow field solutions are then obtained through the application of the global boundary conditions and the assembly of the local grid element solutions. This model and locally analytical solution were then utilized to demonstrate the effects of Reynolds number, mean flow incidence angle, reduced frequency value, and elastic axis location on the complex unsteady airfoil surface pressure distributions and also on the torsional stability of the airfoil.

Viscosity was shown to have a large effect on the complex unsteady surface pressures, particularly the real part, over the front part of the airfoil. Also, the real part of the inviscid unsteady pressure is greatly increased in magnitude as compared to the viscous predictions over the front half of the airfoil, with the imaginary part of the viscous and inviscid solutions of approximately the same magnitude aft of the airfoil leading edge inviscid signularity. In terms of airfoil stability, viscous effects were shown to generally decrease the relative stability of the airfoil, with the largest decrease associated with the lower reduced frequency value. Increasing the Reynolds number caused a decrease in the relative stability of the airfoil stability whereas increasing the incidence angle resulted in increased airfoil stability.

Acknowledgements

This research was sponsored, in part, by the Air Force Office of Scientific Research.

References

1. Yates, J.E., "Unsteady Viscous Thin Airfoil Theory", *AGARD Report Number 671*, September 1978.

2. Chu, W.H., "An Aerodynamic Analysis for Flutter in Oseen type Viscous Flow", *Journal of the Aerospace Sciences*, pp. 781-789, July 1962.

3. Shen, S.F., and Crimi, P., "The Theory for an Oscillating Thin Airfoil as Derived from the Oseen Equation", *Journal of Fluid Mechanics*, Volume 23, Part 3, pp. 585-609, 1965.

4. Mehta, U.B., and Lavan, Z., "Starting Vortex Separation Bubbles and Stall: A Numerical Study of Laminar Unsteady Flow Around an Airfoil", *Journal of Fluid Mechanics*, Volume 67, Number 2, pp. 227-256, 1975.

5. Thompson, J.F., Thames, F.C., Walker, R.L. and Shanka, S.P., "Numerical Solution of the Unsteady Navier-Stokes Equations for Arbitrary Bodies Using Boundary Fitted Curvilinear Coordinates", *Symposium on Unsteady Aerodynamics*, Kinney, R.B., editor, University of Arizona, Tuscon, pp. 453-465, 1975.

6. Wu, J.C., and Sampath, S., "A Numerical Study of Viscous Flow Around an Airfoil", *AIAA Paper 76-337*, 1976.

7. Theodorsen, T., "General Theory of Aerodynamic Instability and the Mechanism of Flutter", *NACA TR-496*, 1935.

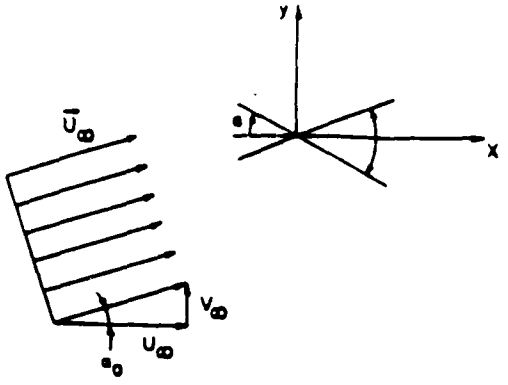

Figure 1. Schematic of oscillating flat plate airfoil flow field

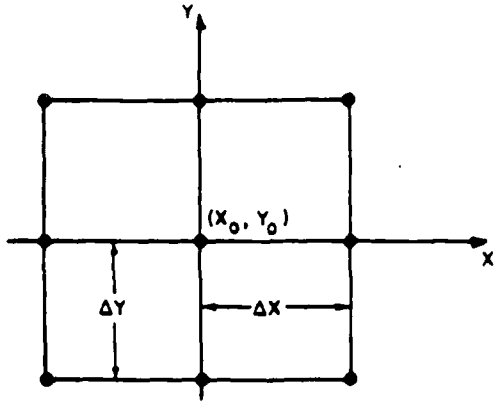

Figure 2. Typical computational grid element

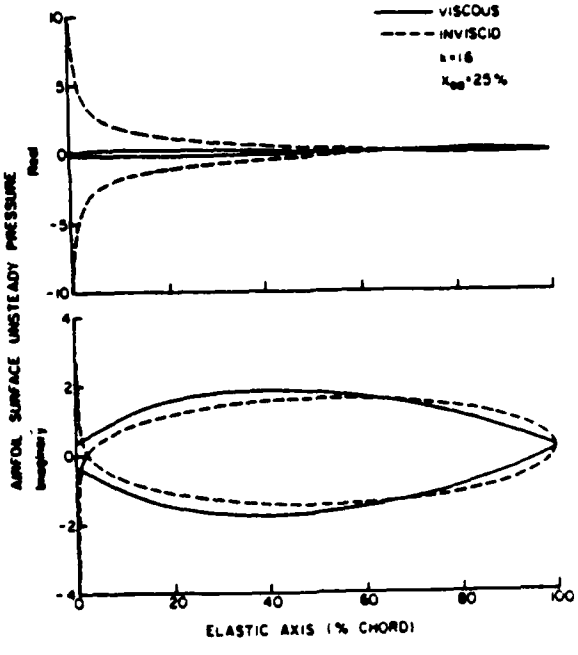

Figure 3. Unsteady airfoil surface pressure distributions for Re = 500 and 0° incidence

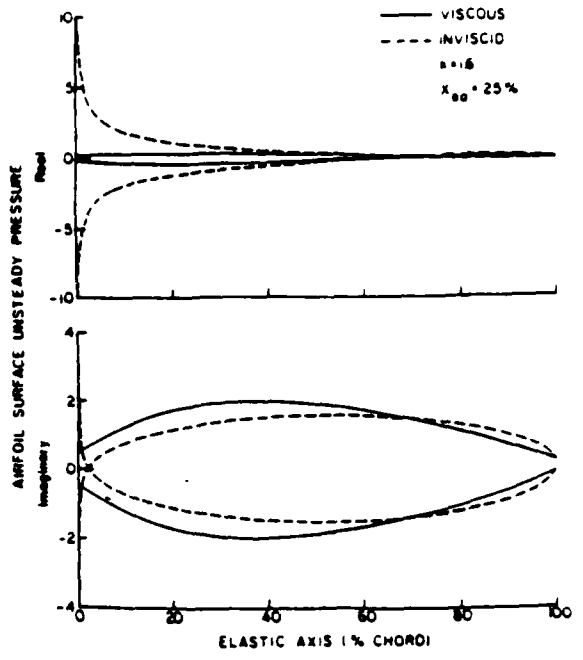

Figure 4. Unsteady airfoil surface pressure distributions for Re = 1,000 and 0° incidence

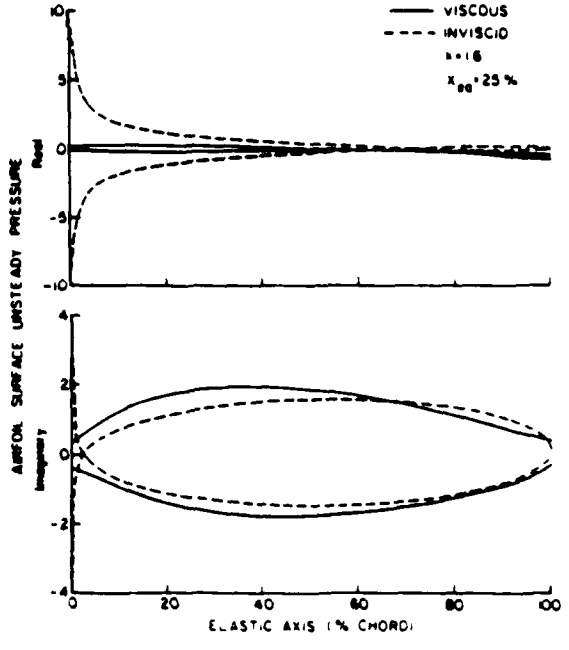

Figure 5. Unsteady airfoil surface pressure distributions for Re = 500 and 4° incidence

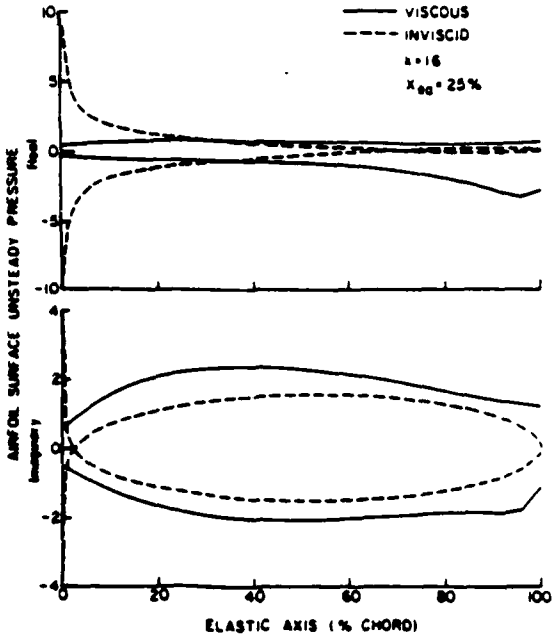

Figure 6. Unsteady airfoil surface pressure distributions for Re = 1,000 and 4° incidence

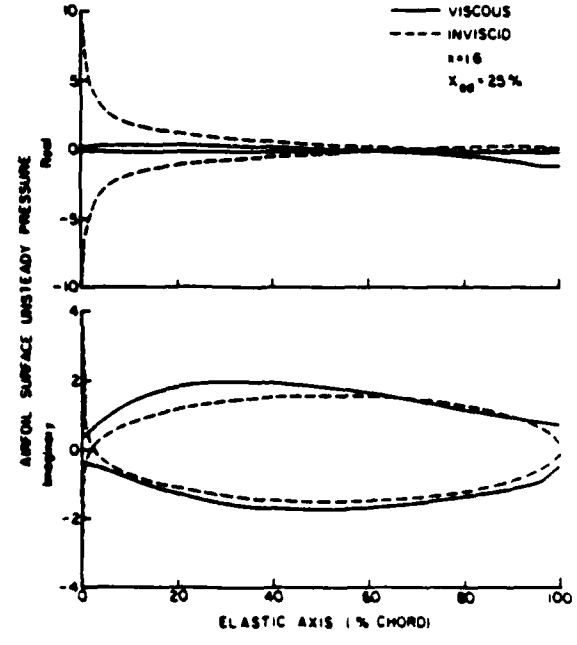

Figure 7. Unsteady airfoil surface pressure distributions for Re = 500 and 8° incidence

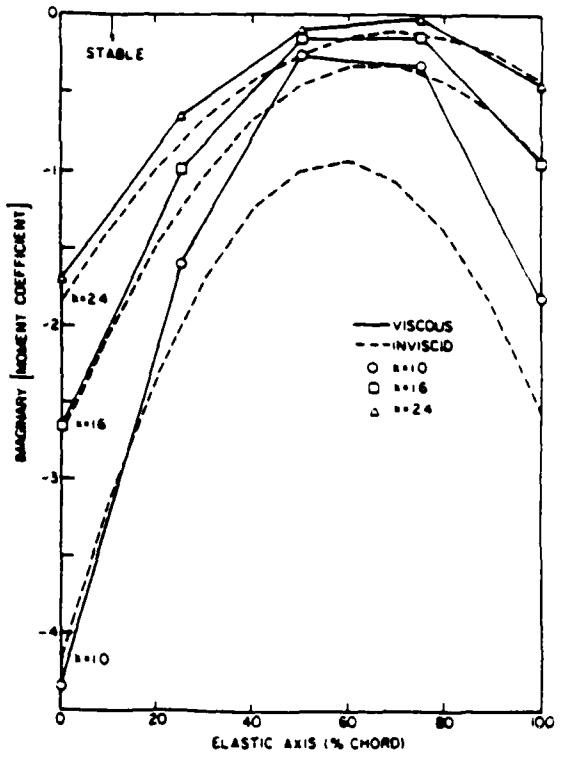

Figure 8. Imaginary aerodynamic moment coefficient versus elastic axis for Re = 500 and 0° incidence

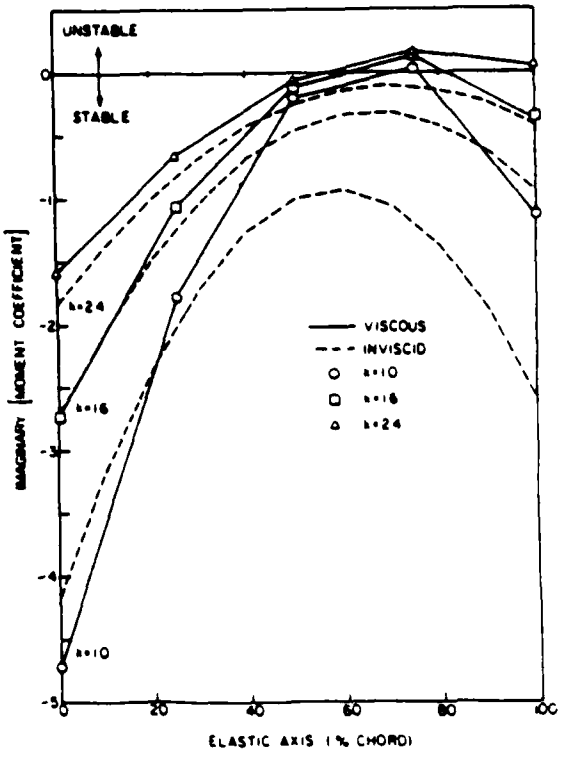

Figure 9. Imaginary aerodynamic moment coefficient versus elastic axis for Re = 1,000 and 0° incidence

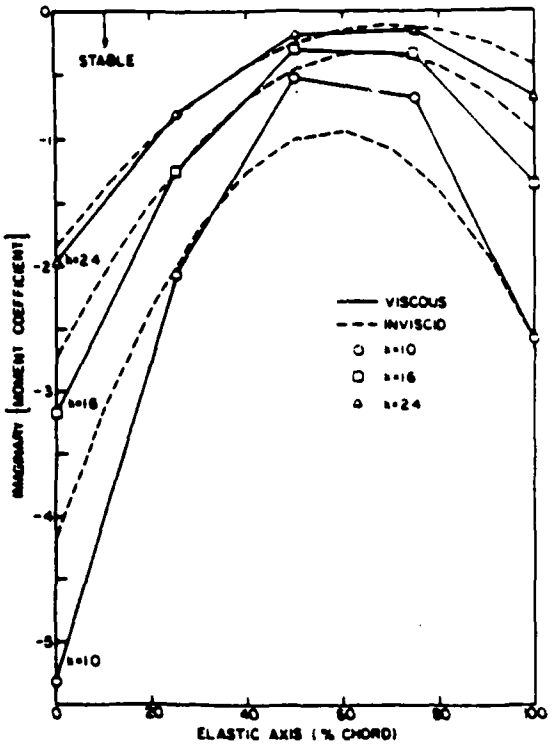

Figure 10. Imaginary aerodynamic moment coefficient versus elastic axis for Re = 500 and 4° incidence

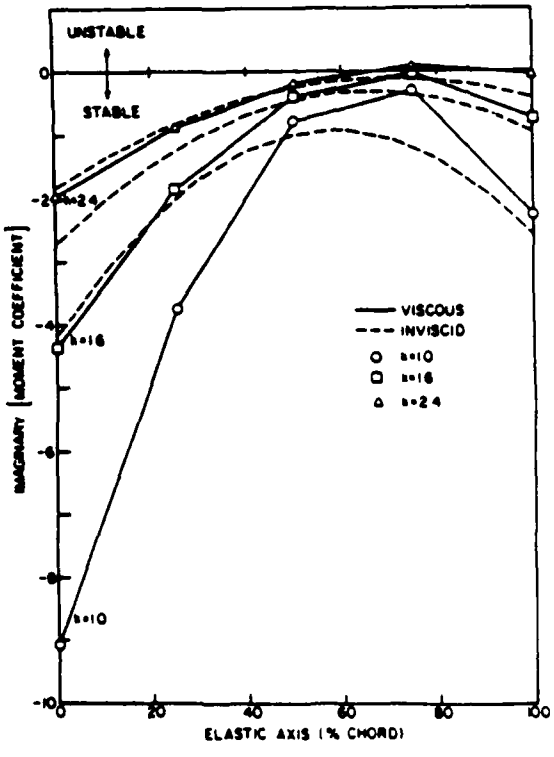

Figure 11. Imaginary aerodynamic moment coefficient versus elastic axis for Re = 1,000 and 4° incidence

	LIFT		MOMENT	
	C_{L_α}	C_{L_q}	C_{M_α}	C_{M_q}
Theodorsen	-1.523	-2.271	+0.375	-1.25
Viscous Solver, $\alpha = 0°$				
Re = 500	-0.071	-2.385	-0.003	-0.977
Re = 1000	-0.376	-2.635	-0.064	-1.048
Viscous Solver, $\alpha = 4°$				
Re = 500	-0.189	-2.578	-0.013	-1.128
Re = 1000	-1.580	-3.339	-1.024	-1.626
Viscous Solver, $\alpha = 8°$				
Re = 500	-0.298	-2.611	-0.132	-1.206

Table 1. Unsteady aerodynamic lift and moment coefficients for x_{ea} = 25% and k = 1.6

APPENDIX XI

PREDICTION OF AERODYNAMICALLY INDUCED VIBRATIONS IN TURBOMACHINERY BLADING

ASME JOURNAL OF FLUIDS ENGINEERING

Reprinted from December 1983, Vol. 105, Journal of Fluids Engineering

Prediction of Aerodynamically Induced Vibrations in Turbomachinery Blading

D. Hoyniak
Graduate Research Assistant

S. Fleeter
Professor of Mechanical Engineering.

Thermal Sciences and
Propulsion Center,
School of Mechanical Engineering,
Purdue University,
West Lafayette, Ind. 47907

To predict the aerodynamically forced response of an airfoil, an energy balance between the unsteady aerodynamic work and the energy dissipated through the airfoil structural and aerodynamic damping is performed. Theoretical zero incidence unsteady aerodynamic coefficients are then utilized in conjunction with this energy balance technique to predict the effects of reduced frequency, inlet Mach number, cascade geometry and interblade phase angle on the torsion mode aerodynamically forced response of the cascade. In addition, experimental unsteady aerodynamic gust data for flat plate and cambered cascaded airfoils are used together with these theoretical cascade unsteady self-induced aerodynamic coefficients to indicate the effects of incidence angle and airfoil camber on the forced response of the airfoil cascade.

Introduction

The structural dynamic response of turbomachinery components to aerodynamic excitations is an item of continuing concern to designers and manufacturers of gas turbine engines. The accurate first principles prediction of the aerodynamically forced response of a turbine engine blade or vane involves the following items.

Spatially periodic variations in pressure, velocity, and flow direction of the exit flow field of an upstream airfoil element appear as temporally varying in a coordinate system fixed to the downstream row. As a result, individual airfoils are subject to a time-variant periodic aerodynamic forcing function. When the forcing function frequency is equal to an airfoil natural frequency, vibrations of the airfoil result. At times these vibrations have relatively large amplitudes which induce high vibratory stress levels. Unfortunately, at present these resonant stress levels are unknown until the first testing of the blade or vane row. If stresses in excess of a predetermined allowable level result, then airfoil life considerations require that these stresses be reduced.

The prediction of the aerodynamically forced response vibratory behavior of a blade or vane row requires a definition of the unsteady forcing function in terms of its harmonics. The time-variant aerodynamic response of the airfoil to each harmonic component of this forcing function is then assumed to be comprised of two distinct but related unsteady aerodynamic parts. One is due to the harmonic forcing function being swept past the non-responding fixed airfoils – termed the gust response. The second is created by the resulting harmonic response of the airfoil – termed the self-induced aerodynamic response and, under certain conditions, also referred to as the aerodynamic damping.

Unsteady aerodynamic gust and self-induced aerodynamic response analyses are both items of fundamental research interest. Linearized unsteady compressible and incompressible small perturbation analyses for isolated and cascaded airfoils are appearing in the open literature with regularity. Of direct application to turbomachinery design are the unsteady aerodynamic analyses for cascaded airfoils. In particular, Whitehead [1] analyzed both the transverse gust response and the torsion and translation mode self-induced aerodynamic response of a cascade of flat plate airfoils in an incompressible flow. This analysis was extended to include the effects of compressibility by Fleeter [2] and Smith [3]. The effect of airfoil profile on the self-induced aerodynamic response of a cascade in an incompressible uniform flow field has been analytically predicted by Atassi and Akai [4].

There are many mathematical and physical assumptions inherent in these models. Hence, a limited number of appropriate fundamental experiments were undertaken to assess the range of validity of the analyses. Included among these are the experiments of Ostdiek [5], Henderson and Frank [6], and Fleeter, Bennett and Jay [7, 8, 9]. A complete review of research related to unsteady flows in turbomachinery, including both experimental and analytical gust response and self-induced aerodynamic response effects, is presented by Platzer in reference 10.

Generally, the aerodynamically forced response of an airfoil is predicted utilizing a classical Newton's second law forced response approach. The unsteady aerodynamic analyses are used to describe the forcing function in conjunction with a lumped parameter description of the airfoil structural dynamic properties [11]. This paper presents an alternative calculation procedure utilizing an energy balance technique. In particular, an energy balance similar to that performed by Carta [12] is conducted between the unsteady aerodynamic work and the energy dissipated by the airfoil structural and aerodynamic damping. This technique is then

Contributed by the Fluids Engineering Division for publication in the JOURNAL OF FLUIDS ENGINEERING. Manuscript received by the Fluids Engineering Division, October 14, 1982.

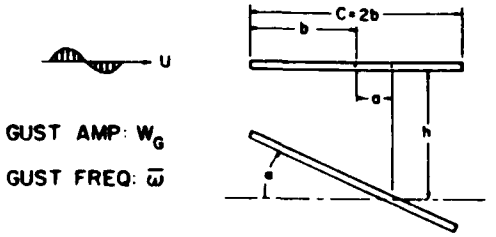

Fig. 1 Airfoil and displacement geometry and notation

applied to an airfoil cascade utilizing theoretical unsteady aerodynamic coefficients which enable the effects of reduced frequency, inlet Mach number, cascade geometry, and interblade phase angle on the aerodynamically forced response of the airfoil to be investigated. In addition, experimental unsteady aerodynamic gust data for a flat plate and a cambered airfoil cascade are used in conjunction with the theoretical zero incidence flat plate cascade unsteady self-induced aerodynamic coefficients to consider the effects of incidence angle and airfoil camber on the forced response of the airfoil cascade.

General Unsteady Aerodynamic Coefficients

Figure 1 presents a schematic representation of a two-dimensional airfoil section displaced in both torsion and translation in a uniform flow with a superimposed convected transverse sinusoidal gust. The complex, time-dependent unsteady lift and moment per unit span are written in influence coefficient form for the gust and the self-induced aerodynamic response cases in equations 1 and 2 respectively.

$$\left.\begin{aligned} L_G &= L_G{}^R + iL_G{}^I = \pi\rho b^3\bar{\omega}^2\left[A_G\left(\frac{W_G}{U}\right)\right] \\ M_G &= M_G{}^R + iM_G{}^I = \pi\rho b^4\bar{\omega}^2\left[B_G\left(\frac{W_G}{U}\right)\right] \end{aligned}\right\} \quad (1)$$

$$\left.\begin{aligned} L_{SI} &= L_{SI}{}^R + iL_{SI}{}^I = \pi\rho b^3\omega^2[A_h\, h + A_\alpha\, \alpha] \\ M_{SI} &= M_{SI}{}^R + iM_{SI}{}^I = \pi\rho b^4\omega^2[B_h\, h + B_\alpha\, \alpha] \end{aligned}\right\} \quad (2)$$

where: $h = \bar{h}\, e^{i\bar{\omega}t}$; $\alpha = \bar{\alpha}\, e^{i\bar{\omega}t}$; $W_G = \bar{W}_G e^{i\bar{\omega}t}$ describes the gust; (A_h, B_h), (A_α, B_α), (A_G, B_G) denote the generalized unsteady lift and moment coefficients due to airfoil translation, airfoil torsion, and the convected sinusoidal gust, respectively; ω is the airfoil natural frequency, and $\bar{\omega}$ is the gust forcing function frequency.

The total unsteady lift and moment on the airfoil are obtained by super-imposing the gust response and the self-induced unsteady aerodynamic forces and moments.

$$L(t) = L_G(t) + L_{SI}(t) = \pi\rho b^3\bar{\omega}^2\left[A_G\left(\frac{\bar{W}_G}{U}\right) + A_h\,\bar{h} + A_\alpha\,\bar{\alpha}\right]e^{i\bar{\omega}t}$$

$$M(t) = M_G(t) + M_{SI}(t) = \pi\rho b^4\bar{\omega}^2\left[B_G\left(\frac{\bar{W}_G}{U}\right) + B_h\,\bar{h} + B_\alpha\,\bar{\alpha}\right]e^{i\bar{\omega}t} \quad (3)$$

It should be noted that the airfoil response occurs at the frequency of the forcing function, hence the gust frequency, $\bar{\omega}$, has been utilized in the specification of the unsteady aerodynamic forces and moments, equation (3).

Energy Balance

The uncoupled equations of motion for the single-degree-of-freedom lumped airfoil model undergoing translation or torsion mode oscillations as depicted in Fig. 1 are given in equation (4).

$$\left.\begin{aligned} m\ddot{h} + (1+ig)sh &= L(t) \\ I\ddot{\alpha} + (1+ig)s\alpha &= M(t) \end{aligned}\right\} \quad (4)$$

where: m denotes the airfoil mass, s is the stiffness coefficient, g is the structural damping, and I is the mass moment of inertia about the elastic axis. The uncoupled equations of motion, equation (4), represent an airfoil whose elastic axis is coincident with its center of gravity.

The response of the uncoupled single-degree-of-freedom system is determined by considering the balance between the energy input to the system and the energy dissipated by the system over one cycle of oscillation of the airfoil. The input energy to the system is obtained from a calculation of the work done by the unsteady gust forces and moments acting on the airfoil. The energy dissipated is obtained by calculating the work done by the structural damping and by the self-induced aerodynamic response (aerodynamic damping) forces and moments. For convenience, only the case of torsion mode oscillations will be considered in the following derivations. It should be noted, however, that the translation mode results can be obtained directly from those for the torsion mode by

Nomenclature

- a = dimensionless distance of elastic axis aft of mid-chord
- b = 1/2 airfoil chord ($C/2$)
- g = structural damping coefficient
- h = complex translation motion
- k = reduced frequency ($k = \bar{\omega}b/U$)
- m = mass of airfoil
- s = stiffness coefficient
- A = unsteady lift
- B = unsteady moment
- C = airfoil chord
- I = mass moment of inertia about the elastic axis
- L = unsteady lift
- M = unsteady moment
- S = airfoil spacing
- U = free-stream velocity
- W = complex transverse gust function
- $\bar{W}$ = amplitude of transverse gust
- α = complex torsion motion
- $\bar{\alpha}$ = amplitude of oscillation in torsion
- λ = phase angle between the gust and the airfoil motion
- ϕ = phase angle between the gust and the resulting moment
- ψ = phase angle between the unsteady moment due to the gust and the airfoil response
- ρ = fluid density
- σ = interblade phase angle
- ω = airfoil natural frequency
- $\bar{\omega}$ = frequency of the transverse gust

Subscripts

- G = gust
- SI = self-induced (aerodynamic damping)
- h = translation
- α = torsion

Superscripts

- R = real part
- I = imaginary part
- $\cdot$ = derivative with respect to time

replacing I, α, and M by m, h, and L, respectively, per equation (4).

The unsteady work done per cycle of oscillation by the unsteady gust aerodynamic moment is given by the integral of the product of the real part of the unsteady moment and the resulting displacement over one cycle of motion.

$$\text{Work}_G = \oint \text{Re}[M_G(t)\, d\alpha] \tag{5}$$

where: $M_G(t) = T_0 e^{i(\omega t + \phi)}$

$$T_0 = \pi \rho b^4 \bar{\omega}^2 \left(\frac{\bar{W}_G}{U}\right)\left[(B_G{}^R)^2 + (B_G{}^I)^2\right]^{1/2}$$

and $\phi = \tan^{-1}[B_G{}^I / B_G{}^R]$ and defines the phase angle between the gust and the aerodynamic moment due to this gust.

Carrying out the integration specified in equation (5) results in the following expression for the unsteady work due to the gust.

$$\text{Work}_G = -\pi T_0 \bar{\alpha} \sin(\lambda - \phi) \tag{6}$$

where λ denotes the phase angle between the gust and the airfoil motion. It should be noted that the quantity $(\lambda - \phi)$ is, in fact, the phase angle between the unsteady moment due to the gust and the airfoil response. It can be determined in terms of the system structural characteristics by a variety of means. For convenience herein, it is determined from the equation of motion, equation (4), per reference [11].

$$\text{Work}_G = -\pi T_0 \bar{\alpha} \sin(\lambda - \phi) = -\pi T_0 \bar{\alpha} \sin(\psi) \tag{7}$$

where:

$$\psi = \text{TAN}^{-1}\left[\frac{[gs - \pi\rho b^4 \bar{\omega}^2 B_\alpha{}^I]}{[(-I\bar{\omega}^2 + s - \pi\rho b^4 \bar{\omega}^2 B_\alpha{}^R]}\right].$$

The energy dissipated per cycle of oscillation is obtained by integrating the real part of the product of the self-induced unsteady aerodynamic response (the aerodynamic damping) moment and the airfoil displacement over one cycle of oscillation. It should be noted that although this term is written as a dissipation term, under certain conditions it can represent an energy input term.

$$\text{Work}_{SI} = \oint \text{Re}[M_{SI}(t)\, d\alpha] \tag{8}$$

This integration leads to the following expression for the energy dissipated per cycle of oscillation.

$$\text{Work}_{SI} = \pi(gs - \pi\rho b^4 \bar{\omega}^2 B_\alpha{}^I)\bar{\alpha}^2 \tag{9}$$

The balance of energy requires that the energy input to the system must be equal to that dissipated by the airfoil, i.e.,

$$\text{Work}_G = \text{Work}_{SI} \tag{10}$$

Substitution of equations (7) and (9) into this energy balance equation results in the following expression for the response amplitude of the oscillation, $\bar{\alpha}$.

$$\bar{\alpha} = \frac{T_0 \sin(\psi)}{gs - \pi\rho b^4 \bar{\omega}^2 B_\alpha{}^I} \tag{11}$$

The term $\sin(\psi)$ can be determined via application of the Pythagorean Theorem to the definition of ψ specified in equation (7) with the following result.

$$\sin(\psi) = \frac{[gs - \pi\rho b^4 \bar{\omega}^2 B_\alpha{}^I]}{[(-I\bar{\omega}^2 + s - \pi\rho b^4 \bar{\omega}^2 B_\alpha{}^R)^2 + (gs - \pi\rho b^4 \bar{\omega}^2 B_\alpha{}^I)^2]^{1/2}} \tag{12}$$

The substitution of this expression for $\sin(\psi)$ into equation (11) results in the following expression for the torsion mode amplitude of response of the airfoil to an aerodynamic excitation.

$$\bar{\alpha} = \frac{T_0}{[(-I\bar{\omega}^2 + s - \pi\rho b^4 \bar{\omega}^2 B_\alpha{}^R)^2 + (gs - \pi\rho b^4 \bar{\omega}^2 B_\alpha{}^I)^2]^{1/2}} \tag{13}$$

Unsteady Aerodynamic Forces and Moments

L_h, M_h, L_α, and M_α denote the standard form for the unsteady aerodynamic forces and moments and represent the unsteady lift and moment in translation and torsion, respectively, calculated about the airfoil 1/4 chord. These standard form 1/4 chord coefficients are related to the general unsteady aerodynamic influence coefficients through the following relationships.

$$\begin{aligned}
A_h &= L_h \\
A_\alpha &= L_\alpha - (1/2 + a) L_h \\
A_G &= L_G \\
B_h &= M_h - (1/2 + a) L_h \\
B_\alpha &= M_\alpha - (1/2 + a)(L_\alpha + M_h) + (1/2 + a)^2 L_h \\
B_G &= M_G
\end{aligned} \tag{14}$$

where a is the dimensionless distance of the torsion axis aft of the airfoil mid-chord, as depicted in Fig. 1.

The unsteady aerodynamic coefficients to be utilized in this investigation are obtained from: (1) the isolated flat plate airfoil at zero incidence in an incompressible flow field analyses of Theodorsen and Sears [13, 14]; (2) the analysis for a cascade of flat plate airfoils at zero incidence in a compressible flow field, presented in reference [2]; (3) the experimental cascade gust response data described in references [7, 8, and 9] in conjunction with the cascade self-induced response analysis of reference [2].

The isolated flat plate unsteady aerodynamic analyses, Case 1, will be utilized to verify the energy balance technique derived in the previous section. This verification will be accomplished through a comparison of the torsional response calculated by this energy balance technique and that calculated by a classical Newton's second law procedure [11].

The flat plate cascade compressible flow unsteady aerodynamic coefficients, Case 2, will be utilized to perform a parametric study on the forced response of a representative flat plate airfoil with structural characteristics based on an airfoil with a 3.18 cm chord, a thickness-to-chord ratio of 4 percent, and an aspect ratio of 2. Parameters to be varied will include the inlet Mach number, the interblade phase angle, the elastic axis location, and the cascade geometry.

The combination of the cascade analysis and the experimental gust response data, Case 3, will enable the effects of the assumptions inherent in the analyses on the response amplitude to be ascertained as well as the effects of incidence angle and airfoil camber. Experimental unsteady aerodynamic gust coefficients for flat plate and cambered airfoil cascades will be calculated from the airfoil surface unsteady pressure data presented in references [7, 8, and 9]. These experimental gust coefficients will then be utilized in conjunction with theoretical flat plate self-induced response coefficients to obtain a semi-empirical prediction of the forced response of the representative airfoil. These semi-empirical results will then be compared with corresponding forced response predictions utilizing only theoretical unsteady aerodynamics.

Results

To verify the energy balance approach for the prediction of aerodynamically induced vibrations, the uncoupled torsion

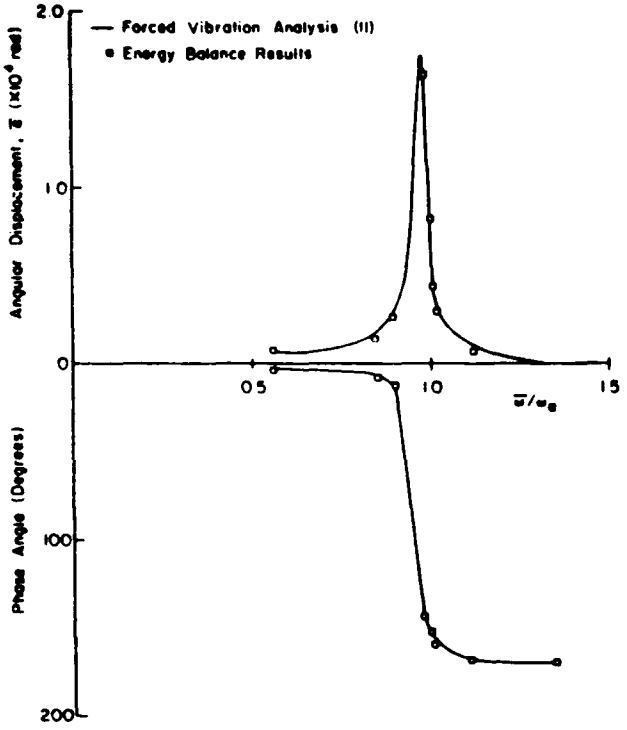

Fig. 2 Comparison of classical forced vibration results with those of the energy balance technique

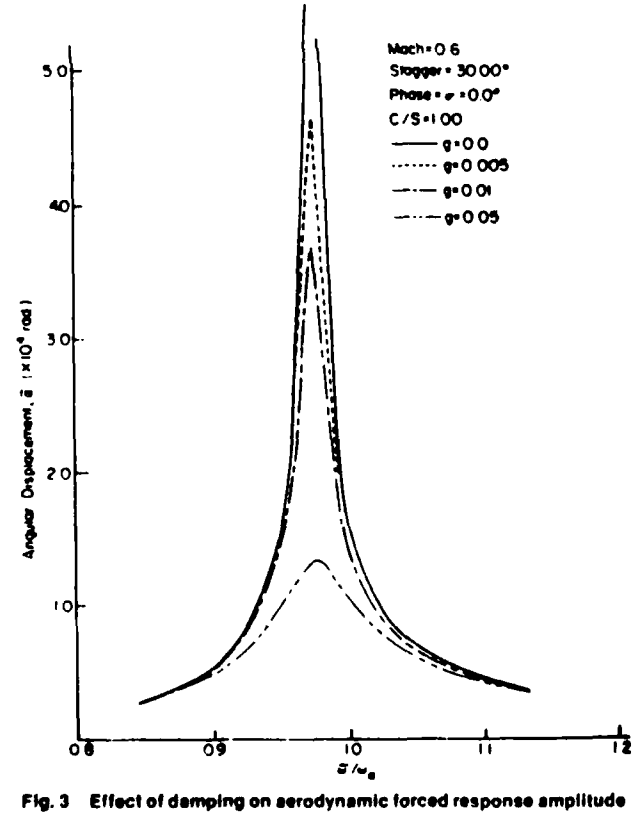

Fig. 3 Effect of damping on aerodynamic forced response amplitude

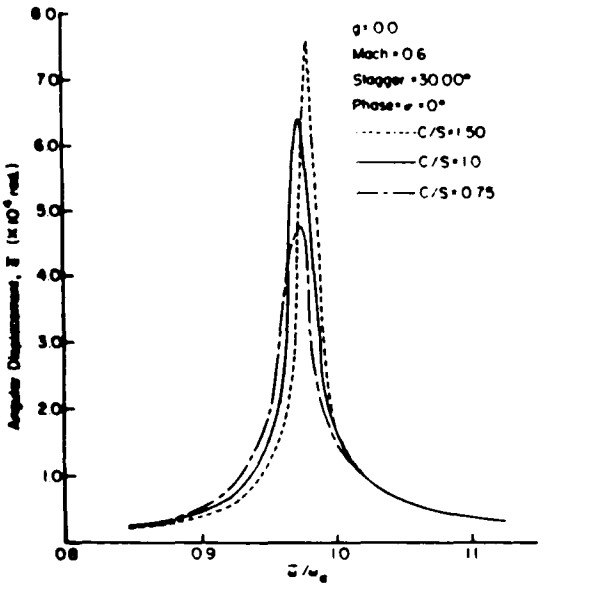

Fig. 4 Effect of cascade solidity on aerodynamic forced response amplitude

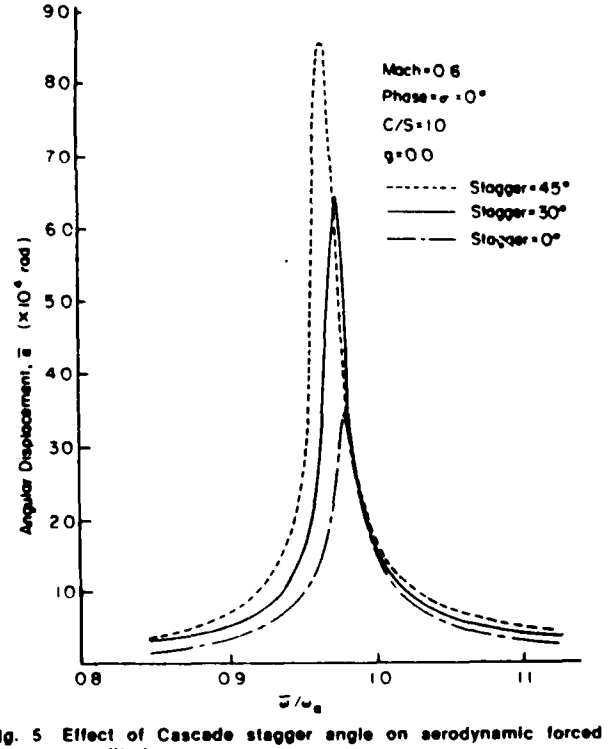

Fig. 5 Effect of Cascade stagger angle on aerodynamic forced response amplitude

mode response of the reprsentative airfoil was calculated by means of both the energy balance technique of this paper and a classical Newton's second law approach [11]. The analytical zero incidence, incompressible flow, isolated airfoil unsteady aerodynamic transverse gust and self-induced coefficients of references [13 and 14] were utilized in these calculations. Figure 2 presents the comparison of these calculation techniques in the form of the torsion mode response as a function of the ratio of the forcing function frequency to the airfoil natural frequency. As seen, the two methods yield identical results, both in terms of the amplitude and the phase of the response.

Figures 3 through 10 describe a parametric study of the aerodynamically induced uncoupled torsion mode response of the representative airfoil utilizing the theoretical flat plate cascade, compressible flow unsteady aerodynamic transverse gust and damping coefficients of reference [2]. Parameters

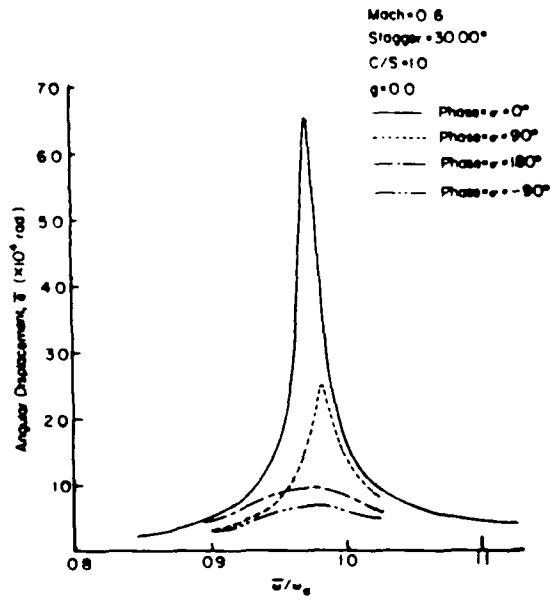

Fig. 6 Effect of interblade phase angle on aerodynamic forced response amplitude

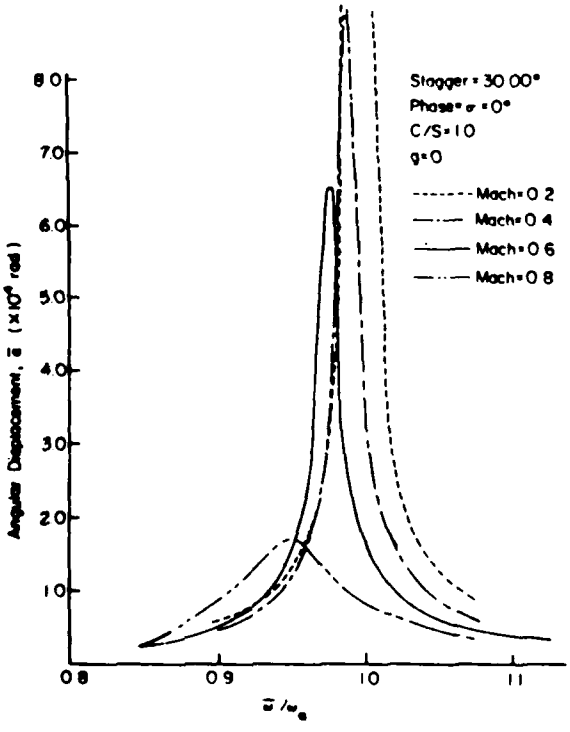

Fig. 7 Effect of inlet Mach number on aerodynamic forced response amplitude

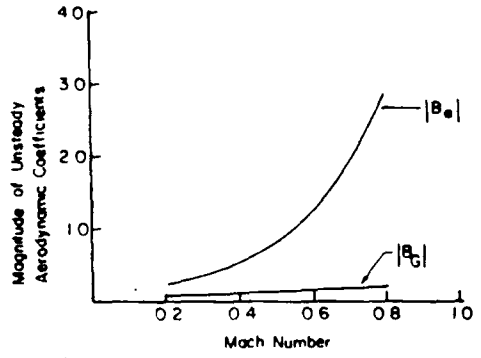

Fig. 8 Magnitude of unsteady aerodynamic coefficients as a function of inlet Mach number

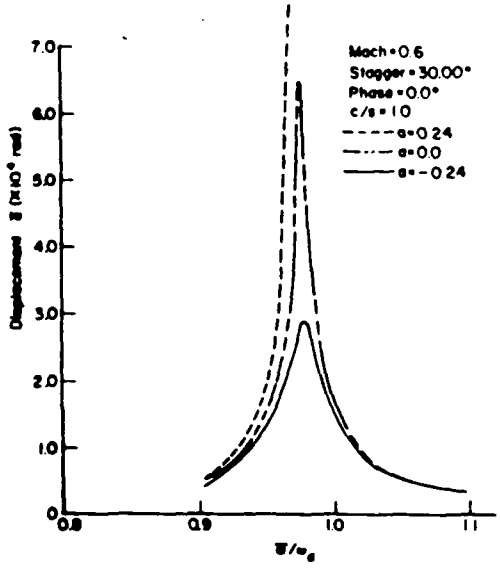

Fig. 9 Effect of elastic axis location on aerodynamic forced response amplitude

varied include the structural damping, the cascade solidity and stagger angle, the interblade phase angle, and the inlet Mach number.

Figure 3 demonstrates the effect of structural damping on the torsional amplitude of response. Decreasing the structural damping value from 0.01 to 0.005, a factor of 2, results in approximately a 25 percent increase in the maximum response amplitude. It should be noted that the peak response amplitude does not occur when the forcing function frequency is equal to the airfoil natural frequency, even for the case of zero structural damping. This is because aerodynamic damping as well as structural damping has been considered. Thus, even when the structural damping is zero, aerodynamic damping is present in the system.

The effects of the cascade solidity and stagger angle on the amplitude of the torsional response are presented in Figs. 4 and 5, respectively. As seen, the amplitude of the response decreases as both the cascade solidity and stagger angle decrease, with the stagger angle having a much more pronounced effect.

Figure 6 demonstrates the effect of the interblade phase angle on the torsional response amplitude. The maximum response is seen to occur at an interblade phase angle of 0 deg. A change in the interblade phase angle from 0 deg to 90 deg results in a significant decrease in the maximum response amplitude. Further changes of the interblade phase angle value, to 180 and −90 deg, result in a continued decrease in the maximum response amplitude, although not nearly of the magnitude of change observed in going from 0 to 90 deg. It should be noted that in terms of a rotor-stator interaction forced response problem, the interblade phase angle represents the ratio of the number of upstream rotor blades to the number of downstream stator vanes as it describes the disturbance phase difference existing between adjacent downstream airfoils. Hence, Fig. 6 shows that minimum amplitude response is predicted when there are more rotor blades than stator vanes, with the gust representing a backward traveling wave to the stators.

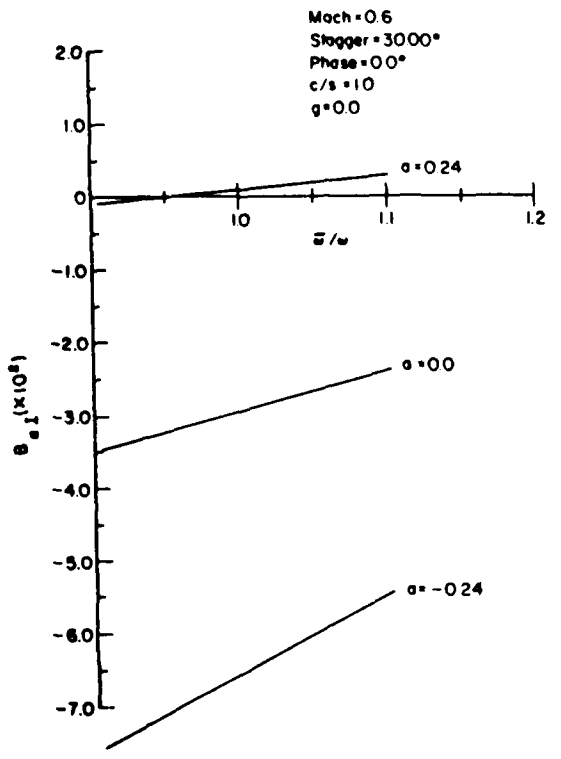

Fig. 10 Imaginary moment coefficient as a function of frequency with elastic axis location as parameter

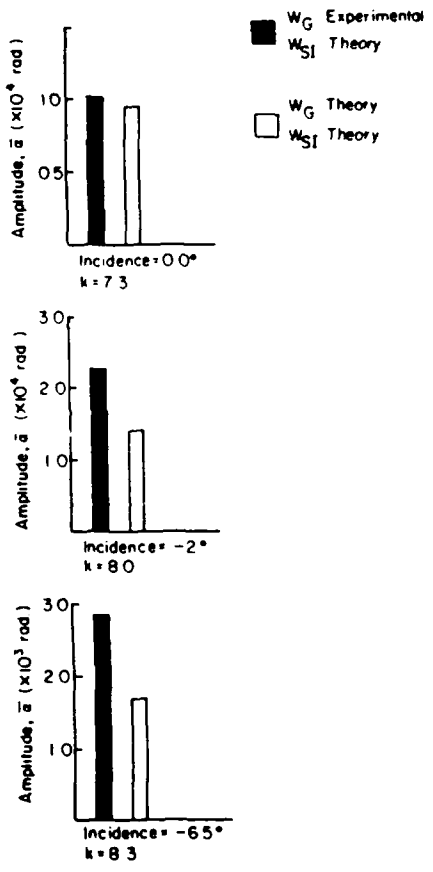

Fig. 11 Comparison of predicted aerodynamic forced response amplitude of a flat plate airfoil using semi-experimental and theoretical aerodynamic coefficients

Figure 7 shows the effect of inlet Mach number on the uncoupled torsion mode response. Increasing the Mach number results in an apparent decrease in the amplitude of response and a decrease in the value of the ratio of the gust forcing frequency to the airfoil natural frequency at which the maximum response amplitude occurs. It should be noted that the airfoil natural frequency is constant. Hence, at a constant value of $\bar{\omega}/\omega$, varying the inlet Mach number also corresponds to a variation in the reduced frequency of the airfoil ($k = \bar{\omega}b/U$). To aid in interpreting the response amplitude variations with Mach number, consider Fig. 8 which presents the magnitude of the unsteady aerodynamic gust and damping as a function of Mach number. As seen, increasing the Mach number results in an increase in the magnitudes of both the aerodynamic gust and the aerodynamic damping, with the aerodynamic damping increasing at a much greater rate. Hence, for the case considered, increasing the Mach number results in a slightly increased gust forcing function magnitude but a greatly increased level of aerodynamic damping, thereby leading to the results of Fig. 7.

Figure 9 indicates the effect that the elastic axis location has on the airfoil torsional response. In particular, this figure shows that as the elastic axis is varied from a location forward of the center of gravity to one aft, the airfoil response increases. For the example case being considered, when the elastic axis parameter, a, has a value of $+0.24$, the airfoil motion becomes unstable. This torsional instability is also demonstrated in Fig. 10 which presents the imaginary part of the unsteady torsional moment coefficient, B_{α}^{I} as a function of forcing frequency with the elastic axis location as parameter. At an elastic axis location specified by $a = +0.24$, B_{α}^{I} becomes positive, thereby indicating a flutter condition. It should be noted that varying the elastic axis location can result in a coupling of the bending and torsional modes, although only the uncoupled torsional mode of vibration has been considered herein.

To indicate the effects of incidence angle on the gust response and also the validity and usefulness of the flat plate cascade analyses, consider Figs. 11 and 12. These figures present the predicted forced torsion mode amplitude of response utilizing: (1) experimentally determined flat plate and cambered airfoil aerodynamic gust coefficients based on the data reported in references [7, 8, and 9] in conjunction with the theoretical flat plate aerodynamic damping coefficients of reference [2]; (2) theoretical flat plate aerodynamic gust and self-induced coefficients of reference [2].

For the flat plate cascade, Fig. 11, at zero incidence there is excellent agreement between the semiexperimental and the theoretical results. Decreasing the incidence angle from 0 results in increased response amplitudes as compared to the zero incidence theoretical results with the difference varying in a smooth manner. It should be noted that the reduced frequency and, hence, the unsteady aerodynamics, vary with incidence angle. Thus, these results cannot be absolutely compared to one another as a function of the incidence angle, but rather must be compared individually to the theoretical predictions.

Figure 12 compares the semiexperimental cambered airfoil cascade predictions with the corresponding flat plate theoretical predictions. As seen, the combination of a cambered airfoil at incidence angle results in a nonlinear variation of the comparison results for the response amplitude.

Summary and Conclusions

The aerodynamically forced response of an airfoil has been predicted based on an energy balance technique. In particular, an energy balance has been performed between the unsteady aerodynamic work and the energy dissipated through the

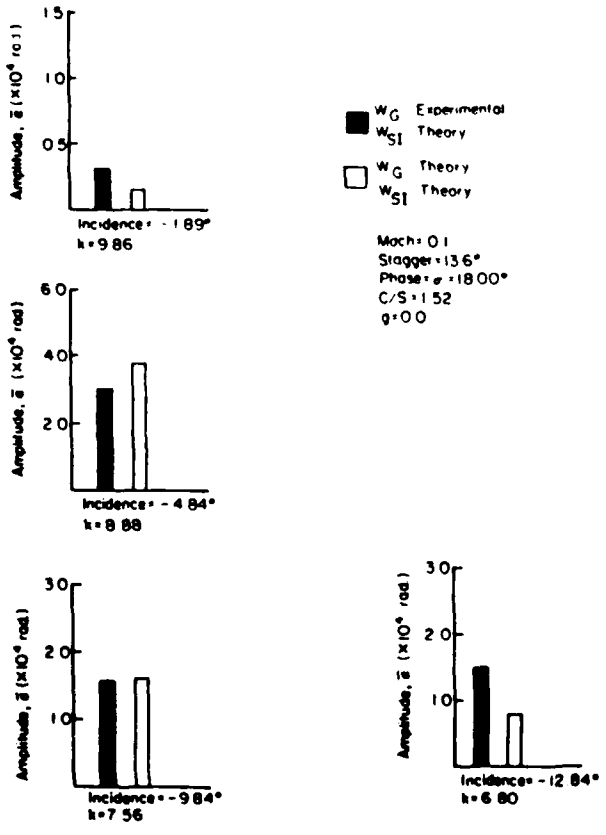

Fig. 12 Comparison of predicted aerodynamic forced response amplitude using semiexperimental and theoretical aerodynamic coefficients

airfoil structural and aerodynamic damping. A parametric study was then undertaken to investigate the effects of reduced frequency, cascade geometry, inlet Mach number, and interblade phase angle on the uncoupled torsion mode response of a representative airfoil. This study demonstrated that the torsional response amplitude decreased with:

- increased structural damping
- decreased cascade solidity
- decreased stagger angle
- increased inlet Mach number
- an interblade phase angle corresponding to a backward traveling wave
- a forward elastic axis location.

In addition, investigation of the torsional forced response of an airfoil based on experimental flat plate and cambered airfoil aerodynamic gust data revealed the following.

- The theoretical flat plate cascade aerodynamic coefficients accurately represent the physics of the problem at zero incidence angle.
- As the incidence angle is changed from a value of zero, the flat plate semiexperimental results diverge from the theoretical results, albeit in a somewhat regular manner.
- The cambered airfoil semiexperimental results differ significantly from the theoretical flat plate results, even at zero incidence.

This variation appears to be non-regular with incidence angle, thereby clearly demonstrating the need for a cambered airfoil cascade unsteady aerodynamic analysis.

Acknowledgment

This research was sponsored, in part, by the Air Force Office of Scientific Research.

References

1 Whitehead, D. S., "Force and Moment Coefficients for Vibrating Airfoils in Cascade," Aeronautical Research Council R&M3254, Feb. 1960.

2 Fleeter, S., "The Fluctuating Lift and Moment Coefficients for Cascaded Airfoils in a Nonuniform Compressible Flow," *AIAA Journal of Aircraft*, Vol. 10, No. 2, Mar. 1973.

3 Smith, S. M., "Discrete Frequence Sound Generation in Axial Flow Turbomachines," University of Cambridge, Department of Engineering Report CUED/A-Turbo/TR29, 1971.

4 Atassi, H., and Akai, T. J., "Aerodynamic and Aeroelastic Characteristics of Oscillating Loaded Cascades at Low Mach Number," ASME Paper No. 79-FT-111, Mar. 1979.

5 Ostdiek, F. R., "A Cascade in Unsteady Flow," Ph.D. thesis, The Ohio State University, 1975.

6 Henderson, R. E., and Frank, G. F., "Investigation of the Unsteady Pressure Distribution on the Blades of an Axial Flow Fan," Pennsylvania State University ARL TM 78-54, Mar. 1978.

7 Fleeter, S., Jay, R. L., and Bennett, W. A., "Rotor Wake Generated Unsteady Aerodynamic Response of a Compressor Stator," ASME *Journal of Engineering for Power*, Vol. 100, No. 4, Oct. 1978.

8 Fleeter, S., Jay, R. L., and Bennett, W. A., "The Time-Variant Aerodynamic Response of a Stator Row Including the Effects of Airfoil Camber," ASME *Journal of Engineering for Power*, Vol. 102, No. 2, Apr. 1980.

9 Fleeter, S., Jay, R. L., and Bennett, W. A., "Wake Induced Time-Variant Aerodynamics Including Rotor-Stator Axial Spacing Effects," *Symposium on Nonsteady Fluid Dynamics*, ASME, Dec. 1978.

10 Platzer, M. F., "Unsteady Flows in Turbomachines—A Review of Recent Developments," AGARD-CP-227, Sept. 1977.

11 Fung, Y. C., *An Introduction to the Theory of Aeroelasticity*, Dover Publications, Inc., 1969.

12 Carta, F. O., "Coupled Blade-Disk-Shroud Flutter Instabilities in Turbojet Engine Rotors," ASME *Journal of Engineering for Power*, Vol. 89, No. 3, July 1967.

13 Theodorsen, T., "General Theory of Aerodynamic Instability and the Mechanism of Flutter," NACA Report 496, 1935.

14 Sears, W. R., "Some Aspects of Non-Stationary Airfoil Theory and Its Practical Applications," *Journal of Aeronautical Sciences*, Vol. 8, No. 3, Jan. 1941.

APPENDIX XII

THE COUPLED RESPONSE OF TURBOMACHINERY BLADING TO AERODYNAMIC EXCITATIONS

AIAA JOURNAL OF AIRCRAFT

The Coupled Response of Turbomachinery Blading to Aerodynamic Excitations

Daniel Hoyniak* and Sanford Fleeter†
Purdue University, West Lafayette, Indiana

An energy balance technique is developed which predicts the coupled bending-torsion mode aerodynamic forced response of an airfoil. The effects of the various aerodynamic parameters are then considered utilizing a subsonic compressible flow/flat plate cascade gust analysis. The increased coupling between the torsion and translation modes as the natural frequencies approach one another is shown. It is also demonstrated that the coupled-response amplitudes increase with: 1) decreased structural damping, 2) increased solidity, stagger angle, and Mach numbers, 3) interblade phase angles corresponding to forward traveling waves, and 4) shifting of the elastic axis location aft.

Nomenclature

a = distance of elastic axis aft of mid-chord
A = unsteady lift influence coefficient
b = airfoil semichord ($C/2$)
B = unsteady moment influence coefficient
C = airfoil chord
C/S = cascade solidity (airfoil chord/airfoil spacing)
C_1 = $\mu x_\alpha + (A_\alpha)^R$
C_2 = $\mu x_\alpha + (B_h)^R$
C_3 = $[\mu - \mu(\omega_h/\bar{\omega})^2 + (A_h)^R]$
C_4 = $(A_h)^I - \mu(\omega_h/\bar{\omega})^2 g_h$
C_5 = $\mu r_\alpha^2 [1 - (\omega_\alpha/\bar{\omega})^2] + (B_\alpha)^R$
C_6 = $(B_\alpha)^I - \mu r_\alpha^2 (\omega_\alpha/\bar{\omega})^2 g_\alpha$
C_7 = $-(W_G/U)(A_G)^R$
C_8 = $-(W_G/U)(A_G)^I$
C_9 = $-(W_G/U)(B_G)^R$
C_{10} = $-(W_G/U)(A_G)^I$
D_I = $[(C_3C_5 + C_4C_6) - [C_2(A_\alpha)^I + C_1(A_h)^I]]$
D_R = $[(C_3C_6 - C_4C_5) - [C_2C_1 - (A_\alpha)^I(B_h)^I]]$
h = complex translational displacement
h_0 = amplitude of translational oscillation
i = $\sqrt{-1}$
I_α = mass moment of inertia per unit span about the elastic axis
k = reduced frequency ($k = \bar{\omega}b/U$)
L = unsteady lift
m = mass per unit span of the airfoil
M = unsteady moment
N_{hI} = $[(C_4C_5 + C_6C_3) - [C_9(A_\alpha)^I + C_1C_{10}]]$
N_{hR} = $[(C_3C_5 - C_4C_6) - [C_1C_9 - C_{10}(A_\alpha)^I]]$
$N_{\alpha I}$ = $[(C_{10}C_1 + C_4C_9) - [C_3(B_h)^I + C_2C_8]]$
$N_{\alpha R}$ = $[(C_1C_9 - C_4C_{10}) - [C_3C_2 - C_8(B_h)^I]]$
Re[ ] = real part of [ ]
r_α = radius of gyration about elastic axis
S_α = airfoil static moment per unit span about the elastic axis
U = freestream velocity
W = complex transverse gust function
W_G = amplitude of transverse gust
WORK = unsteady work per cycle of oscillation
x_α = location of center of gravity relative to elastic axis
α = complex torsional displacement
α_0 = amplitude of torsional motion
μ = mass parameter
ρ = fluid density
σ = interblade phase angle
ω = airfoil natural frequency
$\bar{\omega}$ = frequency of the transverse gust

Subscripts

G = gust
h = translation
SI = self-induced (aerodynamic damping)
α = torsion

Superscripts

I = imaginary part
R = real part
( ) = derivative with respect to time

Presented as Paper 83-0844 at the AIAA/ASME/ASCE/AHS Structures, Structural Dynamics, and Materials Conference, Lake Tahoe, Nev., May 2-4, 1983; received May 13, 1983; revision received Oct. 3, 1983.

*Graduate Research Assistant; presently Aerospace Engineer, NASA Lewis Research Center, Cleveland, Ohio.

†Professor, School of Mechanical Engineering, and Director, Thermal Sciences and Propulsion Center. Member AIAA.

Introduction

AERODYNAMICALLY-induced vibrations of rotor and stator airfoils are one of the more common sources of high-cycle fatigue failure in gas turbine engines. Destructive aerodynamic forced responses of fan, compressor, and turbine blading have been generated by a wide variety of sources including upstream blades and/or vanes, distortion, rotating stall, downstream blades and/or vanes, surge, bleeds, and random or otherwise unidentified sources.

Failure level vibratory responses occur when a periodic aerodynamic forcing function, with frequency equal to a natural blade resonant frequency, acts on a blade row. The rotor speeds at which these forced responses occur are predicted with Campell diagrams, which display the natural frequency of each blade mode vs rotor speed.[1] Whenever these curves cross, aerodynamically-induced forced responses are possible. However, at the present time no accurate prediction for the amplitude of the resulting stress can be made.

The prediction of the aerodynamic forced response vibratory behavior of a blade or vane row requires a definition of the unsteady forcing function in terms of its harmonics. The time-variant aerodynamic response of the

airfoil to each harmonic of this forcing function is then assumed to be comprised of two parts.[3] One part is due to the disturbance being swept past the non-responding fixed airfoils. The second arises when the airfoils respond to this disturbance. These effects are modeled by means of two distinct analyses. A linearized small-perturbation gust analysis is used to predict the time-variant aerodynamics of the fixed non-responding airfoil to each harmonic of the disturbance. A self-induced unsteady aerodynamic analysis, wherein the airfoils are assumed to be harmonically oscillating, is then used to predict the additional aerodynamic effect due to the airfoil response. These self-induced aerodynamic effects can be thought of as an aerodynamic damping which can be either positive or negative. Reviews of state-of-the-art unsteady aerodynamics as applied to turbomachines, including gust and self-induced unsteady aerodynamic analyses, are presented in Refs. 3 and 4.

The classical approach to the prediction of the aerodynamic forced response of an airfoil is based on Newton's second law. The gust and self-induced unsteady aerodynamic analyses are used to describe the harmonic forces and moments acting on the airfoil in conjunction with a lumped parameter description of the airfoil structural and inertial properties.[5]

An alternate approach based on an energy balance technique has been developed by Hoyniak and Fleeter[6] to predict the uncoupled single-degree-of-freedom forced response of an airfoil. In this approach, a balance is established between the energy of unsteady aerodynamic work and the energy dissipated by the airfoil.

The objective of this paper is to extend the energy balance technique to include the more interesting case of coupled bending-torsion mode forced response of an airfoil and, also, to demonstrate the effects of the various aerodynamic and structural parameters on this coupled response.

General Unsteady Aerodynamic Coefficients

Figure 1 presents a schematic representation of a two-dimensional airfoil section displaced in both torsion and translation in a uniform flow with a superimposed convected transverse sinusoidal gust. Equation (1) presents the complex, time-dependent unsteady lift and moment per unit span, written in influence coefficient form, for the gust response and the self-induced unsteady aerodynamic cases.

$$L_G = L_G^R + iL_G^I = \pi\rho b^2\bar{\omega}^2\left[A_G\left(\frac{W}{U}\right)\right]$$

$$M_G = M_G^R + iM_G^I = \pi\rho b^4\bar{\omega}^2\left[B_G\left(\frac{W}{U}\right)\right]$$

$$L_{SI} = L_{SI}^R + iL_{SI}^I = \pi\rho b^3\omega^2\left[A_h\frac{h}{b} + A_\alpha\alpha\right]$$

$$M_{SI} = M_{SI}^R + iM_{SI}^I = \pi\rho b^4\omega^2\left[B_h\frac{h}{b} + B_\alpha\alpha\right] \qquad (1)$$

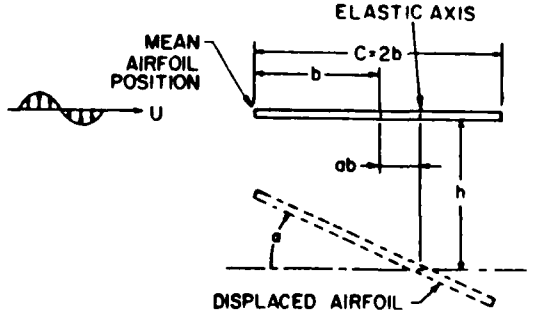

Fig. 1 Airfoil and displacement geometry and notation.

where $h = h_0 e^{i\bar{\omega}t}$; $\alpha = \alpha_0 e^{i\bar{\omega}t}$; $W = W_G e^{i\bar{\omega}t}$ describes the gust; (A_h, B_h), (A_α, B_α), (A_G, B_G) denote the generalized unsteady lift and moment coefficients due to airfoil translation, airfoil torsion, and the convected sinusoidal gust, respectively; ω is the airfoil natural frequency, and $\bar{\omega}$ is the gust forcing function frequency.

The total unsteady lift and moment on the airfoil are obtained by superimposing the gust response and the self-induced aerodynamic forces and moments.

$$L(t) = L_G(t) + L_{SI}(t)$$

$$= \pi\rho b^3\bar{\omega}^2\left[A_G\left(\frac{W_G}{U}\right) + A_h h_0 + A_\alpha\alpha_0\right]e^{i\bar{\omega}t}$$

$$M(t) = M_G(t) + M_{SI}(t)$$

$$= \pi\rho b^4\bar{\omega}^2\left[B_G\left(\frac{W_G}{U}\right) + B_h h_0 + B_\alpha\alpha_0\right]e^{i\bar{\omega}t} \qquad (2)$$

It should be noted that the airfoil response occurs at the frequency of the forcing function. Hence, in Eq. (2) the gust frequency $\bar{\omega}$ has been utilized in the specification of the unsteady aerodynamic forces and moments.

Energy Balance

The equations of motion describing the coupled translational and torsional displacement of the flat plate airfoil depicted in Fig. 1 are given in Eq. (3).

$$m\ddot{h} + S_\alpha\ddot{\alpha} + m\omega_h^2(1 + ig_h)h = L(t)$$

$$S_\alpha\ddot{h} + I_\alpha\ddot{\alpha} + I_\alpha\omega_\alpha^2(1 + ig_\alpha)\alpha = M(t) \qquad (3)$$

where m denotes the mass per unit span of the airfoil, S_α is the airfoil static moment per unit span about the elastic axis, ω_h and ω_α are the translational and torsional mode airfoil natural frequencies of the corresponding undamped single-degree-of-freedom system, respectively, and I_α is the mass moment of inertia per unit span about the elastic axis. As seen, the airfoil structural dynamic system described in Eq. (3) is strongly coupled and the coupling is associated with both the structural and the aerodynamic characteristics of the system. The structural coupling becomes significant whenever the aerodynamic center does not coincide with the elastic axis, in which case a non-zero value for the airfoil static moment results. The aerodynamic coupling arises because the self-induced aerodynamic forces acting on the airfoil are a function of the translational and torsional motions.

In this investigation, the coupled system response is determined utilizing an energy balance technique. The energy input to the system per cycle of airfoil oscillation is generated by the gust and, under certain conditions, the self-induced unsteady aerodynamic forces amd moments.[6] The energy dissipation of the system per cycle is associated with 1) system structural damping, 2) under certain conditions the self-induced aerodynamic forces and moments, and 3) the static moment term S_α. It should be noted that, for the uncoupled single-degree-of-freedom case, the dissipation term S_α was not considered.

The energy balance for the coupled translation-torsion airfoil motion can be expressed as follows.

$$(\text{WORK})_{SI}^h + (\text{WORK})_{g_h}^h + (\text{WORK})_\xi^h = (\text{WORK})_G^h$$

$$(\text{WORK})_{SI}^\alpha + (\text{WORK})_{g_\alpha}^\alpha + (\text{WORK})_\xi^\alpha = (\text{WORK})_G^\alpha \qquad (4)$$

where

$(WORK)^h_{\xi_I}, (WORK)^\alpha_{\xi_I}$ = work done by the self-induced aerodynamic forces and moments in translation and torsion, respectively.

$(WORK)^h_{\xi_h}, (WORK)^\alpha_{\xi_\alpha}$ = work done by the airfoil translation and torsion structural damping, respectively.

$(WORK)^h_{S_\alpha}, (WORK)^\alpha_{S_\alpha}$ = work associated with the static moment, S_α, in translation and torsion, respectively.

$(WORK)^h_G, (WORK)^\alpha_G$ = work done by the gust aerodynamic forces and moments in translation and torsion, respectively.

The work values associated with the self-induced unsteady aerodynamic forces and moments, $(WORK)^h_{\xi_I}$ and $(WORK)^\alpha_{\xi_I}$, have been written as dissipation terms. However, under certain conditions they may actually represent energy input terms. The sign differentiates between energy dissipation and input. Also, matrix techniques are utilized to solve Eq. (4) in order to determine the response of the airfoil system.

The unsteady work done by the self-induced aerodynamic terms, $(WORK)^h_{SI}$ and $(WORK)^\alpha_{SI}$, over one cycle of vibration can be calculated from Eq. (5).

$$(WORK)^h_{\xi_I} = \oint \mathrm{Re}[L_{SI}(t)\,dh]$$

$$(WORK)^\alpha_{\xi_I} = \oint \mathrm{Re}[M_{SI}(t)\,d\alpha] \qquad (5)$$

where $L_{SI}(t)$ and $M_{SI}(t)$ denote the unsteady lift and moment associated with the self-induced harmonic motion of the airfoil [See Eq. (1)].

Carrying out the integrations specified by Eqs. 1 and 5 results in the following expressions for the unsteady work done by the self-induced aerodynamic forces and moments.

$$(WORK)^h_{\xi_I} = \pi^2 \rho b^4 \bar{\omega}^2 [-(A_h)^I h_0^2/h + (A_\alpha)^R h_0 \alpha_0 \times \sin(\lambda_h - \lambda_\alpha) - (A_\alpha)^I h_0 \alpha_0 \cos(\lambda_h - \lambda_\alpha)]$$

$$(WORK)^\alpha_{\xi_I} = \pi^2 \rho b^4 \bar{\omega}^2 \left[(B_h)^R \left(\frac{h_0 \alpha_0}{b}\right) \sin(\lambda_h - \lambda_\alpha) - (B_h)^I \left(\frac{h_0 \alpha_0}{b}\right) \cos(\lambda_h - \lambda_\alpha) - (B_\alpha)^I \alpha_0^2\right] \qquad (6)$$

The angle λ_h denotes the phase angle between the incoming gust and the resulting translational motion of the airfoil. Similarly, the angle λ_α is the phase angle between the incoming gust and the airfoil torsional motion.

The energy input to the airfoil is determined by calculating the work per cycle of oscillation of the unsteady lift and moment associated with the incoming gust.

$$(WORK)^h_G = -\oint \mathrm{Re}[L_G(t)\,dh] = -\pi \rho b^3 \bar{\omega}^2 h_0 [(A_G)^I \cos(\lambda_h) - (A_G)^R \sin(\lambda_h)]$$

$$(WORK)^\alpha_G = \oint \mathrm{Re}[M_G(t)\,d\alpha] = \pi \rho b^4 \bar{\omega}^2 \alpha_0 [(B_G)^I \cos(\lambda_\alpha) - (B_G)^R \sin(\lambda_\alpha)] \qquad (7)$$

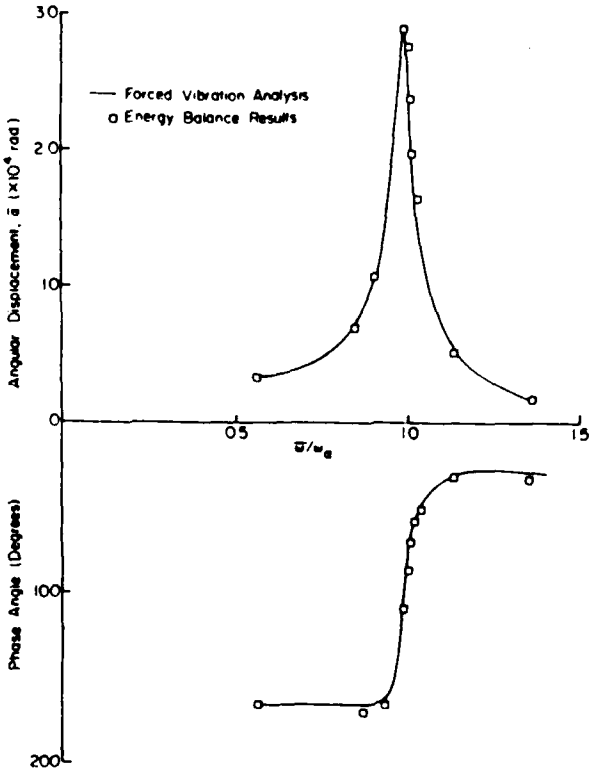

Fig. 2 Comparison of classical and energy balance forced response calculations.

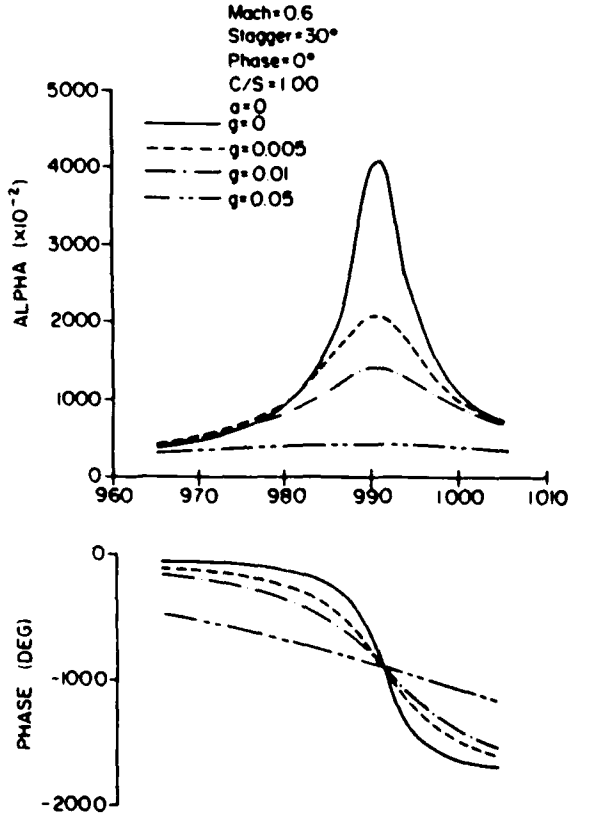

Fig. 3 Structural damping effect on the coupled torsional response amplitude for $(\bar{\omega}/\omega_\alpha)$ near ω_α.

The energy dissipated by the structural damping over one cycle of oscillation can be calculated as follows.

$$(\text{WORK})^{+}_{r_h} = \oint \text{Re}[ig_h m\omega_h^2 h dh] = \pi g_h m\omega_h^2 h_0^2$$

$$(\text{WORK})^{+}_{r_\alpha} = \oint \text{Re}[ig_\alpha I_\alpha \omega_\alpha^2 \alpha d\alpha] = \pi g_\alpha I_\alpha \omega_\alpha^2 \alpha_0^2 \qquad (8)$$

The unsteady work associated with the static moment S_α merits some additional comment. This is the term which couples the system equations of motion when the elastic axis and the aerodynamic center do not coincide. Physically, the S_α term can be considered as either a torsional force applied to the airfoil as the result of a unit translation airfoil displacement, or as a translational force resulting from the application of a unit torsional displacement. Thus, for an airfoil undergoing a translation mode oscillation, there is an apparent torsional load that can either do work on or extract work from the airfoil system. The phase relationship between the translational and torsional displacement determines whether this apparent torsional load adds or dissipates energy in the airfoil system.

The unsteady work per cycle of oscillation associated with the static moment can be determined by Eq. (9).

$$(\text{WORK})^{+}_{S_\alpha} = \oint \text{Re}[S_\alpha \ddot{\alpha} dh] = S_\alpha \omega^2 \alpha_0 h_0 \pi \sin(\lambda_h - \lambda_\alpha)$$

$$(\text{WORK})^{+}_{S_\alpha} = \oint \text{Re}[S_\alpha \ddot{h} d_\alpha] = S_\alpha \omega^2 \alpha_0 h_0 \sin(\lambda_\alpha - \lambda_h) \qquad (9)$$

The substitution of the various work expressions into the energy balance [see Eq. (4)] yields the following matrix expression for the coupled translational and torsional airfoil displacements.

$$\begin{vmatrix} A_{11} & A_{12} \\ A_{21} & A_{22} \end{vmatrix} \begin{vmatrix} \left(\frac{h_0}{b}\right) \\ (\alpha_0) \end{vmatrix} = \begin{vmatrix} B_{11} \\ B_{21} \end{vmatrix} \qquad (10)$$

where

$$A_{11} = [\pi g_h m\omega_h^2 b] + [(A_h)^I \pi^2 \rho b^3 \bar{\omega}^2]$$

$$A_{12} = [S_\alpha \bar{\omega}^2 \pi - (A_\alpha)^R \pi^2 \rho b^3 \bar{\omega}^2] \sin(\lambda_h - \lambda_\alpha) + [(A_\alpha)^I \pi^2 \rho b^3 \bar{\omega}^2 \cos(\lambda_h - \lambda_\alpha)]$$

$$A_{21} = [S_\alpha \bar{\omega}^2 \pi - (B_h)^R \pi^2 \rho b^4 \bar{\omega}^2] \sin(\lambda_\alpha - \lambda_h) + [(B_h)^I \pi^2 \rho b^4 \bar{\omega}^4 \cos(\lambda_h - \lambda_\alpha)]$$

$$A_{22} = \pi g_\alpha I_\alpha \omega_\alpha^2 + (B_\alpha)^I \pi \rho b^4 \bar{\omega}^2$$

$$B_{11} = -\pi \rho b^3 \bar{\omega}^2 \left(\frac{W_G}{U}\right) [(A_G)^I \cos(\lambda_h) - (A_G)^R \sin(\lambda_h)]$$

$$B_{21} = \pi^2 \rho b^4 \bar{\omega}^2 \left(\frac{W_G}{U}\right) [(B_G)^I \cos(\lambda_\alpha) - (B_G)^R \sin(\lambda_\alpha)]$$

The phase angles between the translational and torsional displacements, λ_h and λ_α respectively, can be determined in various ways. For example, they can be determined directly from the classical solution of the coupled system equations of motion, Eq. (3) (see Ref. 5). For convenience and brevity, these phase angle relationships are presented in Eq. (11).

$$\lambda_h = \tan^{-1}\left[\frac{N_{hI} D_R - N_{hR} D_I}{N_{hR} D_R + N_{hI} D_I}\right]$$

$$\lambda_\alpha = \tan^{-1}\left[\frac{N_{\alpha I} D_R - N_{\alpha R} D_I}{N_{\alpha R} D_R + N_{\alpha I} D_I}\right] \qquad (11)$$

where N_{hI}, $N_{\alpha I}$, N_{hR}, $N_{\alpha R}$, D_R and D_I are defined in terms of the airfoil structural properties and the unsteady aerodynamic forces and moments in the Nomenclature.

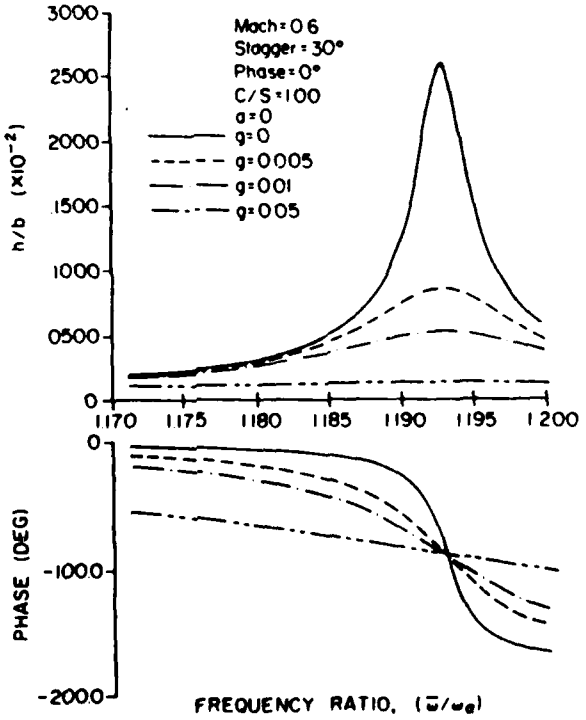

Fig. 4 Structural damping effect on the coupled torsional response for $(\bar{\omega}/\omega_\alpha)$ near ω_h.

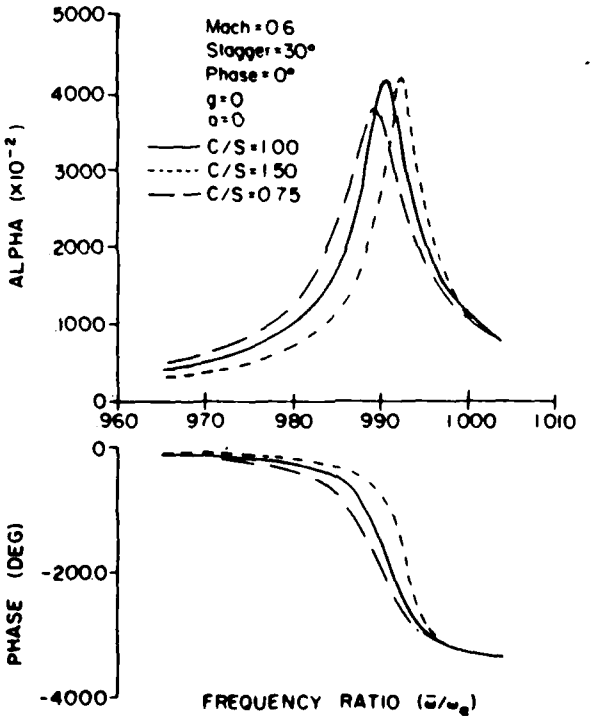

Fig. 5 Cascade solidity effect on the coupled torsional response.

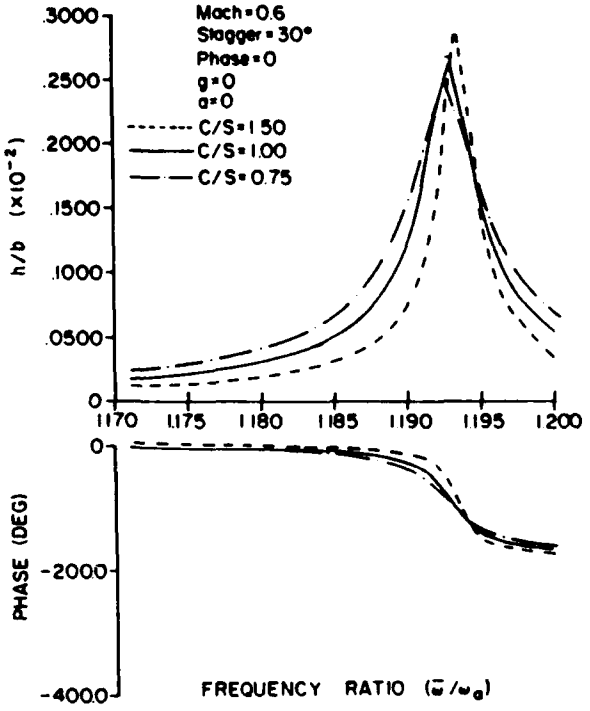

Fig. 6 Cascade solidity effect on the coupled translational response.

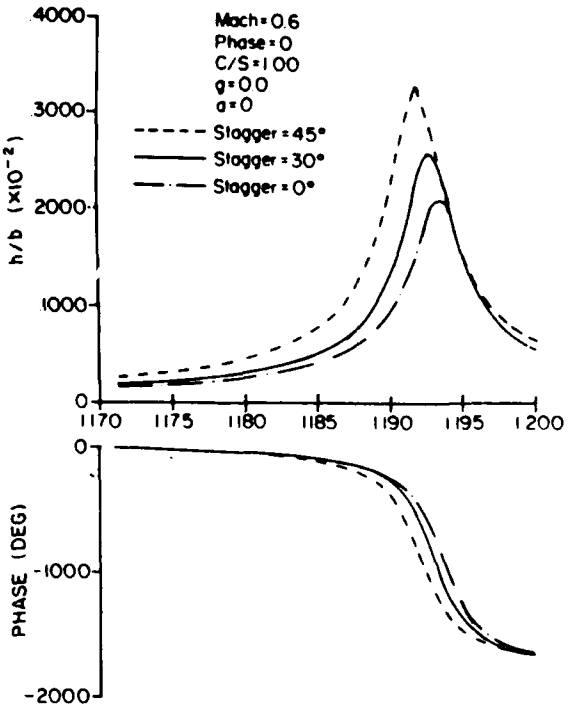

Fig. 8 Effect of stagger angle on the coupled translational response.

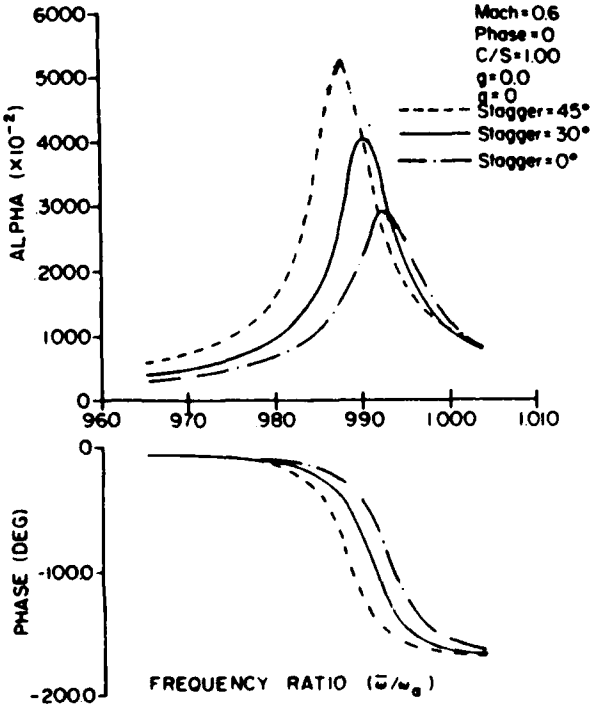

Fig. 7 Effect of stagger angle on the coupled torsional response.

Unsteady Aerodynamic Forces and Moments

L_h, M_h, L_α and M_α denote the standard form for the unsteady aerodynamic forces and moments and represent the unsteady lift and moment in translation and torsion, respectively, calculated about the airfoil ¼ chord. These standard form ¼ chord coefficients are related to the general unsteady aerodynamic influence coefficients through the following relationships.

$$A_h = L_h$$

$$A_\alpha = L_\alpha - (\tfrac{1}{2} + a) L_h$$

$$A_G = L_H$$

$$B_h = M_h - (\tfrac{1}{2} + a) l_h$$

$$B_\alpha = M_\alpha - (\tfrac{1}{2} + a)(L_\alpha + M_h) + (\tfrac{1}{2} + a)^2 L_h$$

$$B_G = M_H \tag{12}$$

where a is the dimensionless distance of the elastic axis measured from the airfoil mid-chord (see Fig. 1).

Results

To demonstrate the effects of the various parameters on the coupled forced response of turbomachinery blading, the unsteady aerodynamic analysis of Ref. 7 will be utilized. This analysis predicts the gust and self-induced unsteady aerodynamic forces and moments in a compressible flow field. The structural properties for this parametric study are based on an airfoil with a 5.08-cm chord, a 4% thickness-to-chord ratio, and an aspect ratio of 3. This representative airfoil has a natural translation mode frequency, ω_h, 12% larger than the natural torsion mode frequency, ω_α. Hence, $\omega_h/\omega_\alpha = 1.12$. Specific parameters to be varied include the structural damping value, the cascade solidity, the interblade phase angle, the inlet Mach number, and the elastic axis location. In addition, to clearly demonstrate the coupling effects, the airfoil stiffness is varied so as to make the torsional and translation mode natural frequencies nearly equal in value.

To verify the energy-balance approach for the prediction of aerodynamically-induced vibrations, the uncoupled torsion mode response of the representative airfoil was calculated by means of both the energy balance technique and a classical Newton's second law approach.[4] Figure 2 presents the comparison of these calculation techniques. As shown, the two methods yield identical results, both in terms of the amplitude and the phase of the response.

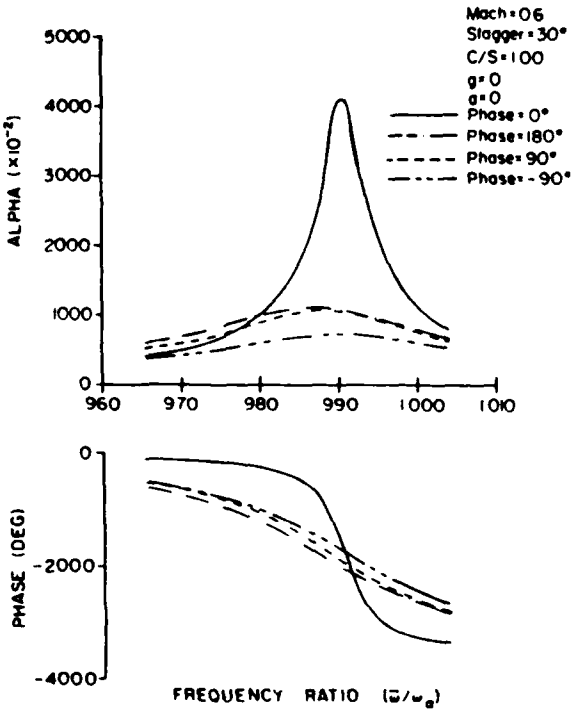

Fig. 9 Effect of interblade phase angle on the coupled torsion mode response.

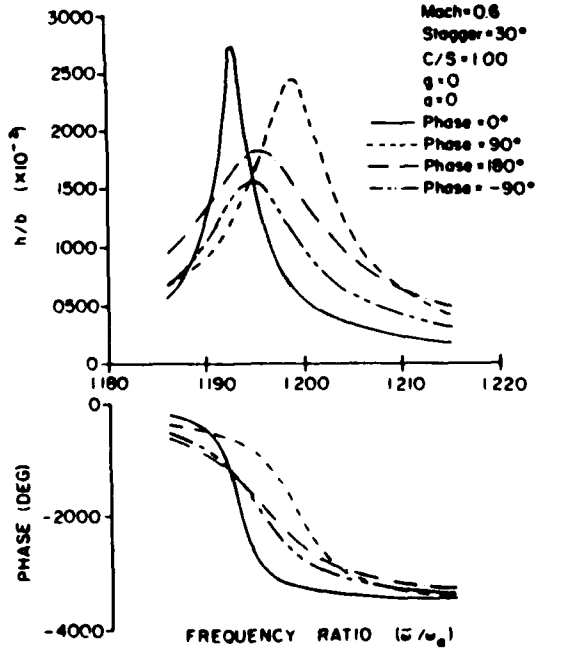

Fig. 10 Effect of interblade phase angle on the coupled translation mode response.

The coupled forced response characteristics of the representative airfoil are determined utilizing this energy balance technique. Results are presented as a function of the nondimensional ratio of the gust forcing frequency to the airfoil natural torsion mode frequency, $\bar{\omega}/\omega_\alpha$. Hence, values of 1.00 and 1.12 for this nondimensional frequency ratio correspond to the situations where the forcing function frequency is equal to the natural torsion and translation mode

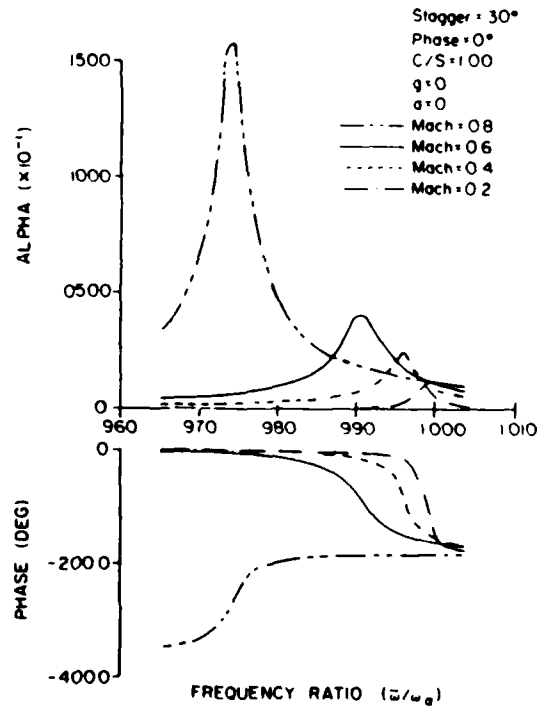

Fig. 11 Inlet Mach number effect on the coupled torsional response.

frequencies, respectively, of the representative airfoil. Results presented include the translational amplitude, the torsion mode amplitude, and the phase angles between the aerodynamic forcing function and the resulting airfoil response as a function of the nondimensional frequency ratio.

As anticipated, when the gust forcing function frequency is close to the natural torsion mode frequency, the torsional response is an order of magnitude greater than the corresponding coupled translation mode response. Thus, only the coupled forced torsional response will be presented for the forcing function close to the airfoil natural torsional frequency ($\bar{\omega}/\omega_\alpha \approx 1.00$), and only the coupled forced translational response for forcing function frequencies near the natural translational frequency ($\bar{\omega}/\omega_\alpha \approx 1.12$) will be presented.

Figures 3 and 4 represent the torsional and translational airfoil responses, respectively, with structural damping as the parameter when the forcing frequency is close to ω_α and ω_h, respectively. As seen, increased structural damping resulting results in decreased amplitude of response. It should be noted that the maximum response amplitudes do not occur at frequency ratio values of 1.00 and 1.12, even for the special case of zero structural damping. This is a result of the self-induced unsteady aerodynamic forces which correspond in this case to aerodynamic damping. Thus, even when there is no structural damping in the airfoil system, the self-induced aerodynamics generate aerodynamic damping.

The effects of cascade solidity (C/S) and stagger angle on the coupled forced response amplitudes are demonstrated in Fig. 5 and 6 and Figs. 7 and 8, respectively. Both the coupled torsional and translational forced response amplitudes increase with increasing values for solidity and stagger angle. Variations in solidity result in a somewhat more pronounced effect on the translational response than on the torsional response. Stagger angle variation has a greater effect on the torsional response than on the translational one. Also, variations in stagger angle have a much greater effect on the response amplitudes, both torsional and translational, than do variations in solidity. It should be noted that the design trend for modern compressors includes increased solidity and

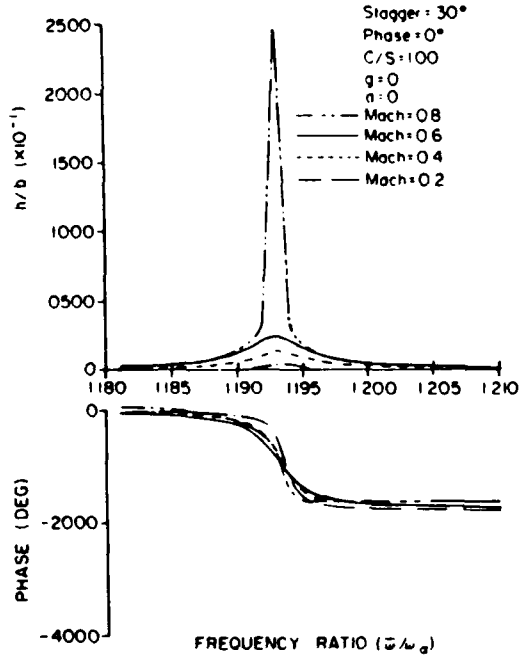

Fig. 12 Inlet Mach number effect on the coupled translational response.

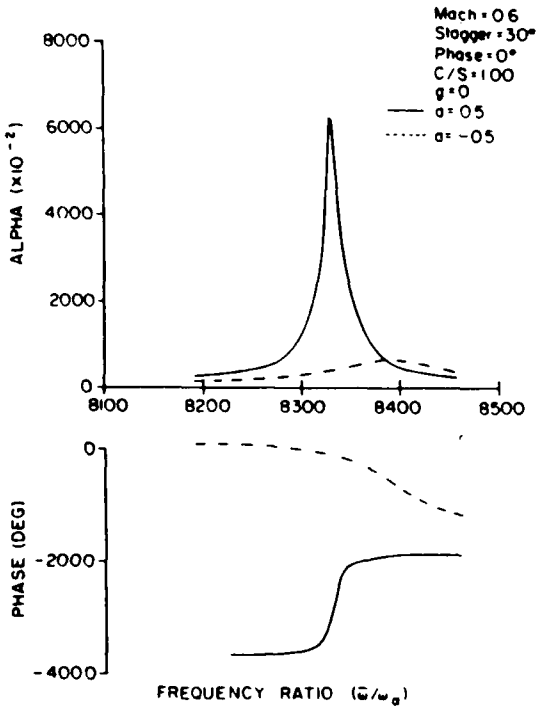

Fig. 13 Effect of elastic axis location on the coupled torsional response for (ω/ω_α) near ω_α.

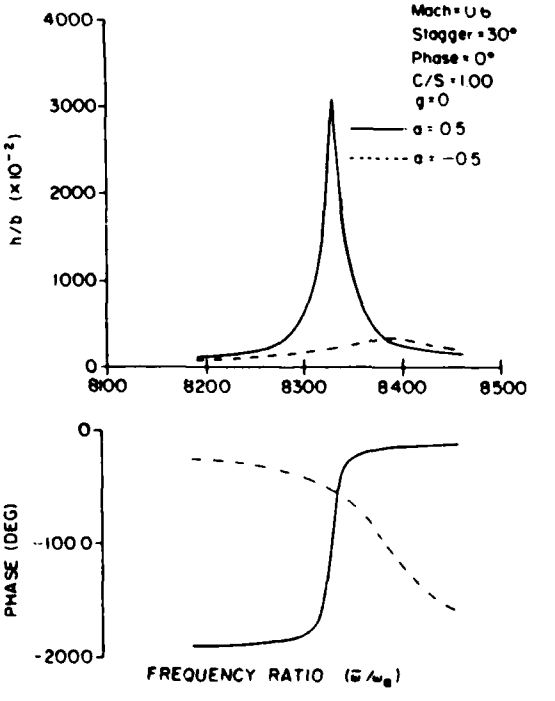

Fig. 14 Effect of elastic axis location on the coupled translational response for (ω/ω_α) near ω_α.

stagger angle values. Hence, these results indicate that increased forced response problems, primarily associated with increased stagger angles, might be anticipated.

Figures 9 and 10 show the effect of interblade phase angle on the coupled airfoil forced response characteristics. The effect of variations in this parameter on the coupled torsional forced response are quite different than on the coupled translational response. For the torsion mode, there is only an extreme maximum response amplitude for a 0 deg interblade phase angle value. For all other values considered, the response amplitude curves are relatively flat and decreased from the 0 deg case by approximately 75 to 85%. The coupled translational response amplitudes all exhibit an extreme maximum response amplitude, i.e. none of the amplitude response curves are relatively flat. Also, although an interblade phase angle value of 0 deg results in the maximum forced translational response amplitude, varying the interblade phase angle away from 0 deg results in noticably smaller decreases in this maximum amplitude than were noted for the forced torsional response. In particular, for both the torsional and the translational cases, the largest decrease in the maximum response amplitude is associated with changing the interblade phase angle value from 0 to - 90 deg. However, the maximum forced translational response decreased only 45%, whereas the corresponding forced torsional response decreased by 85%. In addition, since the smallest coupled torsional and translational response amplitudes correspond to negative interblade phase angle values (- 90 deg in particular), then this would appear to be a desirable forced response design condition. In terms of the rotor-stator interaction forced response problem, a negative interblade phase angle value corresponds to a backward traveling wave as viewed from the stator vane frame of reference and arises when the number of rotor blades is greater than the number of stator vanes.

The effect of the inlet flow Mach number on the coupled torsional and translational forced response characteristics of the representative airfoil is demonstrated in Figs. 11 and 12, respectively. Increasing the Mach number, which also corresponds to decreasing the reduced frequency for a specific gust disturbance, increases both the coupled torsional and translational responses with a very dramatic increase associated with an increase in Mach number from 0.6 to 0.8. Also, for Mach numbers of 0.6 and smaller, the increase in the maximum response amplitude is much larger for the torsional mode than for the translational mode. In addition, the forcing

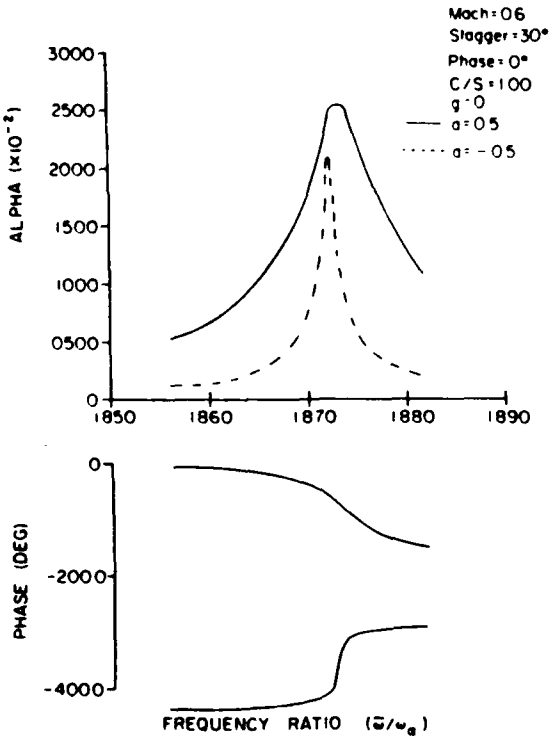

Fig. 15 Effect of elastic axis location on the coupled torsional response for $(\bar{\omega}/\omega_\alpha)$ near ω_h.

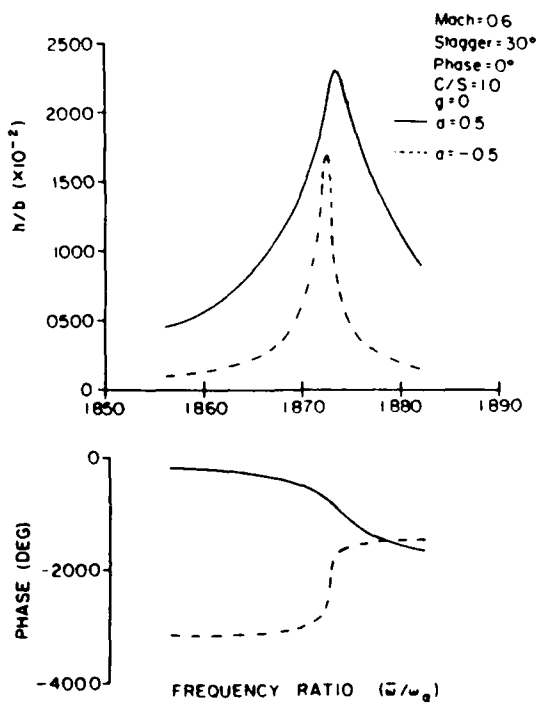

Fig. 16 Effect of elastic axis location on the coupled translational response for $(\bar{\omega}/\omega_h)$ near ω_h.

function frequency at which the maximum amplitude response occurs is highly dependent on the Mach number for the torsional response, but is almost independent of this forcing frequency for the translational response case.

The effect of moving the elastic axis location to the ¼-chord and the ¼-chord locations on the coupled forced response of the representative airfoil is presented in Figs. 13 through 16. These results indicate that not only the response amplitude but also the forcing function frequency at which the maximum amplitude response occurs is strongly dependent on the position of the elastic axis. The maximum torsion and translation response amplitudes are found with the elastic axis at the ¼-chord location. Shifting the elastic axis forward to the ¼-chord location results in significantly decreasing both the torsional and translational response amplitudes near the airfoil torsional natural frequency, but only slightly decreasing these response amplitudes near the airfoil translational natural frequency. Also, shifting the elastic axis location aft from mid-chord to ¼-chord has the result of making the translational response in the neighborhood of the natural torsional frequency $(\bar{\omega}/\omega_\alpha \approx 1.0)$ the same order of magnitude as the torsional response amplitude, indicating the significant additional coupling that arises when the elastic axis and the airfoil center of gravity do not coincide. Similar results are noted when the forcing function frequency is close to the natural translational frequency.

To demonstrate the interaction of two very closely-spaced torsional and translation modes, the bending stiffness of the representative airfoil was altered to make the ratio of translation to torsion natural frequencies 1.02. The variation with interblade phase angle values of these closely coupled forced torsional and translational responses was then investigated. The results are presented in Figs. 17 and 18. The coupled torsional response results (Fig. 17) show that, at a frequency ratio of 0.990, the response decreases as the interblade phase angle is varied from 0 to +90, −90, and 180 deg. At a frequency ratio of 1.015 the response increases by up to 65%.

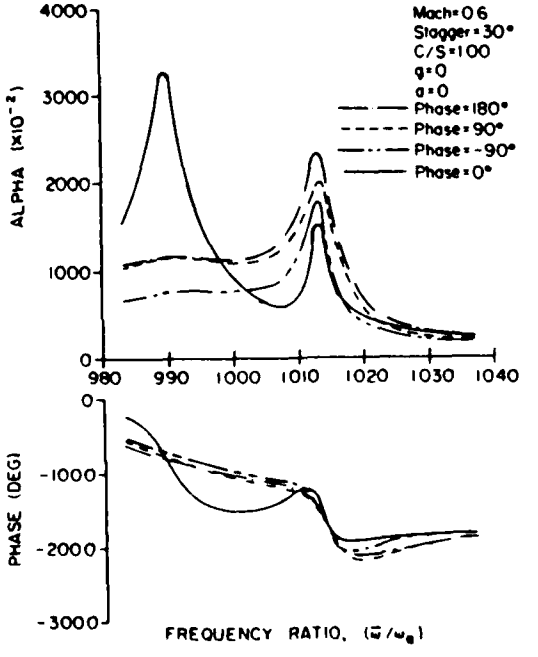

Fig. 17 Interblade phase angle effect on the coupled torsional response for nearly equal natural frequencies.

Figure 18 presents the variation of the forced translational response with the interblade phase angle as the parameter. In contrast to the torsional response results, minimal translational response is noted when the forcing function frequency is near the airfoil natural torsional frequency. However, when the forcing function frequency is near the airfoil natural translational frequency $(\bar{\omega}/\omega_h \approx 1.015)$, the

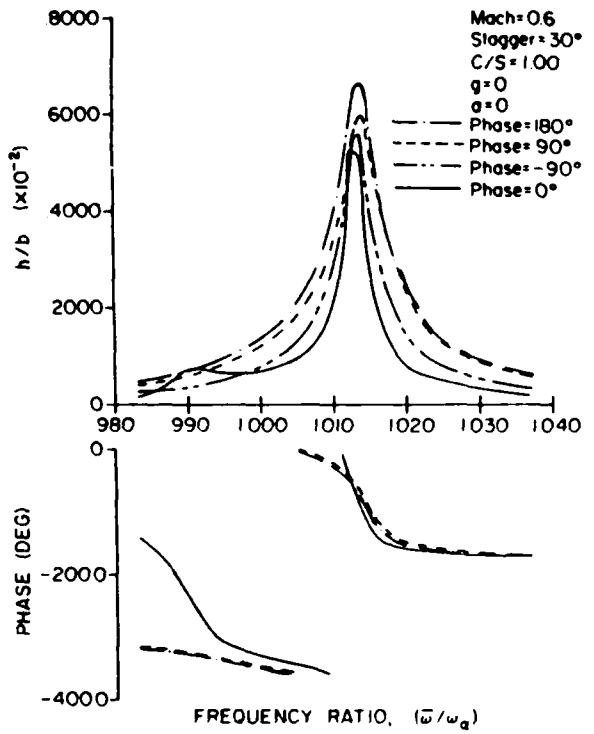

Fig. 18 Interblade phase angle effect on the coupled translational response for nearly equal natural frequencies.

forced translational amplitude is significant and increases as the interblade phase angle value is varied from 0 to 180 deg. A comparison of Figs. 17 and 18 at a frequency ratio close to 1.015 reveals a correspondence between the forced torsional response and the translational one. This is caused by the high degree of coupling that exists between the translational and torsional modes for the altered airfoil.

Summary and Conclusions

In this investigation, the coupled structural dynamic airfoil system forced response was determined utilizing an energy balance technique. The energy input to the system per cycle of oscillation was generated by the gust and, under certain conditions, the self-induced aerodynamic forces and moments. The energy dissipation per cycle of oscillation was associated with system structural damping, under some conditions the self-induced aerodynamic forces and moments, and the static moment term S_{α}. It should be noted that, for the uncoupled single-degree-of-freedom case, the dissipative coupling mechanism, S_{α}, is not considered.

The effects of the various aerodynamic parameters on the coupled translational and torsional mode forced response of a representative airfoil were then considered. The study showed the increased coupling between the torsion and translation modes as the corresponding undamped natural frequencies approach one another. It was also demonstrated that the coupled torsional and translational forced response amplitudes of a representative airfoil increased with: 1) decreased structural damping, 2) increased solidity values, 3) increased stagger angles, 4) increased inlet flow Mach numbers, 5) interblade phase angle values corresponding to forward traveling waves for the rotor-stator interaction case, and 6) shifting of the elastic axis location aft.

It should be noted that variations in the above parameters did not affect the magnitude of the resulting forced response equally nor did they always have equivalent effects on the torsional and translational response modes. For example, increasing the stagger angle and shifting the elastic axis aft resulted in significantly larger increases in all of the response amplitudes than did increasing the solidity. Also, the interblade phase angle, for example, had a much greater effect on the coupled torsion mode responses than on the translational ones. In addition, the forcing function frequencies at which the maximum torsional and translational responses occurred did not generally correspond to the airfoil natural torsional or tanslational frequencies. This was because the self-induced aerodynamic forces and moments result in an aerodynamic damping effect analogous to structural damping.

Acknowledgment

The Air Force Office of Scientific Research and Capt. Michael Francis, who served as the project's technical monitor, are gratefuly acknowledged for their support.

References

[1] "The Aerothermodynamics of Aircraft Gas Turbine Engines," AFAPL-TR 78-52, July 1978.

[2] Fleeter, S., Jay, R.L., and Bennett, W.A., "Rotor Wake Generated Unsteady Aerodynamic Response of a Compressor Stator," *ASME Journal of Engineering for Power*, Vol. 100, No. 4, Oct. 1978, pp. 664-675.

[3] Fleeter, S., "Aeroelasticity Research for Turbomachine Application," *Journal of Aircraft*, Vol. 16, May 1979, pp. 320-326.

[4] Platzer, M.F., "Unsteady Flows in Turbomachines—A Review of Recent Developments," AGARD-CP-227, Sept. 1977.

[5] Fung, Y.C., *An Introduction to the Theory of Aeroelasticity*, Dover Publications, New York, N.Y., 1969.

[6] Hoyniak, D. and Fleeter, S., "Prediction of Aerodynamically Induced Vibrations in Turbomachinery Blading," ASME Symposium in Fluid/Structure Interaction in Turbomachinery, Nov. 1981.

[7] Fleeter, S., "The Fluctuating Lift and Moment Coefficients for Cascaded Airfoils in a Nonuniform Compressible Flow," *Journal of Aircraft*, Vol. 10, Feb. 1973, pp. 93-98.

APPENDIX XIII

FLOW INDUCED VIBRATORY RESPONSE OF A LOADED AIRFOIL

CHINESE-AMERICAN ACADEMIC & PROFESSIONAL CONFERENCE

(INVITED PAPER)

FLOW INDUCED VIBRATIONAL RESPONSE OF A LOADED AIRFOIL

Hsiao-Wei D. Chiang and Sanford Fleeter

Thermal Sciences and Propulsion Center
School of Mechanical Engineering
Purdue University, West Lafayette, Indiana 47907

ABSTRACT

A structural dynamics model is developed and utilized to predict the effects of airfoil thickness, camber, mean flow incidence angle, and two-dimensional gust direction on the aerodynamically induced forced response of an airfoil in an incompressible flow. An energy balance is performed between the unsteady aerodynamic work and the energy dissipated through the airfoil structural and aerodynamic damping, with predictions of the airfoil unsteady aerodynamics obtained from a complete first order model. It is then demonstrated that the steady aerodynamic loading on the airfoil and the direction of the gust strongly affect the amplitude of response. Also, classical thin airfoil unsteady aerodynamic models result in significantly underpredicted airfoil response amplitudes, i.e., the thin airfoil predictions are nonconservative.

NOMENCLATURE

k_1	reduced frequency, $\omega b/U_\infty$
k_2	transverse gust wave number
u^+	chordwise gust component
v^+	transverse gust component
Φ_0	steady velocity potential
Ψ_G	unsteady harmonic gust potential
Ψ_m	unsteady harmonic motion-induced potential
α	complex torsion motion
α_0	mean flow incidence
ω	gust harmonic frequency
ω_α	airfoil natural frequency

INTRODUCTION

The structural dynamic response of turbomachine and turboprop blading to aerodynamic excitations is a problem of increasing design concern. This is because these blades operate in nonuniform and irregular flow fields. As a result, unsteady aerodynamic forces and moments are generated on the blading. When the frequency of these aerodynamic forces and moments is equal to a blade natural frequency, sustained blade vibrations may occur, with the associated dynamic stresses inducing fatigue cracks leading to high cycle fatigue failure.

To predict these dynamic stress levels, the response of an airfoil to aerodynamic excitations must be analyzed. First the unsteady aerodynamic forcing function is defined in terms of harmonics. The time-variant response of the airfoil to each harmonic component is then assumed to be comprised of two distinct but related unsteady aerodynamic parts. One is the gust response due to the harmonic forcing function being convected past the nonresponding fixed airfoil. The motion-induced aerodynamic response, also termed the aerodynamic damping, is the second part and is generated by the resulting harmonic response of the airfoil. Typically, the airfoil vibratory response is then calculated utilizing a classical approach based on Newton's second law.

Unfortunately, accurate predictions of the amplitude of the resulting airfoil vibration and stress cannot be made due to the inadequacies of current unsteady aerodynamic models. In particular, unsteady aerodynamic models have typically been restricted to thin airfoil theory wherein the unsteady flow field is assumed to be small compared to the mean flow, with the latter potential. In addition, the airfoil is considered to be a flat plate at zero incidence. This uncouples the unsteady aerodynamics from the steady potential flow and leads to the approximation wherein the flow is linearized about a uniform parallel flow. Such classical models have been developed for oscillating flat plate airfoils by Theodorsen [1] and for a convected transverse gust by Sears [2].

In many applications, however, airfoils with significant steady loadings, large air turning, and highly cambered shapes, are required. Thus, the classical models were extended to consider thin airfoils with constant very small camber and mean flow incidence. For example, Horlock [3] extended the Sears approach to consider chordwise gusts, while Naumann and Yeh [4] considered transverse and chordwise gusts convected past airfoils with small constant camber. Unfortunately, these linearized models are only approximate, having neglected second order terms. Thus, they cannot be extended to finite mean flow incidence angles or realistic cambered profiles, i.e., loaded airfoil designs. In this regard, Goldstein and Atassi [5] developed a complete systematic model for inviscid incompressible flows past oscillating airfoils or airfoils subject to periodic gusts utilizing classical analytical airfoil analysis techniques.

In this paper the effects of airfoil thickness, camber, mean flow incidence angle, and gust direction on the aerodynamically induced forced response of an airfoil in an incompressible flow are assessed for the first time. This is accomplished by developing a structural dynamics model based on an energy balance technique [6], with predictions of the airfoil unsteady aerodynamics obtained from a complete first order model, i.e. the thin airfoil approximation is not applied. The fluctuating flow velocity is assumed to be small compared to the mean velocity, with the unsteady flow linearized about the full potential flow of the airfoils. Thus, the unsteady aerodynamic effects due to airfoil profile and incidence angle are completely accounted for through the mean potential flow.

AERODYNAMIC MODEL

Figure 1 presents a schematic representation of a thick, cambered, airfoil at finite mean flow incidence α_o with respect to the far field uniform mean flow, $\mathcal{U}_\infty = U_\infty \hat{i}$, executing torsion mode oscillations with a superimposed convected two-dimensional harmonic gust. The gust amplitude and harmonic frequency are denoted by A and $\bar{\omega}$, respectively. The two-dimensional gust propagates in the direction $\mathcal{K} = k_1\hat{i} + k_2\hat{j}$, where k_1 is the reduced frequency and k_2 is the transverse gust wave number, i.e., the transverse component of the gust propagation direction vector.

Steady Flow Field

The model for the steady flow considers the incompressible flow past a thick, cambered, airfoil at finite mean incidence. As the steady flow is assumed to be a potential flow, it is described by the following Laplace equation: $\nabla^2\Phi_o(x,y) = 0$

The steady boundary conditions require the far field steady flow to be uniform, while the airfoil surface boundary conditions specify that the normal velocity is zero. The Kutta condition is also applied and is satisfied by requiring the velocities on the upper and lower airfoil surfaces to be equal in magnitude at the trailing edge.

Gust Unsteady Aerodynamics

The two-dimensional gust unsteady flow field is determined by decomposing the gust generated unsteady flow field into harmonic rotational, $\mathcal{Q}_R$, and potential, $\mathcal{Q}_P$, components. The rotational gust is assumed to be convected with the steady mean flow past the airfoil and, therefore, does not interact with the airfoil. Thus the following solution for the rotational gust is determined by solving the linearized Euler equations in the far upstream where the steady flow field is uniform.

$$\mathcal{Q}_R = u^+\hat{i} + v^+\hat{j} \qquad (1)$$

where: $u^+ = -A\,k_2 \exp[ik_1(t-x) - ik_2y]$;
$v^+ = A\,k_1 \exp[ik_1(t-x) - ik_2y]$.

The potential gust component, Ψ_G, is described by a Laplace equation: $\nabla^2\Psi_G = 0$. The gust generated unsteady rotational and potential flow fields are coupled through the boundary conditions on the potential gust component. In particular, the airfoil is stationary, with the rotational gust convected with the mean steady flow field. Thus the upwash on the airfoil is determined by requiring the normal component of the unsteady flow field to be zero on the airfoil.

$$\frac{\partial\Psi_G}{\partial n}\Big|_{airfoil} = A\left(\frac{\partial f}{\partial x}k_2 + k_1\right)\exp[\,i(k_1x + k_2y)] \qquad (2)$$

where f (x) specifies the airfoil profile

The Kutta condition is also imposed on the unsteady potential flow field by requiring no unsteady pressure difference across the airfoil chordline at the trailing edge. The corresponding relation for the trailing edge unsteady velocity potential difference is then determined from the unsteady Bernoulli equation.

Motion-Induced Unsteady Aerodynamics

The unsteady flow field associated with the harmonic motion of the airfoil is assumed to be potential and, is therefore described by the Laplace equation: $\nabla^2\Psi_m = 0$.

The upwash on the airfoil for this motion-dependent model, W'_m, is a function of both the position of the airfoil and the steady flow field. Thus, this boundary condition couples the unsteady flow field to the steady aerodynamics. For an airfoil executing harmonic torsion mode oscillations about an elastic axis location at x_o as measured from the leading edge, the upwash on the surfaces of the airfoil is:

$$\frac{\partial\Psi_m}{\partial n}\Big|_{airfoil} = \bar{\alpha}\left\{\frac{ik_1[(x-x_o) + y\partial f/\partial x] + U_o + V_o\partial f/\partial x}{|1 + (\partial f/\partial x)^2|^{1/2}}\right. \qquad (3)$$

$$\left. + \frac{\partial U_o/\partial y[(x-x_o)\partial f/\partial x + y]}{|1 + (\partial f/\partial x)^2|^{1/2}} - \frac{\partial V_o/\partial y[(x-x_o) - y\partial f/\partial x]}{|1 + (\partial f/\partial x)^2|^{1/2}}\right\}$$

where U_o and V_o are the steady airfoil surface velocity components, and $\bar{\alpha}$ is the amplitude of the torsional oscillations.

LOCALLY ANALYTICAL SOLUTION

The boundary fitted computational grid developed by Thompson, Thames, and Mastin [7] is utilized. This method permits grid points to be specified along the entire boundary of the computational plane. The complete flow field is described by the steady velocity potential, $\Phi_o(x,y)$, the gust generated unsteady velocity potential, $\Psi_G(x,y)$, and the motion induced unsteady velocity potential, Ψ'_m. These three velocity potentials are each individually described by Laplace equations. In the transformed (ξ,η) coordinate system, these Laplace equations have the following nonhomogeneous form.

$$\frac{\partial^2\bar{\phi}}{\partial\xi^2} + \alpha\,\frac{\partial^2\bar{\phi}}{\partial\eta^2} - 2\,\alpha\beta\,\frac{\partial\bar{\phi}}{\partial\eta} - 2\,\gamma\,\frac{\partial\bar{\phi}}{\partial\xi} = F(\xi,\eta) \qquad (4)$$

where $\bar{\phi}$ is a shorthand method of writing these three velocity potentials in the transformed plane, $F(\xi,\eta)$ contains the cross derivative term $\partial^2\bar{\phi}/\partial\xi\partial\eta$, and the coefficients α, β, and γ are functions of the transformed coordinates ξ and η and are treated as constants in each individual grid element.

To obtain the analytical solution to the transformed Laplace equation, it is first rewritten as a homogeneous equation. The general solution is then determined by separation of variables.

$$\bar{\phi} = [A_1\cos(\lambda\xi) + A_2\sin(\lambda\xi)]\,[B_1\cosh(\mu\eta) + B_2\sinh(\mu\eta)] \qquad (5)$$

where $\mu = [(\gamma^2 + \alpha\beta^2 + \lambda^2)/\alpha]^{1/2}$ and λ, A_1, A_2, B_1, and B_2 are constants to be determined from the boundary conditions.

Analytical solutions in individual computational grid elements are determined by applying proper boundary conditions on each element to evaluate the unknown constants in the general velocity potential solution, Equation 5. The solution of the global problem is then determined through the application of the global boundary conditions and the assembly of the locally analytical solutions.

General Unsteady Aerodynamic Coefficients

The complex, time-dependent unsteady lift and moment per unit span are written in influence coefficient form for the gust and torsion mode motion-induced unsteady aerodynamic cases.

$$L_G = \mathrm{Re}\,[L_G] + i\,\mathrm{Im}\,[L_G] = \pi\rho b^3\bar{\omega}^2\left[A_G\left(\frac{W_G}{U_\infty}\right)\right] \qquad (6)$$

$$M_G = \mathrm{Re}\,[M_G] + i\,\mathrm{Im}\,[M_G] = \pi\rho b^4\bar{\omega}^2\left[B_G\left(\frac{W_G}{U_\infty}\right)\right]$$

$$L_m = \mathrm{Re}\,[L_m] + i\,\mathrm{Im}\,[L_m] = \pi\rho b^3\omega_\alpha^2[A_\alpha\alpha] \qquad (7)$$

$$M_m = \mathrm{Re}\,[M_m] + i\,\mathrm{Im}\,[M_m] = \pi\rho b^4\omega_\alpha^2[B_\alpha\alpha]$$

where $\alpha = \bar{\alpha}\,e^{i\omega t}$; $W_G = \bar{W}_G\,e^{i\omega t}$ describes the gust; (A_α, B_α), (A_G, B_G) denote the generalized unsteady lift and moment coefficients due to airfoil torsion and the convected sinusoidal gust, respectively; ω_α is the airfoil natural frequency, and $\bar{\omega}$ is the gust forcing function frequency.

The total unsteady lift and moment on the airfoil are obtained by super-imposing the gust response and the self-induced aerodynamic forces and moments.

$$L(t) = L_G(t) + L_m(t) = \pi\rho b^3\bar{\omega}^2\left[A_G\left(\frac{\bar{W}_G}{U_\infty}\right) + A_\alpha\bar{\alpha}\right]e^{i\omega t}$$

$$M(t) = M_G(t) + M_m(t) = \pi\rho b^4\bar{\omega}^2\left[B_G\left(\frac{\bar{W}_G}{U_\infty}\right) + B_\alpha\bar{\alpha}\right]e^{i\omega t} \qquad (8)$$

It should be noted that the airfoil response occurs at the frequency of the forcing function, hence the gust frequency, $\bar{\omega}$, has been utilized in the specification of the unsteady aerodynamic forces and moments, Equation 8.

ENERGY BALANCE

The uncoupled equation of motion for the single-degree-of-freedom lumped airfoil model undergoing torsion mode oscillations is given in Equation 9.

$$I\frac{d^2\alpha}{dt^2} + (1 + ig)\,S\alpha = M(t) \qquad (9)$$

where: S is the stiffness coefficient, g is the structural damping, and I is the mass moment of inertia about the elastic axis.

The system response is determined by considering the balance between the energy input and the energy dissipated over one cycle of oscillation of the airfoil. The input energy is obtained from a calculation of the work done by the unsteady gust moment acting on the airfoil. The energy dissipated is obtained by calculating the work done by the structural damping and by the motion-dependent aerodynamic response *moment, i.e., the aerodynamic damping*.

The unsteady work done per cycle of oscillation by the unsteady gust aerodynamic moment is given by the integral of the product of the real part of the unsteady moment and the resulting displacement over one cycle of motion.

$$\mathrm{Work}_G = -\pi\,T_\alpha\,\bar{\alpha}\sin(\lambda' - \psi) = -\pi T_\alpha\,\bar{\alpha}\sin(\psi) \qquad (10)$$

$$\text{where } \psi = \mathrm{TAN}^{-1}\left[\frac{|gS - \pi\rho b^4\bar{\omega}^2\mathrm{Im}|B_\alpha|}{|I\bar{\omega}^2 + S - \pi\rho b^4\,\mathrm{Re}|B_\alpha|}\right].$$

The energy dissipated per cycle of oscillation is obtained by integrating the real part of the product of the motion-induced unsteady aerodynamic response moment (the aerodynamic damping) and the airfoil displacement over one cycle of oscillation. It should be noted that although this term is written as a dissipation term, under certain conditions it can represent an energy input term.

$$\mathrm{Work}_m = \pi(gS - \pi\rho b^4\bar{\omega}^2\mathrm{Im}\,|B_\alpha|)\bar{\alpha}^2 \qquad (11)$$

The balance of energy requires that the energy input to the system must be equal to that dissipated by the airfoil. This energy balance leads to the following expression for the response amplitude of the oscillation, $\bar{\alpha}$.

$$\bar{\alpha} = \frac{T_o \sin(\psi)}{gS - \pi\rho b^4 \bar{\omega}^2 \mathrm{Im}\,[B_\alpha]} \tag{12}$$

where:

$$\sin(\psi) = \frac{|gS \quad \pi\rho b^4 \bar{\omega}^2 \mathrm{Im}[B_\alpha]|}{|(-I\bar{\omega}^2 + S - \pi\rho b^4 \bar{\omega}^2 \mathrm{Re}[B_\alpha])^2 + (gS \quad \pi\rho b^4 \bar{\omega}^2 \mathrm{Im}[B_\alpha])^2|^{1/2}}$$

RESULTS

The structural dynamics model developed herein is utilized to assess the effects of airfoil thickness, steady aerodynamic loading, i.e., airfoil camber and mean flow incidence angle, and also the forcing function as characterized by the direction of the two-dimensional gust on aerodynamically induced forced vibratory response. This is accomplished by considering a series of representative Joukowski airfoils with a 3.18 cm chord, an aspect ratio of two, a midchord elastic axis, and a 0.8 reduced frequency value. These results are presented in Figures 2 through 7 in the format of the torsion mode response amplitude, $\bar{\alpha}$, versus the ratio of the forcing function frequency to the airfoil natural frequency, $\bar{\omega}/\omega_\alpha$.

The thickness of the airfoil has minimal effect on the aerodynamically forced response for a forcing function characterized by a 90° gust at both zero and finite incidence angle values, Figure 2. Also, the response amplitude is seen to decrease with increased incidence angle and, thus, with increased steady aerodynamic loading. However, this decrease in amplitude is associated with the particular two dimensional gust direction. This may be seen by considering Figure 3 which shows the analogous results demonstrating the effect of airfoil thickness and incidence angle for a 45° gust. In particular, for the 45° gust, the amplitude of response increases with increasing incidence angle, thereby reversing the trend noted with the forcing function characterized by a 90° gust. Thus, the amplitude of response is not a strong function of the airfoil thickness. However, the response amplitude is a strong function of both the steady aerodynamic loading on the airfoil and the aerodynamic forcing function, as characterized by the incidence angle and the gust direction, respectively.

Figures 4 and 5 demonstrate the effect of airfoil steady aerodynamic loading as characterized by the camber of the airfoil and the incidence angle, on the amplitude of response for forcing functions defined by 90° and 45° gusts, respectively. Again, the gust direction and the steady loading have a strong influence on the amplitude of response. Increasing the airfoil camber at constant incidence angle results in an increase in the airfoil response, with this effect more pronounced for the 90° gust. Also, increasing the incidence angle for a particular airfoil camber leads to greatly increased amplitudes of response, with the 45° gust having a larger influence. Also shown in these figures are the corresponding results based on the classical thin airfoil unsteady aerodynamic models of Theodorsen, Sears, Horlock, and Naumann and Yeh. As seen, these classical predictions significantly underpredict the amplitude of response of the airfoil, i.e., the classical predictions are nonconservative, thereby clearly demonstrating the need for the complete first order unsteady aerodynamic model developed herein.

Figures 6 and 7 clearly demonstrate the importance of the aerodynamic forcing function as characterized by the direction of the two-dimensional gust on the amplitude of response of a 10% thick airfoil with 20% camber at 0° and 20° of incidence respectively. At each of the incidence angle values, it is readily apparent that the gust direction has a significant effect on the airfoil response. However altering the gust direction has opposite effects. In particular, decreasing the gust direction from 90° results in decreased response at an incidence angle of 0°, but increased response at 20° of incidence.

SUMMARY AND CONCLUSIONS

A structural dynamics model has been developed to predict the aerodynamically induced forced response of an airfoil in an incompressible flow. This model is based on an energy balance between the unsteady aerodynamic work and the energy dissipated through the airfoil structural and aerodynamic damping, with predictions of the airfoil unsteady aerodynamics obtained from a complete first order model which accurately analyzes the effects of airfoil profile, mean flow incidence angle, and also considers a two-dimensional gust.

This model was utilized to demonstrate the effects of airfoil thickness, camber, mean flow incidence angle, and the two-dimensional gust direction on the aerodynamically induced forced response of a typical airfoil. This study showed that the steady aerodynamic loading on the airfoil, and the aerodynamic forcing function, as characterized by the airfoil camber, the mean flow incidence angle, and the direction of the gust, respectively, have a significant effect on the amplitude of response. It is also shown that the classical thin airfoil unsteady aerodynamic models result in significantly underpredicted airfoil response amplitudes, i.e., the thin airfoil predictions are nonconservative.

ACKNOWLEDGEMENTS

This research was sponsored, in part, by the Air Force Office of Scientific Research and the NASA Lewis Research Center.

REFERENCES

1. Theodorsen, T., "General Theory of Aerodynamic Instability and the Mechanism of Flutter," *NACA TR 496*, 1935.

2. Sears, W.R., "Some Aspects of Nonstationary Airfoil Theory and its Practical Applications," *Journal of the Aeronautical Sciences*, Vol. 8 No. 3, pp. 104-108, January 1941.

3. Horlock, J.H., "Fluctuating Lift Forces on Airfoils Moving through Transverse and Chordwise Gusts," *ASME Journal of Basic Engineering*, Series D, Vol. 90, No. 4, pp. 494-500, December 1968.

4. Naumann, H. and Yeh, H., "Lift and Pressure Fluctuations of a Cambered Airfoil under Periodic Gusts and Applications to Turbomachinery," *ASME Paper 72 GT-30, 1972* 1972.

5. Goldstein, M.E., and Atassi, H., "A Complete Second Order Theory for the Unsteady Flow about an Airfoil due to a Periodic Gust," *Journal of Fluid Mechanics*, Vol. 74, pp. 741-766, 1976.

6. Hoyniak, D. and Fleeter, S., "Prediction of Aerodynamically Induced Vibrations in Turbomachinery Blading," *ASME Journal of Fluids Engineering*, Vol. 105, December 1983, pp. 375-381.

7. Thompson, J.F., Thames, F.C., and Mastin, C.W., "Boundary Fitted Curvilinear Coordinate Systems for Solution of Partial Differential Equations on Fields Containing Any Number of Arbitrary Two-Dimensional Bodies," *NASA - CR 2729*, 1977.

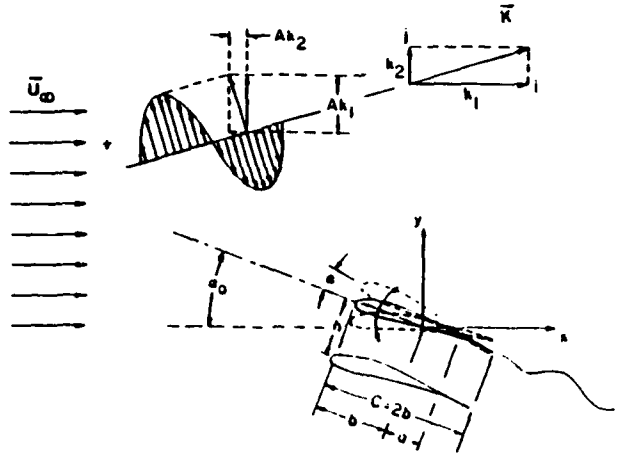

Figure 1. Flow of a Two-Dimensional Gust Past a Thick, Cambered, Oscillating Airfoil at Incidence to the Mean Flow

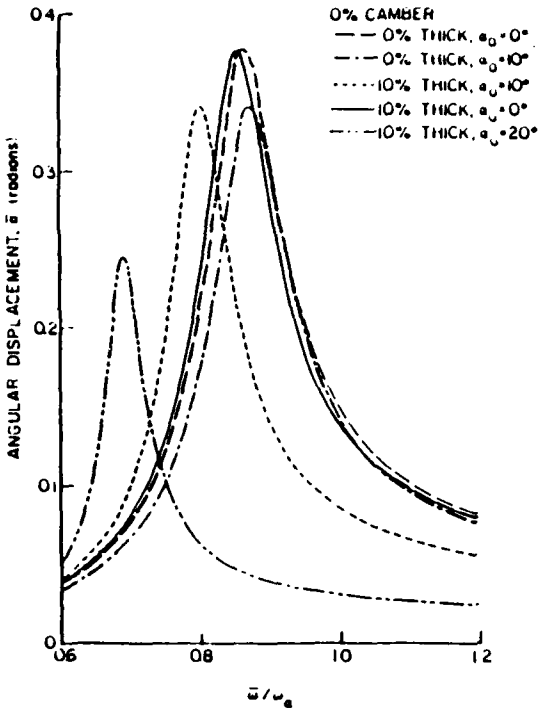

Figure 2. Thickness Effect on the Forced Response of a Flat Plate Airfoil due to a 90° Gust

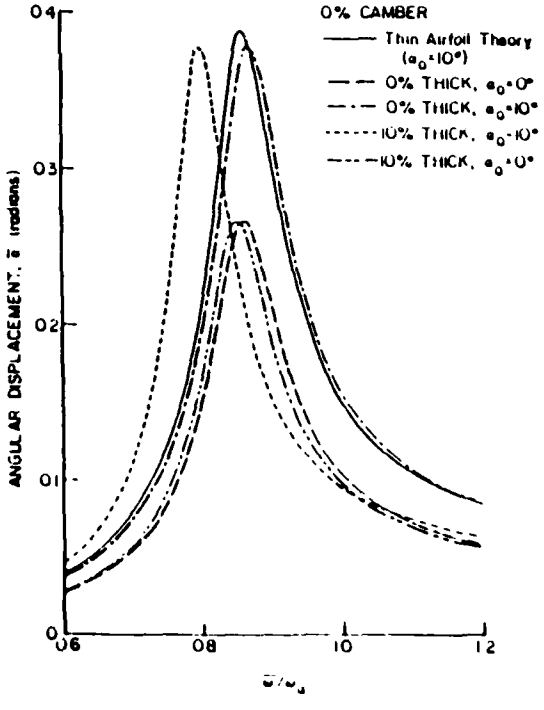

Figure 3. Thickness Effect on the Unsteady Lift of a Flat Plate Airfoil due to a 45° Gust

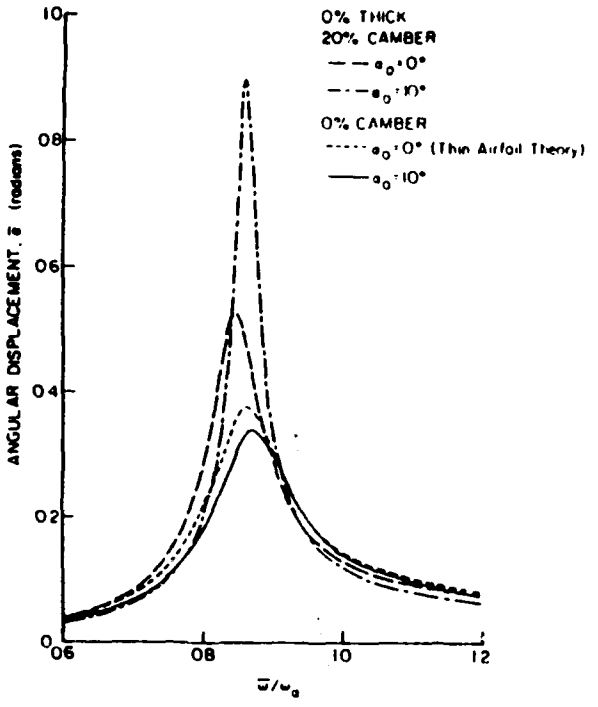

Figure 4. Effect of Camber and Mean Flow Incidence on the Forced Response of a Zero Thickness Airfoil due to a 90° Gust

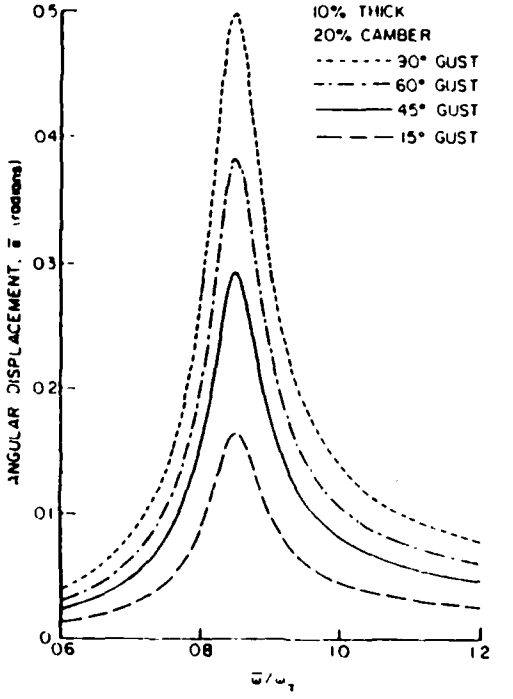

Figure 6. Gust Direction Effect on the Forced Response of a Cambered and Thick Airfoil at 0° of Incidence to the Mean Flow

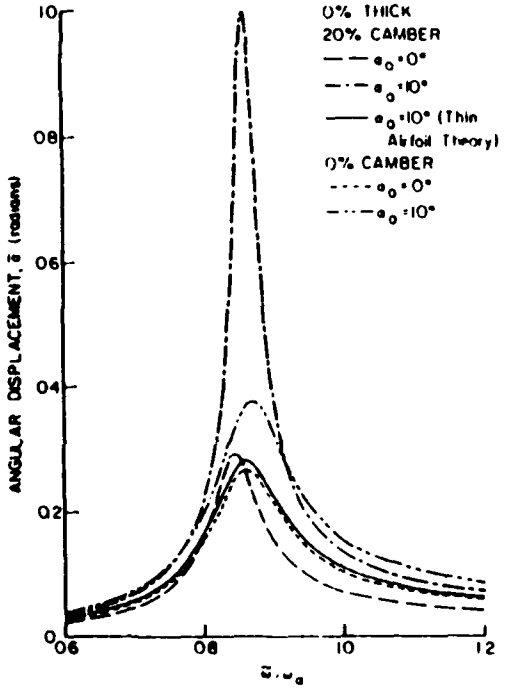

Figure 5. Effect of Camber and Mean Flow Incidence on the Forced Response of a Zero Thickness Airfoil due to a 45° Gust

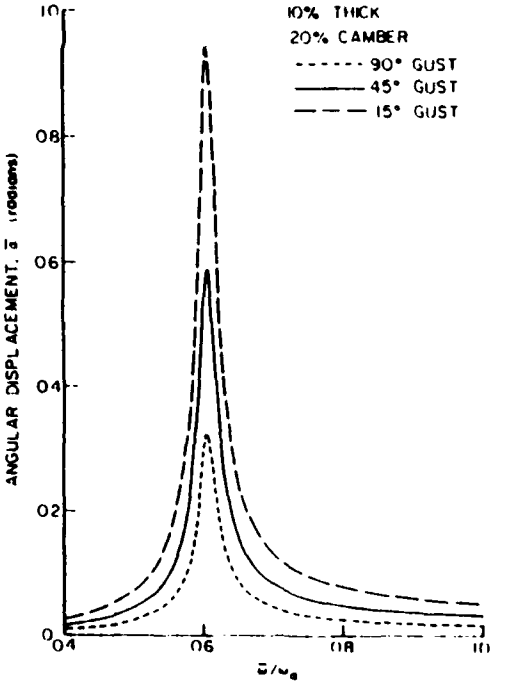

Figure 7. Gust Direction Effect on the Forced Response of a Cambered and Thick Airfoil at 20° of Incidence to the Mean Flow

END

DATE

FILMED

5-88

DTIC